

Integrated Optimisation for Dynamic Modelling, Path
Planning and Energy Management in Hybrid Race
Vehicles

by

Kieran Reeves MSc

Supervisor: Dr Allahyar Montazeri



Department of Engineering
Lancaster University

PhD Mechanical Engineering

October 2020

Lancaster University
Faculty of Science and Technology
Engineering Department

Declaration

I declare that this thesis consists of original work undertaken solely by myself at Lancaster University between 2013 and 2020 and has not been submitted elsewhere in substantially the same form for the award of a higher degree. Where work by other authors is referred to, it has been appropriately referenced. I confirm that I have read and understood the publication *Guidance on Writing Technical Reports* published by the Department.

Kieran Reeves



October 2020

Abstract

Simulation software has for many years been developed to enhance the research and development phase of new vehicle introductions. With the introduction of the testing embargo in most forms of world championship motorsport, model validation is a necessity. To optimise the unknown vehicle and tyre parameters and to reduce the error between measured and simulated data in such a multi-input multi-output non-convex optimisation problem, a novel multi-objective particle swarm optimisation (PSO) technique is applied to ensure a fully validated vehicle model is developed and analysed for speed and performance.

These optimisation algorithms are further developed to explore the trajectory planning problem to improve the lap time for the shortest path, minimum curvature and a combined approach, producing optimal racing line pathways and vehicle dynamic inputs and output responses by exploring trajectories and vehicle traction circle limits.

Finally, a hybrid electric vehicle transient dynamics model for the control of energy management is presented. The hybrid powertrain contains an internal combustion engine, kinetic energy recovery system and heat energy recovery system with deployment and harvesting control parameters.

The performance of single-objective and multi-objective particle swarm optimisation algorithms are compared and analysed. The proposed simulation model and optimisation techniques are applied to address an array of problems, including model validation, racing line trajectory design, fastest lap time problem, and energy management strategies. All results are validated and optimised with respect to the experimental data collected on the real track in Silverstone to ensure the results can be applied to physical real-world scenarios.

Keywords— Particle Swarm Optimisation; Parameter Estimation; Validation; Simulation; Trajectory Planning; Race Optimisation; Hybrid Electric Vehicles; Vehicle Dynamics; Energy Management Strategies; Hybrid Race Vehicles.

Acknowledgements

I would like to thank my Supervisors, firstly Dr Allahyar Montazeri. Your patience, education and understanding has been paramount to the completion of this thesis. Your advice and guidance throughout my studies have been encouraging and helped me forge new understanding in optimisation modelling and their algorithms.

Dr James Taylor, you have been an inspiration to me throughout my time at Lancaster from originally studying at master's level as it was you who encouraged me to start on a path towards a PhD. Your assistance with control algorithms helped me publish my first conference papers and allowed me to present around the world. Both of you have given tremendous support and assistance throughout this endeavour, and for that I am truly grateful.

Thanks go to my family who have supported me throughout my life and to my children for keeping quiet on those long study nights. Most importantly I want to thank my Wife, over many years of study, you have been my psychiatrist, best friend and soul mate. Even through the toughest tests and darkest times you have been an inspiration to me and taught me to always move forward, never give up and always fight on. This thesis would not have been possible or imaginable without your trust, love and support.

“If you always put limit on everything you do, physical or anything else. It will spread into your work and into your life. There are no limits. There are only plateaus, and you must not stay there, you must go beyond them.” (BL circa 1970)

I dedicate this thesis to you, Mrs Sara Reeves.

Table of Contents

1. INTRODUCTION	1
1.1 <i>Vehicle Dynamics</i>	2
1.2 <i>Hybrid Powertrains</i>	12
1.3 <i>Motivation</i>	14
1.4 <i>Contributions and Novelty</i>	16
1.5 <i>Aims & Objectives</i>	17
1.6 <i>Thesis Structure</i>	18
2. VEHICLE MODEL AND SIMULATION.....	20
2.1 <i>Introduction</i>	20
2.2 <i>Tyre models</i>	20
2.3 <i>Vehicle dynamics and variants of DOF</i>	28
2.4 <i>Energy management</i>	30
2.5 <i>Conclusion</i>	31
3. HYBRID RACE VEHICLE DYNAMIC MODEL	32
3.1 <i>Introduction</i>	32
3.2 <i>Vehicle Industry Standard Models</i>	32
3.3 <i>Chassis Model</i>	34
3.4 <i>Tyre Modelling</i>	36
3.5 <i>Load Transfer</i>	39
3.6 <i>Aerodynamics</i>	40
3.7 <i>Conclusion</i>	41
4. HYBRID RACE VEHICLE POWERTRAIN	42
4.1 <i>Introduction</i>	42
4.2 <i>The Formula One Powertrain</i>	43
4.3 <i>Powertrain</i>	47
4.4 <i>MGU Regeneration</i>	49
4.5 <i>GT Race Vehicle Hybrid Powertrain</i>	49
4.6 <i>Conclusion</i>	53
5. VEHICLE DYNAMIC PARAMETER ESTIMATION AND OPTIMISATION	55
5.1 <i>Introduction</i>	55
5.2 <i>Particle Swarm Optimisation for Vehicle Dynamic Validation</i>	55
5.3 <i>Multi Objective PSO Problem Formulation</i>	61
5.4 <i>Optimisation problem formulation</i>	76
5.5 <i>Performance tuning and optimisation</i>	77
5.6 <i>SOPSO versus MOPSO Comparison</i>	95
5.7 <i>Conclusion</i>	100
6. TRAJECTORY PLANNING AND OPTIMISATION	101
6.1 <i>Introduction</i>	101
6.2 <i>Trajectory Planning and Race Driver Simulation</i>	101

6.3	<i>Geometric Parameterisation</i>	102
6.4	<i>The Shortest Path Problem</i>	104
6.5	<i>The Minimum Curvature Problem</i>	108
6.6	<i>Circuit Discretisation and Performance Surfaces</i>	114
6.7	<i>Shortest Path Trajectory – Single Objective PSO</i>	122
6.8	<i>Minimum Curvature Trajectory</i>	134
6.9	<i>Multi Objective PSO</i>	142
6.10	<i>Dynamic Constraints</i>	149
6.11	<i>Optimum Trajectory and Lap Time</i>	153
6.12	<i>Conclusion</i>	166
7.	RACE CAR HYBRID ENERGY MANAGEMENT	168
7.2	<i>Hybrid Race Car Power Balance</i>	168
7.3	<i>Hybrid Race Car Power Characteristics for Deployment</i>	169
7.4	<i>Hybrid Energy Management Scenarios</i>	175
7.5	<i>Fuel Use Analysis of the Hybrid Race Vehicle</i>	191
7.6	<i>Fastest Lap Time of the Hybrid Vehicle</i>	196
7.7	<i>Conclusion</i>	200
8.	CONCLUSION AND FUTURE WORK	201
8.1	<i>Conclusion</i>	201
8.2	<i>Future Work</i>	205
	BIBLIOGRAPHY	206
	APPENDICES	216
	<i>Appendix 1 – Formula One Hybrid Powertrain Energy Flow</i>	216
	<i>Appendix 2. Comparison of Single objective PSO results versus simulated baseline data</i>	217
	<i>Appendix 3. Comparison of multi-objective PSO results versus simulated baseline data</i>	220
	<i>Appendix 4. MOPSO results versus SOPSO</i>	221
	<i>Appendix 5. Trajectory Parameters</i>	222
	<i>Appendix 6. Pareto front and trajectory plots</i>	224
	<i>Appendix 7. Hybrid Energy Management</i>	235
	<i>Appendix 8. Simulink Model with Hybrid Powertrain</i>	238
	<i>Appendix 9. Final Trajectory Plots</i>	242
	<i>Appendix 10 – Equations of Motion Derivation</i>	245

List of Figures

Figure 1.1 Co-ordinate axis of a vehicle (6DOF).....	2
Figure 1.2 Right-handed orthogonal rule.	3
Figure 1.3 Grading resistance applied to a vehicle travelling uphill.	4
Figure 1.4 Tyre pressure distribution for a static(a)and moving vehicle along a hard surface (b)..	5
Figure 1.5 Body shape versus drag coefficient.	6
Figure 1.6 The double-track vehicle model (6 DOF vehicle body).....	8
Figure 1.7 Vehicle under-steer, over-steer, neutral steer with defined critical and characteristic speed.	11
Figure 1.8 The architecture of a Parallel hybrid electric drivetrain.....	12
Figure 1.9 The architecture of a series hybrid electric drivetrain.....	13
Figure 1.10 The architecture of a series-parallel hybrid electric drivetrain.	14
Figure 2.1 The effect of tyre size and camber angle on tyre contact patch size.....	21
Figure 2.2 Tyre slip ratio under (a)deceleration, (b) acceleration, and slip angle (α) definition for (c) pure lateral and (d) combined longitudinal and lateral forces (d).....	22
Figure 2.3 Brush tyre model tread deflection, (a) motionless and (b) during acceleration.	23
Figure 2.4 Brush tyre model deflection during cornering (top) and combined deflection with braking and cornering (bottom).....	24
Figure 2.5 The mathematical development of the Pacejka curve profile (graphical example).	25
Figure 2.6 Lateral and longitudinal tyre forces versus slip ratio, slip angle and aligning torque.	27
Figure 2.7 The measured traction ellipse (G-G diagram) from a Lotus Evora GTE (note right hand corners are negative sign).	28
Figure 3.1 Vehicle dynamics sub-system components including powertrain and driver.	33
Figure 3.2 A comparison of linear tyre model output (red, dashed line) versus Pacejka tyre curve (blue, solid line) with regards to lateral force versus slip angle.	33
Figure 4.1 Motor Usage (60kW) creates 20kW at the crank-train.	46
Figure 4.2 3D CAD model of the intake and exhaust ports (top) and their transfer into GEM 3D for discretisation of pipes and flow splits to ensure accurate modelling in GT Power (1D engine simulation).	50
Figure 4.3 Normalised Power (blue line) and Torque (red line) curves for simulated GT Power model versus Cosworth dynamometer bench testing of the GLC engine.	52
Figure 5.1 Lateral acceleration for Abbey corner with regards to changes in inertia around the z-axis.....	66
Figure 5.2 Lateral acceleration for Village, The Loop/Arena section with regards to changes in inertia around the z-axis.	66
Figure 5.3 Effect of constant C_y ranging from 1 – 10 upon lateral acceleration through Abbey corner vs measured race car data.	67
Figure 5.4 Best results of roll stiffness and damping combined variance for Village/The Loop/Arena section with regards to (a) lateral acceleration, (b) roll velocity and (c) all results for roll velocity.....	68
Figure 5.5 Isometric and plan view of the performance surface for longitudinal acceleration of the error function ($e = \xi m - \xi d$; $J(K\phi, C\phi) = -e^2$) as a function of chassis damping and chassis stiffness through Abbey corner. Here ξm and ξd are the measured and simulated data.	70

Figure 5.6 Isometric and plan view of the performance surface for lateral acceleration of the error function ($e = \xi m - \xi d$; $J(K\phi, C\phi) = -e^2$) as a function of chassis damping and chassis stiffness through Abbey corner. Here ξm and ξd are the measured and simulated data..... 71

Figure 5.7 Isometric and plan view of the performance surface for yaw rate of the error function ($e = \xi m - \xi d$; $J(K\phi, C\phi) = -e^2$) as a function of chassis damping and chassis stiffness through Abbey corner. Here ξm and ξd are the measured and simulated data..... 72

Figure 5.8 Results of roll stiffness and damping combined variance for Village/The Loop section with regards to lateral acceleration, longitudinal acceleration, longitudinal velocity and yaw rate. Least error measured (red line) vs simulated data (blue line). 75

Figure 5.9 Lateral acceleration measured (red line) versus simulated (blue line) for an entire lap of the Silverstone Grand Prix Circuit. 75

Figure 5.10 Combined lateral and longitudinal tyre forces for a front left and front right tyre during the Village/Loop corners. The outside ellipse shows the peak combined force maxima taken from peak tyre forces within the measured vehicle data..... 76

Figure 5.11 Results of SOPS0 during variation of c_1 and c_2 where $c_1 = (0, 4, 10)$ and $c_2 = c_1 + c_2 = 4$ 77

Figure 5.12 Inertia weighting variation convergence during SOPS0 simulation for yaw rate during the Maggots/Becketts complex of corners. 79

Figure 5.13 Silverstone Grand Prix circuit using the Grand Prix paddock and pit lane. 80

Figure 5.14 Simulated output versus PSO model output after optimisation for longitudinal velocity during Abbey corner. 84

Figure 5.15 Simulated output versus PSO output for lateral acceleration during Abbey corner. .85

Figure 5.16 Simulated output versus PSO output for yaw rate during The Loop corner..... 85

Figure 5.17 Simulated output versus PSO output for longitudinal velocity during a full lap of the Silverstone GP circuit. Individual corner names denote the additional simulations performed during tuning of SOPS0..... 85

Figure 5.18 Simulated output versus SOPS0 output for lateral acceleration during a full lap of the Silverstone GP circuit. 86

Figure 5.19 Simulated output versus SOPS0 output for yaw rate during a full lap of the Silverstone GP circuit. 86

Figure 5.20 Partial mutation code, detailing change of μ from a fixed number to a random number per iteration. 92

Figure 5.21 Simulated output versus MOPSO output for longitudinal velocity during a full lap of the Silverstone GP circuit. 96

Figure 5.22 Simulated output results minus MOPSO output result ($V_{xSim} - V_x$) for longitudinal velocity during a full lap of the Silverstone GP circuit. 97

Figure 5.23 Simulated output versus MOPSO output for lateral acceleration during a full lap of the Silverstone GP circuit. 97

Figure 5.24 Simulated output results minus MOPSO output result ($A_{ySim} - A_y$) for lateral acceleration during a full lap of the Silverstone GP circuit..... 98

Figure 5.25 Simulated output versus MOPSO output for yaw rate during a full lap of the Silverstone GP circuit. 98

Figure 5.26 Simulated output results minus MOPSO output result ($Yaw_{Sim} - Yaw$) for yaw rate during a full lap of the Silverstone GP circuit. 99

Figure 5.27 Example of max variation (0.0001) of simulated vs MOPSO. 99

Figure 6.1 Inner, centre and outer parameterisation of Silverstone GP circuit. 103

Figure 6.2 Shortest path trajectory (white line) of Brooklands and Luffield corners of the Silverstone GP circuit.	104
Figure 6.3 Minimum curvature trajectory (white line) of Brooklands and Luffield corners of the Silverstone GP circuit.	108
Figure 6.4 Segmentation nomenclature between two points of the track.	109
Figure 6.5 (a) The definition of outer trajectory paths (red line) for $\alpha = 0$ (b) The definition of inner trajectory paths (red line) for $\alpha = 1$	115
Figure 6.6 Centre line trajectory for $\alpha = 0.5$	115
Figure 6.7 Section of the circular circuit with 361 segments (50 iterations, 100 population size for SOPSO).	116
Figure 6.8 Circular circuit. 50 segments (total) vs 50 iterations and 50 population size for SOPSO.	118
Figure 6.9 Silverstone Grand Prix circuit segmentation using 361 data points connecting the inner and outer boundaries of the circuit. Pink represents the inside boundary and blue the outside boundary.	119
Figure 6.10 Variation to α , performance surface for the left/right chicane (Vale), sections 335 and 336.	120
Figure 6.11 Performance surface for the left-handed Brooklands corner, sections 112 and 113.	121
Figure 6.12 Performance surface for the 1 st right-handed (Abbey) corner, sections 11 and 12.	121
Figure 6.13 Shortest Path Trajectory (red line) with 361 segmentation of the Silverstone GP Circuit.	124
Figure 6.14 Shortest path trajectory (red line) with 50 segmentation sectors of the Silverstone GP circuit. a) from the start/finish line through Abbey corner to f) Copse corner (the black arrow depicts direction of travel).	125
Figure 6.15 Shortest path trajectory (red line) with 50 segmentation sectors of the Silverstone GP circuit. a) from Maggotts and Becketts complex to d) Vale and Club corners to the start/finish line (the black arrow depicts direction of travel).	126
Figure 6.16 Shortest path trajectory (red line) with 50 segmentation sectors versus 30 segmentation sectors for Village, The Loop and Aintree corners. a) 50 segments ($\alpha = \text{rand}$). b) 50 segments, (segment 1, $\alpha = 1$, segments 2-49 $\alpha = \text{rand}$). c) 30 segments ($\alpha = \text{rand}$), The black arrow depicts direction of travel.	127
Figure 6.17 Shortest path trajectory (red line) with 30 segmentation sectors of the Silverstone GP circuit. a) From the start/finish line through Abbey corner to f) Copse corner (the black arrow depicts direction of travel).	130
Figure 6.18 Shortest path trajectory (red line) with 30 segmentation sectors of the Silverstone GP circuit. a) Copse corner to f) Vale and Club corners through to the start/finish line, (the black arrow depicts direction of travel).	131
Figure 6.19 Shortest path trajectory (red line) with 1 by 360 segmentation sector of the Silverstone GP circuit. SOPSO set to 50 iterations, 200 particles.	132
Figure 6.20 Shortest path trajectory (red line) with 1 by 360 segmentation sector of the Silverstone GP circuit. Detailed view of the Maggotts, Becketts and Chapel series of corners. SOPSO set to 50 iterations, 200 particles, (the black arrow depicts direction of travel).	132
Figure 6.21 Shortest path trajectory (red line) with 1 by 360 segmentation sector of the Silverstone GP circuit. SOPSO set to 50 iterations, 800 particles.	133

Figure 6.22 Shortest path trajectory (red line) with 1 by 360 segmentation sector of the Silverstone GP circuit. Detailed view of the Maggotts, Becketts and Chapel series of corners. SOPSO set to 50 iterations, 800 particles, (the black arrow depicts direction of travel).	133
Figure 6.23 30 segments of a 360 segments (total) circular circuit. Inside and outside trajectory (red line) returning a curvature of 0.0034421 and 0.003333 respectively.	134
Figure 6.24 Trajectory of 30 segments of a 360-segment circular track. Curvature result of 0.008637.	135
Figure 6.25 Fitness function development across 50 iterations (200 population) of 360 segment circular track. Curvature result of 0.008637.	135
Figure 6.26 Minimum curvature trajectory (red line) with 50 segmentation sectors of the Silverstone GP circuit. From a) the start/finish line and Abbey corner to f) Copse corner, (the black arrow depicts direction of travel).	137
Figure 6.27 Minimum curvature trajectory (red line) with 30 segmentation sectors of the Silverstone GP circuit. a) Copse corner back to f) the start/finish line, (the black arrow depicts direction of travel).	138
Figure 6.28 Minimum curvature trajectory (red line) with 1 by 360 segmentation sector of the Silverstone GP circuit. SOPSO set to 50 iterations, 200 particles.	139
Figure 6.29 Minimum curvature fitness function versus iteration number (Test 15) with 1 by 360 segmentation sector of the Silverstone GP circuit. SOPSO set to 50 iterations, 200 particles. ..	140
Figure 6.30 Minimum curvature trajectory (red line) with 1 by 360 segmentation sector of the Silverstone GP circuit. SOPSO set to 50 iterations, 800 particles.	141
Figure 6.31 Minimum curvature fitness function vs iteration number (Test 16) with 1 by 360 segmentation sector of the Silverstone GP circuit. SOPSO set to 50 iterations, 800 particles. ..	141
Figure 6.32 MOPSO pareto front for Abbey and Farm corners.	143
Figure 6.33 a) SOPSO shortest path and b) SOPSO minimum curvature trajectory comparison with c) MOPSO best shortest path trajectory result, d) MOPSO best minimum curvature result and e) mid-pareto trajectory result for Sector 1.	147
Figure 6.34 a) SOPSO shortest path and b) SOPSO minimum curvature trajectory comparison with c) MOPSO best shortest path trajectory result, d) MOPSO best minimum curvature result and e) mid-pareto trajectory result for Sector 8.	148
Figure 6.35 Velocity(m/s) vs steering angle (rad), at the wheels, vs lateral acceleration (m/s ²).	150
Figure 6.36 Plan view of velocity(m/s) vs steering angle (rad), at the wheels, vs lateral acceleration (m/s ²).	150
Figure 6.37 Velocity(m/s) vs steering angle (rad), at the wheels, vs lateral acceleration (m/s ²) smoothed data.	151
Figure 6.38 Plan view of velocity(m/s) vs steering angle (rad), at the wheels, vs lateral acceleration (m/s ²).	151
Figure 6.39 Maximum acceleration from 0 to 70 m/s with zero radians of steering through all 6 gears.	152
Figure 6.40 Maximum deceleration from 70 to 0 m/s with zero radians of steering.	152
Figure 6.41 Lap time vs iteration for shortest path SOPSO.	154
Figure 6.42 The vehicle dynamic output for a) Vehicle velocity, b) steering input, c) lateral acceleration and d) longitudinal acceleration vs distance for an ICE only race vehicle around Silverstone GP circuit (shortest path trajectory). Best lap time (blue line) versus best shortest path length (red line)	155

Figure 6.43 a) Distance variation and error variance between best lap fitness function versus trajectory length fitness function for b) vehicle velocity, c) steering input, d) lateral acceleration and e) longitudinal acceleration for an ICE only race vehicle around Silverstone GP.	156
Figure 6.44 Lap time vs iteration for the minimum curvature SOPSO.	157
Figure 6.45 a) Vehicle velocity, b) steering input, c) lateral acceleration and d) longitudinal acceleration vs distance for an ICE only race vehicle around Silverstone GP circuit (minimum curvature trajectory).	158
Figure 6.46 a) Distance variation and error variance between best lap fitness function versus trajectory curvature fitness function for b) vehicle velocity, c) steering input, d) lateral acceleration and e) longitudinal acceleration for an ICE only race vehicle around Silverstone GP.	159
Figure 6.47 Lap time vs distance for shortest path and minimum curvature SOPSO.	160
Figure 6.48 Three-dimensional pareto front, MOPSO.	162
Figure 6.49 Parallel plot results - curvature vs distance vs lap time (Blue = Best 10%).	163
Figure 6.50 MOPSO trajectory (red line) with 1 by 360 segmentation sector of the Silverstone GP circuit.	164
Figure 6.51 a) Vehicle velocity, b) steering input, c) lateral acceleration and d) longitudinal acceleration vs distance for an ICE only race vehicle around Silverstone GP circuit.	165
Figure 6.52 Spline interpolated and smoothed trajectory for the combined trajectory MOPSO.	165
Figure 6.53 Trajectory variation with $\alpha = \text{rand}$ (to 4d.p).	166
Figure 6.54 MOPSO vs Measured Evora GTE Data. a) Vehicle velocity, b) steering input, c) lateral acceleration and d) longitudinal acceleration vs distance for an ICE only race vehicle around Silverstone GP circuit. MOPSO vehicle dynamic output (red line) versus physical measured race car data (blue line)	167
Figure 7.1 Example controller parameters for regeneration and hybrid power deployment, single MGU-K (non-MGU-H).	171
Figure 7.2 Example controller parameters for regeneration and hybrid power deployment, MGU-K/MGU-H system.	171
Figure 7.3 Battery usage during the best lap time (2.08.979) shortest path trajectory, (the black line depicts the maximum power deployment usage allowed).	173
Figure 7.4 a) SOC, b) Motor Power (kW), c) Regen Power(kW) and d) Charge Status (MJ) usage during the best lap time (2.08.979) using trajectory results from the shortest path MOPSO presented in section 6.11.1.	174
Figure 7.5 a) SOC, b) motor power (kW), c) regeneration power (kW) and d) charge status (MJ) usage during the charge depletion strategy utilising the 2.02.10s lap-time trajectory results.	178
Figure 7.6 Motor power (red) and regeneration power (green) along with the vehicle velocity.	178
Figure 7.7 Total energy, Net energy deployment and regenerated energy.	179
Figure 7.8 Total energy flow, total energy deployment and regenerated energy. (The black line depicts total permissible energy deployment over a single lap).	180
Figure 7.9 a) SOC, b) motor power (kW), c) regeneration power (kW) and d) charge status (MJ) for charge sustaining control utilising the 2.02.10s lap-time trajectory results.	182
Figure 7.10 Charge sustaining motor power (red) and regeneration power (green) along with the vehicle velocity.	183
Figure 7.11 Total energy, net energy deployment and regenerated energy for the charge sustaining scenario.	184

Figure 7.12 Total energy flow, total energy deployment and regenerated energy for the charge sustaining scenario (the black line depicts total permissible energy deployment over a single lap).	184
Figure 7.13 a) SOC, b) motor power (kW), c) regeneration power (kW) and d) charge status (MJ) usage for charge depletion during a lap time of 2.02.106.	186
Figure 7.14 Motor power (red) and regeneration power (green) for the charge depleting scenario along with the vehicle velocity.....	187
Figure 7.15 Total energy, net energy deployment and regenerated energy for the charge depleting scenario.....	187
Figure 7.16 Total energy flow, total energy deployment and regenerated energy for the charge depleting scenario (the black line depicts total permissible energy deployment over a single lap).	188
Figure 7.17 a) SOC, b) motor power (kW), c) regeneration power(kW) and d) charge status (MJ) for maximum deployment scenario during the best lap time (2.02.106).....	189
Figure 7.18. Motor power (red) and regeneration power (green) for the maximum deployment scenario along with the vehicle velocity.	190
Figure 7.19 Total energy, net energy deployment and regenerated energy for the maximum permissible deployment scenario.	190
Figure 7.20 Total energy flow, total energy deployment and regenerated energy for the maximum permissible deployment scenario (the black line depicts total permissible energy deployment over a single lap).....	191
Figure 7.21 Transient engine RPM and throttle sites vs brake specific fuel consumption.	193
Figure 7.22 Hybrid Powertrain - normalised power and torque deployment.....	194
Figure 7.23 Engine power and torque; normalised total use with hybrid Motor ON = Normalised Engine Power - Normalised Motor Power.	195
Figure 7.24 Maximum longitudinal acceleration for 100% ICE and Motor deployment.	196
Figure 7.25 Three-dimensional pareto front achieved by running MOPSO algorithm under the maximum permissible deployment scenario.	197
Figure 7.26 Parallel plot results for 5.3MJ deployment, curvature vs distance vs lap time (Orange = Best 50%).	198
Figure 7.27 The final trajectory achieved after optimisation via MOPSO algorithm and smoothed via the spline method (1.58.371 lap time).	199
Figure 7.28 Vehicle dynamic outputs, a) vehicle velocity and b) longitudinal acceleration, utilising additional hybrid power (blue line) vs integrated hybrid power (red line).	199

List of Tables

Table 1.1 Typical rolling resistance co-efficient for tyres on various road surfaces [3].	5
Table 3.1 Dot product assignment.	35
Table 4.1 RPM versus permissible fuel flow [kg/h].	45
Table 4.2 Normalised fuel flow (permissible Engine sites in green).	45
Table 4.3 Engine Architecture of GLC107.	51
Table 4.4 Power and torque error for all RPM thresholds - simulated engine versus Cosworth dynamometer test results.	52
Table 4.5 GLC 4.0L normally aspirated fuel flow (kg/h) versus engine speed and throttle position.	53
Table 5.1 Pacejka tyre curve factors and their coefficients.	59
Table 5.2 Initial Sensitivity Analysis Parameters and Variance	65
Table 5.3 Final results for chassis stiffness and damping with norm 2 cost function for Abbey and Village/The Loop corners at the Silverstone Grand Prix circuit.	73
Table 5.4 SOPSO results of Abbey corner for longitudinal velocity, lateral acceleration and yaw rate. Error = error of measured and simulated PSO output.	81
Table 5.5 SOPSO results of The Loop corner for longitudinal velocity, lateral acceleration and yaw rate. Error = error of measured and simulated PSO output.	81
Table 5.6 SOPSO results of Luffield corner for longitudinal velocity, lateral acceleration and yaw rate. Error = error of measured and simulated PSO output.	81
Table 5.7 SOPSO results of Maggots/Becketts complex of corners for longitudinal velocity, lateral acceleration and yaw rate. Error = mean square error of measured and simulated PSO output.	82
Table 5.8 SOPSO results of Vale corner for longitudinal velocity, lateral acceleration and yaw rate. Error = error of measured and simulated PSO output.	82
Table 5.9 SOPSO results of a lap of the Silverstone GP circuit for longitudinal velocity, lateral acceleration and yaw rate. Error = error of measured and simulated PSO output.	82
Table 5.10 Variation in results of best cost and output mean square error for longitudinal velocity, lateral acceleration and yaw rate for the Silverstone GP circuit. (for p-norm equal to inf, 1 and 2).	87
Table 5.11 Multi-objective and single-objective algorithm run times.	89
Table 5.12 Best cost and mean square error for multi-objective algorithm.	90
Table 5.13 Variation in MOPSO results of best cost and output mean square error for longitudinal velocity, lateral acceleration and yaw rate for the Silverstone GP circuit. (p-norm = inf, 1 and 2).	90
Table 5.14 Difference of linearly decreasing pm and random pm during a 50-iteration optimisation simulation.	93
Table 5.15 Comparison of best cost, mean square error and parameter estimation error (including error based on Equation 5.13).	94
Table 5.16 Comparison of multi-objective and single-objective algorithm simulation parameter estimation. Sum of total errors.	95
Table 5.17 Final tuned MOPSO, best cost and errors versus tuned SOPSO.	100
Table 6.1 A sample of PSO tuning tests (best costs = green, variation from baseline = blue).	117

Table 6.2 Variations to PSO parameters as tested individual samples versus baseline.	122
Table 6.3 A sample of PSO tuning tests (best costs = green, variation from baseline = blue). ..	123
Table 6.4 Summation of 361 and 500 segment track discretisation with singular, fifty and thirty segment sector splits.	129
Table 6.5 SOPSO curvature result, iteration number at best result, number of variables (segments), sector number, outside and inside path curvature and run time for each section of the Silverstone GP circuit.	136
Table 6.6 SOPSO curvature result, iteration number at best fitness function, number of variables (segments), sector number, outside and inside path curvature and run time for a full lap of the Silverstone GP circuit.	142
Table 6.7 MOPSO and SOPSO results including minimum curvature result and shortest path result for best minimum curvature, best shortest path and mid-pareto point.	144
Table 6.8 Error of MOPSO results versus SOPSO results. Best minimum curvature and best shortest path.	145
Table 7.1 Initial scenario used for energy management evaluation.	172
Table 7.2 Charge depleting scenario used for energy management evaluation.	177
Table 7.3 The result of energy charge depletion over one lap of Silverstone GP circuit.	177
Table 7.4 Charge sustaining scenario used for energy management evaluation.	181
Table 7.5 The energy usage and regeneration results for the charge sustaining scenario over one lap of Silverstone GP circuit.	182
Table 7.6 Maximum depletion scenario used for energy management evaluation.	185
Table 7.7 Energy usage, one lap of Silverstone GP circuit - charge depleting.	186
Table 7.8 5.3MJ depletion scenario used for energy management evaluation.	188
Table 7.9 Energy usage, one lap of Silverstone GP circuit - 5.3MJ charge depleting.	189
Table 7.10 Fuel saving over one lap of Silverstone GP for various hybrid strategies.	195

List of Abbreviations, Symbols and Acronyms

A_f	Vehicle frontal area
BOP	Balance of Performance
BSFC	Brake specific fuel consumption
C_D	Coefficient of drag
C_{DF}	Coefficient of downforce
CoG	Centre of gravity
CoP	Centre of pressure
C_α	Cornering stiffness of the tyre
C_ϕ	Total roll damping
D_A	Aerodynamic drag
D_{AF}	Aerodynamic drag (front)
D_{AR}	Aerodynamic drag (rear)
D_{AR_DRS}	Aerodynamic drag during DRS operation (rear)
DF_A	Aerodynamic downforce
DF_F	Aerodynamic downforce (front)
DF_R	Aerodynamic downforce (rear)
DF_{R_DRS}	Aerodynamic downforce during DRS operation (rear)
DOF	Degrees of freedom
DR	Total drive ration of the gearbox and final drive
D_x	Tyre coefficient (longitudinal)
D_y	Tyre coefficient (lateral)
EoT	Equivalence of Technologies
FIA	Fédération Internationale de l'Automobile
FL	Front left
FR	Front right
\dot{F}	Normalised fuel flow

F_r	Resistance (total)
F_t	Tractive effort (total)
F_x	Longitudinal force from tyre
F_{x_0}	Pure longitudinal force from tyre (Pacejka model)
F_{xT}	Total longitudinal force on the body
F_y	Lateral force from tyre
F_{y_0}	Pure lateral force from tyre (Pacejka model)
F_{yT}	Total lateral force on the body
GR	Total gear ratio (gear ratio x final drive ratio)
ICE	Internal combustion engine
I_i	Inertia around the appropriate axis
I_n	Algorithm assignment for reduction of algebraic form
ICE_{RPM}	Engine speed in revolutions per minute
K	Gear ratio ICE to MGU-K
K_ϕ	Total roll stiffness
MGU	Motor/Generator unit
MGU-H	Motor/Generator unit – Heat (turbocharger)
MGU-K	Motor/Generator unit – Kinetic
M_z	Total aligning torque on body
Nm	Newton meter
P_{BICE}	Internal combustion engine power (boosted)
PHEV	Plug-in Hybrid Electric Vehicle
P_{ICE}	Internal combustion engine power
P_{MGU_H}	Power output of the MGU-H
P_{MGU-H}^{add}	Additional power at the crank-train via MGU-H
P_{MGU-H}^{max}	Maximum power output of the MGU-H (motor)
P_{MGU-H}^{min}	Minimum power output of the MGU-H (generator)
P_{MGU-K}	Kinetic Motor/Generator unit power
P_{PT}	Total powertrain power output
PSO	Particle Swarm Optimisation

R	Rolling radius of tyre
R	Radius of corner or segment of track
RL	Rear Left
RR	Rear right
RPM	Revolutions per minute
S_f	Stability factor
T	Trajectory of the corresponding position
T_{ICE}	Internal combustion engine torque
T_{MGU-K}	Kinetic Motor/Generator unit torque
T_{PT}	Total powertrain torque output
T_{reduc}	Total aerodynamic reduction across the entire body (%)
T_{shaft}	Torque at differential output shaft
T_{wheel_i}	Torque delivered to a specific driven wheel
T_{dist}	Torque distribution to drive shafts (%)
V	Vehicle speed
V_w	Headwind velocity
V_x	Vehicle longitudinal velocity
\dot{V}_x	Longitudinal Acceleration
V_y	Lateral Velocity
\dot{V}_y	Lateral Acceleration
W_c	Wheel circumference (including tyre)
$W_{d_rl_i}$	Weight distribution right/left (%)
$W_{d_fr_i}$	Weight distribution front/rear (%)
W_g	Waste-gate position
W_{RPM}	Wheel speed in revolutions per minute
X	Longitudinal Displacement
Y	Lateral Displacement
a	Distance from front axle to CoG
b	Distance from rear axle to CoG

i	assignment of wheels and axis
h	Height of CoG
l	Distance from tyre centre line to CoG
m	Vehicle mass
s	length of curvature for segment.
wb	wheelbase
w_f	Half-track width (front)
w_r	Half-track width (rear)
x	Local direction (longitudinal)
y	Local direction (lateral)
z	Local direction (vertical)
Ω	Rotational velocity of the wheel (rad/s)
Ω_{ICE}	Internal combustion engine speed (RPM)
Ω_{MGU-K}	Kinetic Motor/Generator Unit speed (RPM)
α	Road angle
α_i	Slip angle
α_{TPS}	Throttle position angle
δ	Steering angle at tyre
η_{Gbox}	Mechanical efficiency of the gearbox
κ	Slip ratio
μ_p	Peaking tyre traction coefficient
μ_s	Slipping tyre coefficient
π	Pi (3.142)
ρ	Air density
ϕ	Roll Displacement
$\dot{\phi}$	Roll Velocity
$\ddot{\phi}$	Roll Acceleration
ψ	Yaw Displacement
$\dot{\psi}$	Yaw Velocity

$\ddot{\psi}$	Yaw Acceleration
θ	Angle of segment between position one (P_1) and two (P_2).
ω_{ICE}	Internal combustion engine speed (radians per second)
ω_i	Angular velocity of tyre

1. Introduction

This introductory chapter explains the basic fundamentals of Vehicle Dynamics and stability, hybrid powertrain architecture and electrical energy flow within a hybrid vehicle system. The motivation for the thesis is discussed and the simulation validation, optimisation and control problems are presented. The literature utilised during the thesis is discussed and personal contributions are included. An outline of the remaining chapters is given to conclude the chapter. This thesis firstly develops a twenty-degree of freedom vehicle dynamics model: four degrees of freedom for the vehicle body (longitudinal, lateral, yaw and heave) and 4 degrees of freedom for each tyre (longitudinal, lateral, aligning and vertical force, to mimic race vehicle behaviour. This model is firstly validated against measured race vehicle data and unknown parameters are optimized through the development of a particle swarm optimisation algorithm. This model is then expanded to develop optimisation algorithms through a curvilinear abscissa approach [1], to produce race circuit topology and to optimize the ideal racing line for optimal lap time. Finally, energy management and transient vehicle dynamic and powertrain modelling of a Hybrid race vehicle is investigated using Particle Swarm Optimisation (PSO) algorithms to determine the ideal strategy for energy deployment whilst maintaining an appropriate vehicle motion for best lap times.

The race vehicle model is based on the Federation Internationale de l'Automobile (FIA) 2019 Formula One powertrain architecture and energy flow constraints [2] with some amalgamation to the 2019 Hybrid Le Mans Prototype [60] vehicles to allow a potential new Hybrid GT era to be optimised for inclusion in the 2021 or beyond World Endurance Championship. The powertrain consists of an internal combustion engine, a kinetic energy recovery system and a thermal energy recovery system. In the Formula One race series the motor/generator alone is not permitted to power the wheels and thus places the vehicle into the parallel hybrid drivetrain category [3].

1.1 Vehicle Dynamics

When a vehicle is travelling along a road it is subject to forces both acting upon the vehicle (resistive) and the vehicle acting upon the world (tractive). The vehicles movement and forces act in all three directions (Figure 1.1). The vehicle can be subject to linear movement: longitudinal (x), lateral (y) and vertical (z), and also turning forces around these axes: roll; about the longitudinal axis, pitch; about the lateral axis and yaw; about the vertical axis.

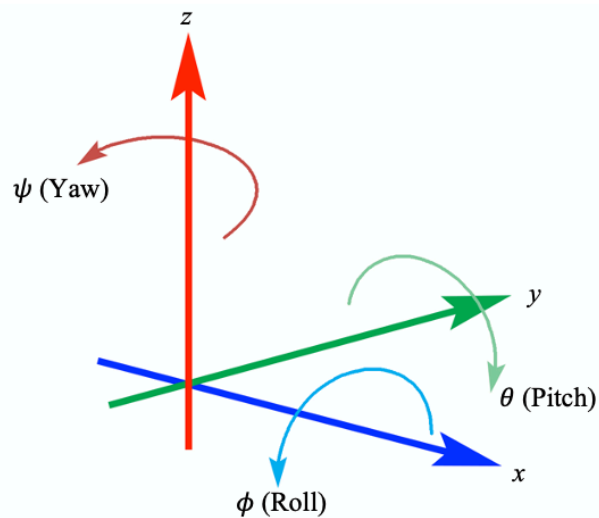


Figure 1.1 Co-ordinate axis of a vehicle (6DOF).

A right-handed orthogonal system is implemented (Figure 1.2) such as that a positive rotation about y rotates z into x, thus when the vehicle is on a flat road the x-axis is horizontal and forward is positive, the positive y-axis points away to the driver's left and the positive z-axis is upward. Anti-Clockwise rotation (yaw) when viewed from above is defined as positive such as when the vehicle enters a left-hand turn, positive pitch occurs during deceleration and weight is transferred to the front of the vehicle (under acceleration negative pitch would occur), and positive roll is to the right when the vehicle is viewed from behind [4].

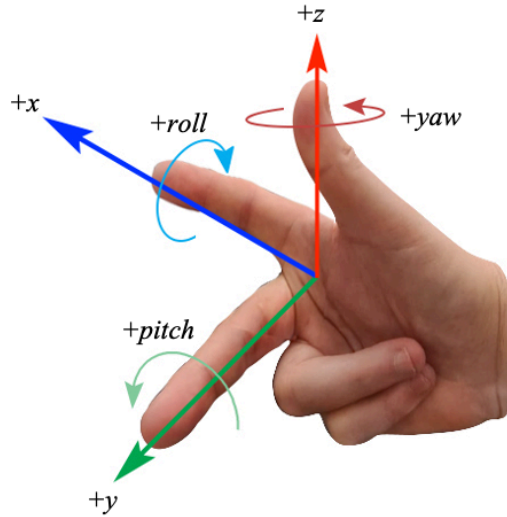


Figure 1.2 Right-handed orthogonal rule.

The vehicle's tractive force is subject to its mass and acceleration, such as defined by Sir Isaac Newton in his second law [5], force is equal to mass multiplied by the acceleration. Therefore, vehicle acceleration can be defined as:

$$\frac{dV}{dt} = \frac{\sum F_t - \sum F_r}{m} \quad (1.1)$$

where

V = Vehicle speed

F_t = Tractive effort (total)

F_r = Resistance (total)

m = Vehicle mass

Vehicle resistance is described as the total forces opposing the vehicle movement; this could be in the form of road gradient (uphill) resistance, aerodynamic drag and rolling resistance of the tyre at the road surface. When a vehicle is travelling along a gradient the vehicle mass will always produce a force in the downward direction (Figure 1.3), this either aids the vehicle if it is travelling downhill or opposes the forward movement when travelling up-hill. This grading resistance with a road angle (α) is expressed in Eqn. 1.2:

$$F_g = M \sin \alpha \quad (1.2)$$

1.1.1 Rolling resistance

The rolling resistance of a vehicle is typically due to the tyre contact patch with the road and the hysteresis of the tyre compound and materials [6]. When a tyre sits on a hard road surface the tyre pressure distribution tends to deflect as shown in (a) of Figure 1.4 and during forward motion the pressure distribution will deflect similar to (b). The tyre will also deform due to impact with raised objects such as kerbs parameterising the edge of the racing circuit on a corner. The rolling radius (r_d) depicted in Figure 1.4 is also subject to change due to acceleration forces and compression of the tyre. Suitable vehicle dynamic behaviour can be simulated without the inclusion of vertical tyre deformation within the tyre model.

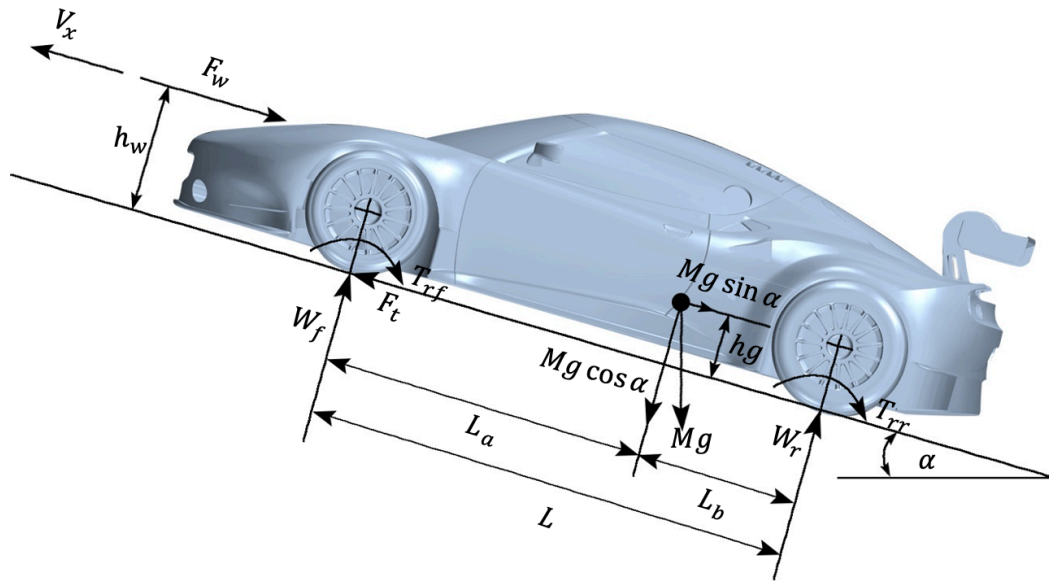


Figure 1.3 Grading resistance applied to a vehicle travelling uphill.

Tyre adhesion and grip is commonly modelled using a brush tyre model [7]. The brush tyre model was one of the first tyre models produced and the origin of every tyre model currently in use can be linked back to the brush model [9] in that two processes within the brush model are assumed for the tyre generating grip; i) shear stiffness of the tyre in contact with the ground causes

resistance; and ii) a sliding tyre causes friction. Three types of tyre model without deformation characteristics are such as those presented in [6, 8, 9] with the inclusion of road adhesion coefficients to mimic that of road surface qualities. This rolling resistance coefficient is a function of the tyre properties and environmental conditions, particularly; tyre materials, structure, tread pattern, tyre pressure, temperature, road material and the road adhesion qualities, for example the presence of rain or spilled liquids (Table 1.1). It is important to note tyre models can be extremely detailed and could be the work of a complete thesis project alone.

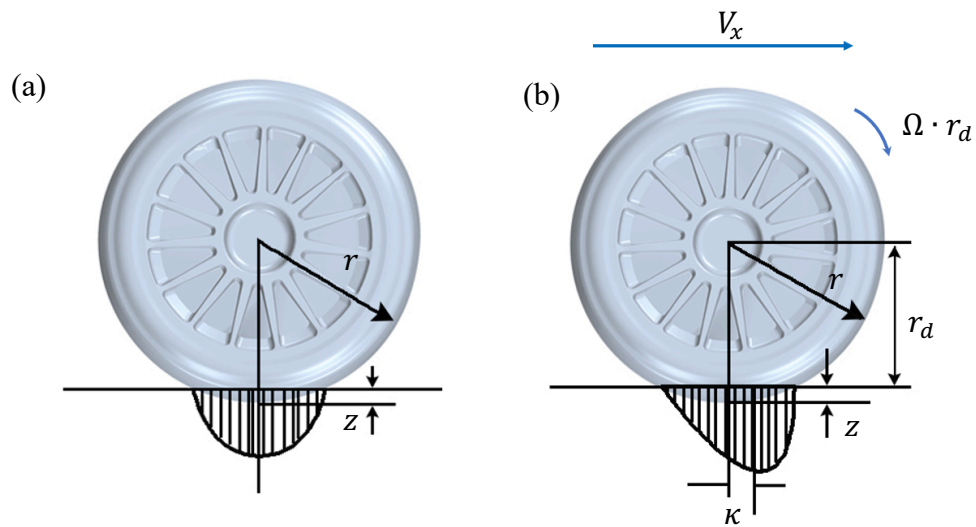


Figure 1.4 Tyre pressure distribution for a static(a)and moving vehicle along a hard surface (b).

Table 1.1 Typical rolling resistance co-efficient for tyres on various road surfaces [3].

Condition	Co-efficient
Car tyres on a concrete or asphalt road	0.013
Car tyres on a rolled gravel road	0.02
Tar macadam road	0.025
Unpaved road	0.05
Field	0.1-0.35
Truck tyre on a concrete or asphalt road	0.006-0.01
Wheel on iron rail	0.001-0.002

Some models include tyre pressures and temperature variations and their effect on grip [27,28]. The complete tyre model is detailed in Chapter 3 and the tyre modelling literature is discussed in Chapter 2. However, for this project tyre temperatures and pressures are ignored and it is assumed the vehicle is in the normal tyre operating range.

1.1.2 Aerodynamics

When a vehicle is in motion, the air that surrounds it acts as a force upon the vehicle's body and floor. This can be in the form of down-force; air pressure in the negative vertical (z-axis) direction to aid handling, lift; air pressure in the positive vertical direction trying to push the car up from the road and finally as a resistance to the forward motion (x-axis), this force is known as aerodynamic drag (negative x). Drag is a function of the environment (air density), the vehicle body shape and its coefficient of drag, the frontal area and the vehicle speed. The drag on a vehicle can differ drastically even for vehicles with the same frontal area, (Figure 1.5). Aerodynamic drag (D_A) and downforce (DF_A) are presented in equations (1.3) and (1.4) respectively:

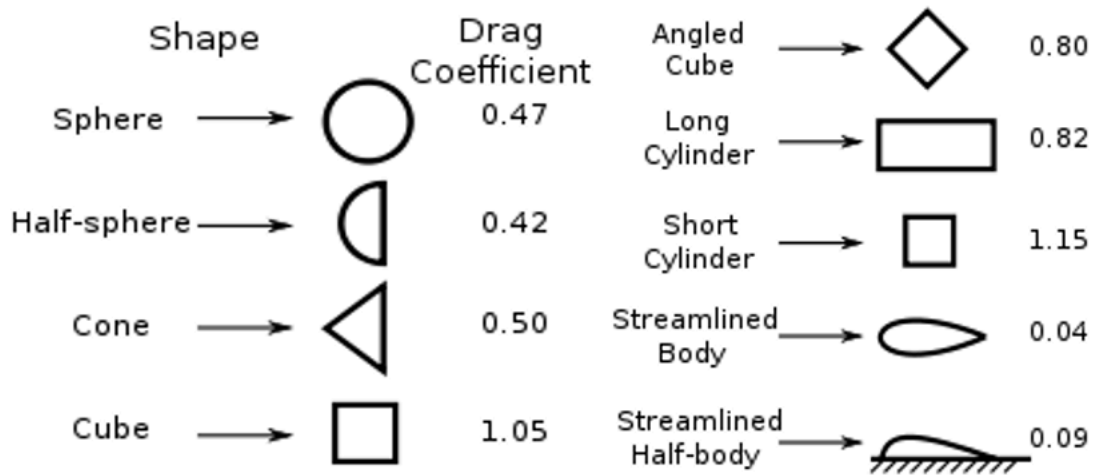


Figure 1.5 Body shape versus drag coefficient.

$$D_A = 0.5\rho A_f C_D V_x^2 \quad (1.3)$$

$$DF_A = 0.5\rho A_f C_{DF} V_x^2 \quad (1.4)$$

where

ρ = Air density

A_f = Vehicle frontal area

C_D = Coefficient of drag

C_{DF} = Coefficient of downforce

V_x = Vehicle longitudinal velocity

The headwind speed (V_w) is also a resistive force and thus also influences the aerodynamic drag. This can be accounted for by subtracting headwind speed from the vehicle speed:

$$D_A = 0.5\rho A_f C_D (V_x^2 - V_w)^2 \quad (1.5)$$

1.1.3 Vehicle Dynamics

Vehicle Dynamic studies tend to use various forms of modelling concepts with several variations to degrees of freedom utilised as will be discussed in Chapter 2. Single track, lumped mass vehicle model simulations can be very effective at producing fast, consistent results for lateral acceleration within a 2-6% tolerance of measured vehicle data [1, 10, 11, 12,]. Single-track models commonly known as the bicycle model tend to be used for steady state analysis and are limited in their degrees of freedom, no roll behaviour or longitudinal acceleration, for instance. For this study, where race circuit position of all four wheels is beneficial and roll dynamics are required for vertical force calculations upon a tyre, a double-track vehicle is utilised, (Figure 1.6), as per the majority of

literature available into vehicle dynamic studies [4, 13, 14]. As can be seen in Figure 1.6 longitudinal force (F_x) is in line with the rim and (F_y) is perpendicular to the rim. It should be noted that the direction of travel of the wheel hub can be different from the direction of the force due to slip angles. In models where a double track vehicle is utilised, but Ackerman angle is omitted $\delta_1 = \delta_2$.

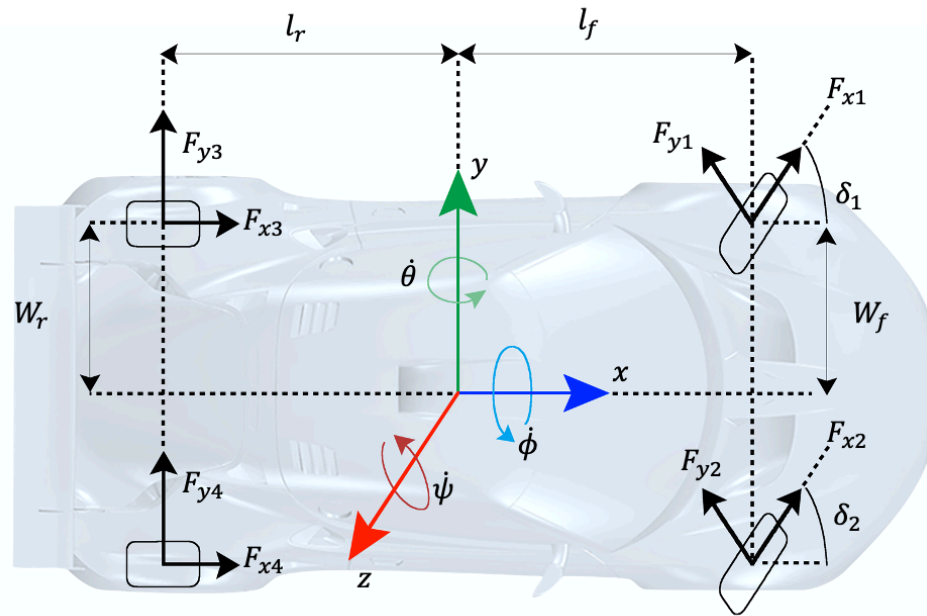


Figure 1.6 The double-track vehicle model (6 DOF vehicle body).

The four degrees of freedom utilised within the body of the vehicle dynamics model are longitudinal motion, lateral motion, yaw motion and roll motion, vertical motion and pitch are negated due to computing performance and time usage of modelling suspension components. The four degrees of freedom model is chosen as an improvement step from the two degrees of freedom and lumped mass models. It will still take some features from the lumped mass model in that Ackermann steering is negated and one steering angle is defined. It is acknowledged that the 4DOF will still contain a reasonably accepted error to a real-world scenario, but it is a sacrifice in order to reduce model complication as during the particle swarm optimisation (PSO) simulations the vehicle dynamic model will have to run 5000 times (50 particles, 100 iterations) and upwards as the PSO is expanded. The equations of motion are described in equations 1.6 – 1.9 respectively and fully derived in Appendix 10. Accelerations for yaw and roll are accented with a double dot and single dot for longitudinal and lateral acceleration:

$$\dot{V}_x = \frac{F_{xT}}{m} + V_y \dot{\psi} - h \sin \phi \left(\frac{M_z - F_{xT} h \sin \phi - 2(I_{yy} - I_{zz}) \sin \phi \cos \phi \dot{\phi} \dot{\psi}}{I_{yy} \sin^2 \phi + I_{zz} \cos^2 \phi} \right) \quad (1.6)$$

$$\begin{aligned} \dot{V}_y = & \frac{F_{yT}}{m} - V_x \dot{\psi} - h \sin \phi \cos \phi \dot{\psi}^2 \\ & + \frac{h}{I_{xx}} (F_{yT} h \cos \phi + mgh \sin \phi - K_\phi \phi - C_\phi \dot{\phi} + \dot{\psi}^2 (I_{yy} - I_{zz}) \sin \phi \cos \phi) \end{aligned} \quad (1.7)$$

$$\ddot{\psi} = \frac{M_z - F_{xT} h \sin \phi - 2(I_{yy} - I_{zz}) \sin \phi \cos \phi \dot{\phi} \dot{\psi}}{I_{yy} \sin^2 \phi + I_{zz} \cos^2 \phi} \quad (1.8)$$

$$\ddot{\phi} = \frac{F_{yT} h \cos \phi + mgh \sin \phi - K_\phi \phi - C_\phi \dot{\phi} + \dot{\psi}^2 (I_{yy} - I_{zz}) \sin \phi \cos \phi}{I_{xx}} \quad (1.9)$$

where

F_{xT} = Total longitudinal force on the body

h = Height of centre of gravity (CoG)

M_z = Total aligning torque on body

I_i = Inertia around the appropriate axis

F_{yT} = Total lateral force on the body

K_ϕ = Total roll stiffness

C_ϕ = Total roll damping

The forces acting on the vehicle body are due to the tractive effort of the tyres. These longitudinal and lateral tyre forces are described in Chapter 3. The total longitudinal (F_{xT}), lateral (F_{yT}) and aligning (M_z), forces applied to the body are given in equations 1.10 – 1.12:

$$F_{xT} = F_{xRL} + F_{xRR} + (F_{xFL} + F_{xFR})\cos\delta - (F_{yFL} + F_{yFR})\sin\delta \quad (1.10)$$

$$F_{yT} = F_{yRL} + F_{yRR} + (F_{yFL} + F_{yFR})\cos\delta - (F_{xFL} + F_{xFR})\sin\delta \quad (1.11)$$

$$M_z = (F_{yFL} + F_{yFR})a \cos\delta - (F_{yRL} + F_{yRR})b + (F_{xFL} + F_{xFR})a \sin\delta \\ + (F_{xRR} + F_{xFR}\cos\delta + F_{yFL}\sin\delta - F_{xRL} - F_{xFL}\cos\delta - F_{yFR}\sin\delta)l \quad (1.12)$$

where

$F_{x(i)}$ = Longitudinal force from tyre (i denotes tyre position on vehicle where the nomenclature describes the front or rear followed by left or right side of the car)

$F_{y(i)}$ = Lateral force from tyre

δ = Steering angle at tyre

a = Distance from front axle to CoG

b = Distance from rear axle to CoG

l = Distance from tyre centre line to CoG (half vehicle track width)

1.1.4 Stability

A vehicles design with regards steering and suspension set-up, power distribution, weight and location of centre of gravity characterises the way it will tend to perform during cornering. The three ways a vehicle negotiates a corner are neutral-steer, over-steer and under-steer.

A car with a forward bias of weight or front-wheel drive tends to hold under-steer characteristics, this is when a driver applies a steered angle, and the vehicle pushes straight on or negotiates a much larger arc than required. Rear wheel drive vehicles tend to display over-steer characteristics whereas the vehicle turns much tighter than required as the rear of the vehicle begins to steer the vehicle. This can be intentional by power application to cause power over-steer. A vehicle that is

travelling the arc intended by the driver is classed as neutral steer. The SAE definitions of under and over steer are:

'A vehicle is in understeer at a given trim if the ratio of the steering wheel angle gradient to the overall steering ratio is greater than the Ackermann steer angle gradient' and 'A vehicle is in oversteer at a given trim if the ratio of the steering wheel angle gradient to the overall steering ratio is less than the Ackermann steer angle gradient' [15, 16], (Figure 1.7).

The stability factor (S_f) of a vehicle is directly related to the tyre cornering force and location of the centre of gravity. Although in the elementary bicycle model [11] the derivatives are independent of speed, further detailed models include velocity and motion as variables, especially for vehicles fitted with aerodynamic packages where down-force will affect the centre of gravity location via centre of pressure as speed increases.

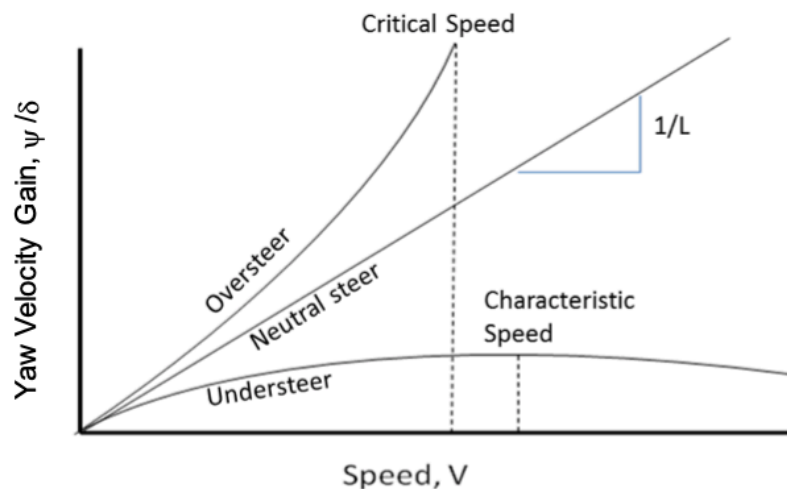


Figure 1.7 Vehicle under-steer, over-steer, neutral steer with defined critical and characteristic speed.

The stability factor (S_f) is defined in Eqn. (1.13) where equilibrium determines neutral steer. A positive stability factor denotes under-steer, and a negative stability factor denotes over-steer. The critical speed is classed as when an oversteering car requires zero degrees of steering angle to

negotiate the turn, and the characteristic speed is defined as when an understeering car requires twice the amount of steering angle to negotiate the same turn as a neutral steering car. [15]

$$S_f = (F_{yFL} + F_{yFR}) - (F_{yRL} + F_{yRR}) \quad (1.13)$$

1.2 Hybrid Powertrains

There are three types of combined Hybrid Electric powertrain architecture: Parallel [17], Series [18] and Series Parallel [19]. The parallel hybrid vehicle (Figure 1.8) consists of an internal combustion engine (ICE) and motor deployed as the name suggests in parallel. The vehicle can be propelled by three power deployment variants: solitary Motor, solitary internal combustion engine and combined motor and internal combustion engine mode.

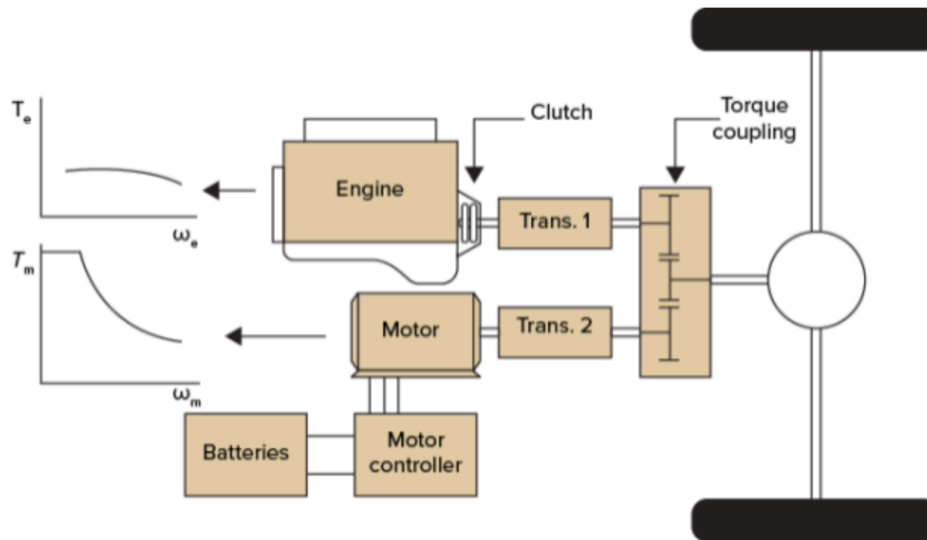


Figure 1.8 The architecture of a Parallel hybrid electric drivetrain.

A series hybrid's powertrain architecture (Figure 1.9) is positioned in line whereby the internal combustion engine can only provide power to the generator to allow re-generation of electrical energy. The motor alone propels the vehicle forward.

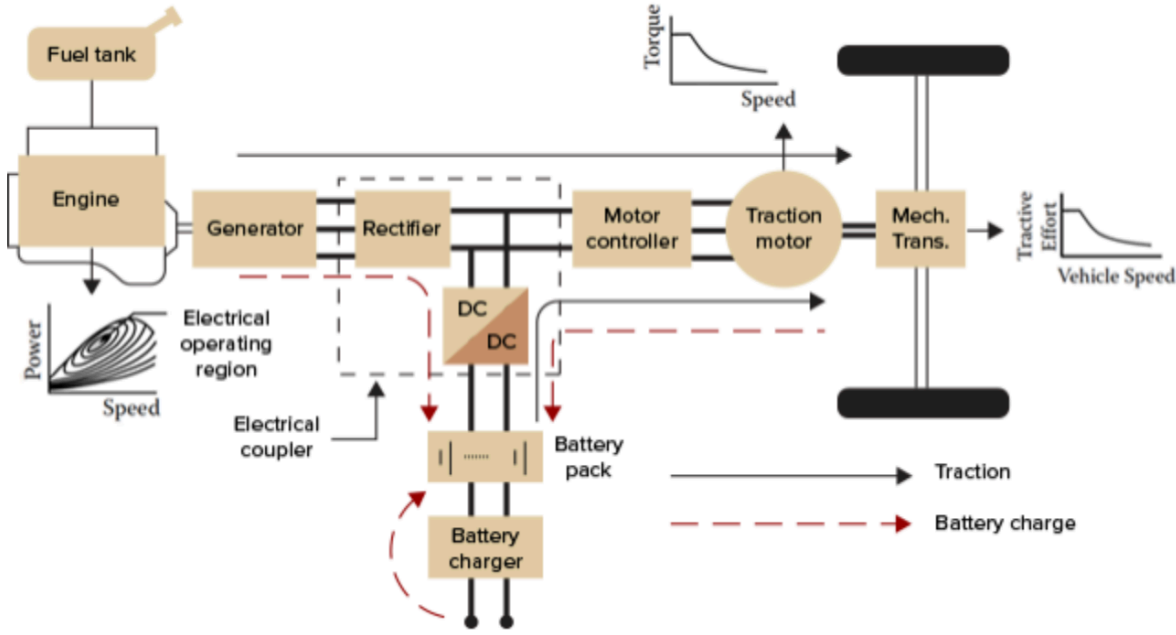


Figure 1.9 The architecture of a series hybrid electric drivetrain.

A series parallel hybrid vehicle (Figure 1.10) takes design considerations from both drive-train layouts above and can be propelled by solitary motor, solitary internal combustion engine or combined. Whilst in motor or regenerative mode the engine can power a second generator to create electrical energy for the energy storage component.

Many hybrid electric vehicles can regenerate energy to store in an energy storage device, which will be discussed in more detail in Chapter 2. However, it is common with current technologies that most road vehicles cannot regenerate enough energy to allow large distances to be covered on electric only power and thus plug-in hybrid electric vehicles (PHEV) are the norm [20]. These vehicles can be connected to the electrical grid either at the home or the roadside. This charge to the energy store can enable an extended range on electric only and combined mode.

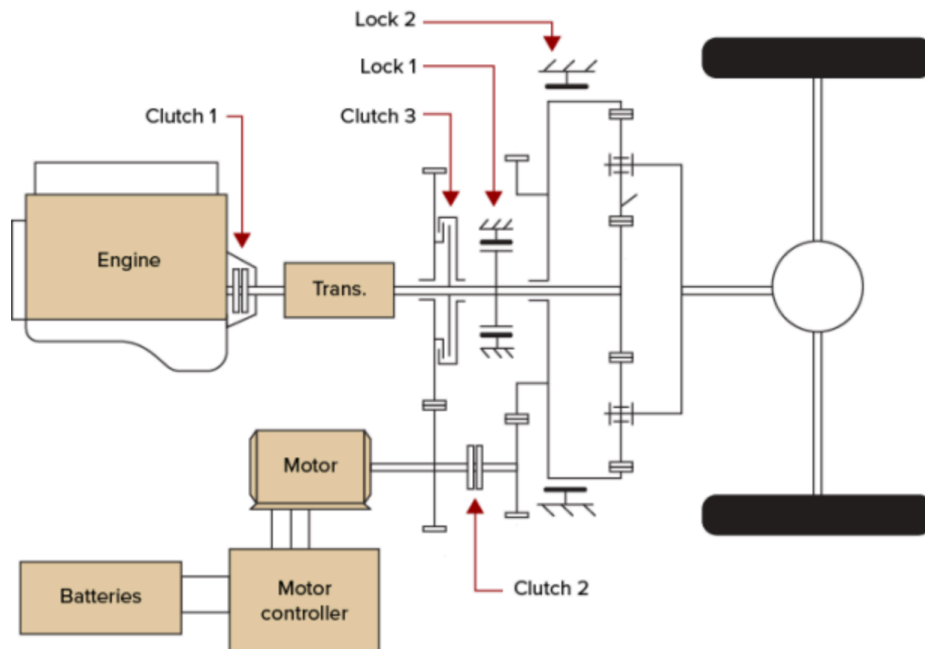


Figure 1.10 The architecture of a series-parallel hybrid electric drivetrain.

1.3 Motivation

The study of vehicle dynamic behaviour by computer modelling and simulation has progressed rapidly over the past few decades due to the constant development of computing power. Many various applications and simulation platforms are utilised in the Motorsport and Automotive industries, developed as pure mathematical simulations [42], or as real time control, optimisation or development models for software in the loop (SiL) [43, 44], hardware in the loop (HiL) [44,45] and driver in the loop (DiL) [46,47] testing. These modelling strategies contain various types of simulation to determine key performance indicators for components and systems such as active suspension modelling [48,49], braking systems [50] and controller designs and validation.

Advanced models are based on several systems and subsystems so complete vehicle models can be utilised for Hybrid race vehicle dynamic modelling incorporating energy management and optimisation [51,52,53], kinematic and dynamic motion planning for ideal vehicle trajectory and lap/race time simulations within the motorsport industry [54,55] or for autonomous vehicle development [56] within the automotive sector.

These models can be furthered utilised as SiL and HiL simulation for controller design in vehicle stability systems [57], fault detection within safety critical applications [58] and uncertainty modelling. All Formula One teams and the majority of WEC and Formula-e teams now use DiL training and full race vehicle simulators [59] for driver training and evaluating vehicle performance and race strategies due to ‘live’ testing restrictions. Furthermore, the necessity of simulators and race simulation prior to a race weekend has been borne from the race rules and regulations [60, 61] that dictate energy management strategies and vehicle set-up analysis difficult to practically assess with the testing embargo.

These rules have created complexity and intricacy of Hybrid Electric Race Vehicle design, development and implementation of the powertrain to maximise fuel saving, use of electric energy and electric machine performance as have the electric regeneration strategies for Electric only race vehicles such as those utilised in Formula-e [62] whereby the electric charge is the only energy available for propulsion. From an automotive industry standpoint, the UK Government in 2017 stated that all sales of new cars with an internal combustion engine, whether it be Diesel or Petrol combustion will be banned from 2040 onwards [63], the main part of that statement that is commonly misinterpreted in the media is the fact that they stated vehicles will not be able to utilise the internal combustion engine as the ‘*sole means of propulsion*’.

Therefore, at the time of writing, not only electric vehicles but also hybrid vehicles have a long future ahead of them; especially until battery technology and charging infrastructures can catch up with demand [64].

Manufacturers have led the design and development of race rules and regulations with the Federation Internationale de l'Automobile (FIA) for both the world endurance Le-Mans Prototype One (LMP-1) category in the World Endurance Championship (WEC) and Formula One whereby both series’ have Hybrid technology incorporated into the design of the race car. Where better to develop future road car applications than in the demanding environment of motorsport where both performance and reliability are crucial.

In an industry as technologically advanced as motorsport it is imperative that the Race Strategists and Vehicle Dynamic Engineers have access to vehicle simulation and optimisation packages whether it be at the race circuit or through Research and Development departments via Race

Simulation Engineers at research laboratories. These models and simulations must incorporate race strategy analysis and the determination and optimisation of lap-times, through performance indexing and energy management strategies, race times (lap time versus fuel and energy use and conservation/regeneration) and vehicle dynamic behaviour.

1.4 Contributions and Novelty

Although there are several simulation packages available to the industry, none of these packages whether used for lap time simulation or vehicle dynamic studies include an integrated dynamic control and energy management optimisation. The main software companies focus their products at either vehicle dynamics, lap time simulation or energy management strategies whilst using look up tables or set vehicle maxima for cornering, braking or speed. If the software is based on vehicle dynamics or lap time, then again, the software will use look up tables for Hybrid deployment if indeed it has the capability.

The main current industry standard software for vehicle modelling is:

- MSC Adams – Multi-Body dynamics software for vehicle dynamics and component motion.
- GT-Suite - Linear emission testing, engine development and drivetrain efficiency based on look up tables.
- Lapsim– lap time simulation based on premeasured data from vehicles.
- ChassisSim – Transient dynamic lap time simulation. Validated through premeasured data from vehicles.
- GT-Drive – Longitudinal drive train dynamics for hybrid vehicles based on pre-defined engine look up tables.

Each software package although used by the industry are limited by look up tables or pre-determined data sets and as such many companies have to purchase several packages to allow all

types of control, simulation and optimisation to be analysed. Typical restrictions of the packages are:

- *'Bring a vehicle to its dynamic limits or near targets you define.'* [21]
- *'Driver simulation with racing environment data import.'* [22]
- *'One can select the corners where there is boost and the corners which are just energy recovery.'* [23]
- *'Cornering simulation can be added with speed/acceleration/braking events pre-defined.'* [24]

The novelty of this thesis is to develop a simulation product within Matlab® and Simulink® that includes the validation of vehicle dynamic models through particle swarm optimisation algorithms, trajectory planning and race line optimisation and the integration of energy management optimisation and vehicle dynamic behaviour for any race circuit or road orientation the user provides by developing Co-operative Particle Swarm optimisation techniques (CPSO – S_k) [72, 73]. Although this study is based on race vehicles in light of the Volkswagen emission scandal [25], the model could be used for true dynamic road driving rather than based on 1D speed data.

During the process of developing this thesis and model the author has presented several papers based on vehicle dynamics [11], control and energy management of hybrid vehicles [26] and at the time of submission two journal papers are being prepared and edited for submission based upon the findings and development of single and multi-objective particle swarm optimisation and their use within the Automotive/Motorsport Industry.

1.5 Aims & Objectives

This thesis aims to investigate, by mathematical design and simulation, various vehicle dynamic models, vehicle trajectory and hybrid energy deployment strategies to establish and create appropriate optimisation algorithms for vehicle model validation and lap time optimisation of ICE only and Hybrid electric race vehicles.

To establish a reasonable outcome to the final model(s) the aims of the project include:

1. Determine appropriate degrees of freedom model for optimal balance of accuracy of results and computing speed.
2. Design and develop vehicle dynamics model in Matlab® and Simulink ®.
3. Design and develop a powertrain and drivetrain model in GT-Power, Matlab® and Simulink®.
4. Design and develop a hybrid electrical system model in Matlab® and Simulink ®.
5. Establish system input and output functions for control system design and optimisation for energy management.
6. Develop race circuit trajectory modelling algorithms.
7. Evaluate through simulation and model analysis appropriate control and optimisation solutions.

1.6 Thesis Structure

Upon completion of the above aims and objectives the thesis has been structured into the chapters as follows:

- **Chapter 2** expands upon the introductory narrative, aims and motivational synopsis from Chapter 1 by discussing further literature and Automotive/Motorsport industry practices.
- **Chapter 3** addresses the longitudinal and lateral behaviour of a race vehicle and develops the mathematical algorithms for the chassis and tyre models.
- **Chapter 4** describes Hybrid-Electric powertrains used in race series' today and identifies the topology of a Formula One race vehicle and proposed GT race vehicle including the Motor/Generator and internal Combustion Engine systems.
- **Chapter 5** explores the implementation of single and multi-particle swarm optimisation for the validation of vehicle dynamic simulation models

- **Chapter 6** details the race circuit mapping, vehicle dynamic constraints and co-operative particle swarm optimisation algorithm for vehicle trajectories.
- **Chapter 7** develops the dynamic energy management parameters.
- **Chapter 8** summarises the results detailed in each chapter and concludes with the observations found for the implementation of PSO algorithms and their use within the Industry. A conclusion is presented and suggestions for future work discussed.

2. Vehicle Model and Simulation

2.1 Introduction

This chapter introduces the major components of a vehicle to be modelled in order to develop a realistic simulation environment to test different hypotheses in design of a hybrid race vehicle. Therefore, as the first step the industry standard tyre models are discussed to show how vehicles create grip. This inevitably has a large impact on vehicle dynamic behaviour and model output. The aim is to validate a tyre model in future chapters, and therefore through further literature review the tyre model is discussed and its impact on the vehicle modelling is analysed. In addition, an overview of various degrees of freedom vehicle dynamic models are discussed and an insight into hybrid energy management strategies is included prior to a detailed description in the following chapter.

2.2 Tyre models

Tyres are a complex and vital component of the vehicle dynamic studies and as such a tyre model can have various inputs and outputs to determine grip. The tyre model can have systems with numerous sub-systems and algorithms, however the main factors that contribute to grip are the tyre's contact patch, slip ratio, slip angle, tyre pressure, tyre temperature, tyre spring rate and tyre compound. Additional system settings on the vehicle may also influence the tyre such as toe and camber; camber has been modelled within the tyre models in various tyre formulae [6, 9]. The most basic of tyre models such as the linear tyre model [10], generate tractive forces based on the contact patch and the deformation.

2.2.1 Tyre Contact Patch

The contact patch is determined as the area of contact between the tyre and road surface. The tyre size, camber angle and pressure all have an effect on the tyre contact patch size (Figure 2.1). The deformation of the contact patch results in longitudinal and lateral grip, the deformation results

from the contact patch moving longitudinally fore and aft of the wheel centre during acceleration and braking events (Figure. 2.2 (a) and (b)) due to friction and the abrasive qualities of the road surface. This movement is known as the slip ratio [9].

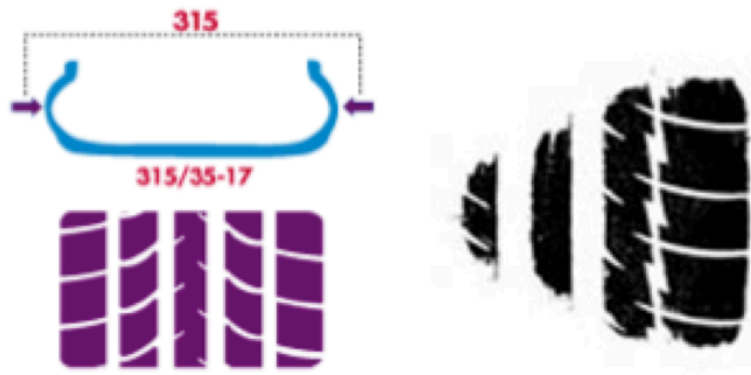


Figure 2.1 The effect of tyre size and camber angle on tyre contact patch size.

The ratio specified is the variation in velocity of the contact patch versus the vehicle velocity, equation (2.1).

$$\kappa = \frac{\Omega \cdot r_d}{V_x} - 1 \quad (2.1)$$

where:

κ = Slip ratio

Ω = Angular velocity of the hub (rad/s)

r_d = Rolling radius of the tyre

V_x = Velocity of the hub in the plane of the rim parallel to the ground.

Lateral forces arise from the shear forces from pure friction. When a steering angle is applied the tyre rotates around the z-axis and due to abrasion, the contact patch has a separate heading than that of the tyre. The variation between the tyre heading and contact patch heading is known as the

slip angle (Figure 2.2, (c)). The tyre model, with the inclusion of empirical data or measured coefficients from a tyre dynamometer, creates a curve that determines the peak force at a specific slip ratio and slip angle, either side of this peak the tyre is not operating at its optimal.

The most basic of tyre models is the linear tyre model [29], equation (2.2), whereby the lateral force of the tyre has a linear relationship with slip. This model allows low computational effort however unless desired or measured vehicle cornering data is parameterised [30] the model is ineffective for optimisation studies or racing car modelling as the tyre will continue to create force as slip angles head to infinity. A common slip angle for a racing slick would be in the region of five to seven degrees [9].

$$F_{y,i} = C_{\alpha,i} \cdot \alpha_i \tag{2.2}$$

Where:

C_{α} = Cornering stiffness of the tyre

α_i = Slip angle

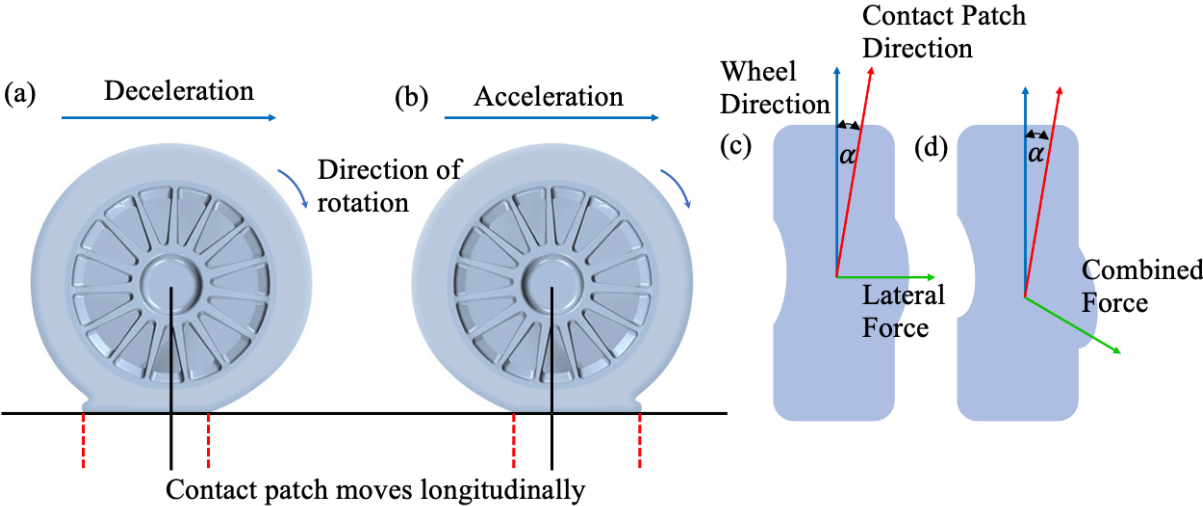


Figure 2.2 Tyre slip ratio under (a) deceleration, (b) acceleration, and slip angle (α) definition for (c) pure lateral and (d) combined longitudinal and lateral forces (d).

2.2.2 Brush Tyre Model

The brush tyre model is so called due to the make-up of the mathematical formulae. The model consists of bristles that are in contact with the surface and can deflect parallel to the road. In longitudinal dynamics the bristles are said to be vertical and do not deflect when there is no tractive effort applied (braking or acceleration). During acceleration the first bristle (front) is pushed into the ground and deflects (Figure 2.3), the combined elasticity of the tread and tyre carcass determines the compliance of the remainder of the bristles. The opposite occurs during braking. This has the effect of moving the contact patch fore or aft of the centre line, generating a slip ratio.

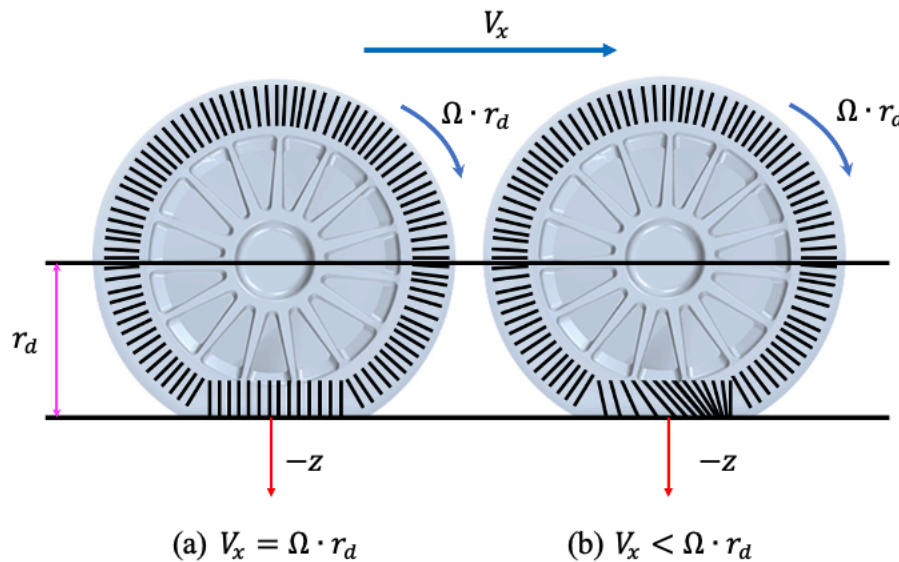


Figure 2.3 Brush tyre model tread deflection, (a) motionless and (b) during acceleration.

During cornering a steered angle is applied to the tyre and the bristles again can deform in the y-axis direction, the angle of the contact patch compared to tyre heading generates the slip angle. The forces generated on the Y-Axis are perpendicular to the contact patch (Figure 2.4). When the tyre is subject to only lateral or longitudinal force the model is described as being in pure lateral slip and pure longitudinal slip [6], whereas when acceleration or braking is present with steered wheel angle the tyre is in combined slip (Figure 2.4).

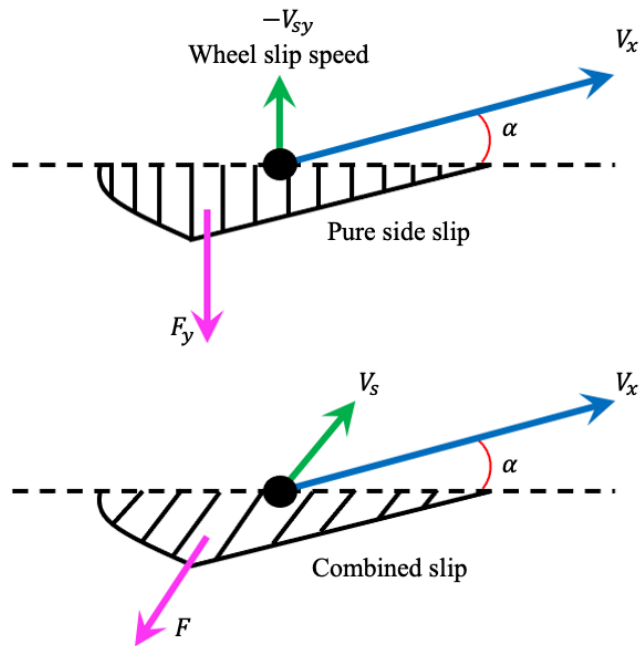


Figure 2.4 Brush tyre model deflection during cornering (top) and combined deflection with braking and cornering (bottom).

2.2.3 Pacejka Tyre Model

Pacejka [6] developed a model based on the brush model equations that includes empirical data for curve fitting from tyre testing. This means a series of coefficients are required to develop accurate results. However, this model is seen as one of the industry standards ‘go to’ models within vehicle dynamic studies [4, 6, 10, 11, 27, 31] due to its accuracy. Pacejka’s Magic Formula has gone through many iterative steps and the current model is the MF 5.2, additional complexities can be added to the model and is used in many of the industry standard software mentioned in Chapter One, Adams and Simulink’s Simscape and Sim-Driveline blocks to name two. Using the complete MF 5.2 model can allow the tyre to be parameterised with over one hundred different variables.

The Pacejka tyre model in one of the simplest forms, taking pure lateral slip as an example, lateral force is defined with equation (2.3).

$$F_y = D_y \sin \left(C_y \tan^{-1} \left(B_y \alpha_i - E_y (B_y \alpha_i - \tan^{-1}(B_y \alpha_i)) \right) \right) \quad (2.3)$$

The constant numbers are determined by the coefficients D , C , B and E . These equations are fully developed in Chapter 3, but equation (2.3) produces lateral force. Varying slip angle allows lateral force to be plotted against slip angle (Figure 2.5) for a given vertical load. The above equation can be manipulated for pure longitudinal force by substituting slip angle with slip ratio.

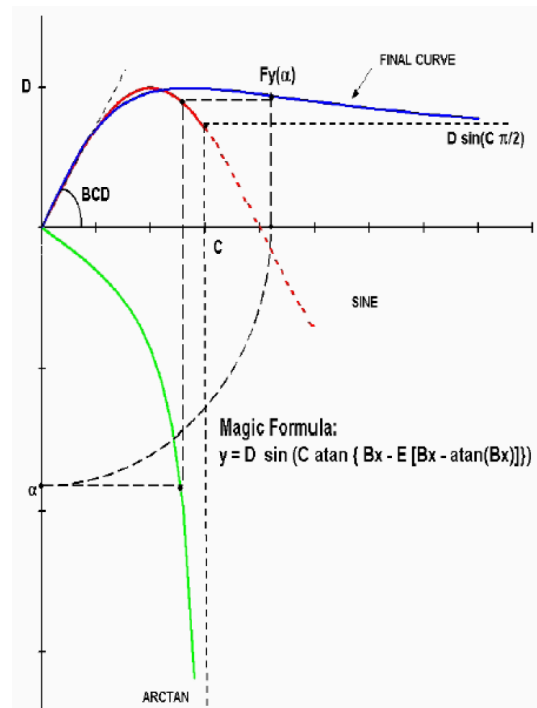


Figure 2.5 The mathematical development of the Pacejka curve profile (graphical example).

The complete model described in Chapter 3 covers longitudinal force versus slip ratio, lateral force versus slip angle and the combined slip angle and slip ratio forces. The aligning torque is also described in detail in the following chapter. Tyre and vehicle behaviour still needs to be understood with the use of the Pacejka model so as not to produce unreasonable results with the use of incorrect Pacejka coefficients, it is important to observe that the maximum co-efficient of friction of the tyre drops off linearly with load, camber angle of the tyre will increase the maximum lateral grip of the tyre to infinity, requiring a maximum camber geometry setting to be observed for the race vehicle being tested, longitudinal forces will decrease as camber angle is increased: peak longitudinal force

will be observed at zero degrees of camber and in the lateral force formulae, post peak slip tends to have a small reduction in force. These observations mean Nowlan [9] proposes the Pacejka model is not ideal for racing tyres and introduces his own model based on look up tables and empirical data from race cars, namely the ChassisSim v3 tyre model. This model is ideal and does eradicate some of the weaknesses of the Pacejka model. However, fully explored and analysed vehicle set-ups and vehicle responses are required of the race vehicle to ascertain limitations, maxima, parameters and look-up tables [32]. For these reasons the ChassisSim tyre is discounted from this study.

2.2.4 TaMe Tyre model

The Pacejka Magic Formula and ChassisSim v3 tyre models are based on empirical data and as such the majority of tyre modelling, vehicle dynamics simulation and studies have been based on the Pacejka model as determined in the previous section. However, there is a derivative of the brush tyre model, produced by Michelin during the time they were last involved in Formula One (c. 2001 – 2006): The Michelin TaMe Tyre model.

The model uses the tyres structural properties and so is derived by three parts, mechanical model (structure), rubber characteristics and a thermal model [28, 33]. The TaMe tyre model generates friction as a function of speed, temperature and pressure, however for this model the structural properties of the tyre must be known alongside the frictional properties of the tyre surface as a function of speed, temperature and pressure. In the mystique of Formula One this data would be very difficult if not impossible to come by and as such, although this may be a superior tyre model (with the correct inputs utilised) the model is beyond the scope of this thesis.

2.2.5 Traction Ellipse

The previous sections have determined that a peak longitudinal and lateral force is generated at a specific slip ratio and angle respectively. This peak force changes due to vertical force on the tyre but none-the-less a maximum is present for all vertical force possibilities. This statement dictates that for a race vehicle with a specific race tyre at a given load there is an optimum point in slip that the tyre will generate peak force. Taking the peak forces for lateral and longitudinal dynamics

(Figure 2.6) it is obvious to see there is no gain to going beyond these maxima. However, this only determines the peak force in purely longitudinal or lateral slip conditions. The tyre can generate forces in both directions, but the peak is only available when no other motion is required.

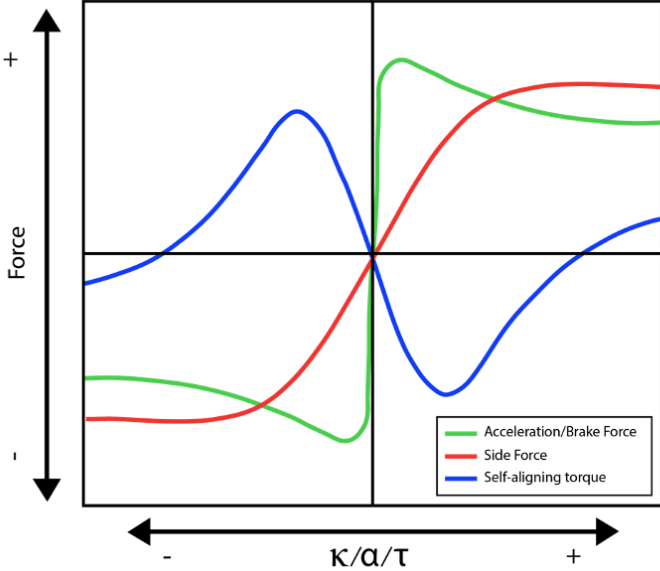


Figure 2.6 Lateral and longitudinal tyre forces versus slip ratio, slip angle and aligning torque.

If the tyre could generate an equal amount of force in pure longitudinal and lateral acceleration then this could be depicted as a circle (Figure 2.7), however race tyres do not work in that way especially when aerodynamic downforce is introduced into the equations and as such the combined forces are depicted analogous to an ellipse.

A race vehicle cannot brake or accelerate and corner at its peak force and if attempted by a driver the vehicle will lose traction and lock a wheel or spin. Through data logging of a race vehicle the traction ellipse [34] can be generated in the terms of longitudinal G-Force versus lateral G-Force (Figure 2.7, note right hand corners are negative). It is clear to see an aerodynamic bias vehicle can corner harder than it can accelerate or brake, and the braking power (deceleration), is far superior to the acceleration rate, due to powertrain output power. The driver whilst searching for the best performance of the car is subconsciously trying to follow the outer circumference of the traction circle. Figure 2.7 depicts the main areas of the traction circle where the driver is attempting to extract the maximum performance from the tyre during the combined forces. Maximum

accelerations are also seen during the combined forces as the vehicle accelerates out of a corner from a slower speed where acceleration is high. During pure acceleration events the vehicle velocity is high enough whereby acceleration is lower, however peak deceleration is always in a straight line, where the driver can extract maximum velocity retardation from the tyre. Peak lateral accelerations for a GT style car tend to occur during pure lateral and combined acceleration up to a maximum of 0.25G (positive and negative) longitudinal acceleration.

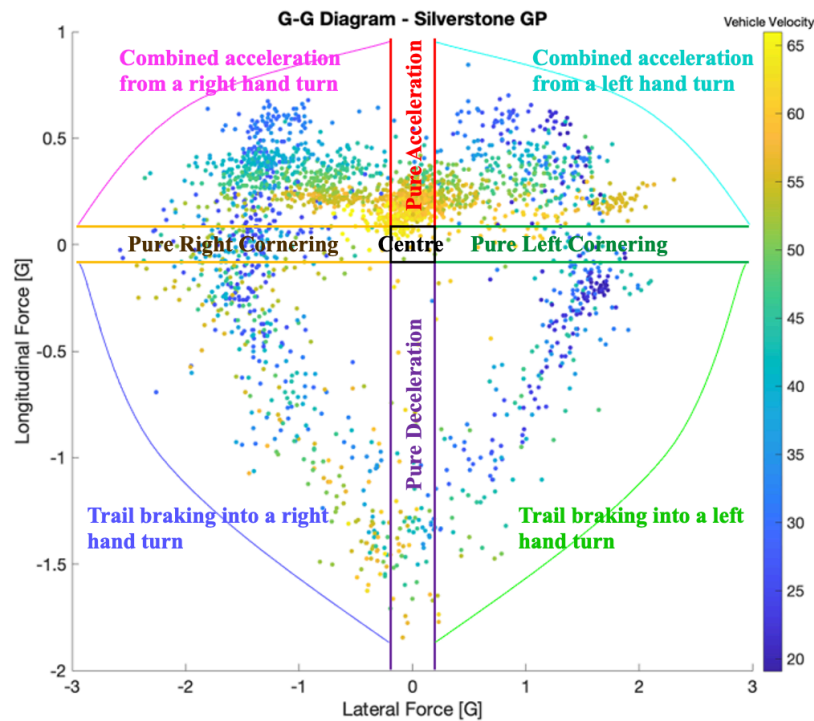


Figure 2.7 The measured traction ellipse (G-G diagram) from a Lotus Evora GTE (note right hand corners are negative sign).

2.3 Vehicle dynamics and variants of DOF

There are several degrees of freedom associated with vehicle modelling and vehicle dynamics [16]. A model can have a plethora of degrees of freedom when all systems and components equations of motion are included together; for simplicity this project takes the vehicle body as the hierarchical component that implies the total degrees of freedom (4DOF). Although the tyre model

has in itself degrees of freedom these are discounted from the model's assignment of motion title. The most basic of vehicle dynamic model consists of i) lateral and ii) yaw motion, therefore, is assigned as a two degree of freedom (2DOF) model. This model tends to be a single-track (bicycle) model and is used for steady state analysis whereby vehicle speed is constant [10].

Studies that do not involve longitudinal acceleration can produce excellent results from the 2DOF model, such as constant speed analysis of the fishhook, J-Turn [4] or lane change [30] manoeuvres for example. The authors of [30] collated measured data from a vehicle and then compared the results to their 2DOF model. The authors conclude for constant speed testing that a simple model can produce lateral dynamic results '*very well*' and that added complexity to the Pacejka tyre gives very little gain in accuracy of the results and that for a 2DOF model the far more complex double track model is not able to enhance the accuracy of results. However, in [10] the same authors do acknowledge '*for more convincing conclusions to be established, additional thorough investigations will be needed, e.g., considering combined lateral and longitudinal dynamics.*'

The three degrees of freedom model adds longitudinal acceleration and therefore can establish results of a vehicle's motion on the X-Y plane. The author of this Thesis in [11] carried out studies based on [10, 30] and from measured data taken from a race vehicle to compare the results with Simulink® 2DOF and 3DOF models. Although the results were close to measured data in constant velocity tests, the lateral acceleration maxima and minima consisted of an error of six percent in some instances as the numbers of corners and speeds varied with a 2DOF model. As roll and pitch effect vertical load and thus tyre performance a 4DOF (roll), 5DOF (pitch) and 6DOF (heave) model may be beneficial to the industry when tyre performance and modelling is important, although additional degrees of freedom add mathematical complexity to the model and increase computing power requirements.

Lot et al [1] concentrate mainly on creating a new approach to road modelling for lap time simulation, to ease computing power of the vehicle model a 3DOF model is utilised. This model maintains single-track geometry and appropriate circuit mapping and racing line plots appear to be produced. However, this paper fails to validate the vehicle model or take any comparisons of measured data into account. To move forward from this point into a 4DOF model, as weight

transfer characteristics are to be included, a double-track model is necessary. In a 2DOF or 3DOF model, double-track models can be implemented [35] but found unnecessary [4] unless tyre modelling temperatures and weight transfer is required. Complexities to a model can be added without the overall expense of computing power by concentrating on a Newton-Euler approach to vehicle dynamic studies, as per [31], a 6DOF study is derived creating a model suitable both for *‘high-accuracy simulation as well as for nonlinear control design.’* The majority of lap time simulation, optimisation and track mapping studies use 2DOF and 3DOF models in various single and multi-track model forms [12, 13, 36, 37], although none compare to measured data. The lap time analysis of [13, 35] however, produces lap time results close to that of 2014 and 2016 Formula One Vehicles (within 0.1s) [38]. In these studies, some effects on horizontal and vertical force are ignored such as drag reduction systems and a constant vehicle mass is used (no fuel mass usage) [38] having an impact on tyre dynamics. Lateral stability control for high lateral acceleration cornering vehicles must take into account roll dynamics as the tyres can have significantly different slip angles and therefore forces, as found in [39], where linear and Pacejka tyre models were tested against various DOF models to develop stability control. Linear tyre models and lower order vehicle dynamic models are unsuitable for stability control in high lateral acceleration events because of the lack of lateral transfer and the lack of saturation of the tyre force at high slip angles.

The focus of this thesis is to create a model that would allow development and implementation of further degrees of freedom and tyre temperature models relatively easy and so a double-track, Pacejka tyre, 4DOF model is developed in Chapter 3, allowing a sensible approach to computing power demand for the optimisation and control problems and somewhat of a novel approach from most of the cited literature.

2.4 Energy management

The priority for hybrid electric vehicles is the use of the electrical motor and in the case of automotive manufacturers how that usage will reduce emissions. For the motor to be used effectively over greater distances the vehicle must be able to regenerate energy somewhat and manage the usage during electric only and combined states. The term used for this monitoring and

usage is energy management. Energy management in road vehicles normally has two states, charge depleting and charge sustaining [40]. During charge depleting mode the energy storage is used continuously, whereas in charge sustaining mode the energy store is depleted to a predefined lower limit that the store will not go beyond. The Formula One regulations [2] include energy flow limitations during a lap (appendix 1). The kinetic energy motor/generator unit (MGU-K) can supply two mega-joules of energy to the energy store and the energy store can provide four mega-joules of energy to the MGU-K, in turn the energy store can store four mega-joules of energy per lap. The additional two mega-joules must come from the thermal energy motor/generator unit (MGU-H). The MGU-H can supply an unlimited amount of energy to both the energy store and direct to the MGU-K. The MGU-H is located on the same common shaft as the compressor and turbine wheels of the turbocharger, allowing turbo compounded [41] internal combustion engines to be utilised. The optimum regeneration from both MGU's is required to provide enough energy to be utilised within the regulations but providing the maximum amount of power available to improve acceleration and improve lap time without impeding stability.

2.5 Conclusion

Tyre models and the appropriate literature have been presented and discussed with reasoning behind the choice of appropriate tyre models, an overview of amounts of degrees of freedom to be utilised has been included along with a brief overview of energy management strategies with regards to current race series.

3. Hybrid Race Vehicle Dynamic Model

3.1 Introduction

Presented in this chapter is a discussion on standard industry modelling as the motivation and justification to dynamic modelling choices within the Thesis. The mathematical vehicle dynamic model is developed including the vehicle chassis, aerodynamic body and tyre models that will be validated in Chapter 5 through optimisation algorithms.

3.2 Vehicle Industry Standard Models

There are a variety of vehicle dynamic studies ranging from basic two degrees-of-freedom (DOF) [54, 65] models up to complex multi-DOF models [48, 66]. Single track, lumped mass vehicle model simulations can be very effective at producing fast, consistent results for lateral acceleration within a 2-6% tolerance of the measured vehicle data [54, 65, 67]. Single-track models commonly known as the bicycle model tend to be used for steady state analysis and are limited in their degrees of freedom, no roll behaviour or longitudinal acceleration, for instance. For this study, where race circuit position of all four wheels are beneficial and roll dynamics are required for vertical force calculations upon a tyre, a double-track vehicle is utilised as per the majority of literature available into vehicle dynamic studies [42, 68, 69]. To allow multi-optimisation of systems or multi-controllers to be utilised the vehicle dynamics model is best developed as a series of subsystems (Figure 3.1). Therefore, all unknown parameters can be estimated through optimisation techniques. All vehicle body dynamic studies have one thing in common: the use of tyre models. There are three common types of tyre model: 1- linear, 2- Pacejka, and 3- Michelin's TaMe [6, 11, 28,]. As previously discussed, the linear tyre model has its limitations. When the tyre is at the extreme slip angles and ratios, it continues to create grip (Figure 3.2), which is unrealistic and must have a defined maximum. The Michelin model is probably the most advanced model as it includes thermal properties; however, it is seen as too memory heavy for some studies [33]. Therefore, the Pacejka Magic Formula model is the most common model utilised and also within this study as well.

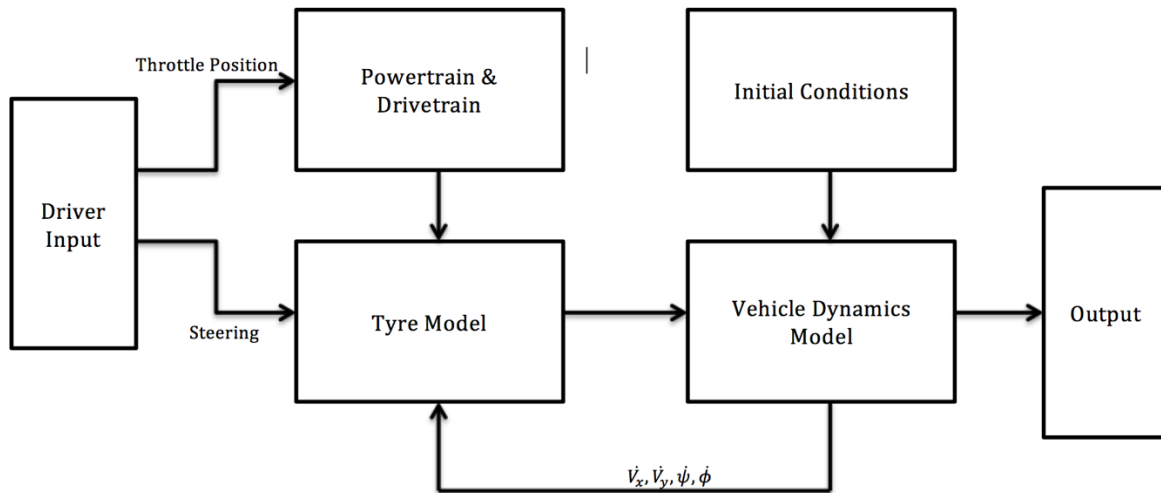


Figure 3.1 Vehicle dynamics sub-system components including powertrain and driver.

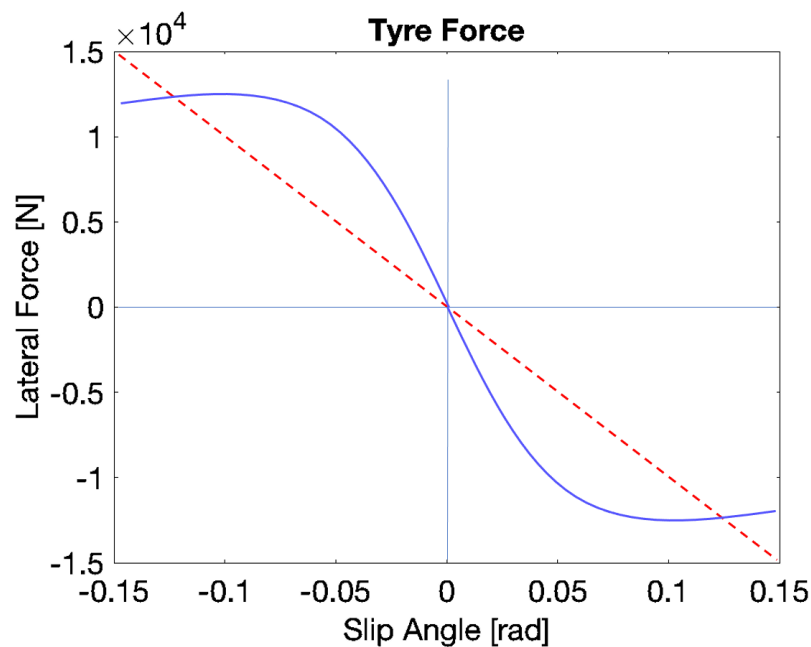


Figure 3.2 A comparison of linear tyre model output (red, dashed line) versus Pacejka tyre curve (blue, solid line) with regards to lateral force versus slip angle.

The latest version of the Pacejka tyre model (named MF5.2), utilises the coefficients in (2.3) as a base to set the shape of the Pacejka curve (Figure 3.2). These coefficients are either taken from a tyre dynamometer test or manufacturers data. In the event that this data is neither available nor is accessible through a dynamometer test, the parameters have to be manipulated to develop an

appropriate curve match to longitudinal and lateral acceleration events. Therefore, the need for an accurate optimisation algorithm is required that can generate the results in a reasonable amount of time.

3.3 Chassis Model

The four DOF chassis dynamic model used in later section of this thesis includes longitudinal motion, lateral motion, yaw motion and roll motion. The equations of motion were described in Eqns. (1.6) – (1.9) respectively and the forces acting upon the body in Eqns. (1.10) – (1.12). Accelerations for yaw and roll are accented with a double dot and a single dot for longitudinal and lateral acceleration. To be able to write the model as an S-Function block, the dynamic model is converted to the standard state-space format.

Combining Eqns. (1.6) – (1.9) with the notations used in Table 3.1, the final equation of motions can be described as follows

$$\ddot{x}_2 = \frac{u_1}{m} + x_4 x_6 - h I_1 I_3 \quad (3.1)$$

$$\ddot{x}_4 = \frac{u_2}{m} - x_2 x_6 - h I_1 I_2 x_6^2 + h I_4 \quad (3.2)$$

$$\ddot{x}_6 = \frac{u_3 - u_1 h I_1 - 2(I_{yy} - I_{zz}) I_1 I_2 x_8 x_6}{I_{yy} I_1^2 + I_{zz} I_2^2} \quad (3.3)$$

$$\ddot{x}_8 = \frac{u_2 h I_2 + m g h I_1 - C_\phi x_7 - K_\phi x_8 + x_6^2 (I_{yy} - I_{zz}) I_1 I_2}{I_{xx}} \quad (3.4)$$

where

$$\sin\phi = I_1$$

$$\cos\phi = I_2$$

$$\dot{x}_6 = I_3$$

$$\dot{x}_8 = I_4$$

$$F_{xT} = u_1$$

$$F_{yT} = u_2$$

$$M_z = u_3$$

Table 3.1 Dot product assignment.

<i>Complete Form</i>	<i>x</i>	<i>Single dot product</i>
	<i>assignment</i>	<i>product</i>
Longitudinal Displacement (X)	x_1	
Longitudinal Velocity (V_x)	x_2	\dot{x}_1
Longitudinal Acceleration (\dot{V}_x)	\dot{x}_2	\dot{x}_2
Lateral Displacement (Y)	x_3	
Lateral Velocity (V_y)	x_4	\dot{x}_3
Lateral Acceleration (\dot{V}_y)	\dot{x}_4	\dot{x}_4
Yaw Displacement (ψ)	x_5	
Yaw Velocity ($\dot{\psi}$)	x_6	\dot{x}_5
Yaw Acceleration ($\ddot{\psi}$)	\dot{x}_6	\dot{x}_6
Roll Displacement (ϕ)	x_7	
Roll Velocity ($\dot{\phi}$)	x_8	\dot{x}_7
Roll Acceleration ($\ddot{\phi}$)	\dot{x}_8	\dot{x}_8

The vehicle body dynamics is written as an S-Function with the R2020a Matlab® and Simulink® environment. There are two outputs, one for displacement and one for acceleration for all 4DOF from the S-function. A simple derivative block allows the acceleration to be calculated externally from the block.

There are three inputs to the S-Function, which are the outputs of equations (1.10) – (1.12), respectively. The inputs are created via a forming matrix. The eight inputs into the B matrix are

the longitudinal and lateral forces from each tyre expressed in equation (3.5) and the three outputs are shown in equation (3.6).

$$v = (F_{xFL} F_{xFR} F_{xRL} F_{xRR} F_{yFL} F_{yFR} F_{yRL} F_{yRR})^T \quad (3.5)$$

$$u = \begin{pmatrix} F_{xT} \\ F_{yT} \\ M_z \end{pmatrix} \quad (3.6)$$

The inputs and outputs are related via the forming matrix $u = Bv$, as shown in (3.7)

$$B^T = \begin{pmatrix} \cos\delta & \sin\delta & (a \sin\delta + l \cos\delta) \\ \cos\delta & \sin\delta & (a \sin\delta - l \cos\delta) \\ 1 & 0 & l \\ 1 & 0 & -l \\ -\sin\delta & \cos\delta & (a \cos\delta - l \sin\delta) \\ -\sin\delta & \cos\delta & (a \cos\delta + l \sin\delta) \\ 0 & 1 & -b \\ 0 & 1 & -b \end{pmatrix} \quad (3.7)$$

3.4 Tyre Modelling

The tyre models for each tyre are developed from the Pacejka magic formula. Each tyre within the Matlab environment has 2 blocks: a slip block and a Pacejka Block. The slip block defines the longitudinal and lateral slip for the tyre whilst the Pacejka block calculates the lateral and longitudinal forces for the input into matrix B.

The Pacejka model is formulated in much the same way for lateral and longitudinal forces with the exception of longitudinal or lateral slip being substituted for the appropriate model. The combined model is developed from both equations.

The pure longitudinal model is expressed in equation (3.8) whilst the lateral model is shown in equation (3.9). The combined model is calculated through (3.10). The two equations shown in (3.10) are the outputs from Pacejka tyre model block 2 as described above, for all four tyres, generating the eight inputs for matrix B as defined in equation (3.5).

$$F_{x_{0_i}} = D_x \sin(C_x \arctan(B_x \kappa_x - E_x(B_x \kappa_x - \arctan(B_x \kappa_x)))) + SV_x \quad (3.8)$$

$$F_{y_{0_i}} = D_y \sin(C_y \arctan(B_y \alpha_y - E_y(B_y \alpha_y - \arctan(B_y \alpha_y)))) + SV_y \quad (3.9)$$

$$\begin{aligned} F_{xi} &= D_{x\alpha} \sin(C_{x\alpha} \arctan(B_{x\alpha} \alpha_s - E_{x\alpha}(B_{x\alpha} \alpha_s - \arctan(B_{x\alpha} \alpha_s)))) \\ F_{yi} &= D_{y\kappa} \sin(C_{y\kappa} \arctan(B_{y\kappa} \kappa_s - E_{y\kappa}(B_{y\kappa} \kappa_s - \arctan(B_{y\kappa} \kappa_s)))) \end{aligned} \quad (3.10)$$

The slip block outputs are tyre slip angle (α) and tyre slip ratio (κ). The two inputs into each tyre Pacejka block, calculated through the slip blocks are defined for all tyres according to equations (3.11) – (3.18). Additionally the Pacejka tyre model includes vertical load as an input.

$$\alpha_{FR} = \arctan\left(\frac{\sin\delta(\dot{\psi}w_f - V_x) + \cos\delta(\dot{\psi}a + V_y)}{\cos\delta(V_x - \dot{\psi}w_f) + \sin\delta(\dot{\psi}a + V_y)}\right) \quad (3.11)$$

$$\alpha_{FL} = \arctan\left(\frac{\cos\delta(\dot{\psi}a + V_y) - \sin\delta(\dot{\psi}w_f + V_x)}{\cos\delta(\dot{\psi}w_f + V_x) + \sin\delta(\dot{\psi}a + V_y)}\right) \quad (3.12)$$

$$\alpha_{RR} = \arctan\left(\frac{V_y - \dot{\psi}b}{V_x - \dot{\psi}w_r}\right) \quad (3.13)$$

$$\alpha_{RL} = \arctan\left(\frac{V_y - \dot{\psi}b}{V_x + \dot{\psi}w_r}\right) \quad (3.14)$$

$$\kappa_{FR} = -\left(1 - \frac{R\omega_{FR}}{\cos\delta(V_x - \dot{\psi}w_f) + \sin\delta(\dot{\psi}a + V_y)}\right) \quad (3.15)$$

$$\kappa_{FL} = -\left(1 - \frac{R\omega_{FL}}{\cos\delta(V_x + \dot{\psi}w_f) + \sin\delta(\dot{\psi}a + V_y)}\right) \quad (3.16)$$

$$\kappa_{RR} = -\left(1 - \frac{R\omega_{RR}}{V_x - \dot{\psi}w_r}\right) \quad (3.17)$$

$$\kappa_{RL} = -\left(1 - \frac{R\omega_{RL}}{V_x + \dot{\psi}w_r}\right) \quad (3.18)$$

where

R = Rolling radius of tyre

ω_i = Angular velocity of tyre

w_f = Half track width (front)

w_r = Half-track width (rear)

3.5 Load Transfer

The peak factor parameters D_x and D_y within the tyre model are a function of the normal force acting on the tyre and the increase/decrease in vertical load due to weight transfer. The curvature factors (E_x and E_y) and the stiffness factors B_x and B_y are also directly linked to load via a stiffness coefficient K_x and K_y . The load on each tyre is determined by the sum of normal load of the vehicle distribution per tyre. These include, equation (3.19), aerodynamic downforce, equation (1.4), and weight transfer during roll equations (3.20) – (3.23), whereby mass is transferred from one wheel to the opposite wheel. As this model omits pitch the weight transfer is purely lateral across wheels of the same axle.

$$F_{z_i} = m \cdot W_{d_{rl_i}} \cdot W_{d_{fr_i}} \quad (3.19)$$

where

$W_{d_{rl_i}}$ = Weight distribution right/left (%)

$W_{d_{fr_i}}$ = Weight distribution front/rear (%)

$$\Delta F_{z_{FL}} = - \frac{K_\phi \phi + C_\phi \dot{\phi}}{4 \cdot w_f} \quad (3.20)$$

$$\Delta F_{z_{FR}} = \frac{K_\phi \phi + C_\phi \dot{\phi}}{4 \cdot w_f} \quad (3.21)$$

$$\Delta F_{z_{RL}} = - \frac{K_\phi \phi + C_\phi \dot{\phi}}{4 \cdot w_r} \quad (3.22)$$

$$\Delta F_{z_{RR}} = \frac{K_\phi \phi + C_\phi \dot{\phi}}{4 \cdot w_r} \quad (3.23)$$

3.6 Aerodynamics

3.6.1 Downforce

According to equation (1.4), the total aero vertical force, is calculated prior to distribution across the four tyres via the centre of pressure location (CoP) and aero balance. The front and rear aero downforce is then calculated via the centre of pressure location, as a percentage of wheelbase from the rear tyres.

$$DF_R = DF_A \cdot CoP \quad (3.24)$$

$$DF_F = DF_A \cdot (1 - CoP) \quad (3.25)$$

Finally, the aero force for each tyre is applied by even distribution across the vehicle body width as:

$$DF_i = \frac{DF_{front\ or\ rear}}{2} \quad (3.26)$$

3.6.2 Aerodynamic Drag

A resistance force to the tractive effort of the vehicle is the aerodynamic drag, or the air resistance to the body as shown in equation (3.27). This resistance can be reduced by a drag reduction system (DRS), whereby the rear aerofoil can open to release drag but inevitably downforce. Therefore, ensuring DRS is only active on the straightaways of the circuit whilst it remains closed during cornering for maximum downforce and stability.

Again, drag is distributed to the front and rear wings as a ratio of the centre of pressure to the wheelbase. This allows the drag reduction system to reduce drag as a function of the rear wing.

$$D_{AR} = D_A \cdot CoP \quad (3.27)$$

$$D_{AF} = D_A \cdot (1 - CoP) \quad (3.28)$$

The loss of drag and downforce is based on the percentage of the whole body and the CoP:

$$Loss = \left(\frac{T_{reduc}}{1 - CoP} \right) / 100 \quad (3.29)$$

where

$Loss$ = Percentage loss

T_{reduc} = Total reduction across the entire body (%)

And therefore, during DRS operation

$$DF_{R_DRS} = DF_R - (DF_A \cdot CoP \cdot Loss) \quad (3.30)$$

$$D_{AR_DRS} = D_{AR} - (D_A \cdot CoP \cdot Loss) \quad (3.31)$$

3.7 Conclusion

This chapter has covered the vehicle dynamic mathematical formulae and details the modelling parameters, systems and subsystems from a mechanistic view of the architecture for a 4 DOF vehicle body dynamic model (16 DOF model including the tyres) that will be utilised to explore particle swarm optimisation.

4. Hybrid Race Vehicle Powertrain

4.1 Introduction

This chapter introduces the hybrid electric powertrain for a proposed GT type race vehicle that can be coupled to the vehicle dynamic model outlined in the previous chapter. It will explain the justification of the GT powertrain utilising current world championship rules and regulations. The mathematical formulae for the separate mechanical and electrical subsystems will be presented and an accurate 1-D engine model will be produced and validated against the physical engine test results to ensure consistency to the physical world counterparts. A GT hybrid powertrain concept is also developed and discussed based on an amalgamation of current and future F1 and WEC rules and regulations.

Current trends in both high-level motorsport and supercar development have been to introduce hybrid technologies. Formula One (F1) and the World Endurance Championship (WEC) have had the inclusion of hybrid systems in various guises since 2009 [74] and 2014 [75], respectively. A major revision to the F1 powertrain in 2014 [76] introduced a much more efficient and powerful hybrid system. In 2020/2021 the World Endurance Championship is set to change again with the removal of the LMP1 category and replacing it with a hypercar class that will include hybrid powertrain technologies [77]. The British Touring Car Championship also aims to include hybrid technologies by 2021 [78]. It is therefore a fair assumption to state that GT racing will also become a hybrid formula prior to all electric powertrain development. Due to the fact that amongst other race series most homologated GT cars are included in the endurance series' in a class below the LMP1(hypercar from 2021) and LMP2 categories, distance is still an important factor for GT racing and a limiting factor for electric only vehicles.

4.2 The Formula One Powertrain

As the Formula One powertrain and the limiting performance parameters are in existence, it is appropriate to develop a model based on this powertrain and the rules and regulations, and later refine it to be used for a GT specification vehicle. WEC hybrid rules allow for four-wheel drive systems, and therefore only some aspects from this series will be used to inform the GT specification. The powertrain model is calculated from three lookup tables; the Internal Combustion Engine's (ICE) torque in Nm, the torque (Nm) of the kinetic energy recovery Motor/Generator Unit (MGU-K) and the fuel flow rate determined from the Brake Specific Fuel Consumption (BSFC) of the ICE.

4.2.1 ICE Power

The torque profile of the engine is a two-dimensional map as a function of the engine speed, revolutions per minute (RPM) and throttle position angle. This is formulated according to equation (4.1).

$$T_{ICE} = f(\Omega_{ICE}, \alpha_{TPS}) \quad (4.1)$$

where:

T_{ICE} = Internal combustion engine torque

Ω_{ICE} = Internal combustion engine speed (RPM)

α_{TPS} = Throttle position angle

The power of the engine (P_{ICE}) is directly related to the torque through equation (4.2)

$$P_{ICE} = T_{ICE} \cdot \omega_{ICE} \quad (4.2)$$

where ω_{ICE} is the engine speed in rad/s

$$\omega_{ICE} = \frac{\Omega_{ICE} \cdot 2\pi}{60000}. \quad (4.3)$$

4.2.2 MGU-K Power

The torque profile of the MGU-K is a x-y axis data set as a function of the motor speed (RPM), which is directly related to the ICE speed through a fixed ratio (K).

$$T_{MGU-K} = f(\Omega_{MGU-K} \cdot K) \quad (4.4)$$

The power of the motor is directly related to the torque through equation (4.5):

$$P_{MGU-K} = T_{MGU-K} \cdot (\omega_{ICE} \cdot K) \quad (4.5)$$

4.2.3 Brake Specific Fuel Consumption

The brake specific fuel consumption of an engine is determined by the fuel used for the power created over time (as grams per kilowatt hour, g/kW-h) and is a function of the engine speed and the throttle position

$$BSFC = f(\Omega_{ICE}, \alpha_{TPS}) \quad (4.6)$$

The Formula One regulations state that fuel flow rate cannot exceed one hundred kilograms per hour (100kg/h) when the engine speed is above 10500RPM. Section 5 of the Formula 1 rules and regulations stipulate that:

5.1.4 Fuel mass flow must not exceed 100kg/h.

5.1.5 Below 10500rpm the fuel mass flow must not exceed: $Q \text{ (kg/h)} = 0.009 N(\text{rpm}) + 5.5$. [2]

Table 4.1 RPM versus permissible fuel flow [kg/h].

RPM	4000	5000	6000	7000	8000	9000	10000	10500+
Fuel Flow [kg/h]	41.5	50.5	59.5	68.5	77.5	86.5	95.5	100

By applying the formulae from the rules and regulations, the allowable fuel mass flow can be produced as shown in Table 4.1. The instantaneous fuel flow from an engine model simulation (similar to the one described in Section 4.4), can be used to determine engine load parameters. Engine map sites for normalised fuel flow (\dot{F}) can be determined as in Table 4.2, where 1 = 100kg/h.

Table 4.2 Normalised fuel flow (permissible Engine sites in green).

RPM \ TPS	4000	5000	6000	7000	8000	9000	10000	11000	12000	13000	14000
0	0.11	0.14	0.14	0.07	0.05	0.02	0.02	0.02	0.02	0.02	0.02
10	0.41	0.50	0.59	0.68	0.76	0.32	0.43	0.58	0.54	0.42	0.46
20	0.41	0.50	0.59	0.68	0.77	0.85	0.92	0.94	0.95	0.98	1.48
30	1.36	0.90	0.91	0.92	0.77	0.84	0.93	0.94	0.96	0.98	1.01
40	1.11	1.06	0.94	0.90	0.91	0.85	0.92	0.95	0.97	1.02	1.03
50	0.82	1.13	0.96	0.90	0.90	0.86	0.93	0.95	0.97	1.02	1.16
60	0.90	1.09	0.98	0.89	0.90	0.88	0.94	0.95	0.98	1.14	1.19
70	0.90	1.03	0.99	0.89	0.90	0.91	0.94	0.95	0.98	1.14	1.20
80	0.91	1.11	0.99	0.89	0.90	0.92	0.94	0.95	0.98	1.14	1.20
90	0.86	0.72	0.99	0.88	0.90	0.92	0.94	0.95	0.98	1.14	1.20

From empirical data¹, it can be seen that the common speed range of a Formula One V6 hybrid engine is between 9500RPM and 12500RPM. The power below this RPM would be mapped in a way that meets the regulations, however, it would produce an unusable low power output.

The power output of the ICE is increased by the use of a turbocharger. The turbocharger also consists of a motor/generator unit (MGU) that can be used to spin the turbocharger and create boost, which in turn creates additional power at the crankshaft and avoids lag at low turbine speeds if only exhaust gases are used to rotate the turbine side of the turbocharger. It can also be used to regenerate energy from the spinning turbine that is rotated by the flowing exhaust gases. Since these gases are hot in nature the MGU unit is known commonly as Motor/Generator Unit – Heat (MGU-H). Representatively, the MGU-H may utilise 60kW of power to rotate the compressor wheel of the turbocharger and the ICE output is boosted by 20kW, the waste gate is open and purely electrical power is rotating the compressor, however when the waste gate closes and exhaust gases are used to rotate the turbine wheel, 40kW of power can be regenerated from the MGU-H and the ICE power drops by 20kW. (Figure 4.1).

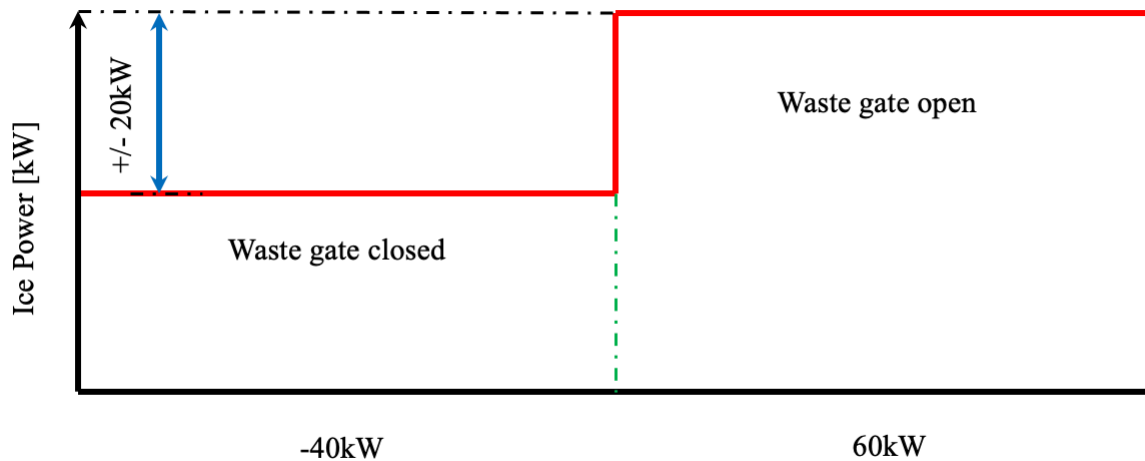


Figure 4.1 Motor Usage (60kW) creates 20kW at the crank-train.

¹ Onboard footage from rounds of the 2019 & 2020 Formula One championship.
<https://www.formula1.com/en/video.html>

4.3 Powertrain

The combined ICE and MGU-H power can be calculated via equations (4.7) and (4.8).

$$P_{MGU-H}^{add} = f(P_{MGU-H}, W_g) \quad (4.7)$$

where

P_{MGU-H}^{add} = additional power at the crank-train

W_g = waste-gate position (normalized to 1 = open, 0 = closed).

Thus, the boosted engine power output is

$$P_{BICE} = \frac{P_{MGU-H}^{add}}{P_{MGU-H}^{max} - P_{MGU-H}^{min}} \cdot (P_{MGU-H} - P_{MGU-H}^{min}) + P_{ICE} \quad (4.8)$$

where

$$P_{MGU-H} = \{(P_{MGU-H}^{max} - P_{MGU-H}^{min}) \cdot W_g + P_{MGU-H}^{min}\} \cdot \dot{V}. \quad (4.9)$$

Finally, total powertrain power can be calculated

$$P_{PT} = P_{BICE} + P_{MGU-K}. \quad (4.10)$$

The total powertrain torque (in Nm) is

$$T_{PT} = \frac{P_{PT}}{\omega_{ICE}} \cdot 1000 \quad (4.11)$$

and therefore, the total torque at the driven shafts is

$$T_{shaft} = T_{PT} \cdot GR \cdot \eta_{Gbox} \quad (4.12)$$

where η_{Gbox} is the mechanical efficiency of the gearbox and GR is the total gear ratio (instantaneous gear ratio multiplied by the constant final drive ratio).

Equation (4.12) can be distributed to each powered wheel through division by the number of driven wheels. It would be beneficial in the case of Formula 1 vehicles to distribute the power via a percentage of torque to simulate an electronically operated differential as a function of steering angle δ and yaw rate ψ .

$$T_{dist} = f(\delta, \psi) \quad (4.13)$$

Finally, torque at the wheel shaft is shown in equation (4.14), where i indicates the wheel location (rear left for example)

$$T_{wheel_i} = T_{shaft} \cdot T_{dist} \quad (4.14)$$

The speed at the driven wheel is calculated according to equation (4.15) and is an input to the slip model for slip ratio and forms part of the numerator as shown in equations (3.15) – (3.18).

$$\omega_i = \frac{\omega_{ICE}}{GR} \quad (4.15)$$

4.4 MGU Regeneration

The regeneration mode for the MGU-H is determined by the power required at the wheel and the amount of energy stored. The MGU-K energy harvest storage flow is limited to 2MJ per lap [2], however, additional harvested energy can be transferred to the MGU-H at an unlimited amount (Appendix 1). The regeneration and deployment of both MGU machines can be via optimization or control parameters, however, it is inevitable that the MGU-K should harvest as a function of deceleration (braking).

The braking torque is assumed to be at the maximum based on tyre braking force peak curves, and hence an additional braking above that of the MGU-K is assumed to come from the hydraulic braking system. As a result, for all braking instances, the brake force $F_{brake} \in [0,1]$ but is a function of longitudinal grip:

$$F_{brake} = f(F_x) \tag{4.16}$$

4.5 GT Race Vehicle Hybrid Powertrain

Formula One and a GT race vehicle engine model have been developed through the use of GT Suite 1D simulation and the GT engine has been validated against measured data. It is imperative that the engine model produces the same power as that installed in the vehicle to ensure the dynamic internal combustion engine model matches the performance parameters as that used in the vehicle dynamic model where the measured data will be utilised to validate the performance index of the Matlab/Simulink models versus measured data. To ensure the model performance outputs compared to the Cosworth engine installed in the Lotus Evora GTE car, a spare engine was stripped down, measured and casts taken of the intake and exhaust ports.

The castings were then converted into 3D models to allow appropriate discretisation of the port shapes as shown in Figure 4.2. All measurements and architecture of the engine were used to develop a 1D simulation model within the GT-Power software package.

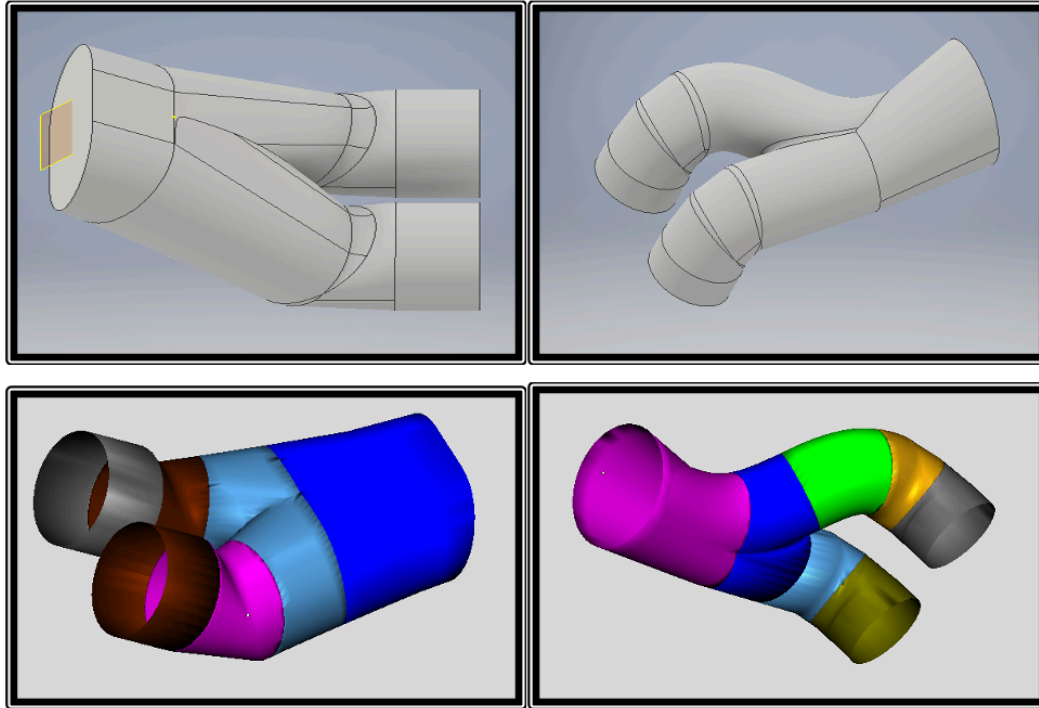


Figure 4.2 3D CAD model of the intake and exhaust ports (top) and their transfer into GEM 3D for discretisation of pipes and flow splits to ensure accurate modelling in GT Power (1D engine simulation).

The engine architecture dimensions, and specific design parameters forms part of a non-disclosure agreement between the Author and Lotus Cars (GB). Therefore, the basic information only could be provided in Table 4.3.

The input parameters, such as environment and combustion model were identical to that as utilised in the Cosworth dynamometer test bench results to allow validation of the performance output from the simulated engine. Figure 4.3 illustrates an overlay of the simulated engine model (1000RPM to 8500RPM) compared to the data provided by Cosworth from their dynamometer bench tests (4500RPM to 8500RPM). It is worth noting that, due to the non-disclosure agreement the values are normalised.

Table 4.3 Engine Architecture of GLC107.

Part	Measurement
Stroke	94mm
Bore	94mm
Compression Ratio	14.75:1
Connecting Rod Length	147.5mm
Inlet Valve Diameter	38.15mm
Intake Port	38.15x 37mm
Intake Runner Post Throttle Exit	56.5mm x 37mm
Intake Runner Post Throttle Length	122mm
Intake Runner Post Throttle Entrance Diameter	56.5mm
Throttle Butterfly Diameter	57.4mm
Intake Trumpet Entrance Diameter	91mm
Exhaust Valve Diameter	32.25mm
Exhaust Port Diameter	40.4mm
Exhaust Manifold Entrance Diameter	40.4mm
Exhaust Manifold Runner Diameter	48mm
Exhaust Manifold Runner Length	500mm (3 runners for each manifold)
Exhaust Single Pipe Diameter	60mm
Exhaust Single Pipe Length	500mm

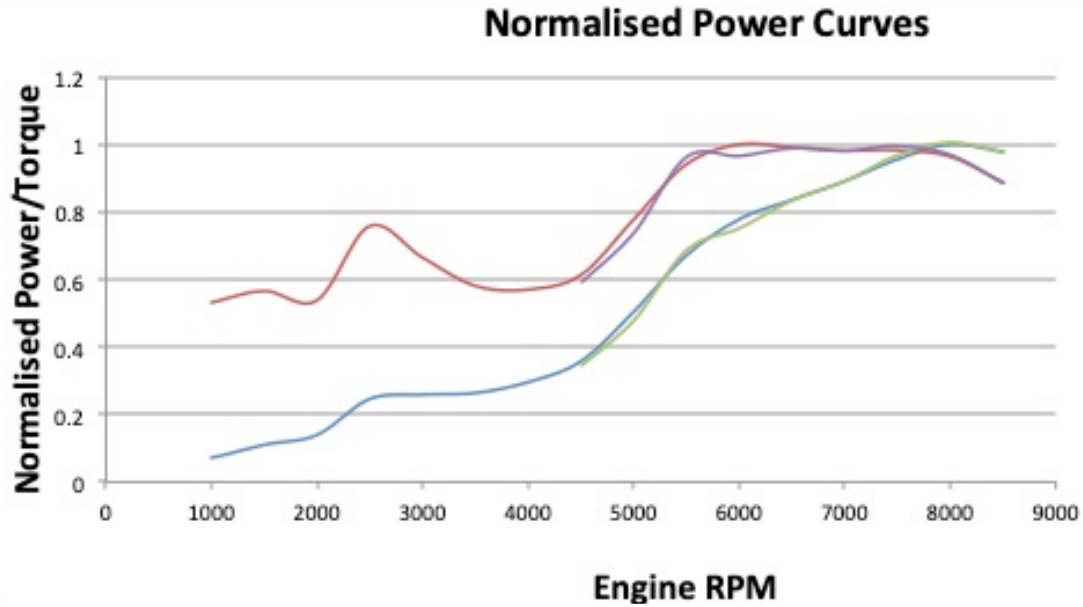


Figure 4.3 Normalised Power (blue line) and Torque (red line) curves for simulated GT Power model versus Cosworth dynamometer bench testing of the GLC engine.

Although Cosworth only provided test data for 4500RPM onwards, the plot shows a very accurate simulated engine model as shown in Table 4.4. The measured racetrack data from Silverstone that will be used for comparison of the simulated vehicle dynamic data shows that a minimum RPM during one flying lap is 4314RPM.

Table 4.4 Power and torque error for all RPM thresholds - simulated engine versus Cosworth dynamometer test results.

RPM	4500	5000	5500	6000	6500	7000	7500	8000	8500	
Power Error [%]	3.752	5.238	-2.244	3.422	0.279	0.034	-1.228	-0.564	0.309	Average Error [%] 1.000
Torque Error [%]	3.757	5.243	-2.238	3.427	0.285	0.039	-1.222	-0.558	0.314	Average Error [%] 1.005

This fully validated engine model allows equations (4.1) – (4.15) to be utilised and through the brake specific fuel consumption model a fuel limit can be set. Energy usage across a lap will be determined based on the World Endurance Championship rules and regulations, whereby 8 MJ of energy is allowed to be deployed across a lap of Le Mans (circuit de la Sarth layout), Formula One

cars are restricted to 4 MJ at all circuits. As this is the longest lap distance of the race calendar, the WEC rules state ‘the amount of releasable energy per lap will be limited in the proportion of length of circuit relative to the length of Le Mans circuit multiplied by a factor 1.55 and the amount of fuel allocation per lap will be limited in the proportion of length of circuit relative to the length of Le Mans circuit multiplied by factor 1.11’ [75].

Table 4.5 GLC 4.0L normally aspirated fuel flow (kg/h) versus engine speed and throttle position.

RPM \ TPS [°]	4000	4500	5000	5500	6000	6500	7000	7500	8000	8500
0	9.0	8.2	8.2	8.5	8.9	9.0	9.1	9.2	9.2	9.2
10	26.6	31.0	38.1	48.0	54.6	57.7	59.7	61.4	62.7	63.4
20	27.4	32.8	45.7	55.4	64.1	69.8	72.6	74.1	76.4	78.3
30	26.9	32.2	46.7	57.6	65.6	72.9	77.1	78.8	80.8	83.1
40	26.0	32.0	45.9	59.4	66.0	74.3	80.1	82.1	83.8	86.2
50	25.3	32.3	44.5	60.4	66.2	74.4	81.6	84.1	85.4	87.6
60	24.7	32.7	42.9	61.1	66.6	74.0	82.5	85.8	86.8	88.5
70	24.5	32.9	42.1	61.2	66.9	73.7	82.7	86.5	87.3	88.8
80	24.4	33.1	41.5	61.1	67.2	73.3	82.7	87.1	87.9	89.0
90	25.7	30.8	42.0	57.2	70.7	72.2	79.8	88.8	92.4	91.7

This gives the LMP1 8 MJ class at the Silverstone GP event a max deployment of 5.3 MJ, they are also limited to 82.9kg/h of fuel flow, restricting the hybrid model proposed in Chapter 7 to 7000RPM. The fuel and hybrid deployment limitations will be determined during the optimisation and control process, however, based on the brake specific fuel consumption and fuel injector flow, the Evora GTE GLC engine’s fuel flow (kg/h) is shown in Table 4.5.

4.6 Conclusion

A detailed description of current world series’ powertrains has been discussed and a new prototype GT Hybrid series has been presented. The architecture, system mathematical topology and engine model simulations have been implemented and validated against real world data. The engine fuel flow and energy limitations have also been determined. The mathematical model detailed in this

chapter will be coupled with the transient vehicle dynamic model previewed in the previous chapter.

5. Vehicle Dynamic Parameter Estimation and Optimisation

5.1 Introduction

A plethora of algorithms have been used for optimisation over the decades and the literature outlined in this chapter shows there have been many varied results and viewpoints on preferred methods and techniques. This chapter discusses particle swarm optimisation algorithms and the literatures headline statements, both for and against the algorithm. Single objective and multi objective optimisation techniques are implemented and evaluated to validate the transient dynamic model detailed in Chapter 3. The numerical optimisation results are analysed for accuracy, computing power, and computational time.

5.2 Particle Swarm Optimisation for Vehicle Dynamic Validation

Evolutionary based optimisation techniques are proven effective techniques in design and analysis of various engineering problems [107, 108, 109]. The optimisation algorithms may have various levels of success depending on the optimisation problem in hand, number of objectives, computing power and the range of variable parameters. Over the decades, evolutionary based algorithms [79], such as genetic algorithm optimisation (GA) [80], differential evolution (DE) [81], and particle swarm optimisation (PSO) [82] have all been studied and compared against each other. Montazeri et al [83] developed single objective (SO) and multi-objective (MO) optimisation for a 7-DOF robotic arm manipulation, comparing both SOGA and MOGA algorithms and found the MOGA approach more favourable in terms of the improved accuracy in parameter estimation and lower values for the output error estimation. The new method proposed in [83] relies on the multi-objectivization technique to convert a single objective output error identification problem to a multi-objective problem. This research is continued in [84] and [110] by comparing MOGA to SOPSO and MOPSO for the same robotic arm. In both lines of research, the input output data used for parameter estimation of robot is collected from one joint of the robotic manipulator. In

conclusion, the results in [84] found that the non-dominated sorting genetic algorithm (NSGA-II) and MOPSO, both performed well in finding a solution to the problems posed; however, depending on what we are looking for as a measure in an optimisation algorithm, i.e., convergence speed versus estimation accuracy, both algorithms can have their own advantages. As shown in [84], the NSGA-II algorithm is three times slower than PSO and although both algorithms show an error when the estimated values are compared to measured experimental data, the NSGA-II algorithm and MOPSO produce very similar results and therefore accuracy benefits are inconclusive.

Several automotive studies now utilise PSO as an optimisation tool with the domination method one of the most popular. Multi-objective optimisation tends to use a Pareto dominance method [85] although many variations of the algorithm exist [79,86]; it is observed that Pareto dominance algorithms produce the best results [86]. A 5-DOF vehicle vibration model was optimized by using a multi-objective uniform-diversity genetic algorithm (MUGA) [88]. This study was based once again on Pareto optimisation and comparisons made to the results generated by Bouazara et al [87]. In relation to the data in [87] the GA generated excellent convergence results. Wang [89] as Weiling [84] also compare PSO to GA, in this instance the neighbourhood cultivation genetic algorithm (NCGA), with the faster convergence rate accredited to the MOPSO algorithm and in this case, the results are much more accurate than that of the NCGA. A Hybrid PSO and GA algorithm is proposed in [79]. The results in [79] shows that the combined model is more favourable in terms of both convergence time and the result accuracy, when compared with that of Zadeh [91]. Several algorithms and optimisation techniques, including but not limited to Nelder–Mead simplex, differential evolution and particle swarm optimisation are tested against the Pacejka coefficients in [90]. The algorithms are utilised to match Pacejka curve shapes for lateral, longitudinal and aligning forces. This research uses the algorithm to create the Pacejka curves, and hence is based upon the curve matching of the known tyre measured data and curves with very limited success in fit success of the Pacejka curve.

Latest developments in PSO algorithms within the literature suggest a PSO model is the most suitable algorithm in terms of the convergence speed. In the current investigation a single and multi-objective PSO algorithm is developed to create a new generation of simulation environment for dynamic modelling and optimisation of a hybrid powertrain race vehicle such as those that can

be found in Formula One and the World Endurance Championship. In this way, it is possible to make a detailed numerical study to compare the performance of different PSO algorithms within the search space objective function(s). Unlike the previous results, in this thesis, the tyre coefficients are found by comparing the outputs of the vehicle dynamic simulated data to the data measured from the vehicle in the real race circuit. Therefore, by creating a Pacejka tyre shape the tyre model is generated by each particle searching for 20 tyre coefficients that enable the cost function to match closely the simulation vehicle dynamic output, with the data measured from the real race vehicle. By looking at the parameter search space, the PSO algorithm tries to match the data measured from the vehicle at each corner, each acceleration, and deceleration event around the circuit with the outputs from the developed simulation environment. This strategy allows three major contributions to vehicle dynamic modelling: 1. Enables data driven modelling to include both the vehicle dynamic system and tyre modelling system to work in harmony, 2. Multi-objectivisation of the output-error problem for the parameter estimation, 3. Numerical analysis and comparison of the single and multi-objective evolutionary algorithms.

Single-objective particle swarm optimisation (SOPSO) and a modified derivative of the same brethren multi-objective particle swarm optimisation (MOPSO) have improved performance over other optimisation algorithms as discussed within the literature review section. It is imperative that in both cases the algorithm should be tuned for the best performance to ensure accurate results.

To ensure the best performance, in terms of minimization of the cost function and to ensure that the search space is fully explored, the parameters of the particle swarm optimisation algorithm must be tuned carefully. In the case of this study each particle used within the swarm contains a number of parameters determined by tyre coefficients and chassis parameters. The PSO algorithm contains the initial conditions for each particle and the update equation for each iteration. Each particle is subject to an inertia weighting coefficient (w) and personal ($c1$) and social ($c2$) acceleration coefficients. These coefficients affect the direction and distance a particle travels within the search space. The mutation of such particles (pm) also has to be considered to ensure local minima and false plateaus are avoided.

As the first step and to determine the suitable parameters for the algorithm are tuned, the PSO algorithm is evaluated to estimate some known parameters. This is carried out by taking measured data from a race vehicle and using this data as an input (wheel speed and steering angle only at this stage) and simulating a twenty degrees of freedom (total) vehicle dynamics model through Matlab and Simulink. The output data obtained from the simulation of the vehicle dynamic model with known parameters were then used to tune the particle parameters of the PSO algorithm to estimate these twenty-two parameters in the vehicle dynamic model. As the particles containing these parameters within the PSO are swarming around a search space to find an optimum result, they each contain twenty variables for the Pacejka tyre model and two variables from chassis stiffness and damping. This stage enables a sanity check and tuning of the PSO through the observation of results of the error between known simulation data and PSO output data as opposed to measured data versus PSO data. After the tuning stage the PSO will be utilised to optimise the parameters of a vehicle dynamic simulation model for accuracy against measured data from a physical race vehicle.

To address the complexity and non-convexity of the optimisation problem a multi-objective PSO, is also developed and the results are compared with the single objective algorithm (one single vehicle dynamic output) to analyse the suitability of the algorithms in terms of convergence speed and estimation accuracy of the parameters. (closeness of the actual vs simulated parameters) and finally the best appropriate fitness function for comparing dynamic output plots of the vehicle model to actual data. The 4DOF model is utilised to determine best vehicle behaviour. The model consists of five inputs: steering and all four, wheel angular velocities ($\delta, \Omega_{fl}, \Omega_{fr}, \Omega_{rl}, \Omega_{rr}$) taken from the measured race car data. The four outputs (and their integrals) are the vehicle dynamic outputs from (3.1) to (3.4), and a various number of parameters for the PSO search space to be determined after sensitivity analysis. The parameters are based upon the tyre model and chassis stiffness and damping. The tyre model parameters are firstly tested at the top level: shaping factor, peak factor, stiffness factor and curvature factor (B to E respectively in (3.10)), and later at the lower coefficient level as shown in Table 5.1 with the inclusion of an axis shifting parameter $SV_{y\kappa}$.

Table 5.1 Pacejka tyre curve factors and their coefficients.

Tyre Factor	Coefficient
$B_{x\alpha}$	rB_{x1}, rB_{x2}
$C_{x\alpha}$	rC_{x1}
$D_{x\alpha}$	rH_{x1}
$E_{x\alpha}$	rE_{x1}, rE_{x2}
$B_{y\kappa}$	$rB_{y1}, rB_{y2}, rB_{y3}$
$C_{y\kappa}$	rC_{y1}
$D_{y\kappa}$	rH_{y1}, rH_{y2}
$E_{y\kappa}$	rE_{y1}, rE_{y2}
$SV_{y\kappa}$	$rV_{y1}, rV_{y2}, rV_{y3}, rV_{y4}, rV_{y5}, rV_{y6}$

Each particle will vary the parameters and determine best positions based upon the fitness of the vehicle dynamic output plots (cost function). Therefore, two conditions will be analysed: the parameter estimation versus known data for these parameters and the PSO cost function comparing measured or simulated vehicle dynamic data against the PSO output vehicle dynamic data. The parameter estimation error will simply be based upon known parameter results minus the PSO parameter results and the dynamic data cost function will be based up fitness of the curves to known dynamic data (5.0). After the sensitivity analysis is concluded in the following section details of the best error and cost functions are discussed in Section 5.5 and shown in (5.12) and (5.14). However it is important to acknowledge at this stage that the overall cost function algorithm can use two sources to calculate the errors: 1. the vehicle dynamic measured data from the race car (from this point forward named as measured data), 2. the results of the 4DOF model simulation, completed with known variables from the car and tyre manufacturer given to the tyre and chassis parameters, (from this point known as simulated data). Dependant on accuracy and validation of data each of the measured or simulated data can be assigned as a base to determine the accuracy of the output vehicle dynamic data from the vehicle dynamic model whilst using PSO, (from this point forward named as PSO data). In the case of trying to find the best fit of one vehicle dynamic output this would be detailed as single optimisation particle swarm optimisation (SOPSO) and in

the case of trying to find the best fit for multiple vehicle dynamic outputs this would be detailed as multi-objective particle swarm optimisation (MOPSO).

$$PE = \left| \frac{x - \hat{x}}{x} \right|$$

$$J(\xi_c) = -\|\xi_c - \xi_{d_c}\|_p$$
(5.0)

where

$$\|x\|_p = \left[\int_{-\infty}^{\infty} |x|^p dx \right]^{\frac{1}{p}}$$

and

PE is the relative parameter estimation error

x is the value of the known parameter

\hat{x} is the value of the parameter within the PSO iteration

J is the cost function error

p is the norm and can be 1, 2 or ∞

ξ_{d_c} is the known vehicle dynamic output(s) from measured or simulated data.

ξ_c is the best vehicle dynamic output(s) from the PSO. ξ_1 is longitudinal velocity (V_x), ξ_2 is longitudinal acceleration (\dot{V}_x), ξ_3 is lateral acceleration (\dot{V}_y) and ξ_4 is yaw rate ($\dot{\psi}$).

The measured data are collected from the race vehicle in a qualifying lap of Silverstone GP circuit. Therefore, the parameter estimation problem is further analysed by using the data collected from several corners around the lap and the entire lap. The main purpose for the use of PSO in this chapter is to validate a vehicle dynamics model against track data so that in the following chapter the model can be utilised to find the fastest path around a circuit.

5.3 Multi Objective PSO Problem Formulation

Multi objective algorithms were borne from a need to establish a result whereby not one objective function is to be optimised but several, therefore there is an assembly of solutions rather than one unique solution.

The objective of the MOPSO is to optimise k objective functions simultaneously. This means the k objective functions has to be maximised, minimised or a combination of both.

The basis of the MOPSO algorithm is to find a solution vector \mathbf{x} to satisfy both equality and inequality constraints, $h_j(x)$ and $g_i(x)$ in (5.2) and (5.3), respectively.

$$\vec{\mathbf{x}}^* = [x_1^*, x_2^*, \dots, x_n^*]^T \quad (5.1)$$

$$h_j(\mathbf{x}) = 0, j = \{1, 2 \dots p\} \quad (5.2)$$

$$g_i(\mathbf{x}) \geq 0, i = \{1, 2 \dots m\} \quad (5.3)$$

The aim of the multi-objective optimisation problem is to find a solution vector \mathbf{x} for the vector function (5.4)

$$\vec{\mathbf{f}}(\vec{\mathbf{x}}) = [f_1(\vec{\mathbf{x}}), f_2(\vec{\mathbf{x}}), \dots, f_k(\vec{\mathbf{x}})]^T \quad (5.4)$$

such that

$$\vec{\mathbf{x}} = [x_1, x_2, \dots, x_n]^T \quad (5.5)$$

is a vector of decision variables. In the scenario of optimising race car dynamic behaviour f_1, f_2 etc would be the norm function error of each given vehicle dynamic output and x_1, x_2 etc would be for example the tyre factor or coefficients parameters as given in Table 5.1. Solutions are then compared to determine the domination property. Domination is determined if the following two conditions are satisfied:

1. Solution 1 is not worse than solution 2 in all objectives
2. Solution 1 is better than solution 2 in one objective

If these conditions are not met, then solution 1 does not dominate.

For the PSO algorithm to reasonably explore the solution space, each particle is given a minimum and maximum value for its position, velocity, and the inertia value used to control the behaviour of the algorithm. The initial value of the position and velocity of each particle is usually assigned randomly within the given minima and maxima. The velocity of each particle is then updated by having the local and global best solutions during each iteration. The velocity of the particle is updated as

$$v_{id}^{k+1} = w \times v_{id}^k + c_1 \times r_1^k \times (p_{id}^k - x_{id}^k) + c_2 \times r_2^k \times (p_{gd}^k - x_{id}^k) \quad (5.6)$$

and the new position for each particle is calculated from

$$x_{id}^{k+1} = x_{id}^k + v_{id}^{k+1} \quad (5.7)$$

where

w = inertia weight based on a linear reduction or increase in a range between 0 and 1. This allows scaling of the velocity and control the search behaviour. Low values equate to exploitation around a particular particle results whereas high values allow exploration.

v_{id}^k = dimension velocity of the particle

c_1 = personal learning coefficient

r_1^k, r_2^k = random number values defined in range [0,1]

p_{id}^k = personal (local) best dimensional position of particle i

x_{id}^k = dimensional position of the particle i

c_2 = global learning coefficient

p_{gd}^k = global best dimensional position of particle i

The pseudo-code for the MOPSO algorithm used for optimisation can be outlined as follows

1. Initialisation Loop

2. Particle initialisation – Twenty-two parameter results randomly selected within an upper and lower bound.
3. Simulate Vehicle Dynamic Model and produce cost result.
4. Individual Particle and Global best positions are recorded
5. **Main Loop** – Simulate vehicle dynamic model per iteration until stopping criteria is met
6. Stopping criteria is not satisfied
 - a. Evaluate vehicle dynamic output versus known result (error)
 - b. Update Personal and Global best positions. Parameter results within the particle are stored along with best cost of dynamic output error.
 - c. Random swarm movement by updating the velocity of each particle.
 - d. Select the personal best
 - e. Select the global best
 - f. Update
7. End

To ensure the results stay within the boundaries of the solution space, the updated values are checked after each iteration according to these inequalities

$$(x_{id}^k) = \begin{cases} (min_{id},) & \text{if } x_{id} < min_{id} \\ (max_{id},) & \text{if } x_{id} > max_{id} \end{cases} \quad (5.8)$$

Then the personal best is selected for each particle and its value is compared to the global best. The global best is only updated if $pbest > gbest$.

Without the use of a tyre dynamometer or access to tyre manufacturer data it is not possible to determine full data for tyre simulation modelling and empirical knowledge isn't the ideal, the same can be said for some aspects of the vehicle itself, in particularly as in equation (1.9), roll stiffness and damping affect overall roll that in turn affects the remaining 3-DOF of the model due to coupling of the formulae. Again, unless the vehicle manufacturer provides this information, or the

chassis stiffness is measured dynamically it is not possible to truly know the result without parameter estimation and therefore remain an unknown. Prior to developing an algorithm to identify exact parameters through a genetic algorithm a sensitivity analysis process should be employed to identify the minima and maxima of the system parameters.

5.3.1 Sensitivity Analysis

As described in Section 5.2 the tyre model contains co-efficients that generate the shaping factors. As there are seventy-three various co-efficients the first stage of the sensitivity analysis was to use the co-efficients that relate to the combined Pacejka model. Basing the sensitivity analysis on the topology of the model, namely B, C, D and E, further reduction of the parameters can be established, this ensures that rather than seventy-three parameters for each tyre having to be tested reductions can be made from analysis of results. Other unknown parameters for the vehicle were the Inertia values around the X, Y and Z axes of the race car and the Chassis Stiffness and Damping.

After successful analysis of the results, it is then possible to run sensitivity analysis on the coefficients under each tyre parameter if the outputs are modestly affected. The sensitivity of cost functions $J(V_x)$, $J(\dot{V}_x)$, $J(\dot{V}_y)$ and $J(\dot{\psi})$ were carried out (as measured car data was available) as an error formulation with respect to the eight tyre parameters and the chassis stiffness, damping and finally the inertia around the X, Y and Z axes, Table 5.1 identifies the variance of parameters. The initial parameters listed in Table 5.1 are taken from dynamometer testing of a race tyre and from the vehicle manufacturer. Dependent on the sensitivity of the system the next stage of analysis is plotting the model output (V_x , \dot{V}_x , \dot{V}_y and $\dot{\psi}$) versus measured data so that the parameters can be ignored, or the variance refined. The analysis was carried out over several corners around the race circuit. In this instance the Silverstone Grand Prix circuit and corners: Abbey and Village, The Loop and Arena section. (Figure 5.14).

Table 5.2 Initial Sensitivity Analysis Parameters and Variance

Input Parameter	Initial Parameter	Minimum/Maximum/Variance
B_x	12.3	0/24/1
B_y	13.1	0/24/1
C_x	1.14	1/2/0.1
C_y	1.14	1/2/0.1
D_x	1500	1000/2000/100
D_y	-4000	-6000/-2000/100
E_x	0.3	0/1/0.1
E_y	0.32	0/1/0.1
C_ϕ	19000 [Nm-s/rad]	1000/20000/1000
K_ϕ	100000 [Nm/rad]	10000/200000/10000
I_{xx}	300 [kg-m ²]	100/1000/100
I_{yy}	700 [kg-m ²]	100/1000/100
I_{zz}	1500 [kg-m ²]	500/2500/100

Initial analysis to determine the sensitivity of the system shows that there are several parameters that cause large variations in results but that these results can change from output to output due to coupling of the system (3.1) to (3.4). As per Figures 5.1 and 5.2 it is clear to see that the inertia around the Z axis varies the lateral acceleration immensely, introducing noise. However, the results show that an inertia in the range of 1500 to 2500kg-m² have little effect on the lateral acceleration. The same results were also observed for Yaw rate. However as expected a less than 1% change was made to longitudinal dynamic results. Using a progressive approach to test each parameter as listed in Table 5.1, it was observed that for C_x and C_y (Figure 5.3) the value is changing across the duration of the simulation and therefore a constant number model creates unrealistic results. Therefore, for detailed analysis they would have to be returned back to their constituent numerical input co-efficients that includes two and three separate inputs respectively. The same conclusion was drawn for B_x , B_y , D_x , D_y , E_x , and E_y . These six tyre formulae components make up 91% of the co-efficient parameters within the tyre model and therefore results were inconclusive by testing these topology parameters and are re-evaluated through a PSO process in Section 5.3.

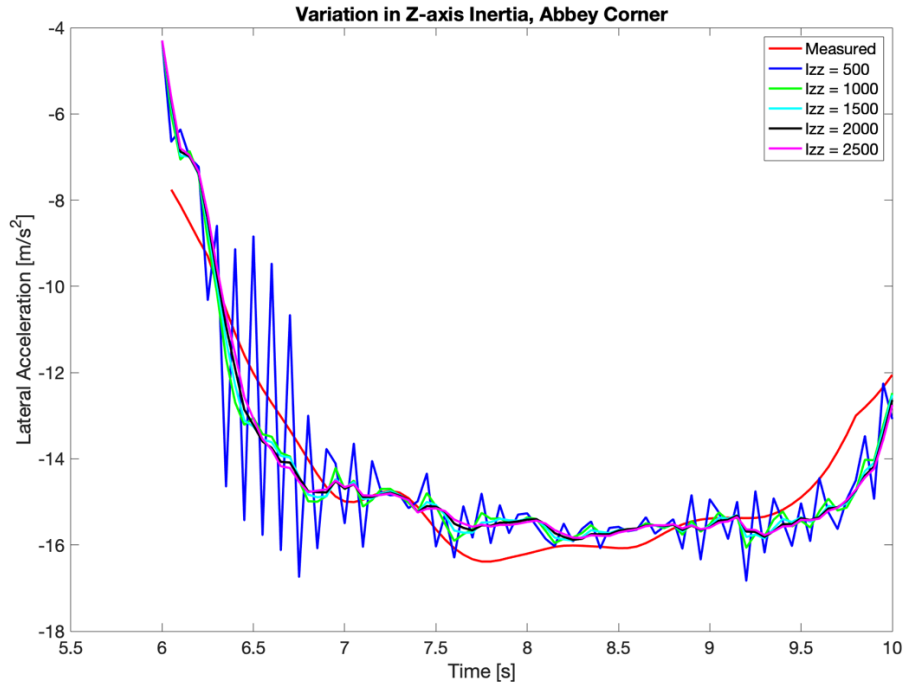


Figure 5.1 Lateral acceleration for Abbey corner with regards to changes in inertia around the z-axis.

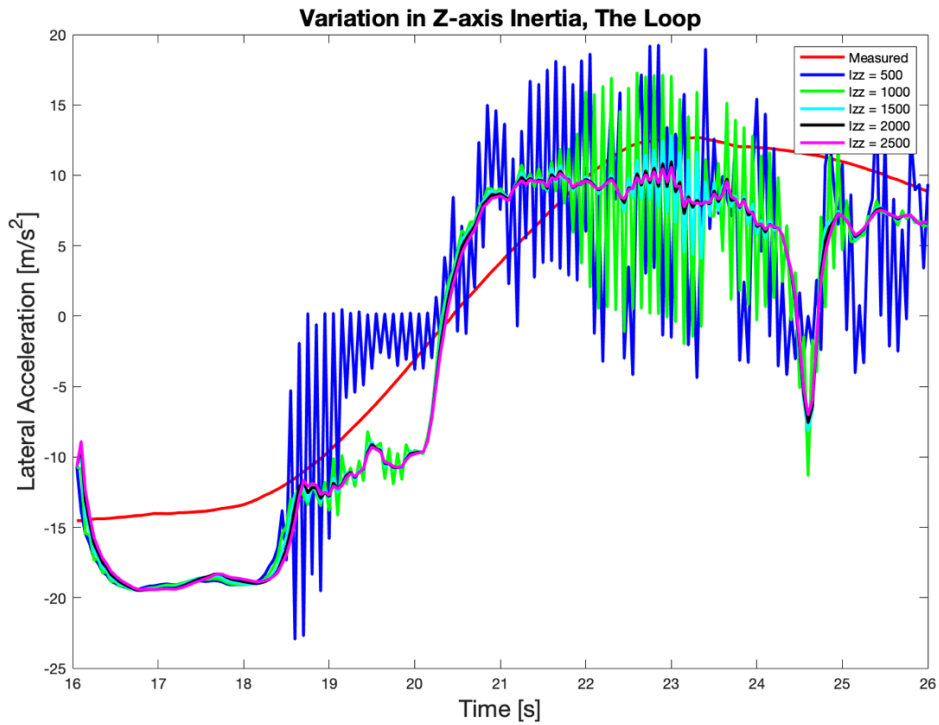


Figure 5.2 Lateral acceleration for Village, The Loop/Arena section with regards to changes in inertia around the z-axis.

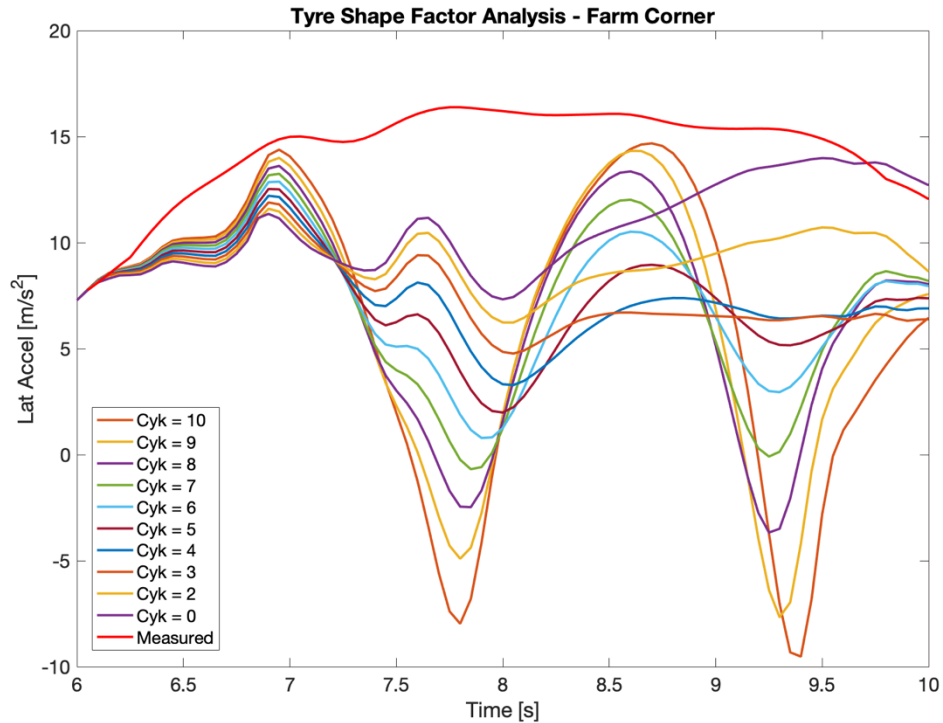


Figure 5.3 Effect of constant C_y ranging from 1 – 10 upon lateral acceleration through Abbey corner vs measured race car data.

The remaining tyre parameters in initial modelling analysis shows that they stay constant throughout any race car manoeuvre and conclusive testing could be carried out. It was observed that very little changed for all outputs of the system when varying C_x and C_y by a 10% change between 0 and 100% with a final value of 1.2 returning the least error for longitudinal dynamics and no change to lateral when varying C_x and vice versa when varying C_y . When this variance was increased to a 100% change from 0 to 1000%, larger variations once again in results were observed both in longitudinal and lateral dynamics when moving further from a constant of three.

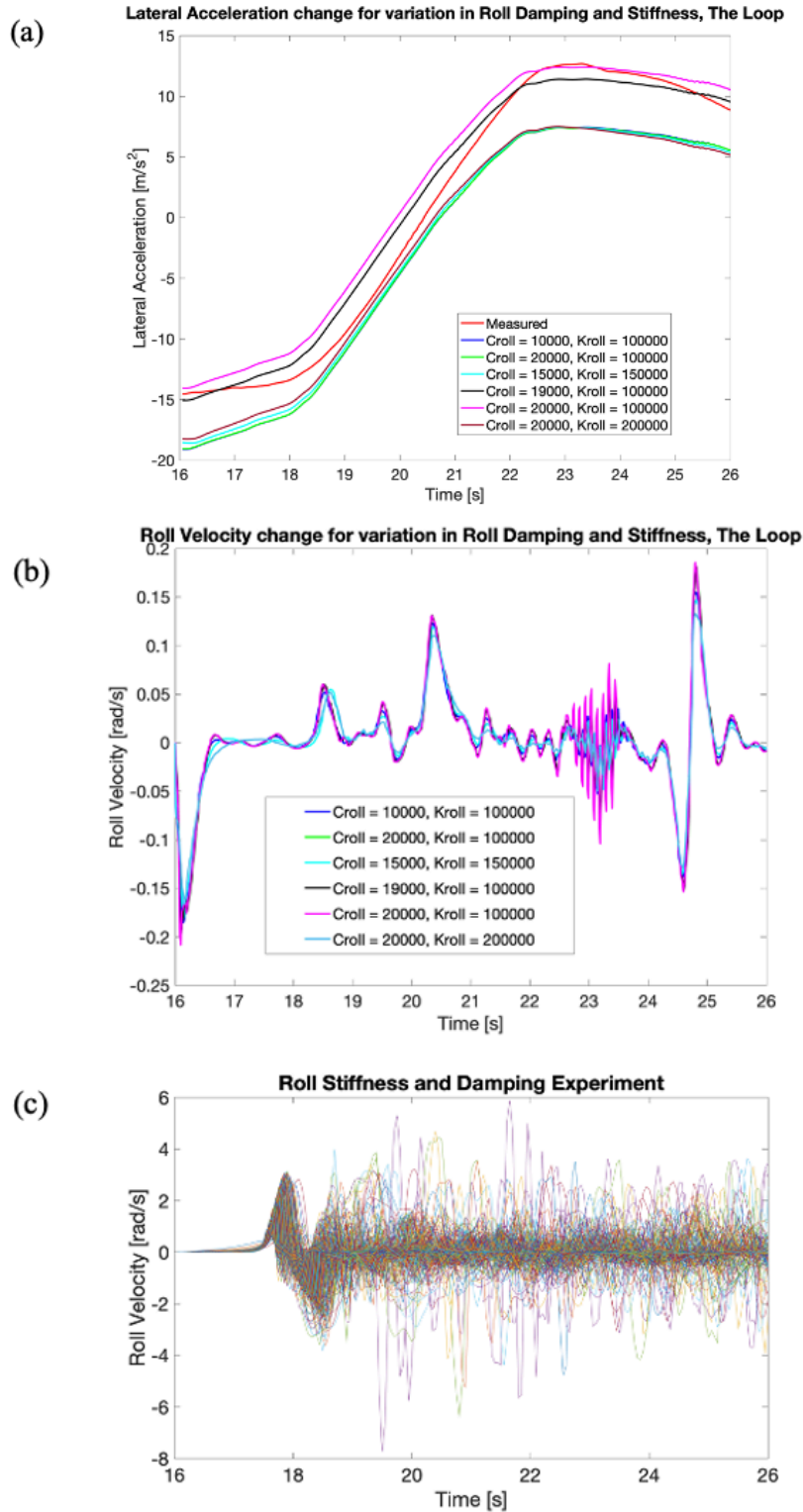


Figure 5.4 Best results of roll stiffness and damping combined variance for Village/The Loop/Arena section with regards to (a) lateral acceleration, (b) roll velocity and (c) all results for roll velocity.

Throughout the initial sensitivity analysis, it was observed that ranging to extremes and unrealistic numerical data would cause chaos in the results. But it was apparent that tyre data even with some small changes can have a great effect on various dynamic outputs. However, the greatest change was from the stiffness and damping of the chassis itself. Figure 5.4 (a) and Figure 5.4 (b) show that satisfactory results can be found within a tolerance of real data however utilising a large variation in stiffness and damping can create a large change in roll behaviour (Figure 5.4 (c)). It was determined that empirically sourced GT inertia numerical data [9] should be utilised as this included a typical GT style vehicle inertia value and returned the least error ($V_x = -0.1475$, $\dot{V}_x = -0.53$, $\dot{V}_y = 60$, $\psi' = 11.2$). Tyre manipulation would form part of the particle swarm optimisation algorithm. However, as stiffness and damping are coupled a design-of experiments loop was created to test all variations of damping against all variations of stiffness (Figure 5.4 (c)).

5.3.2 Performance surface

Observing Figure 5.4 (c), it is almost impossible to analyse the data sufficiently with such a plethora of results and variation; therefore, a more desirable analysis method is through the creation of performance surfaces. This allows a detailed understanding of the system behaviour and can determine the selection of an appropriate optimisation model. The visualization of the system behaviour is created by generating a 3-dimensional surface of 2 input parameters listed in Table 5.2 against the error of the measured data versus simulated data for various corners.

As can be seen through Figures 5.5 to 5.7 a variation in results occurs dependent upon the measured data comparison. The surface performance plots also allow a visual representation to determine whether local minimum (Figure 5.6) could occur during an optimisation algorithm and whether the variable limits should be reduced or extended. As observed in the plan views of Figures 5.5 to 5.7 the trend to lowest error is based around the $C_{roll} = 19000\text{Nm-s/rad}$ and $K_{roll} = 1000000\text{Nm/rad}$ results.

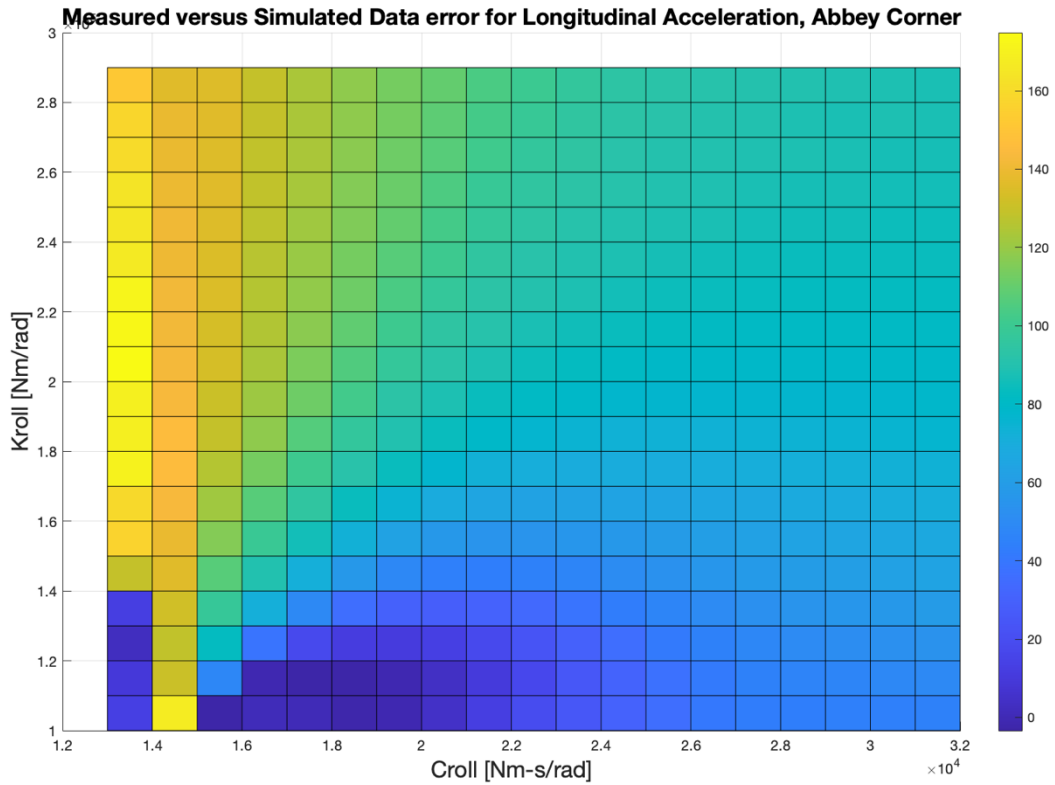
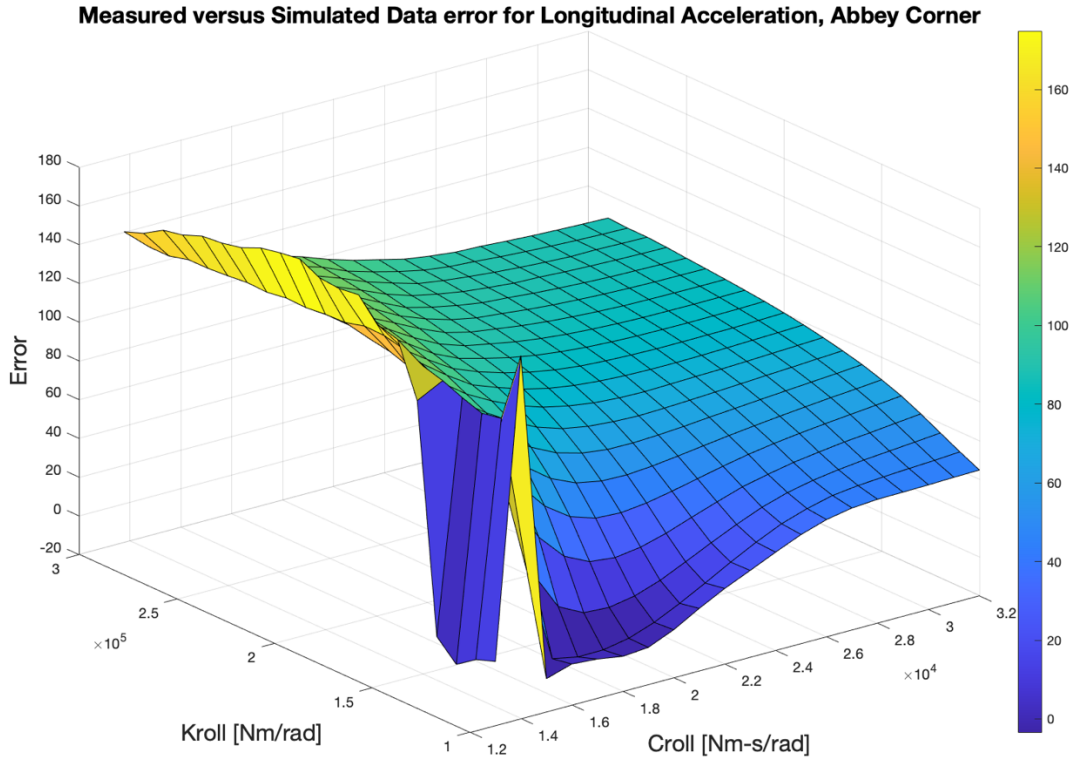


Figure 5.5 Isometric and plan view of the performance surface for longitudinal acceleration of the error function ($e = \xi_m - \xi_d$; $J(K\phi, C\phi) = -\|e\|_2$) as a function of chassis damping and chassis stiffness through Abbey corner. Here ξ_m and ξ_d are the measured and simulated data.

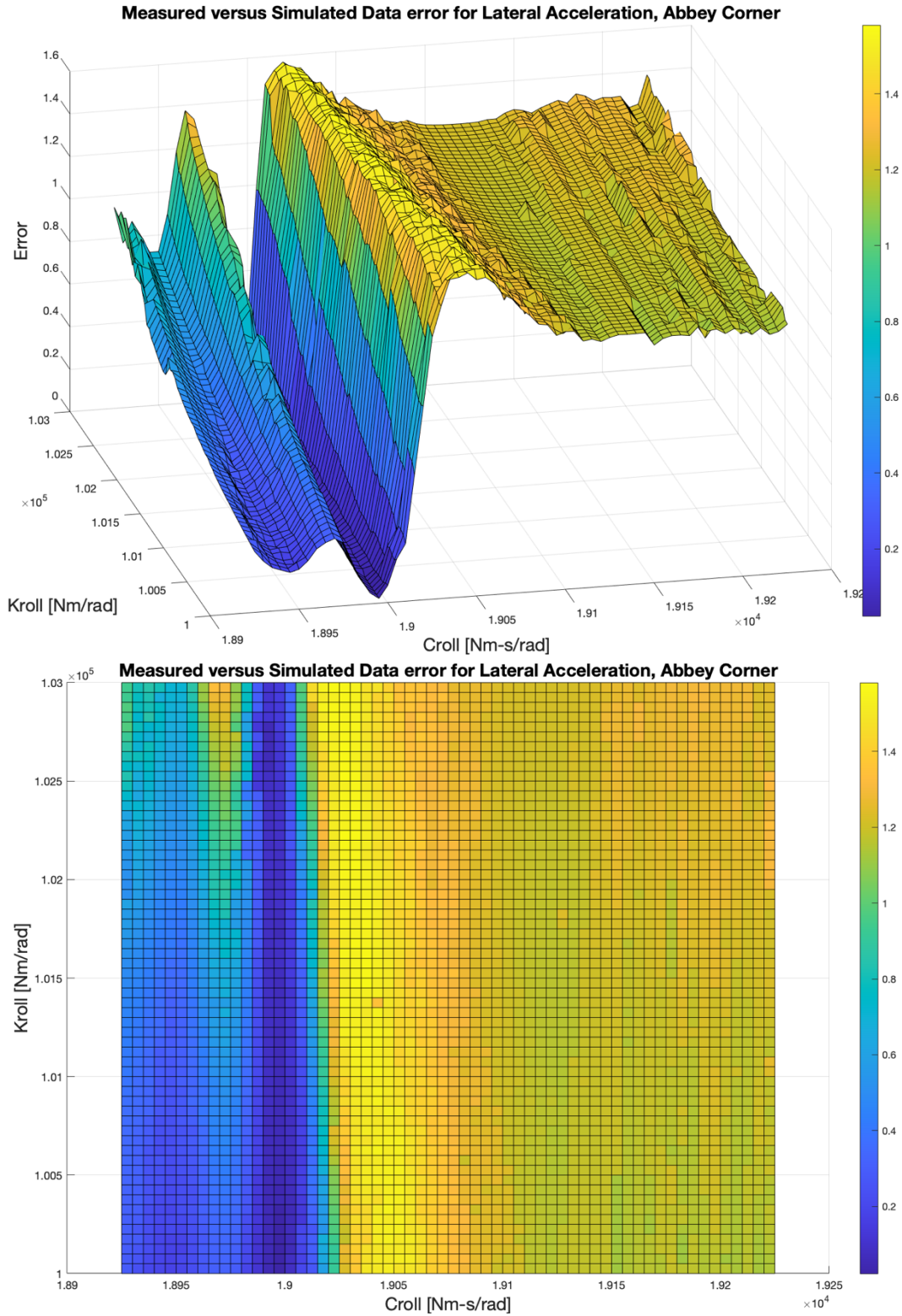


Figure 5.6 Isometric and plan view of the performance surface for lateral acceleration of the error function ($e = \xi_m - \xi_a$; $J(K\phi, C\phi) = -\|e\|_2$) as a function of chassis damping and chassis stiffness through Abbey corner. Here ξ_m and ξ_a are the measured and simulated data.

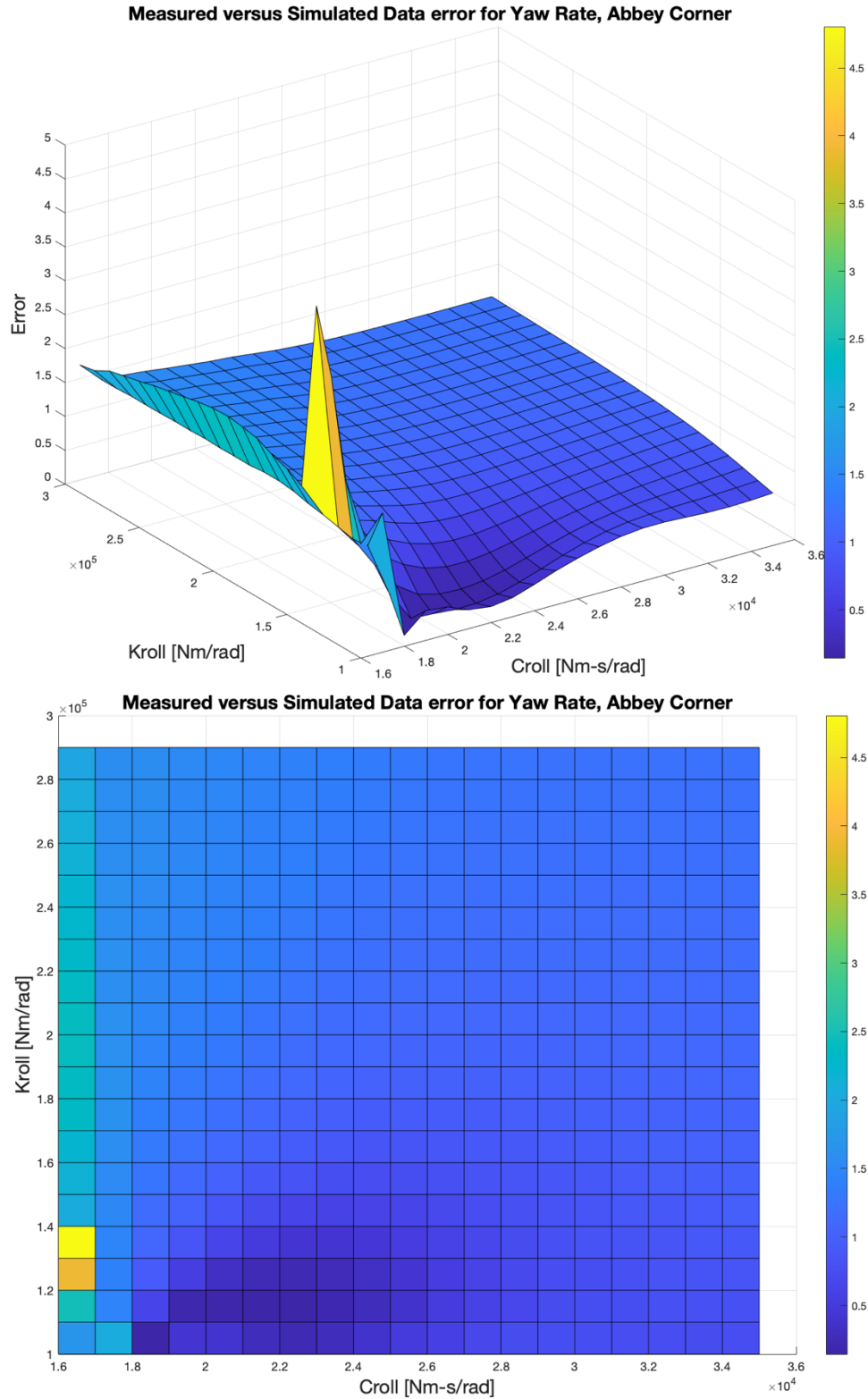


Figure 5.7 Isometric and plan view of the performance surface for yaw rate of the error function ($e = \xi_m - \xi_d$; $J(K\phi, C\phi) = -\|e\|_2$) as a function of chassis damping and chassis stiffness through Abbey corner. Here ξ_m and ξ_d are the measured and simulated data.

The final results of surface analysis are presented in Table 5.3 after refinement of the variables and testing of both Abbey and Village/The Loop complex a compromise of best results can be determined. Although the results indicate a large variation between the error for longitudinal acceleration across a performance surface all vehicle dynamic outputs tend towards zero at $C_{roll} = 19000 \text{ Nm-s/rad}$ and $K_{roll} = 1000000 \text{ Nm/rad}$ results. The remaining vehicle dynamic output results, further analysis of the measured versus simulated data demonstrates that Yaw and Lateral Acceleration generate least error results.

Table 5.3 Final results for chassis stiffness and damping with norm 2 cost function for Abbey and Village/The Loop corners at the Silverstone Grand Prix circuit.

Abbey Corner	K_{ϕ}	C_{ϕ}	Cost
Longitudinal Velocity (m/s)	100000	19000	-1.98
Longitudinal Acceleration (m/s^2)	20000	3000	2.21
Lateral Acceleration (m/s^2)	10000	7600	0.04
Yaw Rate (rad/s)	10000	3000	0.07
Village/The Loop	K_{ϕ}	C_{ϕ}	Cost
Longitudinal Velocity (m/s)	19000	1000	-3.68
Longitudinal Acceleration (m/s^2)	19000	1000	-0.58
Lateral Acceleration (m/s^2)	13000	2600	0.45
Yaw Rate (rad/s)	13000	2800	0.21

Reducing the variation to within the parameters shown in Table 5.2 and refining the step size a best result can be determined. Although a compromise has to be established it is apparent from surface performance analysis that a plateau is available to work within and as such a final result of $K_{\phi} = 100000$ $C_{\phi} = 19000$ was established as a best possible measured versus simulated error compromise (Figure 5.8 and 5.9).

Further analysis of the response at standard tyre coefficients, standard inertia values and the improved result for chassis stiffness and damping show that the inertia is good as I_{xx} and I_{yy} caused very little interference and the response in Yaw from one direction to the other has an error of almost zero so for future analysis inertia can be ignored. Figure 5.8 does show that an issue occurs for peak Yaw rate and Lateral acceleration during left hand cornering. Firstly, it should be observed that the response seen at the 1080m marks is due to the steering input parameter. At this point on the circuit in the measured data the driver was catching some over-steer and although the

measured data does not catch a large response to this but settles the car the simulated data responds much faster and causes an unnecessary spike in the data so can be ignored. This was also true when this vehicle data was used for a full lap analysis simulation. (Figure 5.9). It can be justified that the issue is down to tyre modelling. For simulation speed a 4-DOF model has been built that ignores suspension geometry therefore wheel camber (although set in the tyre model) cannot change with time and is not coupled to the roll dynamics.

With roll, and inevitable weight transfer, (equations (3.20) to (3.23)) a left tyre can generate much more grip during right-handed corners and the right tyre during left hand corners. As can be seen in Figure 5.10, where a right, left section of corners in quick succession has taken place the tyre responds accordingly establishing weight transfer and vertical force is working appropriately. However, the tyre fails to reach maximum performance as per the manufacturers tyre data for the same load, depicted as the peak traction ellipse. This can change dependant on corner and load, but a change in camber to the wheel in the tyre model may improve the maximum forces produced for certain corners. Camber values can form part of optimisation problem and therefore can be added to the PSO as another parameter.

These results demonstrate that many parameters dictate the overall performance index of the vehicles behaviour and how due to coupling of the system that a compromised final parameter must be established. Therefore, it can be determined that a multi-objective algorithm would be suited for this problem. However, simulation time and computing power should still be considered and so a SOPSO and MOSPSO will be compared for overall result accuracy of the model outputs versus measured data as a function of time.

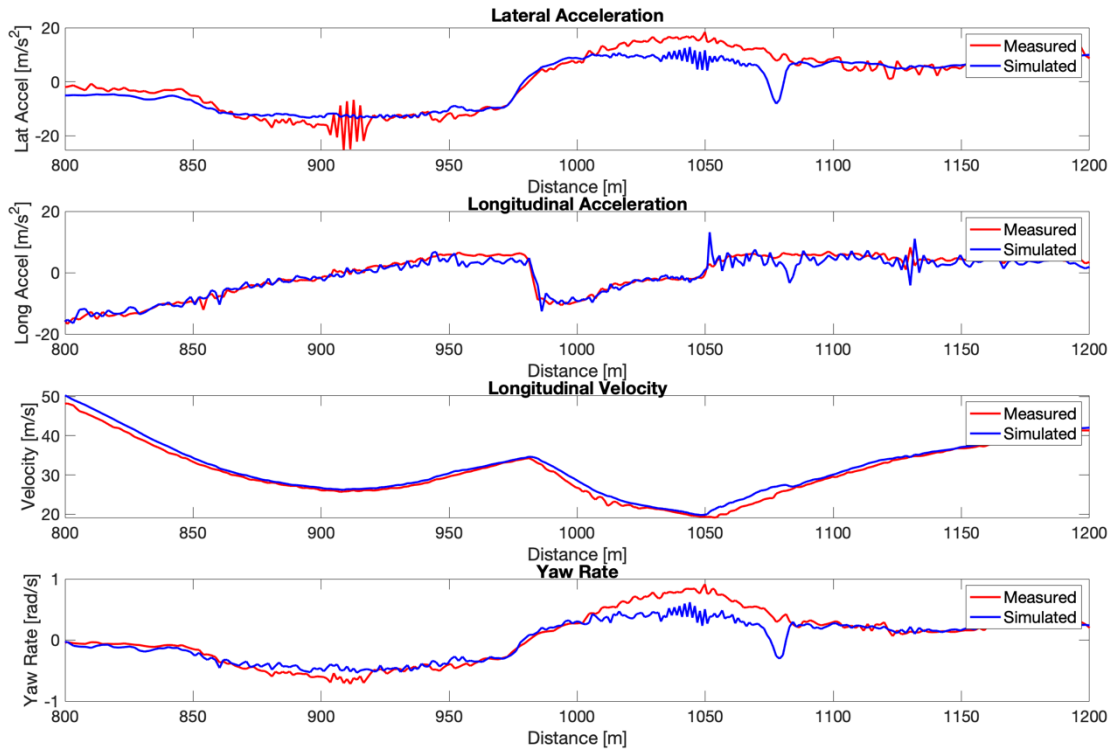


Figure 5.8 Results of roll stiffness and damping combined variance for Village/The Loop section with regards to lateral acceleration, longitudinal acceleration, longitudinal velocity and yaw rate. Least error measured (red line) vs simulated data (blue line).

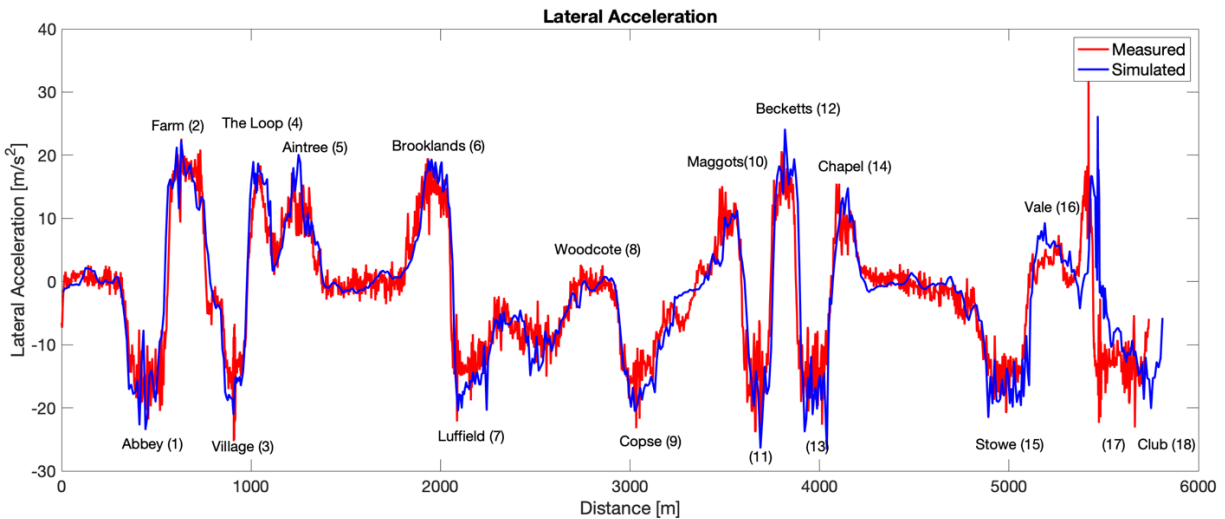


Figure 5.9 Lateral acceleration measured (red line) versus simulated (blue line) for an entire lap of the Silverstone Grand Prix Circuit.

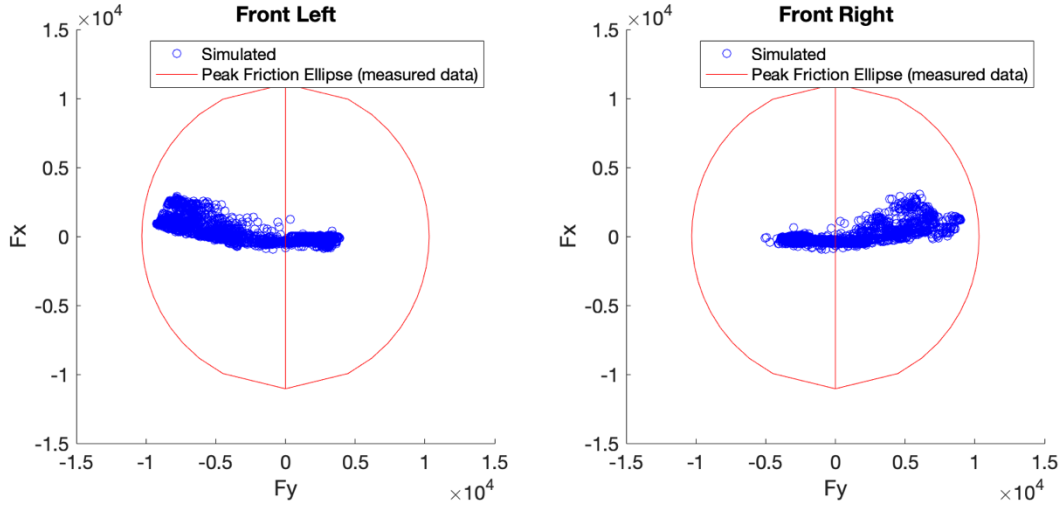


Figure 5.10 Combined lateral and longitudinal tyre forces for a front left and front right tyre during the Village/Loop corners. The outside ellipse shows the peak combined force maxima taken from peak tyre forces within the measured vehicle data.

5.4 Optimisation problem formulation

The cost function of the particle swarm optimisation problem is to minimise the error between the measured data and simulated output of the Simulink vehicle dynamic output (equation. 5.9). A single objective PSO would minimise the error of one of these outputs whereas multi-objective is minimising the error for all output parameters simultaneously.

$$output = [V_x, \dot{V}_x, \dot{V}_y, \psi] \quad (5.9)$$

The input parameters (u) to the Simulink model are the measured vehicle input data based on the physical vehicle telemetry data, each individual wheel speed and the steering input.

$$u = [\Omega_{wheel}, \delta] \quad (5.10)$$

Within the sensitivity analysis section, it was apparent that changing the top level Pacejka shaping and curvature factors were not ideal as they change with time due to vehicle dynamic behaviour and corner architecture. Therefore, the PSO parameters to be optimised are the Pacejka tyre

coefficients, that are constant numbers and used to establish the combined Pacejka tyre model shaping factors. These coefficients be optimised along with and the chassis stiffness and damping.

$$\theta = [rB_{x1}, rB_{x2}, rC_{x1}, rE_{x1}, rE_{x2}, rH_{x1}, rB_{y1}, rB_{y2}, rB_{y3}, rC_{y1}, rE_{y1}, rE_{y2}, rH_{y1}, rH_{y2}, rV_{y1}, rV_{y2}, rV_{y3}, rV_{y4}, rV_{y5}, rV_{y6}, K_{\phi}, C_{\phi}] \quad (5.11)$$

5.5 Performance tuning and optimisation

5.5.1 PSO Acceleration Co-efficients

From the literature [70, 71] it has been established that PSO algorithms work best when $c_1 + c_2 = 4$. As shown in (5.6), c_1 and c_2 are the acceleration coefficients for the particle best position vector and global best position vector respectively, whereby they can aid/inhibit movement towards the local best or global best solution. Therefore, a loop was created to establish the optimal c_1 and c_2 within each iterative step to find Best Tune. The PSO was set to use a swarm of 50 particles (all containing 22 parameters) over 10 iterations with each iteration having a further 10 iteration loops to change c_1 and c_2 . Changing c_1 stepped linearly between 0 and 4 (basing the linear step on maximum iterations) and changing c_2 based upon $c_2 = c_1 - 4$ ensured the literature research of $c_1 + c_2 = 4$ could be maintained.

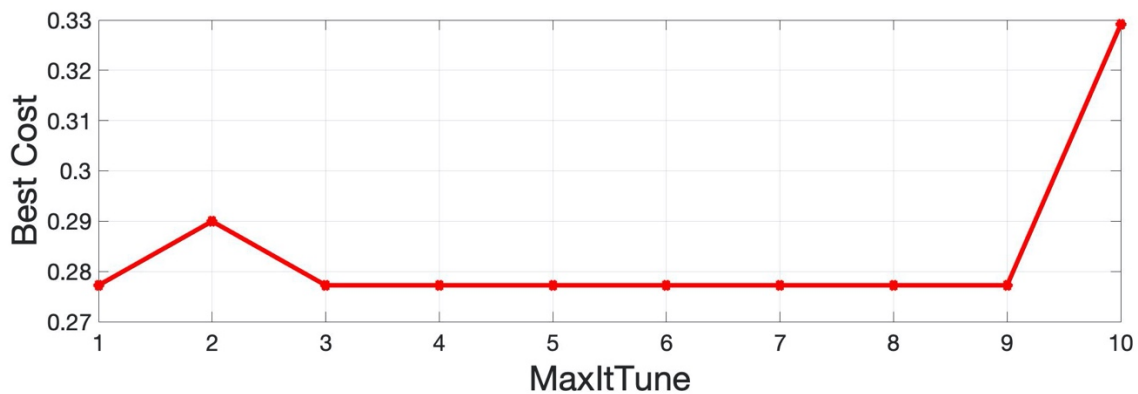


Figure 5.11 Results of SOPSPO during variation of c_1 and c_2 where $c_1 = (0, 4, 10)$ and $c_2 = c_1 + c_2 = 4$.

A trend appeared during all iterations of the SOPSO and for all outputs (longitudinal velocity, lateral acceleration, and yaw rate). As seen in Figure 5.11 the SOPSO found the lowest best cost during the internal loop on iterations 3 to 9. During only 1 tuning simulation (lateral acceleration, 50 population and 10 iterations) did the results change. In figure 5.11, the best iterations (3 to 9) refer to $c_1 = 1.278$ to 3.61 and $c_2 = 2.722$ to 0.39 respectively: a broad spectrum of change. During the one simulation mentioned above where results differing from these were established found that $c_1 = 0.5$ to 3.61 yields the same result with regards to best cost. Therefore, it was determined that c_1 and $c_2 = 2$ would be utilised.

As per Figure 5.12 changing the inertia weighting (w) of the particle has an effect on the time to convergence. However, it is apparent that with a lower inertia weighting the best cost for each iteration starts much lower to the final convergence number. This means that there is a chance that a false minimum could be located as the entire search space may not be explored and therefore a local best is found rather than a global best. The best option for convergence and speed is to find the compromise whereby the entire search space is explored but convergence occurs within the number of iterations required.

After initial testing of inertia weight, it is apparent that a compromise is to be sought. 0.1, 0.3 and 0.5 all deliver their own desirable results so it was determined that a final test should be carried out whereby the inertia weighting can linearly change from 0.1 to 0.5 across the simulation iterations and also vice versa 0.5 to 0.1.

It was established that a 0.5 to 0.1 ($w = \text{linspace}(0.5, 0.1, \text{MaxIt})$) linear change was preferred as to allow high diversity during the early stages of optimisation whilst limiting the search space during the final iterations of the optimisation ensuring the global maximum, Figure 5.12 illustrates that by using a 0.1 to 0.5 linear change meant the best cost converged at a higher rate than that of a 0.5 to 0.1 linear change.

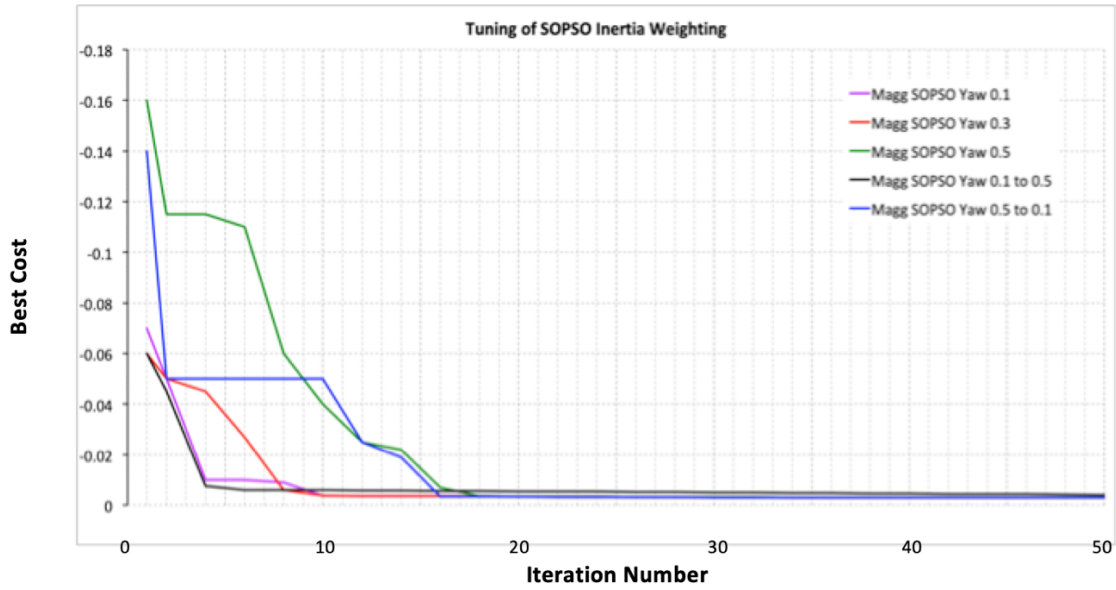


Figure 5.12 Inertia weighting variation convergence during SOPSO simulation for yaw rate during the Maggots/Becketts complex of corners.

The comparison of these curves with regards to fixed state inertial weightings shows that high weightings (0.5) generate greater diverse particles compared to low weightings (0.1). Therefore, a combined inertia weighting is a suitable compromise to utilise.

Once the particle behaviour had been tuned, six optimisation simulations were carried out for several corners around the Silverstone GP Circuit (Abbey, The Loop/Arena section, Luffield, The Maggots and Becketts complex and Vale, followed by a full lap simulation (Figure 5.13.) to measure best cost and accuracy of variables whereby the variables from norm were set with a large range exploration criterion to generate the search space.

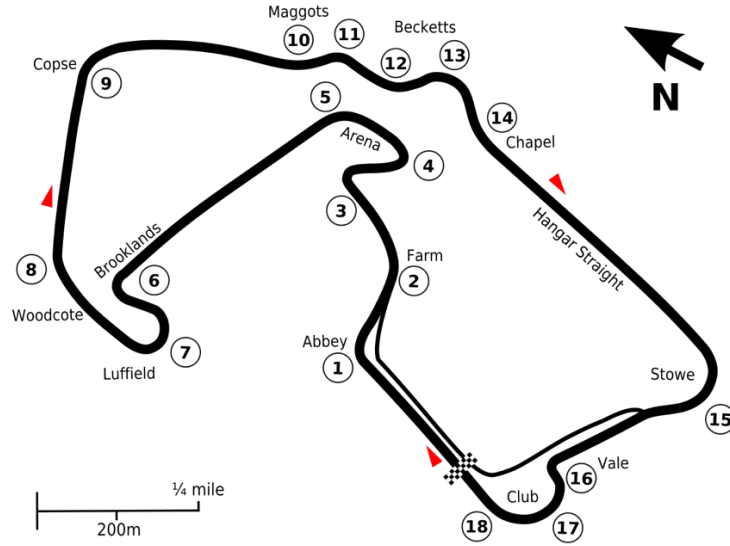


Figure 5.13 Silverstone Grand Prix circuit using the Grand Prix paddock and pit lane.

5.5.2 Single-Objective PSO

To evaluate the performance of single objective particle swarm optimisation, the algorithm is running by considering each individual vehicle dynamic output (longitudinal velocity, lateral acceleration and yaw rate) as the cost function. By running the algorithm over each individual vehicle dynamic output, the cost function (5.12) is evaluated for each vehicle dynamic output and is defined in (5.0). The results are recorded alongside the error for all vehicle dynamic outputs mentioned above against the simulated race car outputs within the time domain, as the vehicle dynamic output errors will place the car on different paths. The results are evaluated for a manoeuvre for specific corners of the Silverstone track and the entire lap. The input parameter variables remained the same as used in the tuning process (Table 5.2)

$$J(\xi_c) = -\|\xi_c - \xi_{d_c}\|_p \tag{5.12}$$

Due to the coupling of the four degrees of freedom vehicle body dynamic, the issue with SOPSO in these scenarios is that optimising for longitudinal behaviour can have a negative effect on lateral and yaw outcomes. As can be seen from Tables 5.4 to 5.9 the best cost and mean square error is

changing for each channel depending on the corner and output used for the optimisation. The results for the full lap of Silverstone are listed in Table 5.9 to 4d.p.

Table 5.4 SOPSO results of Abbey corner for longitudinal velocity, lateral acceleration and yaw rate. Error = error of measured and simulated PSO output.

Abbey			
	SOPSO Vx	SOPSO Ay	SOPSO Yaw
Best Cost	-0.0521	-1.9596	-0.0692
Error Vx	3.30E-04	4.2E-04	0.0003
Error Ay	0.1853	0.1711	0.1906
Error Yaw	8.15E-05	8.37E-05	0.0001

Table 5.5 SOPSO results of The Loop corner for longitudinal velocity, lateral acceleration and yaw rate. Error = error of measured and simulated PSO output.

The Loop			
	SOPSO Vx	SOPSO Ay	SOPSO Yaw
Best cost	-0.0226	-1.4749	-0.0890
Error Vx	4.38E-05	4.57E-05	6.01E-04
Error Ay	0.0806	0.0722	0.0939
Error Yaw	0.122	0.0001	0.0001

Table 5.6 SOPSO results of Luffield corner for longitudinal velocity, lateral acceleration and yaw rate. Error = error of measured and simulated PSO output.

Luffield			
	SOPSO Vx	SOPSO Ay	SOPSO Yaw
Best cost	-0.0688	-3.5003	-0.0230
Error Vx	5.85E-05	5.85E-05	6.02E-05
Error Ay	0.1056	0.1056	0.1060
Error Yaw	9.38E-06	9.38E-06	1.18E-05

Table 5.7 SOPSO results of Maggots/Becketts complex of corners for longitudinal velocity, lateral acceleration and yaw rate. Error = mean square error of measured and simulated PSO output.

Maggots/Becketts			
	SOPSO Vx	SOPSO Ay	SOPSO Yaw
Best cost	-0.0077	-3.5307	-0.0037
Error Vx	1.77E-06	1.12E-05	2.43E-06
Error Ay	0.0811	0.0857	0.0802
Error Yaw	1.18E-06	7.28E-06	6.23E-07

Table 5.8 SOPSO results of Vale corner for longitudinal velocity, lateral acceleration and yaw rate. Error = error of measured and simulated PSO output.

Vale			
	SOPSO Vx	SOPSO Ay	SOPSO Yaw
Best cost	-0.0224	-1.9265	-0.1000
Error Vx	1.94E-04	2.43E-04	2.43E-04
Error Ay	0.2605	0.2597	0.2597
Error Yaw	2.67E-04	2.80E-04	2.80E-04

Table 5.9 SOPSO results of a lap of the Silverstone GP circuit for longitudinal velocity, lateral acceleration and yaw rate. Error = error of measured and simulated PSO output.

Silverstone GP			
	SOPSO Vx	SOPSO Ay	SOPSO Yaw
Best cost	-8.95E-08	-1.27E-05	-2.46E-07
Error Vx	1.49E-11	7.38E-13	4.69E-11
Error Ay	1.94E-08	1.10E-09	1.42E-08
Error Yaw	8.68E-12	6.18E-13	1.07E-11

The full GP circuit results yielded a best cost and error range of 1.42E-08 to 6.18E-13. The objective of this study is to compare SOPSO and MOPSO algorithms in terms of convergence time and parameter estimation accuracy and as such an error of accuracy of resultant input parameters vs real data was also analysed. The results shown in Appendix 2 to 4 has shown a significant change from one corner to another corner for the parameter results, that is a physical impossibility

as the parameters would be the same in a physical chassis and tyre. Therefore, the results for parameter estimation are optimised for each corner individually to ascertain the best results for each corner, irrelevant of the fact they would be a fixed number on the physical vehicle. Basing the analysis on the error results for each vehicle dynamic output it can also be concluded that not all parameters are sensitive to the outcomes as they can change for each corner but produce very accurate results when compared to the measured data. It can be concluded that parameters that vary largely from corner to corner but have no effect on the dynamic output are less sensitive to the overall output.

The main discrepancy within the SOPSO results is with the best cost for lateral acceleration due to the variation between the initial condition of simulated data to PSO. When lateral acceleration is not the focus of the PSO the error within the lateral acceleration result is also higher than any other vehicle dynamic output.

A precise simulation requires the consideration of the initial conditions of the car just before each corner that is to be optimised around the lap. The vehicle dynamic model requires lateral velocity (equation 3.1) and is a requirement of the initial conditions for time = 0, this is then differentiated to calculate acceleration. However, several initial conditions for independent corners are unknown and therefore the simulation converges after several time steps (Figure 5.15). This is eradicated in the full GP simulation, as the initial conditions from measured data are known as there is data available prior to the start of the full lap simulation. The measured data was taken from a qualifying lap of Silverstone, this lap is preceded by several laps (out of pit lap and one warm up lap). Therefore, initial conditions for all velocities and accelerations are known or can be calculated at time = 0, based upon the previous lap's final conditions. This allows a much more accurate calculation from the vehicle dynamics model at time = 0, for a full lap (Figure 5.18). The start finish line of the full lap is also situated on a straight away ensuring yaw rate and lateral acceleration are equal to zero. This leaves a discrepancy between simulated data and the vehicle dynamic data that is subject to PSO optimisation at the start of each individual corner simulation as the initial condition for lateral velocity has to be approximated so the model can calculate lateral acceleration.

Figures 5.14 – 5.19 show a range of results for various corners and as can be seen for lateral acceleration (Figure 5.16) and yaw rate (Figure 5.16) there is a discrepancy between simulated and PSO results at the start of each individual corner simulation due to velocity not being known as an initial condition as discussed above. This is clearly eradicated in Figures 5.17 to 5.19. Interestingly the SOPSO works extremely well to optimise one single vehicle dynamic output, lateral acceleration for example in Figure 5.15, but as the particles will only find best solutions to the parameters that directly influence the vehicle dynamic output to be optimised the other outputs suffer. This can be seen in figures 5.17 to 5.19 where longitudinal velocity is the optimisation, Figure 5.17 shows an almost identical solution to that of the simulated data, however lateral acceleration and yaw rate have not been optimised. This analysis shows that multi-objective PSO is what is required so all vehicle dynamic outputs can be optimised to match the simulated data and therefore the particles are searching for the best solution by locating the best parameter that matches those used within the 4DOF simulation testing.

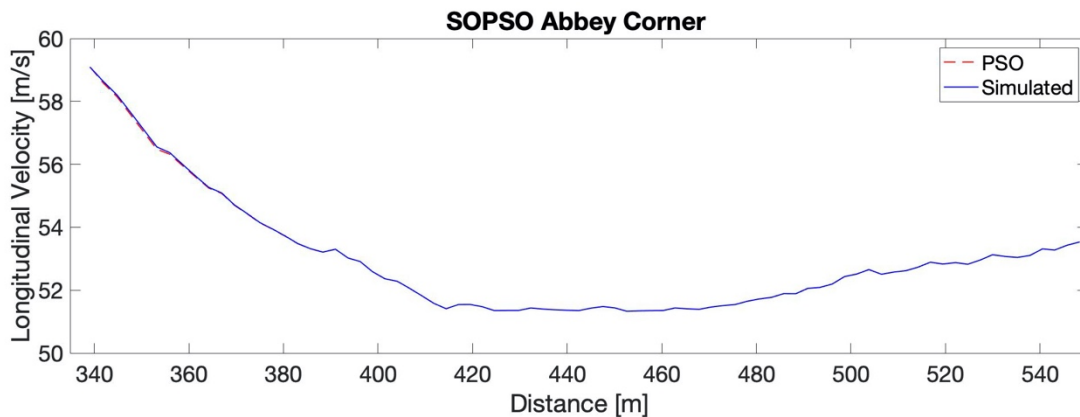


Figure 5.14 Simulated output versus PSO model output after optimisation for longitudinal velocity during Abbey corner.

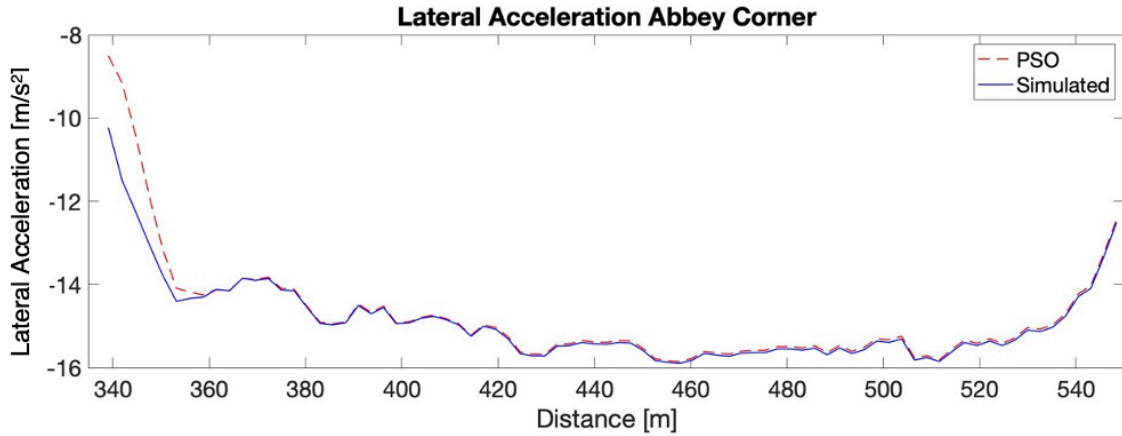


Figure 5.15 Simulated output versus PSO output for lateral acceleration during Abbey corner.

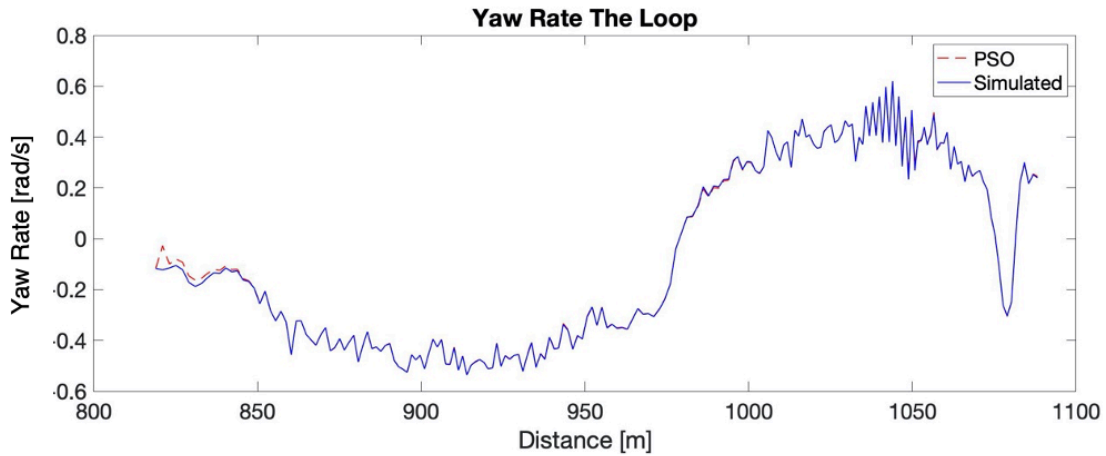


Figure 5.16 Simulated output versus PSO output for yaw rate during The Loop corner.

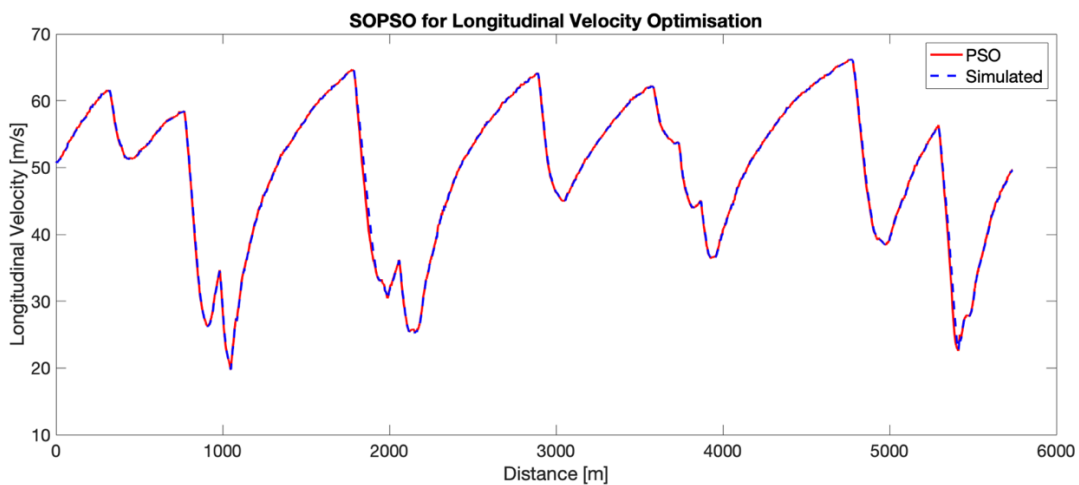


Figure 5.17 Simulated output versus PSO output for longitudinal velocity during a full lap of the Silverstone GP circuit. Individual corner names denote the additional simulations performed during tuning of SOPSO.

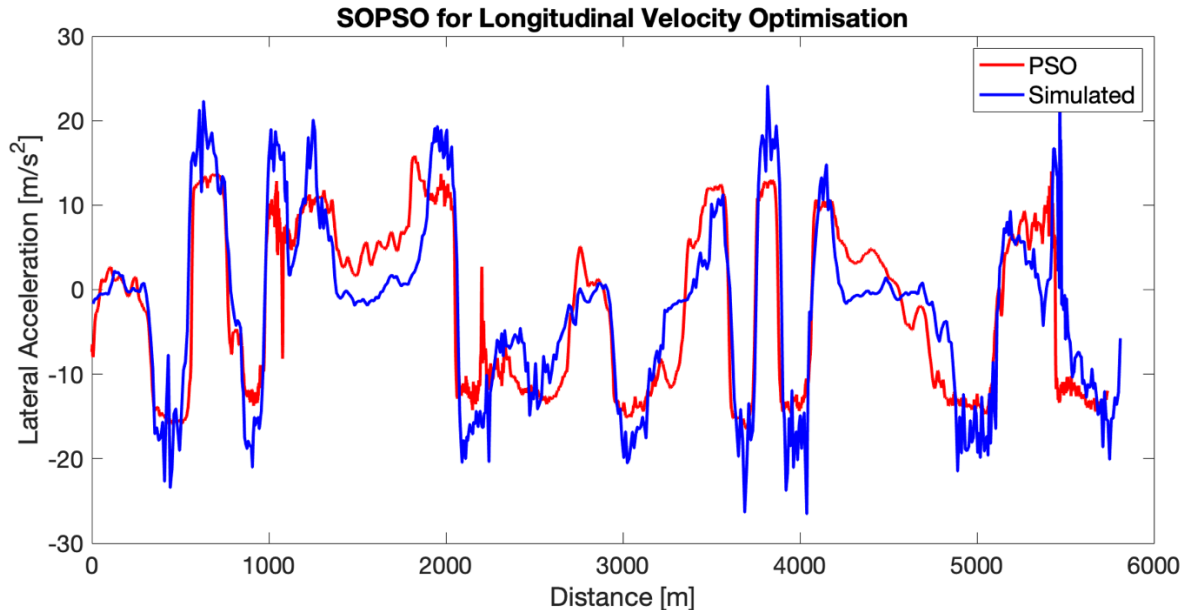


Figure 5.18 Simulated output versus SOPSO output for lateral acceleration during a full lap of the Silverstone GP circuit.

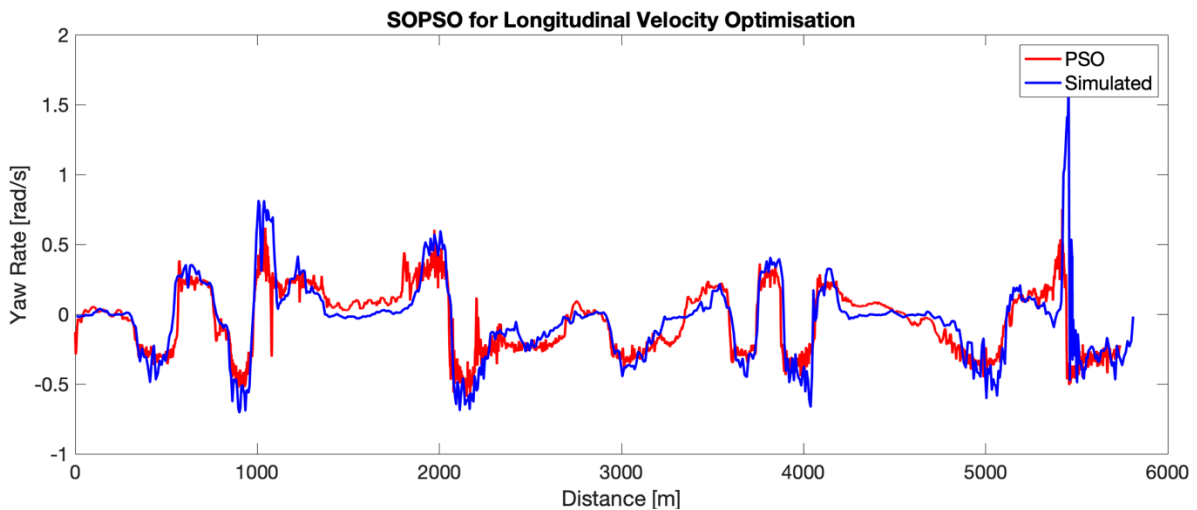


Figure 5.19 Simulated output versus SOPSO output for yaw rate during a full lap of the Silverstone GP circuit.

Once these results have been analysed, one final tuning of the SOPSO was carried out to compare SOPSO for each change of p-norm as described after (5.0) where p-norm = 1 is the integral absolute error, p-norm = 2 is the root mean square error and p-norm = infinity is $\max|x|$. The work in [84] shows that p-norm infinity is generally the best fit for genetic algorithms in terms of cost function, however, SOPSO may not necessarily perform best with p-norm infinity. To evaluate the effect of different cost functions on the overall performance of the algorithm, the p-norm cost

function with p equal to infinity, 1 and 2 are all tested. The results are compared for best cost and output error purely based on the entire Silverstone GP lap to ensure a correct initial condition is used in the simulations. The simulation results are summarised in Table 5.10.

Table 5.10 Variation in results of best cost and output mean square error for longitudinal velocity, lateral acceleration and yaw rate for the Silverstone GP circuit. (for p-norm equal to inf, 1 and 2).

	V _x p-norm = inf	V _x p-norm = 1	V _x p-norm = 2	A _y p-norm = inf	A _y p-norm = 1	A _y p-norm = 2	Y _{aw} p-norm = inf	Y _{aw} p-norm = 1	Y _{aw} p-norm = 2
Best cost	-8.95E-08	-3.03E-05	-7.34E-07	-1.27E-05	-0.0005365	-3.73E-06	-2.46E-07	-3.15E-06	-1.71E-06
err V_x	1.49E-11	1.93E-11	2.64E-10	7.38E-13	2.42E-10	3.03E-14	4.69E-11	6.27E-10	1.00E-08
err A_y	1.94E-08	2.05E-08	9.12E-08	1.10E-09	2.53E-07	1.52E-11	1.42E-08	6.44E-07	8.13E-06
err Y_{aw}	8.68E-12	1.16E-11	6.28E-11	6.18E-13	1.48E-10	1.01E-14	1.07E-11	3.74E-10	5.14E-09

As can be seen from the table, for most simulations the minimum best cost is achieved using a p-norm infinity cost function. However, for Lateral Acceleration the results for p-norm equal to two has yielded an improved result. Looking at the data plot error for different norms shows that since the difference for error values is so small for various norms the infinite norm is chosen as the overall best cost function for SOPSO algorithm.

Finally, for comparison of the results with MOPSO algorithm the convergence time of SOPSO algorithm for each run is recorded. The results show that the average time for convergence of SOPSO is six minutes per corner per vehicle dynamic output and it is 49 minutes for a full lap simulation per vehicle dynamic output when using a 2.7 quad core i7 MacBook with 16GB of memory.

5.5.3 Multi-Objective PSO

To evaluate the performance of MOPSO algorithm, we follow the same methodology used for SOPSO algorithm in the previous section. Here, a similar set of parameters such as population

count, iteration number, particle acceleration factor, particle weighting, and number of variables (parameters) should be tuned. The MOPSO algorithm has been used for optimisation over the identical corners as the previous simulations and for a full lap of the Silverstone GP Circuit. The objective functions used for the optimisation problem at this stage is a collection of the single objective functions used for each output channel in SOPSO algorithm.

The initial and obvious advantage of running a MOPSO is that the vehicle dynamic output objectives can all be optimized in one simulation. Table 5.10 highlights the run-time for both SOPSO and MOPSO algorithms. As to be expected, the SOPSO completes the optimisation simulation on average 12 – 17% quicker than the MOPSO, however, when taking into consideration that only one output is being used for optimization at a time, the MOPSO can use all three outputs for optimisation, 254% quicker than that of the SOPSO algorithm.

More importantly, the performance of SOPSO and MOPSO algorithms are compared in terms of the mean square error of the vehicle outputs and the accuracy in estimating the vehicle parameters.

The first analysis that should be considered for critical scrutiny is the best cost and mean square error of the vehicle dynamic outputs. The numerical results achieved from MOPSO algorithm are summarised in Table 5.12. A full comparison of mean square errors provided in Appendix 4 confirms that the results are not as accurate as SOPSO. The main differences lie with the best cost for lateral acceleration whereby MOPSO gives a much larger value. The simulation results from SOPSO for lateral acceleration at each individual corner shows the best cost range between -1.4749 (The Loop) to -3.5307 (Maggots/Becketts) whereby the simulation results for MOPSO are ranged between -3.78 and -17.30 for each individual corner, resulting in the SOPSO generating much better dynamic output responses close to the simulated data plots. Although the MOPSO is searching for values to improve three vehicle dynamic outputs simultaneously it doesn't produce results as good as each individual dynamic output from SOPSO and therefore further tuning of the MOPSO is required.

Table 5.11 Multi-objective and single-objective algorithm run times.

Comparison of MOPSO and SOPSO run time [minutes, decimal clock]					
Simulation	MOPSO	SOPSO Vx	SOPSO Ay	SOPSO Yaw	SOPSO Total
Abbey	4.2	4.1	4.4	4.1	12.6
The Loop	8.3	7.5	8.1	8.6	24.2
Luffield	5.9	7.1	7.5	5.2	19.8
Maggots/Becketts	9.2	9.9	10.9	8.3	29.1
Vale	5.1	3.9	4.5	4.5	12.8
GP	49.4	35.7	36.9	37.4	110.0
Total	82.1	68.2	72.3	68.1	208.5

Percentage run time comparison MOPSO vs SOPSO					
Simulation	MOPSO	SOPSO Vx	SOPSO Ay	SOPSO Yaw	SOPSO Total
Abbey	Baseline	97.6%	104.8%	97.6%	300.0%
The Loop	Baseline	90.4%	97.6%	103.6%	291.6%
Luffield	Baseline	120.3%	127.1%	88.1%	335.6%
Maggots/Becketts	Baseline	107.6%	118.5%	90.2%	316.3%
Vale	Baseline	76.5%	88.2%	88.2%	251.0%
GP	Baseline	72.3%	74.7%	75.7%	222.7%
Total	Baseline	83.1%	88.1%	82.9%	254.0%

It should be noted that, the majority of the discrepancy in the best cost results is due to the initial conditions being unknown for corners. Although the mean square errors for both MOPSO and SOPSO are very similar, SOPSO would find a greater accuracy in results of parameter estimation error and best cost, with parameter estimation error to 1×10^{13} and best cost to 1×10^8 , while MOPSO would only give a result to 1×10^7 accuracy for parameter estimation error and 1×10^2 . The greatest anomaly between SOPSO and MOPSO is that MOPSO has a much larger cost for lateral acceleration for the full lap simulation. With the initial conditions known for this simulation, a deeper analysis into the parameter estimation accuracy would be possible.

As per the SOPSO algorithm, the first tuning option for MOPSO is to test the fitness values for different norms (inf, 1, and 2) are tested listed in Table 5.13. As can be seen in Table 5.13 these can greatly influence the final results. To eradicate any anomalies with initial conditions the fitness function was altered for the full lap simulation only.

Table 5.12 Best cost and mean square error for multi-objective algorithm.

MOPSO Best Cost and Vehicle Dynamic Mean Square Error						
	Abbey	The Loop	Luffield	Magg/Beck	Vale	GP
Cost Vx	-0.06	-0.03	-0.07	-0.04	-0.03	-0.03
Cost Ay	-3.78	-14.97	-16.30	-17.30	-8.89	-23.02
Cost Yaw	-2.06	-1.60	-3.57	-3.55	-2.23	-1.30
Error Vx	0.00035689	0.00003896	0.000053402	2.2077E-06	0.00020266	4.3323E-06
Error Ay	0.1793	0.0699	0.1069	0.0801	0.2615	0.004
Error Yaw	0.000081221	0.000062605	9.7292E-06	4.7261E-07	0.00026775	2.4424E-06

By changing the p-norm the best cost has been improved significantly for the lateral acceleration, but it is detrimental to the longitudinal velocity and Yaw Rate in the case of p-norm equal to 1. In the case of p-norm equal 2, lateral acceleration yields the lowest best cost with only a slight change to the longitudinal velocity (+ 0.2) but again a larger change to the Yaw Rate as can be inferred from Table 5.13. However, the values for the output errors are largely unchanged.

Table 5.13 Variation in MOPSO results of best cost and output mean square error for longitudinal velocity, lateral acceleration and yaw rate for the Silverstone GP circuit. (p-norm = inf, 1 and 2).

Variation of p-norm for MOPSO Silverstone GP			
	p-norm = inf	p-norm = 1	p-norm = 2
Cost Vx	-0.03	-4.58	-0.23
Cost Ay	-23.02	-2.48	-0.14
Cost Yaw	-1.30	-91.74	-5.12
Error Vx	4.33E-06	9.79E-06	1.16E-05
Error Ay	0.004	0.005	0.004
Error Yaw	2.44E-06	3.48E-06	3.54E-06

Although different fitness functions have an effect on the error value for three vehicle dynamic outputs, it does not produce any conclusive evidence on which fitness function is preferred for MOPSO. Further analysis into the parameter estimation accuracy proves that several parameters are moving to the predefined range and getting stuck at that their minima or maxima. This has occurred on average on 5 of the 22 variables and in every case three parameters have the same values, i.e., tyre coefficients rBx1 and rHy1 and chassis stiffness kroll.

The particle acceleration and inertia weights are tuned by changing their values inside a loop within each iteration of the SOPSO. This loop is utilised to change the acceleration and weight parameters in a linear step, allowing each iteration to test all possibilities of particle acceleration and inertia weights within the proposed parameters. The best costs yielding the best c_1 to be between 1.2 and 1.8. whereby all best cost results were identical. Since the sum of c_1 and c_2 values should be equal to four the values found for c_2 would be between 2.2 to 2.8. Therefore, it was decided $c_1 = 1.5$ and $c_2 = 2.5$ as the final tuning and the inertia weight is changing linearly from 0.5 to 0.1. Setting the inertia weight between 0.1 and 1 would produce the risk that the algorithm fails to explore the whole search space or moves quickly around the search space and misses the potential areas of maxima.

Having the newly tuned parameters for the MOPSO algorithm, the GP circuit simulation is tested once again. The best cost generating a much-improved result of -0.03, -0.02 and -1.2 for longitudinal velocity, lateral acceleration and Yaw Rate respectively. However, two of the twenty-two parameters, in this instance chassis stiffness and damping (kroll and croll), reached their minimum or maximum values during each iteration.

The final conclusion from this result is that the algorithm is failing to generate a diverse set of population to explore the search space properly. Therefore, a more effective mutation scheme compared to the Binary Tournament Selection scheme used currently would be required.

It is important to note that one way to improve the diversity of the population is to extend the iteration number or the number of particles in each iteration. In this way, the MOPSO algorithm will perform for a longer time, to the length of three times greater than SOPSO. However, the purpose of the analysis is to generate a MOPSO algorithm, showing the same performance with an identical population and iteration size at a fraction of time. Therefore, tuning and development of such an algorithm is at the forefront of the research.

Using binary tournament selection, the initial parameter estimation is carried out by a fixed mutation rate. Through mutation the algorithm is searching for a better solution based on a single random number generation. If the new solution dominates the previous one it will be substituted

into the population. The mutation probability, pm , is reducing linearly by the iteration number as in (5.13).

$$pm = \left(1 - \frac{it - 1}{MaxIt - 1}\right)^{\frac{1}{mu}}$$
(5.13)

where

pm is the mutation probability

it is the current iteration

$MaxIt$ is the maximum number of iterations

mu is the mutation rate

In the first case, mu is assumed to be constant at 0.3. However, since the algorithm cannot explore the entire search space properly it fails to find a global best. Therefore, as an improvement of the algorithm the mutation rate (mu), is randomly selected as a number between 0 and 1.

```

% Apply Mutation
murand = randperm(numel(mu));
murandout = mu(murand(1));

pm=(1-(it-1)/(MaxIt-1))^(1/murandout);

%pm=(1-(it-1)/(MaxIt-1))^(1/mu);

if rand<pm
NewSol.Position=Mutate(popm(k).Position,pm,VarMin,VarMax);
```

Figure 5.20 Partial mutation code, detailing change of mu from a fixed number to a random number per iteration.

To address this problem, a new mutation algorithm is illustrated by pm in Figure 5.20. In this scheme, by randomly selecting a mutation rate ($murandout$) rather than a constant mu , a new random number is generated for the selected particles in the population, allowing for a much broader search space per generation. As an example, for one particle, the values for pm using a constant mu and a random value for mu are compared in Table 5.14 for 10 iteration step sample.

Table 5.14 Difference of linearly decreasing pm and random pm during a 50-iteration optimisation simulation.

10 iteration gap sample mu mutation generation						
Iteration	1	10	20	30	40	50
Linear decreasing pm	1	0.83	0.65	0.47	0.28	0.1
Random pm	0.28	0.12	0.81	0.93	0.54	0.45

By applying the mutation algorithm proposed above the MOPSO algorithm has been executed for the whole lap in Silverstone GP. The new results for the best cost and parameter estimation are listed in Table 5.15, showing a much more desirable performance than the previous MOPSO algorithm. As can be seen from this table, the best cost value for the longitudinal velocity is reduced from -0.03 to -0.000845, the value for the lateral acceleration is reduced from -23.02 to -0.000964, and the value for the Yaw Rate is reduced from -1.3 to -0.03. Although these values are still slightly higher than that of their SOPSO counterparts, i.e., -8.95E-08, -1.27E-05, and -2.46E-07 respectively, the results show a much smaller error in terms of the mean square error of the outputs and the parameter estimation error, reduced from 20.3 for the SOPSO algorithm to 2.181 for the MOPSO algorithm.

According to the sensitivity analysis and results achieved from the MOPSO algorithm, it is apparent that certain parameters in the vehicle dynamic are less sensitive to the cost function, however, the MOPSO algorithm because of using different objective functions is capable of producing a result closer to the true value. By removing the least sensitive parameters (choosing 10 most sensitive parameters compared to 22 parameters), and maintaining the same particle count and iteration number, the best cost can be further reduced to -5.47E-14, -5.69E-16 and -5.22E-11 for longitudinal velocity, lateral acceleration and yaw rate respectively. Moreover, the square error for the output is reduced to 8.33E-28, 4.65E-28, and 6.59E-32 respectively.

Table 5.15 Comparison of best cost, mean square error and parameter estimation error (including error based on Equation 5.13).

Comparison of MOPSO Initial Simulation versus Tuned (Silverstone GP)							
				<u>Initial MOPSO</u>		<u>Tuned MOPSO</u>	
Cost Vx				-0.03	-8.45E-04		
Cost Ay				-23.02	-9.64E-04		
Cost Yaw				-1.30	-0.03		
MS err Vx				4.33E-06	1.86E-09		
MS err Ay				0.004	1.84E-06		
MS err Yaw				2.44E-06	1.15E-09		
<u>Variable Parameters Validated</u>						<u>Initial</u>	<u>Tuned</u>
				<u>Range Min</u>	<u>Range Max</u>	<u>Range</u>	<u>Range</u>
				<u>Error</u>	<u>Error</u>	<u>Error</u>	<u>Error</u>
rBx1	13.2	5	20	10.00	13.41	0.242	0.016
rBx2	-13.9	-20	-5	-15.00	-14.00	0.079	0.007
rCx1	1.14	0	2	0.00	1.47	1.000	0.291
rEx1	0.317	0	1	0.32	0.34	0.024	0.072
rEx2	0.109	0	1	0.23	0.10	1.069	0.083
rHx1	-0.00856	-0.1	0	-0.02	-0.01	1.336	0.168
rBy1	14.6	5	20	10.00	14.50	0.315	0.007
rBy2	10.9	5	20	15.00	10.84	0.376	0.006
rBy3	0.0156	0	0.2	0.00	0.02	0.908	0.114
rCy1	1.14	0	3	0.00	1.20	1.000	0.053
rEy1	0.389	0	2	0.00	0.40	1.000	0.028
rEy2	0.358	0	2	0.00	0.31	1.000	0.128
rHy1	-0.0635	0	1	-0.20	-0.07	2.150	0.102
rHy2	-0.0492	0	1	-0.20	-0.05	3.065	0.016
rVy1	0.56	0	2	1.84	0.60	2.291	0.071
rVy2	18.5	10	30	19.05	18.63	0.030	0.007
rVy3	0.0188	0	0.2	0.00	0.01	1.000	0.468
rVy4	0.0203	0	0.2	0.02	0.03	0.084	0.467
rVy5	1.9	0	5	0.67	2.00	0.645	0.053
rVy6	19.2	10	30	15.00	19.00	0.219	0.010
kroll	100000	80000	200000	85000.00	99900.00	0.150	0.001
croll	19000	8000	30000	25269.44	19216.65	0.330	0.011
						<u>Total Error</u>	18.314 2.181

Table 5.15 includes a range error as per (5.14) for all parameters. The variance in the error between the validated parameter and the output from the PSO can be quantified with this equation. The tuned range error column shows how tuning the MOPSO mutation algorithm has a beneficial effect

on the parameter estimation result. The total error is the Sum of all errors giving an indication to how the overall parameters have been improved.

$$\sum \left| \frac{x - \hat{x}}{x} \right| \tag{5.14}$$

5.6 SOPSO versus MOPSO Comparison

Throughout the testing of both SOPSO and MOPSO it became apparent that both optimisation techniques yield exceptional results, and both have a place in the optimisation algorithm arena. It is essential that both optimisation algorithms are tuned appropriately for the presented problem, and in some cases the algorithms behaviour can be identical with regards to the inertia and acceleration coefficients.

A full comparison of the results can be seen in Appendices 2 through 6. The main difference between SOPSO and MOPSO was the value achieved for the best cost. When scrutinised prior to the mutation change, the MOPSO performed worse with regards to best cost value but generated identical results for the mean square output error (Appendix 4) and in most cases the accuracy of the parameter estimation was much closer to the actual values for each individual parameter and as a sum of the total error (Table 5.16 and Appendix 4). Table 5.15 show the sum of each parameter estimation error (equation 5.13) for all parameters included in the optimisation prior to the mutation change within the MOPSO algorithm.

Table 5.16 Comparison of multi-objective and single-objective algorithm simulation parameter estimation. Sum of total errors.

	Sum of Total Error	
	MOPSO	SOPSO Average
Abbey	30.01050604	25.01061203
The Loop	22.80505002	25.73865931
Luffield	24.4423585	26.47802094
Maggots/Becketts	29.80540662	22.99515024
Vale	22.03292139	24.07985867
GP	18.31395458	20.32646805

Having the new mutation scheme, it can be seen that the best cost has been reduced to a value that can be positively compared to SOPSO. However, the sum of square error, parameter estimation error, and sum of total parameter estimation error has been improved significantly compared to SOPSO. Taking into consideration the computation time of MOPSO (44 minutes for the Silverstone GP lap) compared to the average computation time of 36 minutes for SOPSO, the main advantage of MOPSO algorithm will become clear. It is worth noting that, the MOPSO algorithm is dealing with all three objective functions in 40% of the time taken to run three SOPSO algorithms for the same objective functions. Therefore, for this vehicle dynamic optimisation problem, SOPSO would not be the preferred method due to the unsuitability of tuning the parameters for one equation at a time. The coupling within the vehicle dynamic equations insists that all objectives are tuned together. As can be seen in Figures 5.14 to 5.19 and Figures 5.21 to 5.26, both optimisation algorithms produce satisfying results that can be utilised within the industry as a parameter estimation technique, however SOPSO is only suitable for single optimisation problems. In this study where outputs and algorithms are coupled, SOPSO does not produce an overall satisfactory result. The MOPSO results are so close it is difficult to see the variation within the vehicle dynamic outputs across a full lap (Figures 5.21, 5.23 and 5.25). Therefore, the error between the simulated data and PSO data is presented in Figures 5.22, 5.24 and 5.26. The achieved numerical results although differ, it is evident that such a minute numerical result difference does not affect the dynamic output of the vehicle.

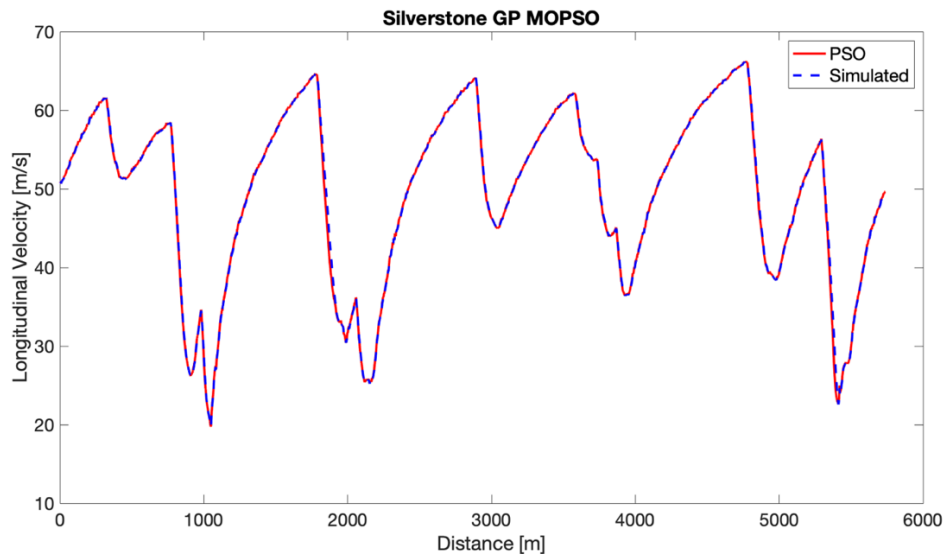


Figure 5.21 Simulated output versus MOPSO output for longitudinal velocity during a full lap of the Silverstone GP circuit.

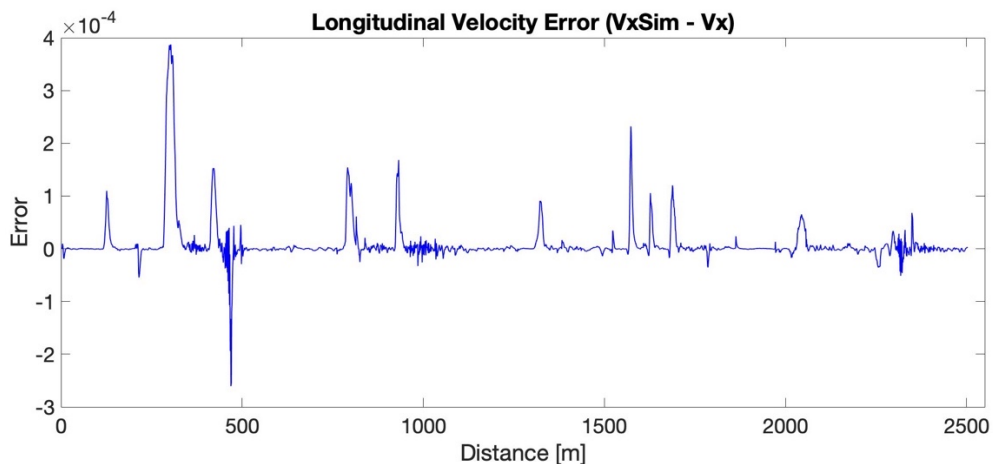


Figure 5.22 Simulated output results minus MOPSO output result ($V_{xSim} - V_x$) for longitudinal velocity during a full lap of the Silverstone GP circuit.

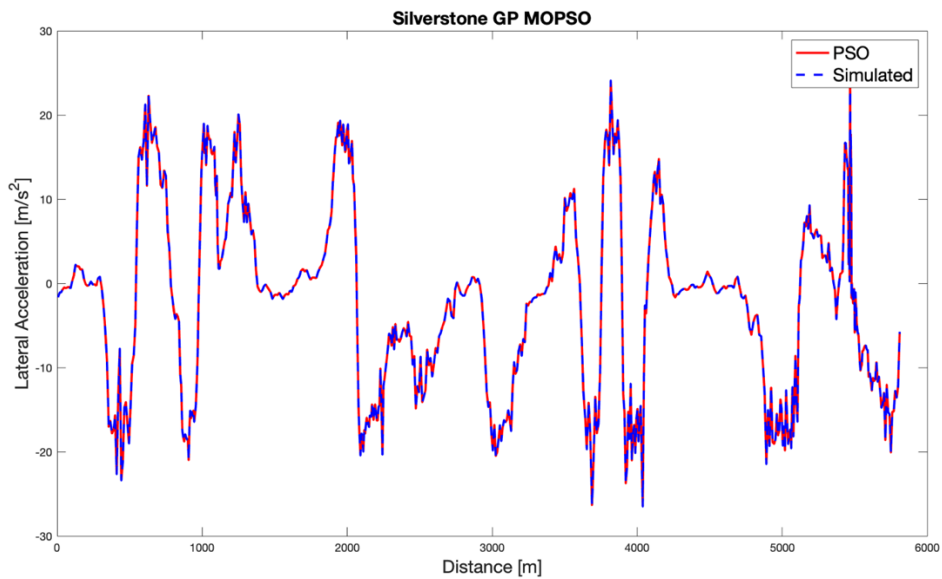


Figure 5.23 Simulated output versus MOPSO output for lateral acceleration during a full lap of the Silverstone GP circuit.

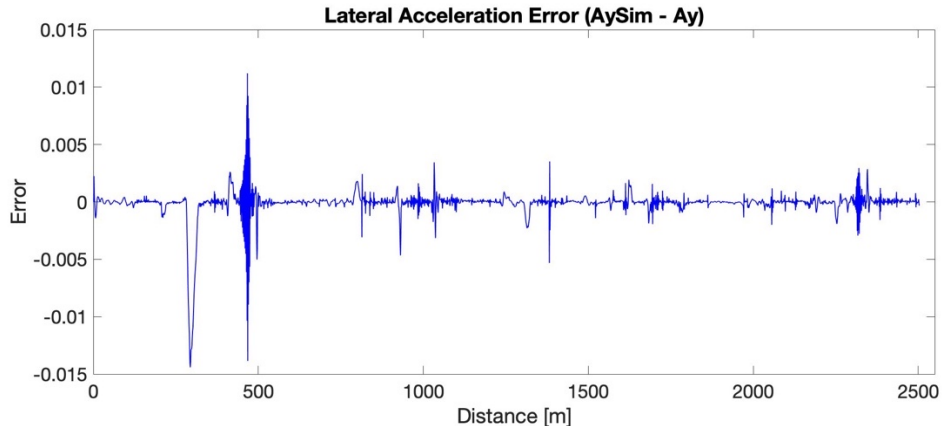


Figure 5.24 Simulated output results minus MOPSO output result ($A_{ySim} - A_y$) for lateral acceleration during a full lap of the Silverstone GP circuit.

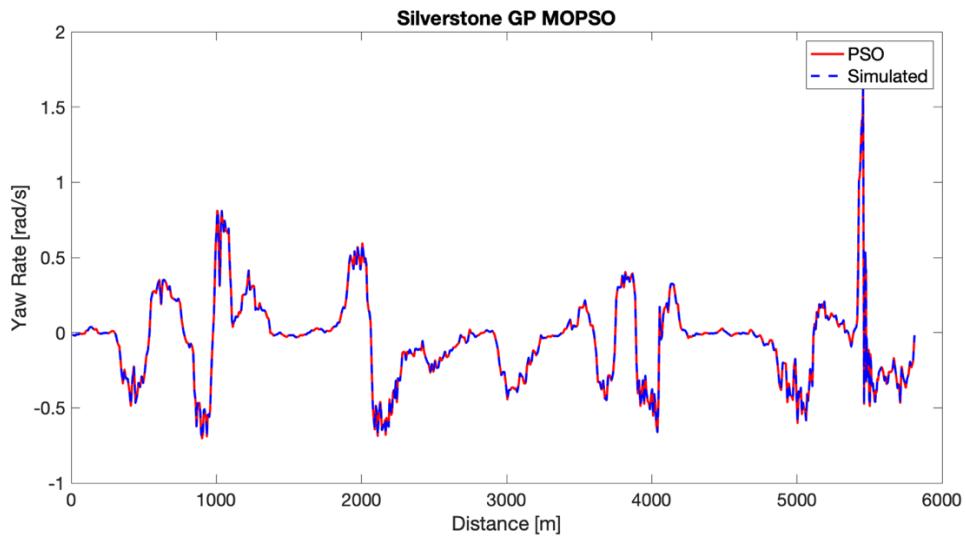


Figure 5.25 Simulated output versus MOPSO output for yaw rate during a full lap of the Silverstone GP circuit.

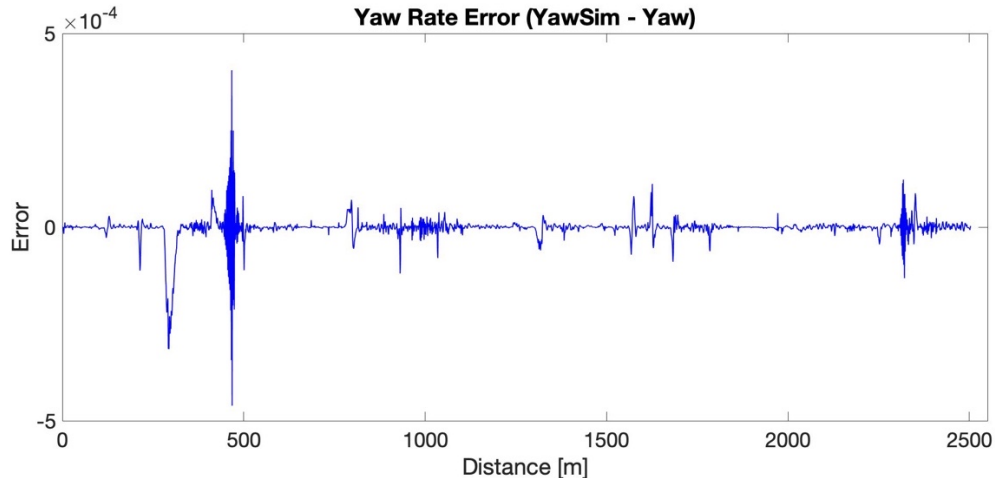


Figure 5.26 Simulated output results minus MOPSO output result ($YawSim - Yaw$) for yaw rate during a full lap of the Silverstone GP circuit.

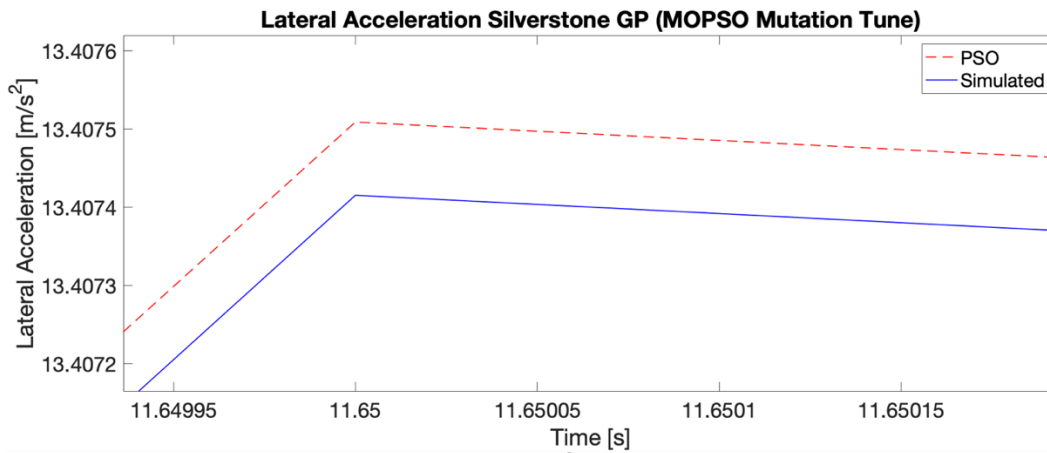


Figure 5.27 Example of max variation (0.0001) of simulated vs MOPSO.

Figure 5.27 presents a zoomed in area of the final output achieved for lateral acceleration at from running the MOPSO algorithm. The results are so close as shown in Figures 5.22, 5.24 and 5.26 with the error between the PSO plot and simulated plot within the order of 4 decimal places it can be concluded the MOSPO results are extremely accurate.

Table 5.17 Final tuned MOPSO, best cost and errors versus tuned SOPSO.

Comparison of best cost, errors and sum of errors (SOPSO vs MOPSO mutation tuning)				
Silverstone GP				
	SOPSO Vx	SOPSO Ay	SOPSO Yaw	MOPSO
				-8.45e-04
				-9.64e-04
Best cost	-8.94E-08	0.0000127	-2.45E-07	-0.03
Error Vx	1.49E-11	7.38E-13	4.69E-11	1.86E-09
Error Ay	1.93E-08	1.09E-09	1.42E-08	1.84E-06
Error Yaw	8.68E-12	6.18E-13	1.07E-11	1.15E-09
Sum of error Vx	14.456			
Sum of error Ay		21.828		
Sum of error Yaw			24.695	
Sum of total error				
	SOPSO combined			MOPSO
Sum of Total Error	20.326			2.181

5.7 Conclusion

In this chapter particle swarm optimisation algorithms and tuning parameters have been discussed and the importance of sensitivity analysis has been detailed. The results presented in this chapter show that with appropriate tuning of the parameters and critical analysis of the results, a very accurate particle swarm algorithm can be produced that satisfies the optimisation problem to an acceptable error for the parameter estimation and within a reasonable convergence time. It can also be concluded that for certain outcomes a SOPSO is relevant, however as the complexity of the problem increases, MOPSO algorithm with multi-objectivisation approach must be utilised. Aside the problem output count forcing the algorithm used, both SOPSO and MOPSO produced excellent results and taking into consideration the output counts the convergence has the same net time spent on locating best costs.

6. Trajectory Planning and Optimisation

6.1 Introduction

The ensuing chapter details the next stage of particle swarm optimisation (PSO) algorithm, testing and assessing the PSO for its appropriateness within the automotive industry. A typical engineering problem is posed whereby the PSO does not know the target solution, differentiating the process from that in the previous chapter, whereby best cost is the minimum value of either the shortest path or least curvature fitness functions. These trajectories are discussed with regards to a racing line around a circuit. The single objective PSO (SOPSO) and multi-objective PSO (MOPSO) will be evaluated through various problems included vehicle dynamic behaviour to locate best racing lines and best lap times.

6.2 Trajectory Planning and Race Driver Simulation

To realise the vehicles full potential with regards to the lap time, the trajectory path of the vehicle must be optimised. There are several approaches to trajectory planning based upon the limitation of vehicle's dynamic acceleration capabilities [92], whereby the vehicles maximum performance (longitudinal acceleration, deceleration and lateral deceleration) is already known and therefore the G-G diagram is used as a limitation to the vehicle performance and ultimately lap-time. Other limitations include that of the tyre limitations [1] whereby a lumped mass bicycle model is used, and forces calculated based on known maximum tyre performance. This work differs from these approaches as single and multi-objective particle swarm optimisation algorithms are used for trajectory planning. Firstly, utilising the SOPSO, the shortest path and minimum curvature trajectories are established and finally a MOPSO is utilised to include the parametric values of the vehicle by optimising the shortest path, minimum curvature and a combined fastest trajectory.

The literature in this area is usually split between the utilisation of a lumped mass bicycle model [1, 93] and four-wheel models of various degrees of freedom [92, 94, 95, 96]. The literature discusses various optimisation techniques from using a genetic algorithm [97] to simple linear minimisation algorithmic techniques [96] and the use of feedback controllers to match simulated

speeds. None of the literature compares various techniques aside Cardamone et al [97], who compare their GA approach to that of the Simplex bot [98]. The results show where one approach may create a faster lap time to another, but none compared to measured data, meaning evaluation of the lap time is inconclusive. In [92], the controller is designed to follow the maximum longitudinal and lateral acceleration rates based on a G-G diagram (traction ellipse) and therefore, although the conclusion satisfactorily shows that the controller can follow peak acceleration conditions this does not necessarily equate to the best lap time or ideal trajectory profile as the measured data is not included.

The race driver model in [96], generates a least curvature and shortest distance optimisation problem. The model is then optimised to find a weighting between the two cost functions to approximate the best lap time. However, this approach negates the possibility that one of the two solutions could be beneficial per corner, and therefore calculates a preferential weighting between least curvature and minimum distance for the entire lap.

The track models utilised are also extremely important in the trajectory optimisation and planning and can vary in the literature from a 2-D model (X and Y co-ordinates) [95] to a 3-D model [96] and finally a complex 3-D model [1] containing X, Y and Z coordinates generating camber of the road surface and creating a three-dimensional curvilinear track map. In all instances, the boundaries of the track are known as is the centre line of the track. For this study, continuing with the measured race vehicle data, the Silverstone-GP circuit will be utilised.

6.3 Geometric Parameterisation

The constraints of the track map are limited by the inner and outer limits of the tarmacadam surface and curbs. This produces two opportunities for optimisation: the shortest distance and the least curvature. The shortest distance would follow the tightest curve around a corner whereby the least curvature optimisation algorithm for the radii of the corner mathematically is trying to establish a straight line and therefore would tend to zero.

The track must be broken down into sections that can include individual non-linear increments to include straight aways and left and right turns.

Firstly, the physical race vehicle was driven around the outer edge of the race circuit and the inner edge of the circuit so that the GPS and distance [m] coordinates could be plotted. The width of the track at each point was dissected so that a centre line could also be established (Figure 6.1).

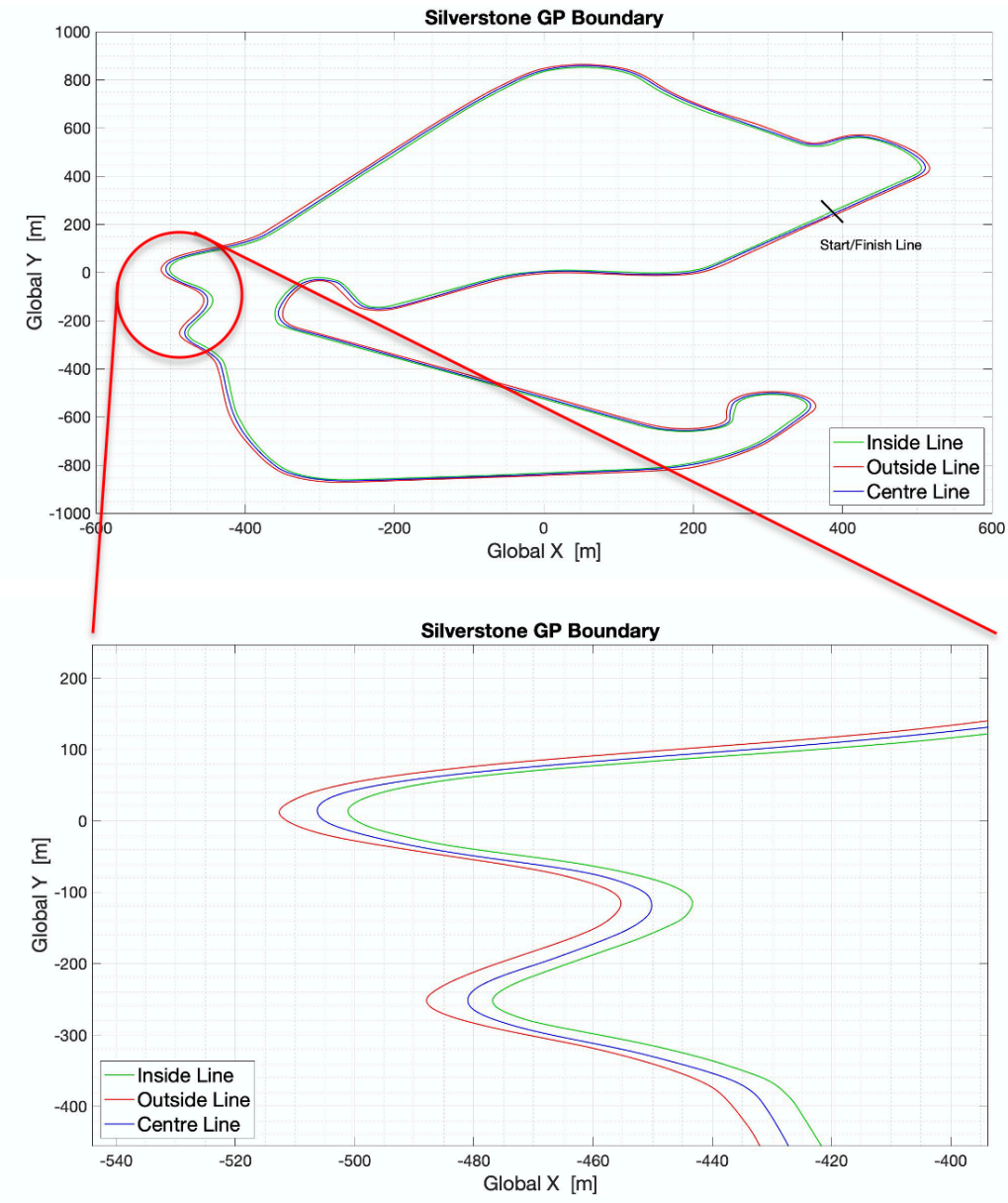


Figure 6.1 Inner, centre and outer parameterisation of Silverstone GP circuit.

6.4 The Shortest Path Problem

The fastest lap time is a compromise between shortest path and minimum curvature due to the vehicle dynamic limitations, tyre grip, and ultimately accelerations. The shortest path line is the path taken to appropriately navigate the circuit whilst maintaining the least amount of distance necessary for all corners and straights. Figure 6.2 depicts the shortest path trajectory for Brooklands and Luffield corners.

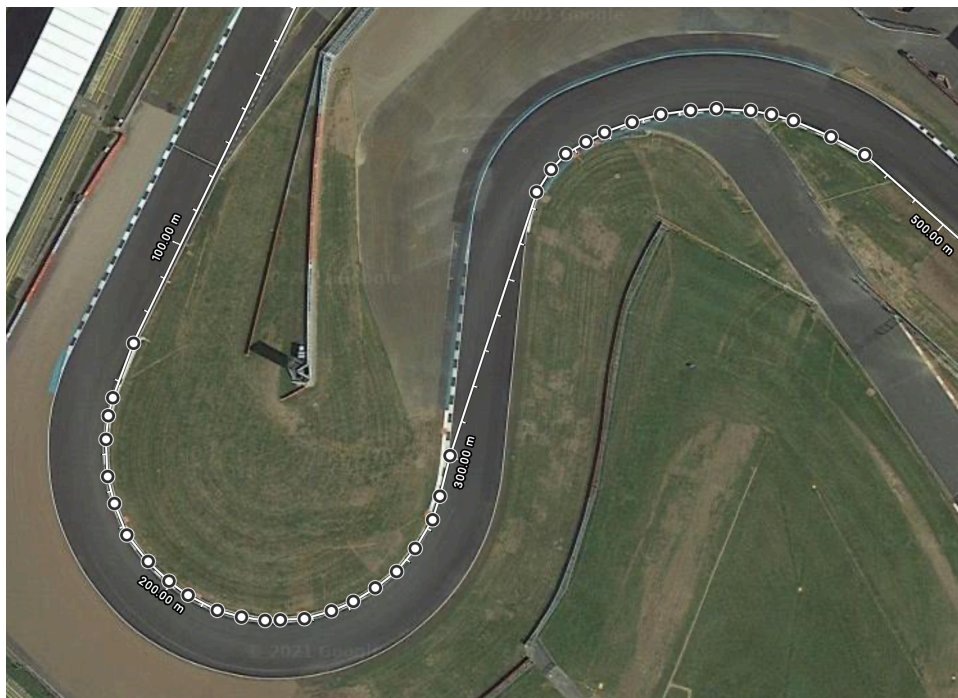


Figure 6.2 Shortest path trajectory (white line) of Brooklands and Luffield corners of the Silverstone GP circuit.

The position (α) at the beginning or ending of a segment will be determined by the width of the track and is directly related to the x and y coordinates of the inner and outer parameters of the circuit, α therefore will be a number between $[0,1]$.

$$\alpha(s) = (x(s), y(s)) \tag{6.0}$$

With the circuit segmented the total squared length of the trajectory is:

$$\begin{aligned}
 L^2 &= \sum_{i=1}^{n-1} \Delta P_{x,i}^T \cdot \Delta P_{x,i} + \Delta P_{y,i}^T \cdot \Delta P_{y,i} \\
 &= [\Delta P_{x,1} \ \Delta P_{x,2} \ \cdots \ \Delta P_{x,n}]^T \begin{bmatrix} \Delta P_{x,1} \\ \Delta P_{x,2} \\ \vdots \\ \Delta P_{x,n} \end{bmatrix} + [\Delta P_{y,1} \ \Delta P_{y,2} \ \cdots \ \Delta P_{y,n}]^T \begin{bmatrix} \Delta P_{y,1} \\ \Delta P_{y,2} \\ \vdots \\ \Delta P_{y,n} \end{bmatrix}
 \end{aligned} \tag{6.1}$$

where P refers to the length of the projections at each segment.

$$\begin{aligned}
 \Delta P_{x,i} &= [\Delta x_{i+1}, \Delta x_i] \begin{bmatrix} \alpha_{i+1} \\ \alpha_i \end{bmatrix} + \Delta x_{i,r} \\
 \Delta P_{y,i} &= [\Delta y_{i+1}, \Delta y_i] \begin{bmatrix} \alpha_{i+1} \\ \alpha_i \end{bmatrix} + \Delta y_{i,r}
 \end{aligned} \tag{6.2}$$

with clarity to the Matlab script the auxiliary variables are defined as

$$\begin{aligned}
 [\Delta x_{i+1}, \Delta x_i] &= tmpX_i^T \\
 [\Delta y_{i+1}, \Delta y_i] &= tmpY_i^T
 \end{aligned} \tag{6.3}$$

$$\begin{bmatrix} \alpha_{i+1} \\ \alpha_i \end{bmatrix} = \bar{\alpha}_i \tag{6.4}$$

$$\begin{aligned}
 \Delta x_{i,0} &= xr(i+1) - xr(i) \\
 \Delta y_{i,0} &= yr(i+1) - yr(i)
 \end{aligned} \tag{6.5}$$

where

xr and yr are the X and Y co-ordinates for the right-hand side of the track at the given segment.

Therefore, equation (6.1) can be written for the x co-ordinates in the more compact form

$$\sum_{i=1}^{n-1} \Delta P_{x,i}^T \cdot \Delta P_{x,i} = \sum_{i=1}^{n-1} \bar{\alpha}_i^T \text{tmp}X_i \text{tmp}X_i^T \bar{\alpha}_i + 2\bar{\alpha}_i^T \text{tmp}X_i \Delta x_{i,0} + \Delta x_{i,0}^2 \quad (6.6)$$

The first term of the objective function (6.6) can be written in the matrix form as

$$I_1 = [\bar{\alpha}_1^T \quad \bar{\alpha}_2^T \quad \dots \quad \bar{\alpha}_n^T] \begin{bmatrix} \text{tmp}X_1 \text{tmp}X_1^T & 0 & \dots & 0 \\ 0 & \text{tmp}X_2 \text{tmp}X_2^T & \dots & 0 \\ \vdots & \vdots & \ddots & \vdots \\ 0 & 0 & 0 & \text{tmp}X_n \text{tmp}X_n^T \end{bmatrix} \begin{bmatrix} \alpha_1 \\ \alpha_2 \\ \vdots \\ \alpha_n \end{bmatrix} \quad (6.7)$$

In the same way, the second term can be written as

$$I_2 = [\bar{\alpha}_1^T \quad \bar{\alpha}_2^T \quad \dots \quad \bar{\alpha}_n^T] \begin{bmatrix} \text{tmp}X_1 \cdot \text{Delta}R_{x1} \cdot 2 \\ \text{tmp}X_2 \cdot \text{Delta}R_{x2} \cdot 2 \\ \vdots \\ \text{tmp}X_n \cdot \text{Delta}R_{xn} \cdot 2 \end{bmatrix} \quad (6.8)$$

where $\text{Delta}R_x$ refers to the x coordinate for the right-hand side of the circuit determined via $x_{i+1} - x_i$. Similarly, matrices are created for $\text{Delta}R_y$ and all y coordinate components.

In (6.7) and (6.8), the parameter $\bar{\alpha}_i$ can be written as

$$\bar{\alpha}_i = E_i \cdot \bar{\alpha} \quad (6.9)$$

where

$$E_i = \begin{bmatrix} 0 & \dots & 0 & 1_i & 0 & 0 & \dots & 0 \\ 0 & \dots & 0 & 0 & 1_{i+1} & 0 & \dots & 0 \end{bmatrix} \quad (6.10)$$

$$\bar{\alpha} = \begin{bmatrix} \alpha_i \\ \vdots \\ \alpha_n \end{bmatrix} \quad (6.11)$$

$$\bar{\alpha}_i = \begin{bmatrix} \alpha_{i+1} \\ \alpha_i \end{bmatrix} \quad (6.12)$$

Therefore, (6.6) can be written as

$$\sum_{i=1}^{n-1} \Delta P_{x,i}^T \Delta P_{x,i} = \sum_{i=1}^{n-1} \bar{\alpha}^T E_i^T tmpX_i tmpX_i^T E_i \bar{\alpha} + \sum_{i=1}^{n-1} 2\bar{\alpha}^T E_i^T tmpX_i DeltaRx_i + \sum_{i=1}^{n-1} DeltaRx_i^2 \quad (6.13)$$

By defining the matrices above

$$H_{s,x} = \sum_{i=1}^{n-1} E_i^T tmpX_i tmpX_i^T E_i \quad (6.14)$$

$$B_{s,x} = 2E_i^T tmpX_i DeltaRx_i \quad (6.15)$$

The cost function to formulate the optimisation problem for the x coordinate can be written as

$$\sum_{i=1}^{n-1} \Delta P_{x,i}^T \Delta P_{x,i} = H_s \bar{\alpha}^T + B_s \bar{\alpha}^T + \sum_{i=1}^{n-1} DeltaRx_i^2 \quad (6.16)$$

Moreover, the complete shortest distance equation by including both x and y coordinates can be written as

$$L = \sqrt{H_{s,x} \bar{\alpha}^T + H_{s,y} \bar{\alpha}^T + B_{s,x} \bar{\alpha}^T + B_{s,y} \bar{\alpha}^T + DeltaRx^2 + DeltaRy^2} \quad (6.17)$$

6.5 The Minimum Curvature Problem

In conflict with the shortest path problem mentioned in the previous section, to achieve the best lap time an overall optimal trajectory is somewhere near to the minimum curvature. The minimum curvature is the line taken to appropriately navigate the circuit whilst maintain the least amount of steering angle necessary for all corners and straights as shown in Figure 6.3.

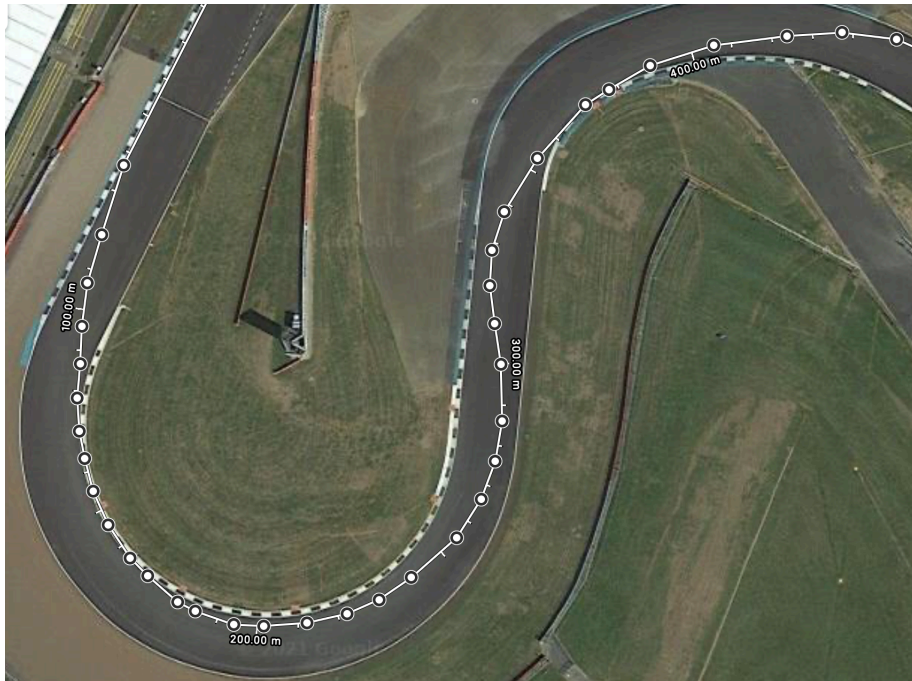


Figure 6.3 Minimum curvature trajectory (white line) of Brooklands and Luffield corners of the Silverstone GP circuit.

As depicted in Figure 6.4, the curvature k can be determined from

$$s = R\vartheta \tag{6.18}$$

where

$$R = \left\| \frac{ds}{d\theta} \right\|$$

and

$$k = \frac{1}{R} = \left\| \frac{d\theta}{ds} \right\| \quad (6.19).$$

here

s is the length of curvature for the segment between P_1 and P_2 .

R is the radius of the circle.

θ is the angle of segment between points P_1 and P_2 .

Assuming that T is the trajectory tangent to the corresponding points

$$T = re^{i\theta} \Rightarrow \frac{dT}{ds} = i \frac{d\theta}{ds} re^{i\theta} \quad (6.20)$$

and this yield

$$\left\| \frac{dT}{ds} \right\| = \left\| \frac{d\theta}{ds} \right\| = k \quad (6.21)$$

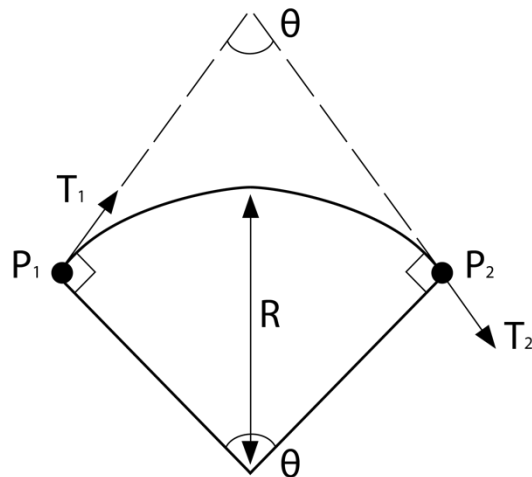


Figure 6.4 Segmentation nomenclature between two points of the track.

In this way, the curvature at each point shown in Figure 6.4 can be calculated through Eqn. (6.22)

$$\begin{aligned}
 T_i &= \left. \frac{dx}{ds} i + \frac{dy}{ds} j \right|_{s=p_i} \\
 \frac{dT_i}{ds} &= \frac{d^2x}{ds^2} i + \frac{d^2y}{ds^2} j \\
 k &= \sqrt{\left(\frac{d^2x}{ds^2}\right)^2 + \left(\frac{d^2y}{ds^2}\right)^2}
 \end{aligned}
 \tag{6.22}$$

when a cubic spline has the second derivative, the first term in (6.22) can be written in the matrix form as

$$\frac{d^2\bar{\mathbf{x}}}{ds^2} = \mathbf{D}\bar{\mathbf{x}}
 \tag{6.23}$$

where

\mathbf{D} is the $n \times n$ matrix for the shape of the track

$\bar{\mathbf{x}}$ is the $n \times 1$ vector containing the segment points.

As can be inferred from (6.23) the curvature can be calculated from the weighted distance of the points on the track with respect to the origin of the track coordinates. The total curvature is calculated from the square root of the norm of the vector resulting from this weighted distance in both x and y directions.

The parameterisation of the track and the vector of each point of the trajectory at the end of each segment can be written in the matrix form as follows

$$\bar{\mathbf{x}} = \mathbf{x}_r + \mathbf{d}\mathbf{x} \alpha
 \tag{6.24}$$

where \mathbf{x} and \mathbf{x}_r are two $n \times 1$ column vectors and \mathbf{dx} and $\boldsymbol{\alpha}$ are $n \times n$ and $n \times 1$ matrices, used to parametrise a point with the track. Therefore, by substituting (6.24) in (6.23) and squaring both sides

$$\begin{aligned} \frac{d^2\bar{\mathbf{x}}}{ds^2} &= \mathbf{D}\mathbf{x}_r + \mathbf{D}\mathbf{dx}\boldsymbol{\alpha} \\ \Rightarrow \left(\frac{d^2\bar{\mathbf{x}}}{ds^2}\right)^2 &= (\mathbf{D}\mathbf{x}_r + \mathbf{D}\mathbf{dx}\boldsymbol{\alpha})^T (\mathbf{D}\mathbf{x}_r + \mathbf{D}\mathbf{dx}\boldsymbol{\alpha}) \\ &= \mathbf{x}_r^T \mathbf{D}^T \mathbf{D} \mathbf{x}_r + 2\boldsymbol{\alpha}^T \mathbf{dx}^T \mathbf{D}^T \mathbf{D} \mathbf{x}_r + \boldsymbol{\alpha}^T \mathbf{dx}^T \mathbf{D}^T \mathbf{D} \mathbf{dx} \boldsymbol{\alpha} \end{aligned}$$

Therefore, the least curvature (Γ) equation can be derived as

$$\begin{aligned} Cnst &= \mathbf{x}_r^T \mathbf{D}^T \mathbf{D} \mathbf{x}_r \\ H_\Gamma &= \boldsymbol{\alpha}^T \mathbf{dx}^T \mathbf{D}^T \mathbf{D} \mathbf{dx} \boldsymbol{\alpha} \\ B_\Gamma &= 2\boldsymbol{\alpha}^T \mathbf{dx}^T \mathbf{D}^T \mathbf{D} \mathbf{x}_r \\ \Gamma &= \sqrt{\boldsymbol{\alpha}^T [H_\Gamma] \boldsymbol{\alpha} + \{B_\Gamma\} \boldsymbol{\alpha} + Cnst} \end{aligned} \tag{6.25}$$

The equations and matrices above are derived on the x axis direction. All equations can be derived for the y axis in a similar way and summed within the current ones.

The cubic spline interpolation is determined by calculating the distance between two segment points (h_j) and developed through equations (6.26) to (6.32) as follows

$$b_{x,j} = \frac{1}{h_j} (x_{j+1} - x_j) \tag{6.26}$$

$$z_{x,j} = \left(\frac{b_{x,j+1} - b_{x,j}}{h_j} \right) = \frac{1}{h_j} \left[\frac{1}{h_{j+1}} (x_{j+2} - x_{j+1}) \right] - \frac{1}{h_j} \left[\frac{1}{h_j} (x_{j+1} - x_j) \right]$$

$$\begin{aligned}
&= \frac{1}{h_j h_{j+1}} (x_{j+2} - x_{j+1}) - \frac{1}{h_j^2} (x_{j+1} - x_j) \\
\Rightarrow z_{x,j} &= \frac{1}{h_j h_{j+1}} x_{j+2} - \left(\frac{1}{h_j h_{j+1}} + \frac{1}{h_j^2} \right) x_{j+1} + \frac{1}{h_j^2} x_j \\
\Rightarrow z_{x,j} &= \begin{bmatrix} \frac{1}{h_j h_{j+1}} & - \left(\frac{1}{h_j h_{j+1}} + \frac{1}{h_j^2} \right) \frac{1}{h_j^2} \end{bmatrix} \begin{bmatrix} x_{j+2} \\ x_{j+1} \\ x_j \end{bmatrix}
\end{aligned} \tag{6.27}$$

Developing matrices where:

$$\begin{aligned}
q_{j+2} &= \frac{1}{h_j h_{j+1}} \\
q_{j+1} &= \frac{1}{h_j h_{j+1}} + \frac{1}{h_j^2} \\
q_j &= \frac{1}{h_j^2}
\end{aligned} \tag{6.28}$$

and putting the elements in (6.27) in the matrix form we have

$$\mathbf{z}_x = \begin{bmatrix} z_{x,1} \\ z_{x,2} \\ z_{x,3} \\ \vdots \\ z_{x,n-2} \end{bmatrix} = \begin{bmatrix} q_1 & q_2 & q_3 & 0 & 0 & \cdots & 0 \\ 0 & q_2 & q_3 & q_4 & 0 & \cdots & 0 \\ 0 & 0 & q_3 & q_4 & q_5 & \cdots & 0 \\ \vdots & \vdots & \vdots & \vdots & \vdots & \ddots & \vdots \\ 0 & 0 & 0 & 0 & q_{n-2} & q_{n-1} & q_n \end{bmatrix} \begin{bmatrix} x_1 \\ x_2 \\ x_3 \\ \vdots \\ x_n \end{bmatrix} \tag{6.29}$$

A more convenient way to derive the (6.29) in the closed form is by stacking the elements in (6.26) in the matrix form as follows

$$\begin{bmatrix} b_{x,1} \\ b_{x,2} \\ b_{x,3} \\ \vdots \\ b_{x,n-1} \end{bmatrix} = \underbrace{\begin{bmatrix} -\frac{1}{h_1} & \frac{1}{h_1} & 0 & 0 & \cdots & 0 \\ 0 & -\frac{1}{h_2} & \frac{1}{h_2} & 0 & \cdots & 0 \\ 0 & 0 & -\frac{1}{h_3} & \frac{1}{h_3} & \cdots & 0 \\ \vdots & \vdots & \vdots & \vdots & \ddots & \vdots \\ 0 & 0 & 0 & 0 & -\frac{1}{h_{n-1}} & \frac{1}{h_{n-1}} \end{bmatrix}}_{\mathbf{B}_{x,n-1 \times n}} \begin{bmatrix} x_1 \\ x_2 \\ x_3 \\ \vdots \\ x_n \end{bmatrix}$$

(6.30)

Moreover, the relationship between $z_{x,i}$ and $b_{x,j}$ can be written in the matrix form as

$$\begin{bmatrix} z_{x,1} \\ z_{x,2} \\ z_{x,3} \\ \vdots \\ z_{x,n-1} \end{bmatrix} = \underbrace{\begin{bmatrix} -\frac{1}{h_1} & \frac{1}{h_1} & 0 & 0 & \cdots & 0 \\ 0 & -\frac{1}{h_2} & \frac{1}{h_2} & 0 & \cdots & 0 \\ 0 & 0 & -\frac{1}{h_3} & \frac{1}{h_3} & \cdots & 0 \\ \vdots & \vdots & \vdots & \vdots & \ddots & \vdots \\ 0 & 0 & 0 & 0 & -\frac{1}{h_{n-1}} & \frac{1}{h_{n-1}} \end{bmatrix}}_{\bar{\mathbf{H}}_{x,n-1 \times n}} \begin{bmatrix} b_{x,1} \\ b_{x,2} \\ b_{x,3} \\ \vdots \\ b_{x,n} \end{bmatrix}$$

(6.31)

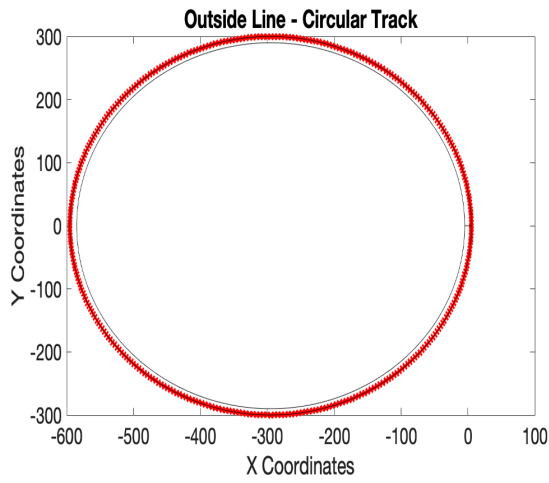
By defining \mathbf{H}_x in (6.23) as to be equal to $\bar{\mathbf{H}}$ when the las row and column are eliminated, it is possible to write \mathbf{z}_x directly in terms of x_i by multiplying the matrices as shown in (6.33).

$$\mathbf{H}_x = \begin{bmatrix} -\frac{1}{h_1} & \frac{1}{h_1} & 0 & 0 & \dots & 0 \\ 0 & -\frac{1}{h_2} & \frac{1}{h_2} & 0 & \dots & 0 \\ 0 & 0 & -\frac{1}{h_3} & \frac{1}{h_3} & \dots & 0 \\ \vdots & \vdots & \vdots & \vdots & \ddots & \vdots \\ 0 & 0 & 0 & 0 & -\frac{1}{h_{n-2}} & \frac{1}{h_{n-2}} \end{bmatrix}_{n-2 \times n-1} \quad (6.32)$$

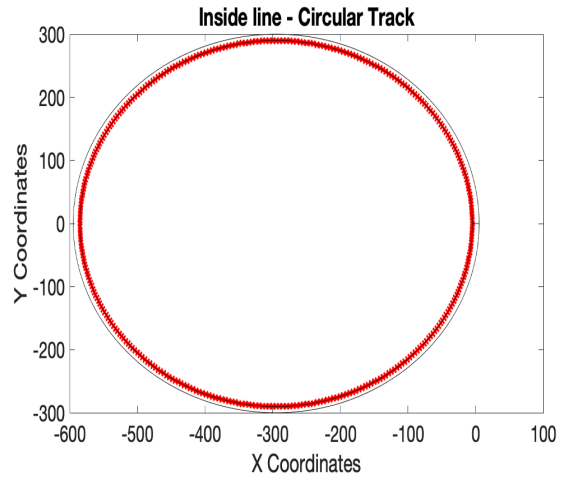
$$\mathbf{z}_x = \begin{bmatrix} z_{x,1} \\ z_{x,2} \\ \vdots \\ z_{x,n-3} \\ z_{x,n-2} \end{bmatrix} = \mathbf{H}_x \mathbf{B}_x \begin{bmatrix} x_1 \\ x_2 \\ \vdots \\ x_{n-1} \\ x_n \end{bmatrix} \quad (6.33)$$

6.6 Circuit Discretisation and Performance Surfaces

For the initial test of the algorithm a circular track is created consisting of an inside radius boundary of 590m and an outside boundary of radius 600m, giving a constant 10m track width. As this track was generated within MATLAB, the co-ordinates are generated in an anti-clockwise fashion. For the track position, $\alpha = 0$ means the boundary for the outside track, and $\alpha = 1$ means the inside track boundary. A test was carried out through the PSO with no tuning to see how the alpha is used. When alpha is forced to zero the outside track trajectory is followed with a trajectory total distance and PSO cost function of 1884.93m (equivalent to πd) and when alpha is set to one the inside trajectory is followed with a cost function of 1822.10m. The definition of inner and outer trajectories is illustrated in Figure 6.5. Similarly, the value $\alpha = 0.5$ follows the centreline between the track boundaries (length of 1853.52m). This ensures that the algorithm is correct and distance testing for minimum distance or radius for least curvature is purely down to the PSO algorithm tuning once α is set to be optimised in the range $[0, 1]$.



(a)



(b)

Figure 6.5 (a) The definition of outer trajectory paths (red line) for $\alpha = 0$ (b) The definition of inner trajectory paths (red line) for $\alpha = 1$.

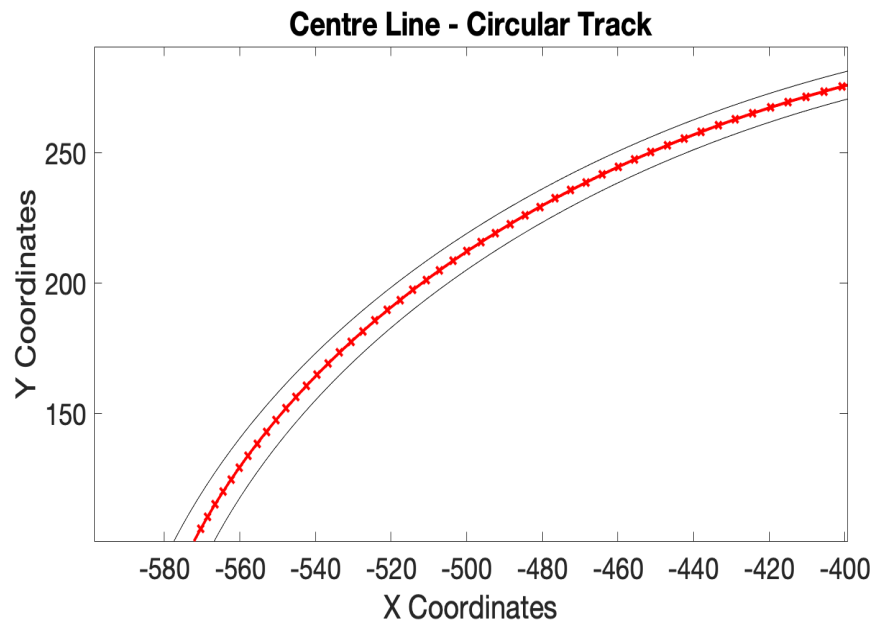


Figure 6.6 Centre line trajectory for $\alpha = 0.5$.

As this is a simple circle rather than an ellipse or a track that varies through left and right corners, then the PSO algorithm can also be tested for shortest distance as this should find the minimum circumference as the distance, in this case the inside line. During this testing and tuning of the PSO it became apparent that the number of variables to be optimised affected simulation time and accuracy and once again a compromised solution had to be found to play off accuracy against simulation time.

For the circular track, it was found that the personal and social acceleration coefficients in the PSO algorithm were found to be best at $c_1 = 3$ and $c_2 = 1$. Whilst the inertia coefficient produces the best results when determined by a linear increment between 0.1 and 1, dictated by the number of iterations. Reducing the number of segments within the track means a loss to geometric accuracies and shape. Increasing the population size of the PSO algorithm to coincide with the segmentation size, increases the simulation time and the required computing power.

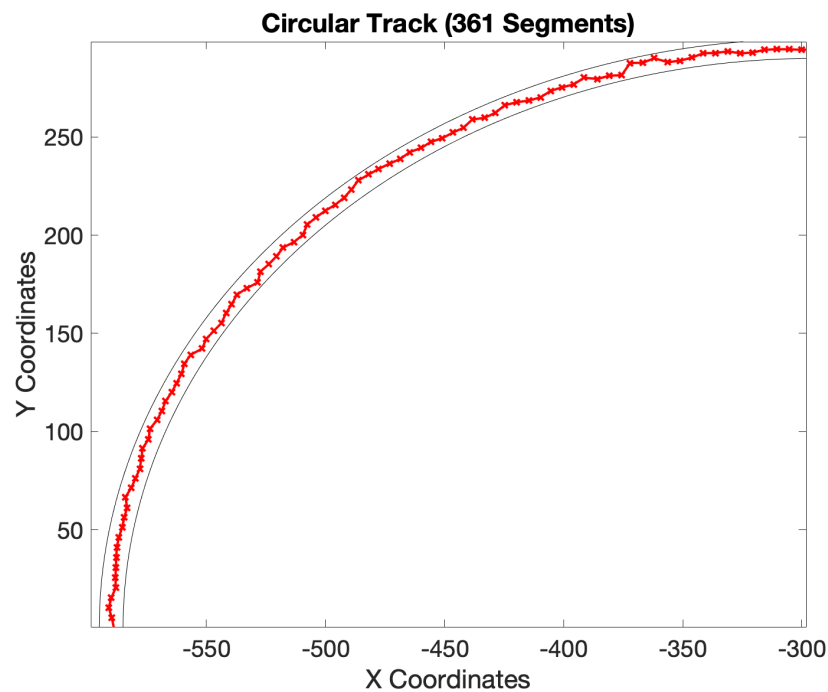


Figure 6.7 Section of the circular circuit with 361 segments (50 iterations, 100 population size for SOPSO).

As can be seen in Figure 6.7, the SOPSO with a 361-segment circuit cannot find the minimum distance using 50 iterations and a 100-population size. This simulation, however, only takes 11 minutes to complete with a 2.3GHz Quad-core i7 processor and 16GB memory. Increasing the population or iteration has an exponential growth rate on simulation time and therefore a reduced number of segments (nVar) were tested (Table 6.1)

Table 6.1 A sample of PSO tuning tests (best costs = green, variation from baseline = blue).

Test	c1	c2	w	Best cost	@It	Its	Pop	nVar	Run Time
1	3	1	linspace(0.1,1,MaxIt)	1894	37	50	100	361	10.94m
2	2	2	linspace(0.1,1,MaxIt)	2192	31	50	100	361	10m
3	3	1	linspace(0.1,1,MaxIt)	1820	49	50	50	50	9.5 s
4	3	1	linspace(0.1,1,MaxIt)	1848	43	50	100	100	38 s

The data from several tests (Table 6.1) determines that for a reasonable run time and accuracy of results, 50 segments are a limit to the SOPSO accuracy. Test 3 gives the exact minimum curvature of the circle (inside circumference) and the segments are plotted in Figure 6.8. Although the time at this stage appears reasonable and could be increased by increasing the track segmentation, iterations and population size, time may become an issue when the track shape becomes more complex.

Once the track shape is updated to a more complex pathway, the PSO will need tuning for speed and accuracy. To this end, the outer and inner track trajectory will be tested by holding alpha to zero or one and then the output number is observed so that the inner and outer lengths of the track will be achieved. Least curvature will be checked against the curvature of each corner. Therefore, it is essential to correctly discretise the circuit geometry. It may be feasible to test sectors of the circuit in 50 segment sections, however, including longer segments inevitably requires a MOPSO so that all sectors could be optimised within one execution of the algorithm.

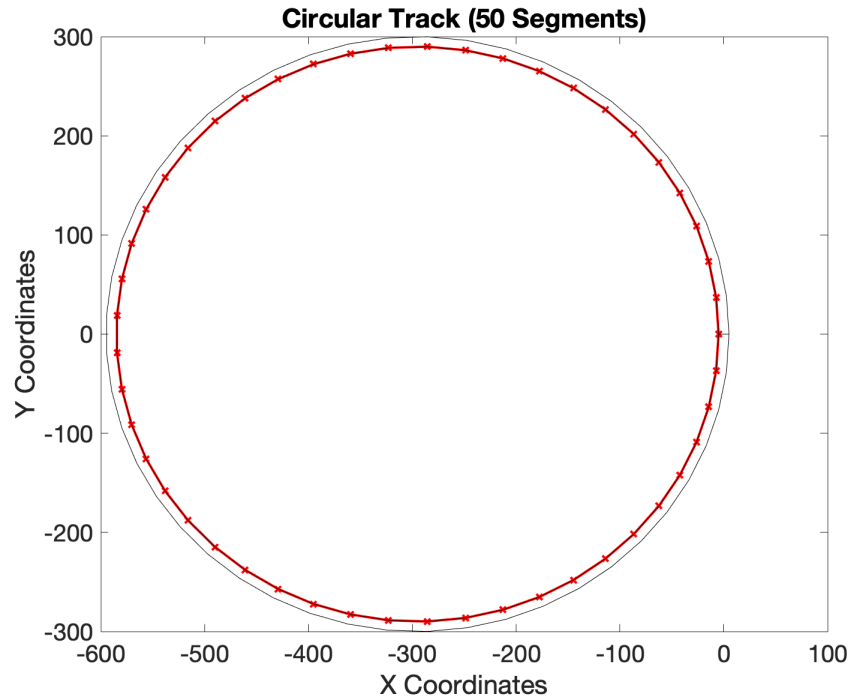


Figure 6.8 Circular circuit. 50 segments (total) vs 50 iterations and 50 population size for SOPSO.

The results of the circle testing show that the track parameters and section lengths will be sensitive inputs for the results achieved from PSO. Therefore, to gain accuracy detailed track maps are required. This concludes that the inner and outer track boundaries are required for any given circuit. The discretisation of this data may also change dependant on number of sections required for suitable results. Using a physical car to continuously drive the inner and outer circuit parameters each time a change is required to the track parameters or section count is unfeasible. Therefore, a laser scanned model of the grand prix Silverstone circuit was used to find the boundaries. The GPS and track co-ordinate telemetry were taken from the iRacing simulator, whereby a Ferrari 488 GT3 car was used to drive the inner and outer boundary of the track. This telemetry data was exported to Motec i2 data analysis software and later exported to Excel for further processing. As the data can only be exported in Hz, the time taken to drive at a slow pace the inner and outer boundaries of the track meant the data had unequal data samples across the distance of the circuit length. The data was cleansed to allow appropriate data points to be stored at similar co-ordinates around the track albeit at the inside or outside track boundary, leaving 361 data points that could determine the track geometry, boundaries and sectors as shown in Figure

6.9. This inevitably produces unequal sector lengths. This amount of data points was chosen so as to represent the same amount of data points from the physical measured data, so vehicle dynamic behaviour can be compared.

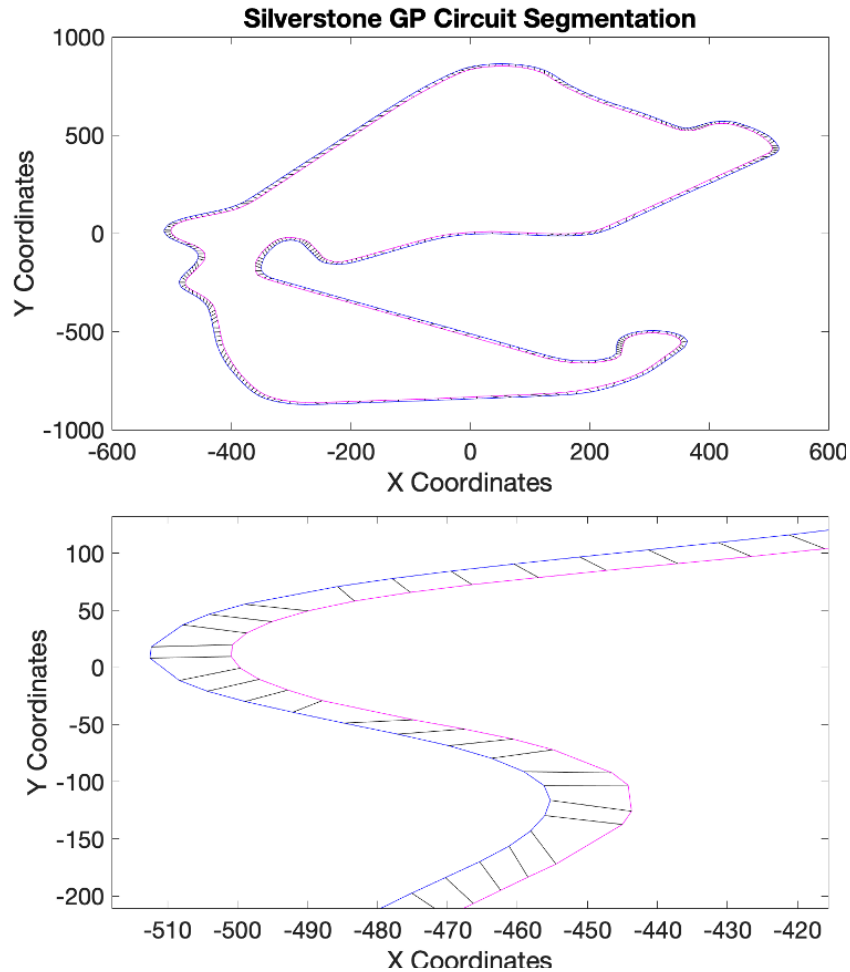


Figure 6.9 Silverstone Grand Prix circuit segmentation using 361 data points connecting the inner and outer boundaries of the circuit. Pink represents the inside boundary and blue the outside boundary.

Once the segments have been established a performance surface analysis procedure was carried out to determine the PSO tuning and correct the implementation of α . As the Silverstone GP circuit is an anticlockwise circuit, $\alpha = 0$ indicates the inside boundary of the circuit or the drivers' right-hand side and $\alpha = 1$ indicates the left-hand boundary.

As a sanity check, various sectors of the circuit were chosen to analyse the performance surface behaviour. In the right-hand corners, the surface should tend towards zero and the left-handed corners should tend towards one. The actual result is dependent on the transition from the previous sector or into the next sector, due to the straight-aways or corner direction. Since the shortest distance or least curvature (straight line) between sectors may lie away from a certain boundary edge it is important to utilise a section that is mid corner so as to reveal a result close to 0 or 1.

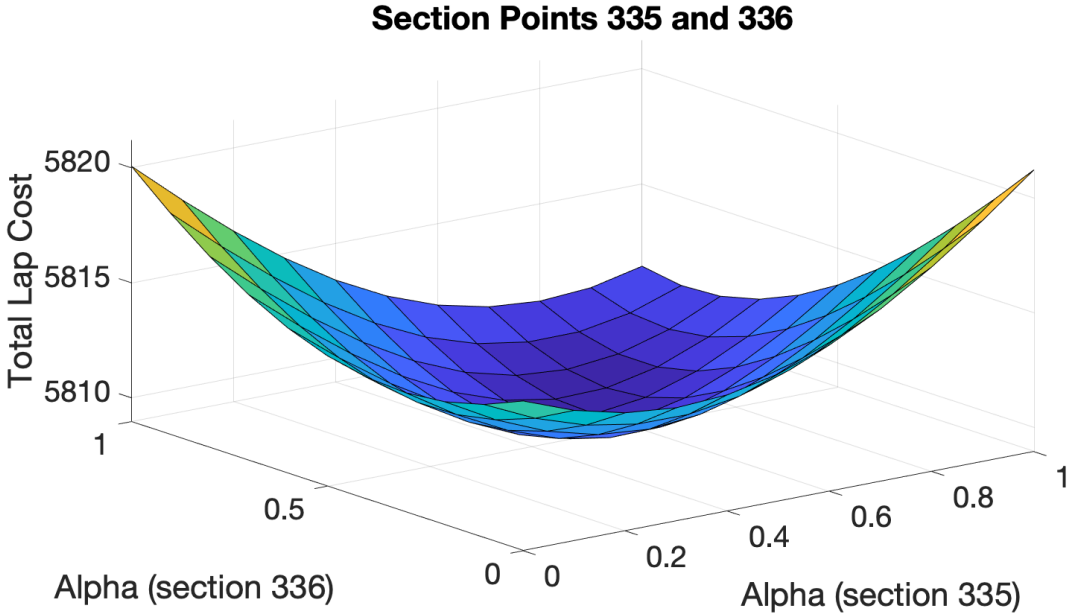


Figure 6.10 Variation to α , performance surface for the left/right chicane (Vale), sections 335 and 336.

The two middle sections of the Vale Left/Right chicane have been chosen for the performance surface. Figure 6.10 depicts a best line tending to the middle of the circuit ($\alpha = 0.5$). As would be expected, a straight line between the left and right corner would be presumed the shortest path from one apex to the following corner apex. For a range of juxtaposed left or right-handed sectors, the performance surface should result in ones and zeros for the parameter α as illustrated in Figures 6.11 and 6.12, respectively.

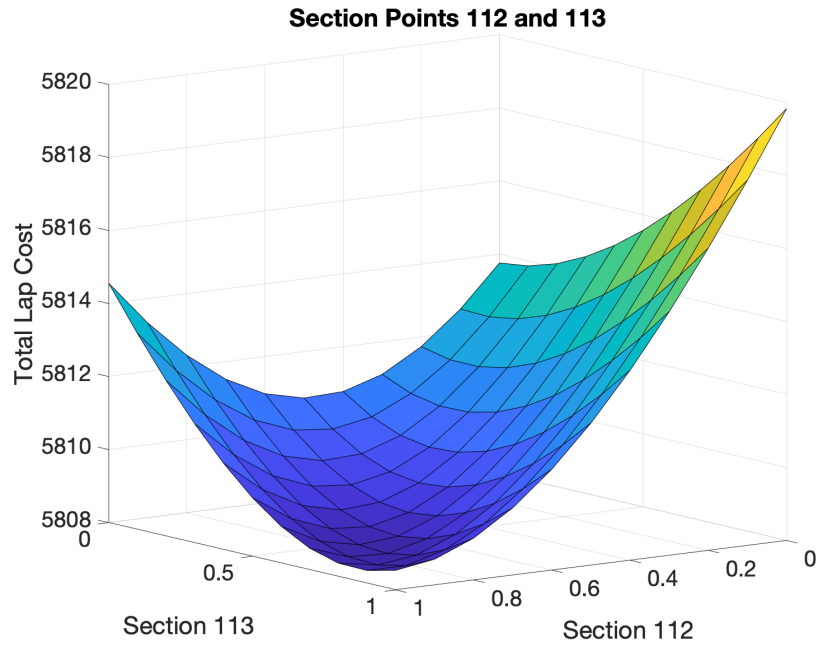


Figure 6.11 Performance surface for the left-handed Brooklands corner, sections 112 and 113.

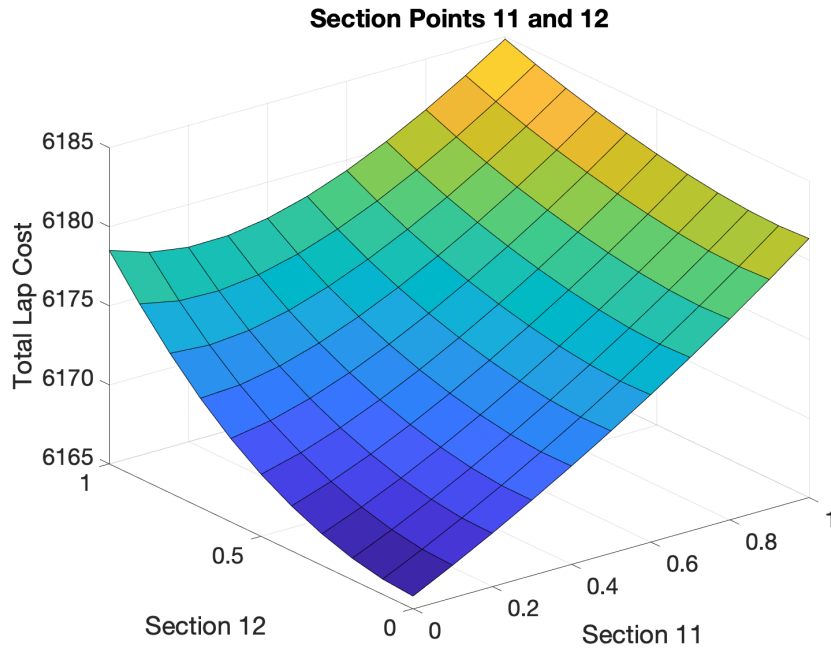


Figure 6.12 Performance surface for the 1st right-handed (Abbey) corner, sections 11 and 12.

Once established that the performance surfaces were responding as assumed the tuning of the PSO algorithm could begin to locate the least curvature and shortest distance trajectories around the Silverstone Grand Prix circuit.

6.7 Shortest Path Trajectory – Single Objective PSO

The PSO was set to maintain $\alpha = 0$, followed by $\alpha = 1$, so that the length of the right-hand and left-hand trajectory paths could be checked against known measured data. The right trajectory was recorded as 5832m as opposed to the driver in the loop data of 5811m and the left trajectory recorded as 5902m as opposed to 5892m. The discrepancies could lie in GPS data accuracy from the race car simulator and the ability of a driver to stick exactly to the inside and outside line perfectly. As the distances were close to measured data the 5832m and 5902m will be used as the distance for PSO. It is, however, clear that the shortest path trajectory should be lower than either of these numbers due to optimising the shortest path through a left or right corner. Using straight lines through any S shaped turns such as the Maggots and Becketts complex, and the inside line on all other corners the actual shortest path around Silverstone is 5560m.

As per the tuning for the vehicle dynamics model (Chapter 5), the particle acceleration (c_1 , c_2), inertia coefficient (w), iteration size, population size and mutation coefficient (pm) are all tested for cost accuracy and speed of convergence. The samples listed in Table 6.2 show a variation across parameters, however, one parameter change at a time was also included in the tuning study. In all cases, $c_1+c_2 = 4$ must be adhered to.

Table 6.2 Variations to PSO parameters as tested individual samples versus baseline.

	c_1	c_2	w	Iter.	Pop	pm
Baseline	2	2	linspace(0.1,1,MaxIt)	50	50	0.95
Sample 1	1	3	linspace(0.5,1,MaxIt)	20	20	0.5
Sample 2	2	2	linspace(0.1,0.5,MaxIt)	100	100	0.1
Sample 3	3	1	linspace(0.1,1,MaxIt)	50	50	0.95

As previously found in the vehicle dynamic PSO tuning, the personal and social acceleration coefficients (c_1 , c_2) make a large difference on the cost function outcome, however they do not affect time. The best cost result was always found whilst using $c_1 = 3$ and $c_2 = 1$, whether just these variables were varied or when used with a change in other parameters.

Table 6.3 A sample of PSO tuning tests (best costs = green, variation from baseline = blue).

Shortest Path SOPSO Results							
Test	c_1	c_2	w	Best cost	Iterations	Population	Run Time(m)
Pre_1	2	2	linspace(0.1,1,MaxIt)	5850	50	50	10.97
Pre_2	2	2	linspace(0.1,1,MaxIt)	5832	50	50	10.97
1	2	2	linspace(0.1,1,MaxIt)	6019	20	20	1.78
2	2	2	linspace(0.1,1,MaxIt)	5771	50	50	10.75
3	2	2	linspace(0.5,1,MaxIt)	5993	50	50	15.08
4	2	2	linspace(0.1,0.5,MaxIt)	5767	50	50	15.1
5	2	2	linspace(0.1,1,MaxIt)	5849	50	50	15.08
6	3	1	linspace(0.1,1,MaxIt)	5681	50	50	15.03
7	1	3	linspace(0.1,1,MaxIt)	5963	50	50	14.98
8	3	1	linspace(0.1,0.5,MaxIt)	5753	50	50	16.48
9	3	1	linspace(0.1,0.5,MaxIt)	5722	100	100	59.75
10	3	1	linspace(0.1,1,MaxIt)	5665	100	100	47.18
11	3	1	linspace(0.1,1,MaxIt)	5674	50	100	24.7
12	3	1	linspace(0.1,0.5,MaxIt)	5740	50	100	24.7
19	3	1	linspace(0.1,1,MaxIt)	5648	50	100	24.15

With tuning complete it was once again, as in the case of the circular track, apparent 361 segments were a limitation to finding the optimum shortest distance without the use of high-end computing or extraordinary long simulation times.

The trajectory plot within Figure 6.13, shows that with a 24-minute simulation an optimum is not found. The trajectory does not follow the inside curvature of several corners and within the straightaways the trajectory creates a wandering effect, adding length to the overall path. Increasing population and iteration size has an exponential effect on the simulation time, and although a 100 iteration, 1000 population simulation (40 hours) was carried out a similar result was found, suggesting a limitation on the number of variables is a factor for the accuracy of a SOPSO.

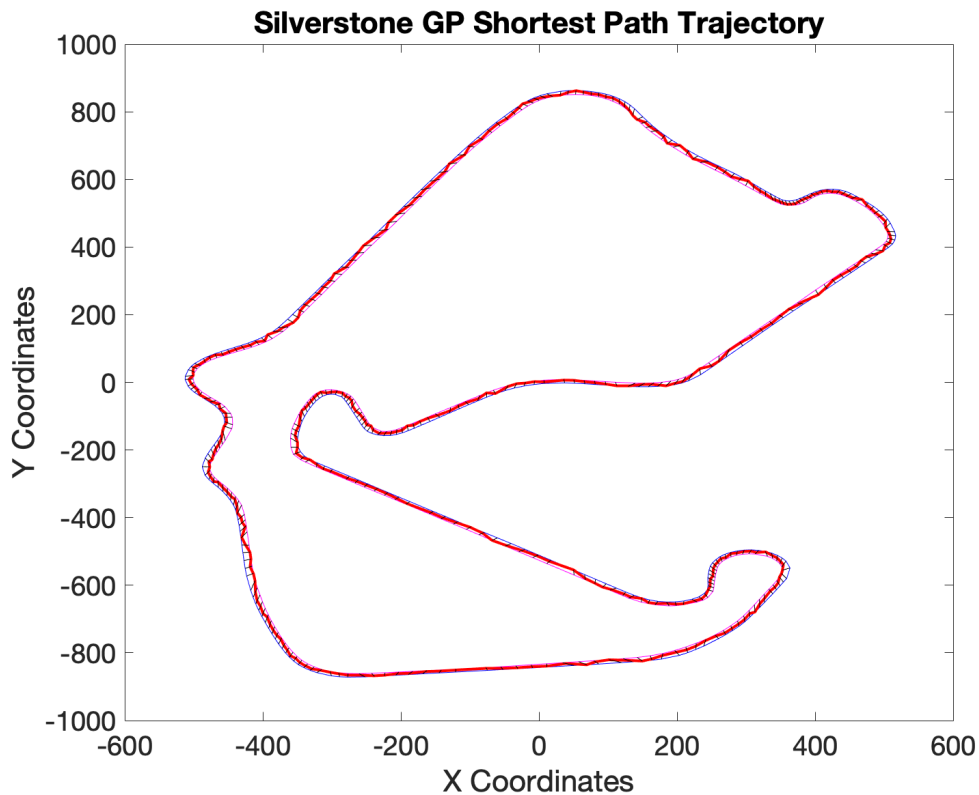


Figure 6.13 Shortest Path Trajectory (red line) with 361 segmentation of the Silverstone GP Circuit.

With the use of the driver in the loop simulation and utilising a centre line, the data can be exported at a greater or lower rate, creating an increase or decrease in data points if required. The centre line allows the left and right co-ordinates to be produced by assuming a 15m wide track as per the majority of Silverstone circuit. The centre line data is offset by +/- 7.5m and new data points are plotted. The use of the centre line ensures each segment has an equal length. A 500-segment equal length (as opposed to 361 unequal length), Silverstone was produced to further refine all corners. This data was split into ten sectors of the circuit, each consisting of fifty segment sections. The iterations remained at 50 and population size was increased to 200 (Appendix 5).

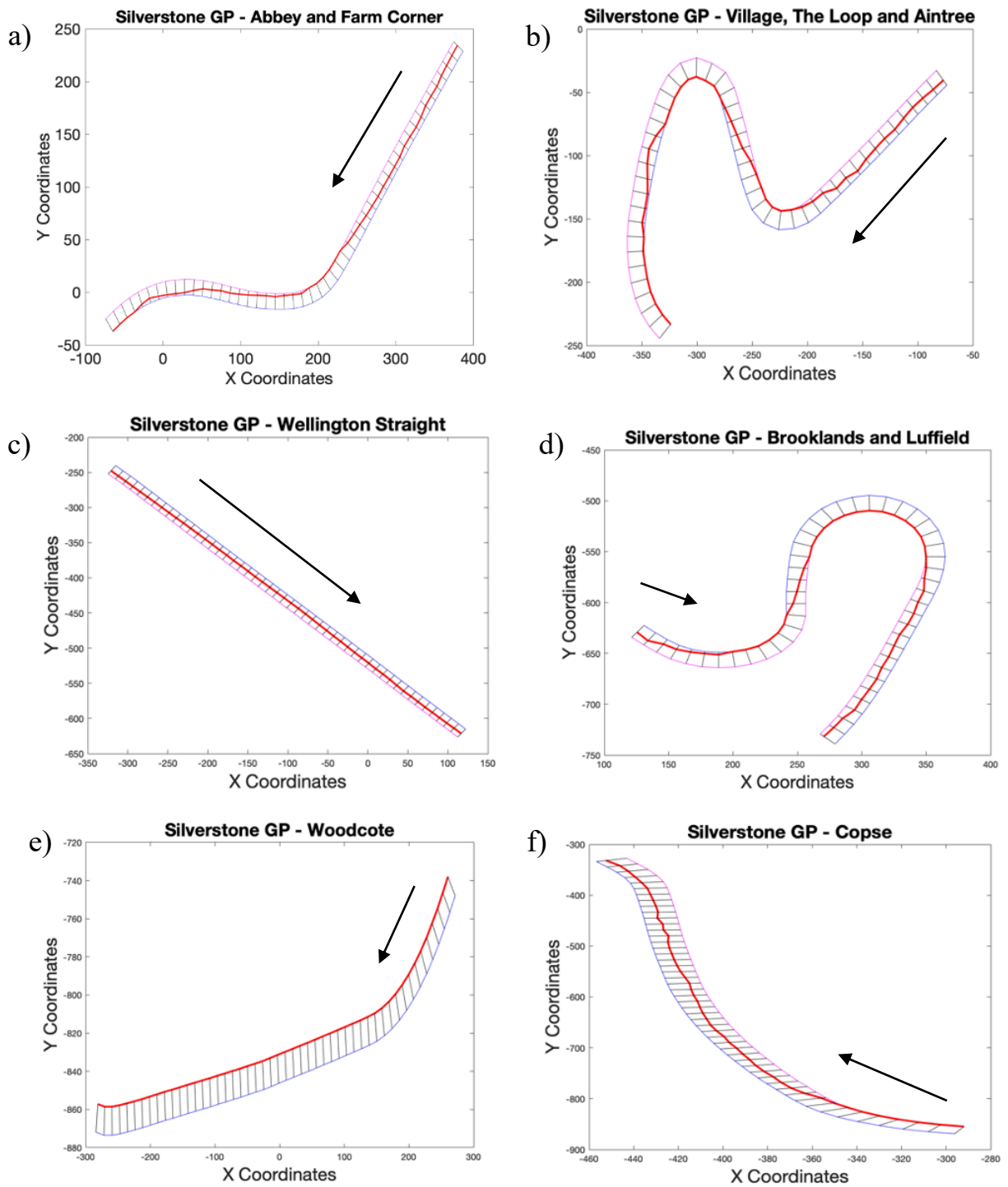


Figure 6.14 Shortest path trajectory (red line) with 50 segmentation sectors of the Silverstone GP circuit. a) from the start/finish line through Abbey corner to f) Copse corner (the black arrow depicts direction of travel).

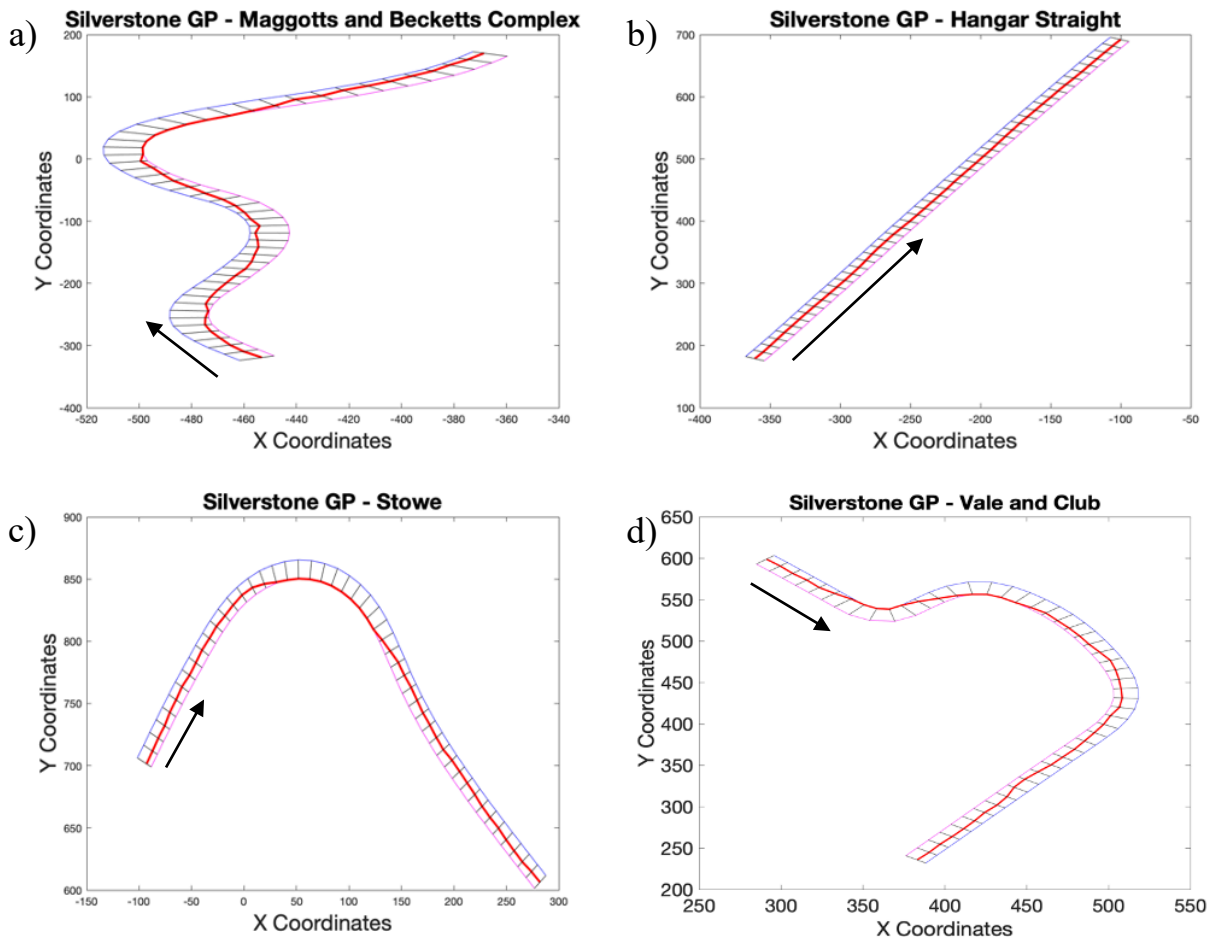


Figure 6.15 Shortest path trajectory (red line) with 50 segmentation sectors of the Silverstone GP circuit. a) from Maggotts and Becketts complex to d) Vale and Club corners to the start/finish line (the black arrow depicts direction of travel).

Figures 6.14 and 6.15 detail that in some cases the shortest path is found for the overall sector and in some cases only for certain segments of the sector (such as Village and The Loop). There is also the issue that the end of one sector may not align with the start of the next sector when looking for overall shortest path. Using the α result from the last segment of the previous sector and applying that value to segment in one of the next sector results in a least favoured path as shown in Figure 6.16 compared to the results shown in Figures 6.14 and 6.15. However, reducing the sectors had a beneficial effect on the trajectory as shown in Figure 6.16. It is clear that the segment number and initial starting condition for α can have a positive and negative effect on the outcome (Figure 6.16).

It is important to note that within the literature [96, 97] the final trajectory is subject to spline manipulation and smoothing.

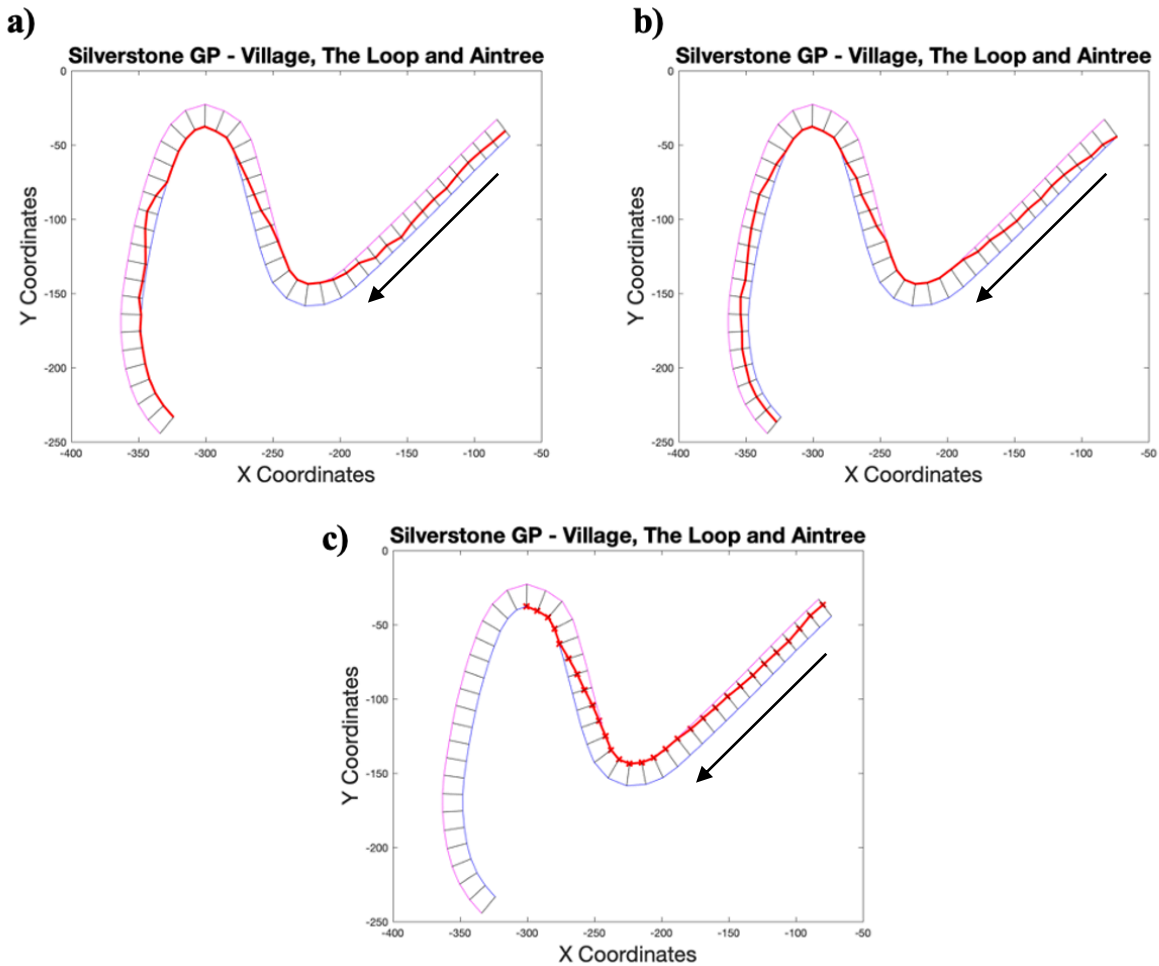


Figure 6.16 Shortest path trajectory (red line) with 50 segmentation sectors versus 30 segmentation sectors for Village, The Loop and Aintree corners. a) 50 segments ($\alpha = \text{rand}$). b) 50 segments, (segment 1, $\alpha = 1$, segments 2-49 $\alpha = \text{rand}$). c) 30 segments ($\alpha = \text{rand}$), The black arrow depicts direction of travel.

Each 50-segment path took approximately fifteen minutes to converge and 30 segment sectors took 14.8 minutes, ten minutes quicker than the first full lap, a 361-segment optimisation utilising a 50 iteration, 200 population usage. For a 500-segment lap, splitting the lap up takes

approximately 150 minutes at 50 segments (10 sectors) and a 480-segment lap takes 250 minutes for 30 segments (16 sectors) to complete all sectors of a lap.

Maintaining a 50 iteration, 200 particle PSO and re-plotting the circuit once more with a variation in the data collection rate. The sample rate is changed so that 360 segments could be created (to coincide with the original measured data of 361 sections), a 12 sector, 30 segment discretisation of the circuit can be utilised (Appendix 5). This resulted in a 187-minute total run time; however, the shortest distance cost function was greatly reduced to a total lap length of 5513m as opposed to 5614m for the 480-segment combined sector lap. The more accurate trajectory can be seen in Figures 6.17 – 6.18, the trajectory plot is far more accurate than the 50 segmented sectors, Vale and Club corner for instance follow the inside line throughout the corner.

There are still some anomalies in the SOPSO whereby start and finish points of a sector may not connect, The Loop to Aintree and Brooklands to Luffield corners in particular. This means the PSO must use the initial condition so the first segment start point (α) is equal to the last segment of the previous sector. This is clearly illustrated in Figure 6.17 whereby the shortest path through Luffield is found perfectly but has not taken into account the preceding corner Brooklands as a left-hand corner and therefore a transition of left to right should be included. Only choosing sectors that start and finish on a straight away would be a preferred choice, however, this is difficult if splitting each sector into equal amounts as they may not always start and end on a straight away, inevitably over complicating the number of sectors and segments used. An optimisation was incorporated to include one full lap, with 360 segments to test for accuracy, but very poor trajectory profiles were created (Figures 6.19 – 6.22) even when increasing the particle population size to allow similar PSO simulation time as that of the 12 sector, 30 segment optimisations. The simulation time and best cost compromise suggests 12 x 30 segment sectors are feasible for Spline intervention, as in Table 6.4 where the results and simulation time of the SOPSO are summed.

The single sector simulations returned a poor cost function (5844m) when compared to the that of the split sectors ranging between 5620m and 5513m when using a similar population size. The increase in population size to 800 reduced the best cost to 5828m some 300m worse than that of the 12 sector, 30 segment PSO with a saving of 18 minutes (Table 6.4).

Table 6.4 Summation of 361 and 500 segment track discretisation with singular, fifty and thirty segment sector splits.

Sectors	Segments per sector	Best cost (Total length)	Total simulation time(m)	Iterations	Population
1	361	5648	24.15	50	100
10	50	5620.63	146.50	50	200
16	30	5614.72	241.23	50	200
12	30	5513.87	187.98	50	200
1	360	5844.48	39.44	50	200
1	360	5828.98	169.7	50	800

The final output is plotted by means of straight lines connected together for each segment as practiced in [96]. Therefore, the final raw data will be manipulated by the spline function in Matlab to create a more realistic arced path. However, as the track sectors are split, it is considered to be more effective to combine all simulations into a multi-objective PSO whereby all sectors can be optimised simultaneously, and the best costs summed prior to Spline manipulation. The raw data will be subject to optimisation of vehicle dynamic behaviour with an MOPSO algorithm. This may eradicate some impossibilities of direction change within the trajectory, so it is proposed that the trajectory data is not manipulated until after the dynamic constraints and lap time optimisation is included as the final step. By utilising a suitable track section segmentation and an appropriate population size to ensure computer power and optimisation results are optimised the result of 5513.87m and 5614.72m are within 47m and 54m of the defined shortest path possible (5560m). This suggests the 12 x 30 segment path may be losing some detail and showing an overall shorter path but is the closest to the actual figure and therefore will be used for the remainder of the study. It must be added that a straight line was proposed for some sections of the Maggots and Becketts section when calculating the official shortest path length whereas in Figure 6.18b each corner follows the inside line of the corner exactly allowing for some reduction in distance.

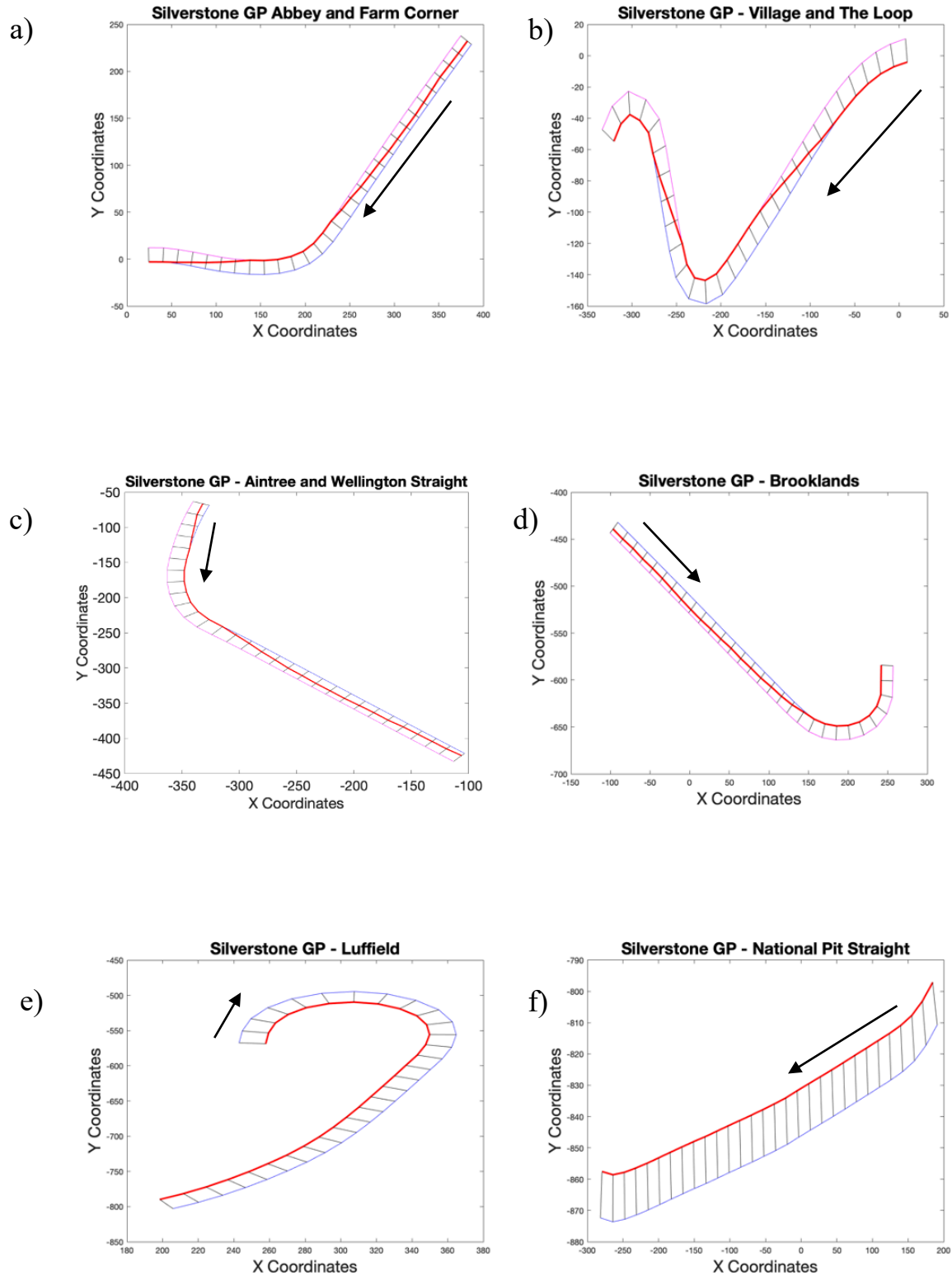


Figure 6.17 Shortest path trajectory (red line) with 30 segmentation sectors of the Silverstone GP circuit. a) From the start/finish line through Abbey corner to f) Copse corner (the black arrow depicts direction of travel).

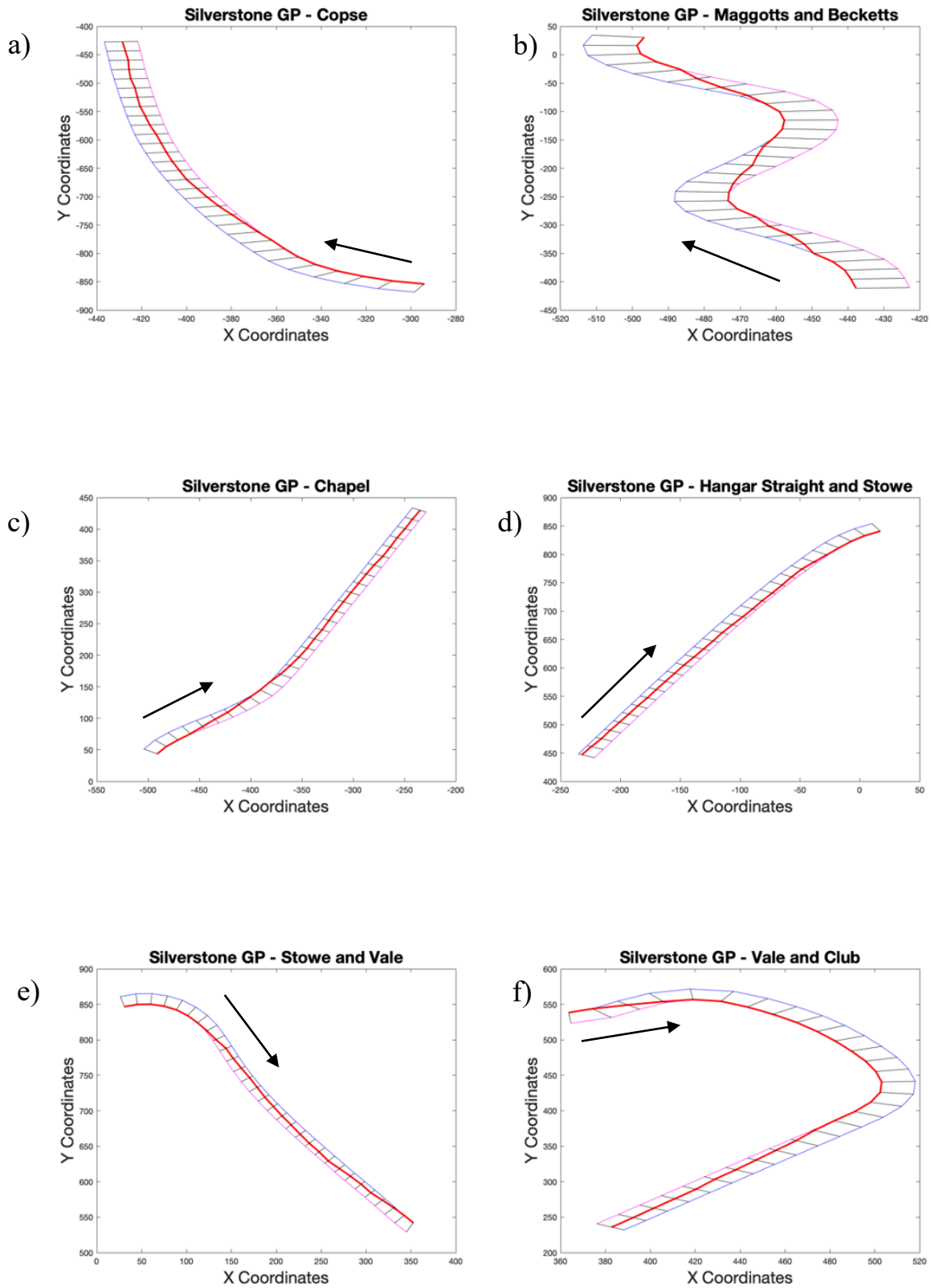


Figure 6.18 Shortest path trajectory (red line) with 30 segmentation sectors of the Silverstone GP circuit. a) Copse corner to f) Vale and Club corners through to the start/finish line, (the black arrow depicts direction of travel).

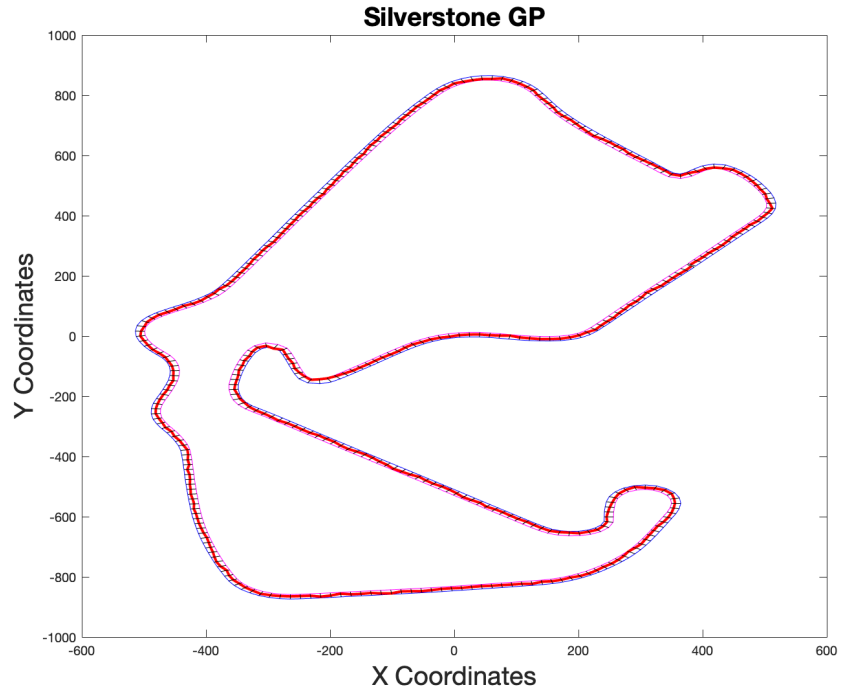


Figure 6.19 Shortest path trajectory (red line) with 1 by 360 segmentation sector of the Silverstone GP circuit. SOPSO set to 50 iterations, 200 particles.

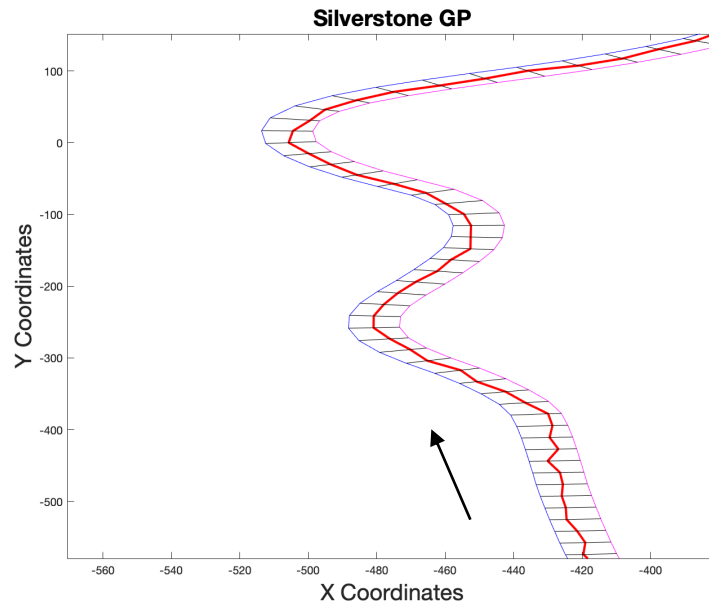


Figure 6.20 Shortest path trajectory (red line) with 1 by 360 segmentation sector of the Silverstone GP circuit. Detailed view of the Maggotts, Becketts and Chapel series of corners. SOPSO set to 50 iterations, 200 particles, (the black arrow depicts direction of travel).

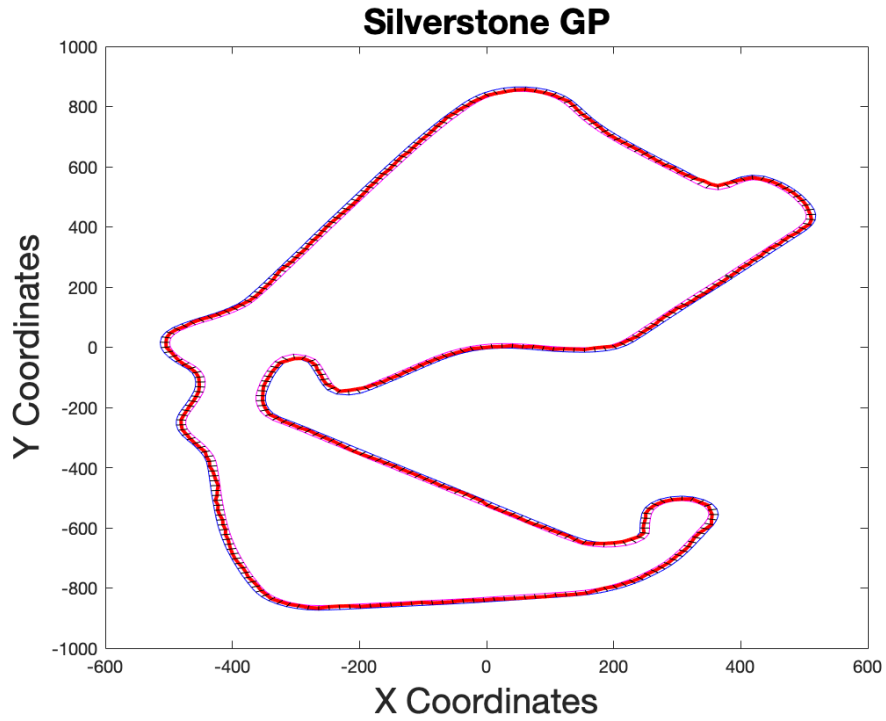


Figure 6.21 Shortest path trajectory (red line) with 1 by 360 segmentation sector of the Silverstone GP circuit. SOPSO set to 50 iterations, 800 particles.

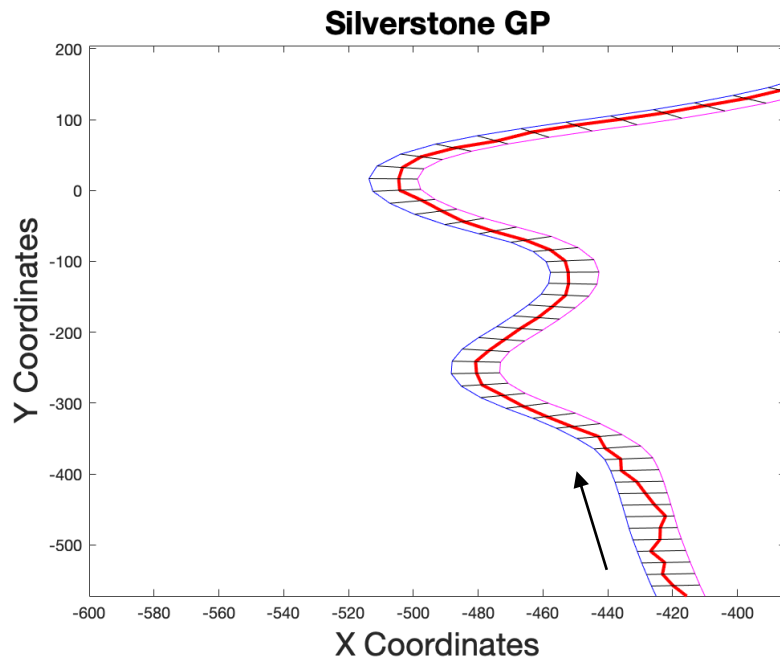


Figure 6.22 Shortest path trajectory (red line) with 1 by 360 segmentation sector of the Silverstone GP circuit. Detailed view of the Maggotts, Becketts and Chapel series of corners. SOPSO set to 50 iterations, 800 particles, (the black arrow depicts direction of travel).

6.8 Minimum Curvature Trajectory

As per the shortest path validation a circular track was first utilised to establish correct functionality of the SOPSO and minimum curvature algorithm. The same circular track was used with an outer path consisting of a constant radius (R) of 300m and the inside path radius of 290m. The centre line therefore (for basing the segment length upon) has a radius of 295m. Curvature is calculated for a circle simply as $1/R$. This determines that the curvature for the inside path is 0.00345 and the outside path is 0.00333. Using the PSO algorithm and setting α to 1 (inside line) the algorithm returned a cost of 0.0034421 and setting alpha to 0 returned 0.003333.

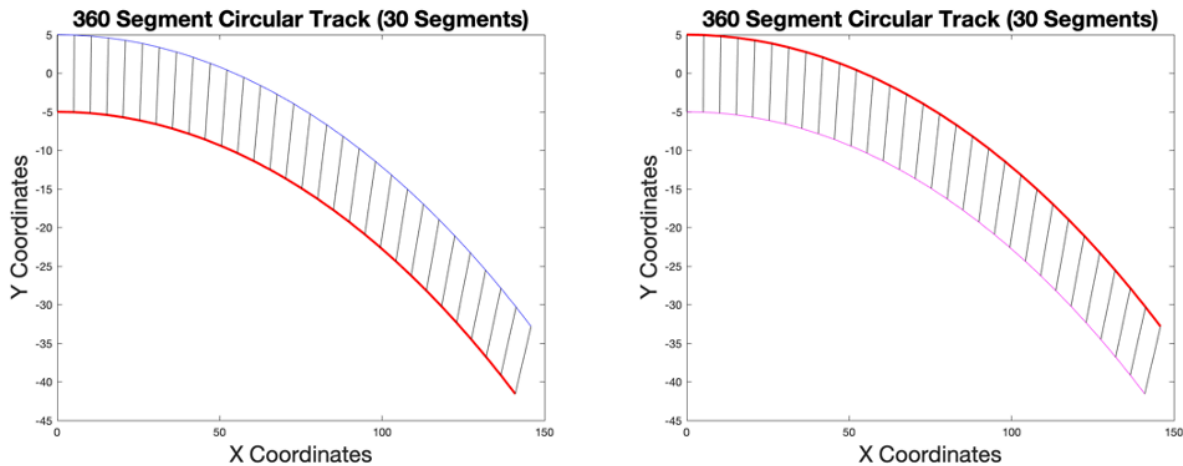


Figure 6.23 30 segments of a 360 segments (total) circular circuit. Inside and outside trajectory (red line) returning a curvature of 0.0034421 and 0.003333 respectively.

With the inner and outer curvature established as accurate, the SOPSO was set to minimise the curvature with $\alpha = \text{rand}$, for 50 iterations and a population of 200. The minimum best cost was located at iteration 42, with a best cost of 0.008637. The circular track although perfect for analysing inner and outer curvature as mathematically it can be calculated with ease, it is not ideal for minimum curvature as the trajectory will always be attempting to straighten up (tend to infinity), but the constant radius effects the results. Again, it is apparent segment size influences the results significantly.

Using a 360-segment track but minimising the SOPSO to 30 segments of that track, the trajectory as can be seen from Figure 6.24 is attempting to straighten as much as possible, tending curvature

to infinity. It is possible to see from the trajectory in Figure 6.24 that the curvature is larger than the outside path as the trajectory has sections of the straight lines (lower curvature) but section of higher radius therefore skewing the result. It is inevitable from these results that the PSO once again has a tendency to struggle with large amounts of parameters.

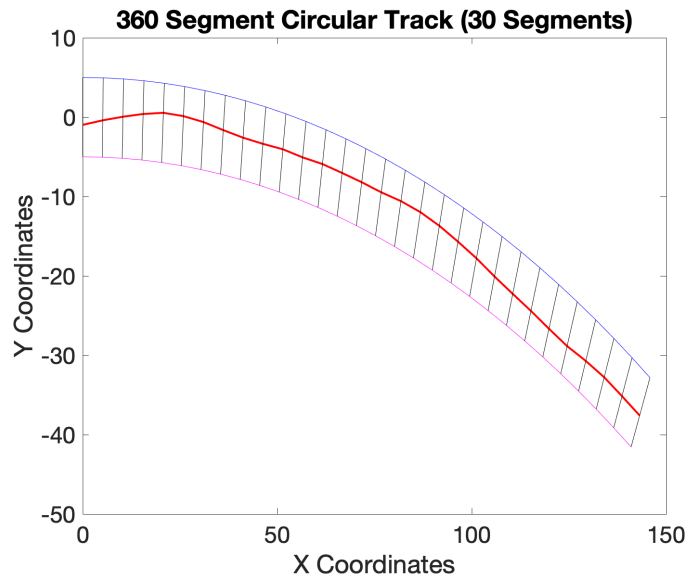


Figure 6.24 Trajectory of 30 segments of a 360-segment circular track. Curvature result of 0.008637.

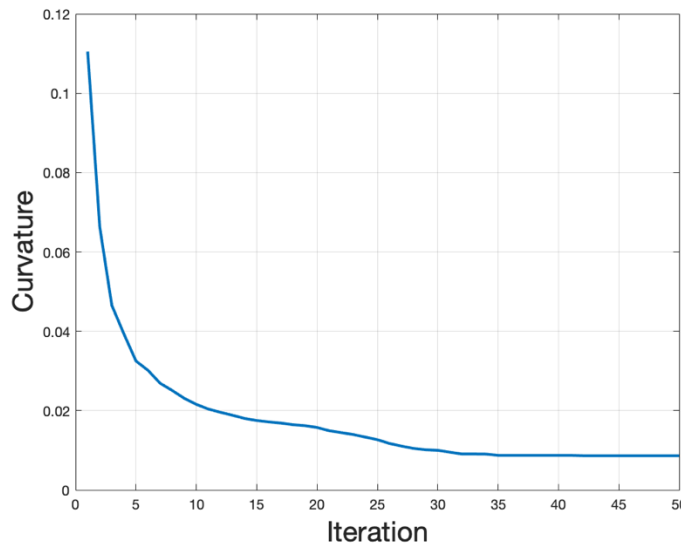


Figure 6.25 Fitness function development across 50 iterations (200 population) of 360 segment circular track. Curvature result of 0.008637.

6.8.1 – Minimum Curvature of Silverstone GP

Utilising a 30-segment sector to minimise the parameters required for SOPSO show a very good return on the trajectory as listed in Table 6.5. Figures 6.27 and 6.26 show all sectors of the circuit without any use of spline manipulation of the results as suggested is required in the literature [96]. The minimum curvature results are more analogous to that of what is expected as the ‘racing line’ as opposed to the shortest path results whereby in the case of shortest path a vehicle would need to slow dramatically to follow a tighter curve.

It is possible to see once again that some sections start, and end points vary from those that precede or follow that segment. This suggests that MOPSO may be a preferred way to run all segments in parallel or to include an initial condition for alpha so that the consecutive segments start with the final alpha of the preceding segment.

Table 6.5 SOPSO curvature result, iteration number at best result, number of variables (segments), sector number, outside and inside path curvature and run time for each section of the Silverstone GP circuit.

Minimum Curvature SOPSO Results						
Test	Curvature	iteration	nVar	Sector	Out/In Curvature	Run Time(m)
3	0.026741	40	30	1	0.0328/0.029	15.77
4	0.072307	39	30	2	0.10052/0.10865	15.68
5	0.024006	40	30	3	0.026/0.03	15.74
6	0.046769	38	30	4	0.047571/0.059665	15.83
7	0.063945	39	30	5	0.076374/0.059178	15.58
8	0.0066796	41	30	6	0.014624/0.013447	15.63
9	0.016251	40	30	7	0.026/0.023	15.20
10	0.033624	33	30	8	0.045092/0.043364	15.75
11	0.019228	36	30	9	0.021705/0.020473	15.63
12	0.011359	42	30	10	0.016956/0.015654	15.63
13	0.02682	34	30	11	0.037863/0.032885	15.80
14	0.050482	43	30	12	0.074516/0.061866	15.79

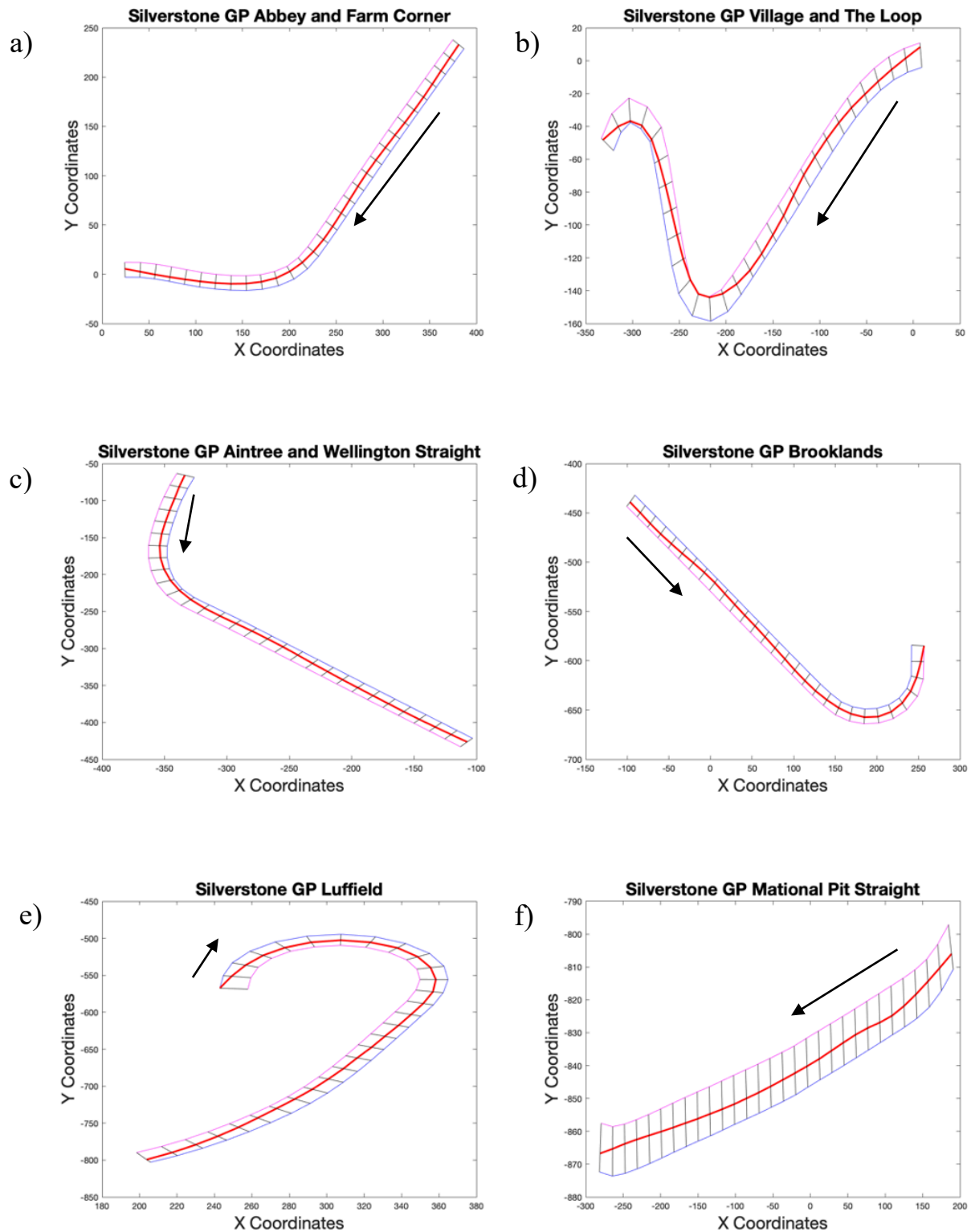


Figure 6.26 Minimum curvature trajectory (red line) with 50 segmentation sectors of the Silverstone GP circuit. From a) the start/finish line and Abbey corner to f) Copse corner, (the black arrow depicts direction of travel).

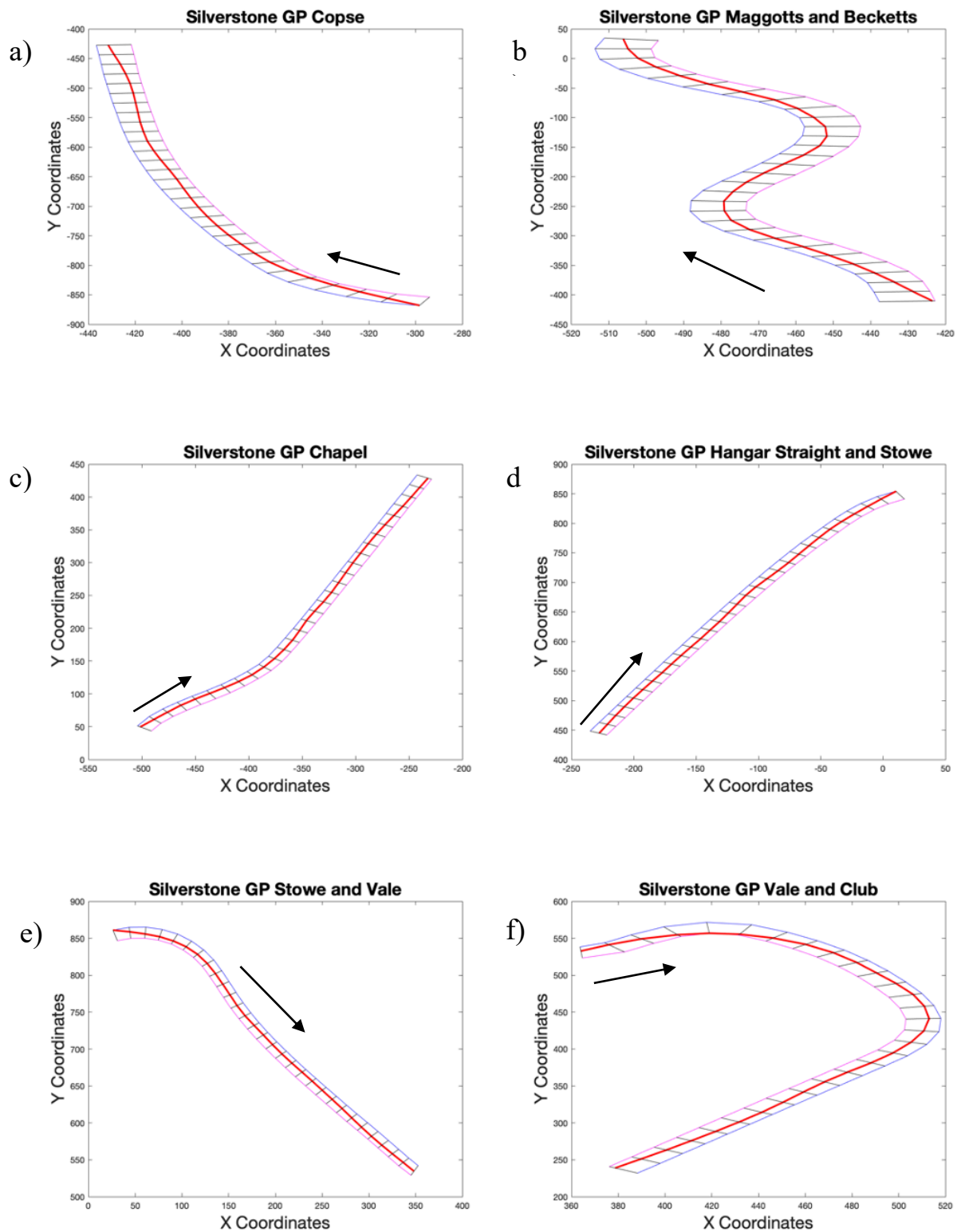


Figure 6.27 Minimum curvature trajectory (red line) with 30 segmentation sectors of the Silverstone GP circuit. a) Copse corner back to f) the start/finish line, (the black arrow depicts direction of travel).

Finally, as a comparison to the shortest path results, a full circuit, a 360-segment optimisation was carried out with the simulation criteria set to 50 iterations and a 200 population (Table 6.6, Test 15) followed by 50 iterations and an 800 population (Test 16).

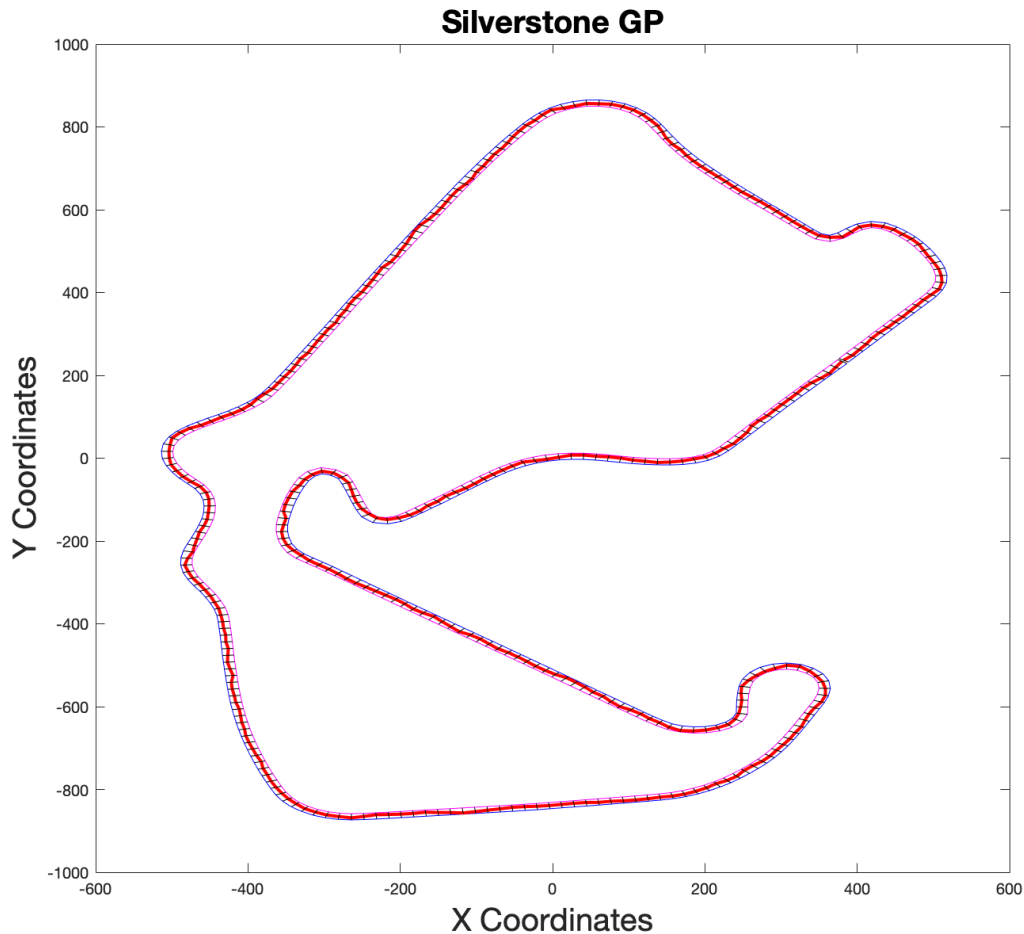


Figure 6.28 Minimum curvature trajectory (red line) with 1 by 360 segmentation sector of the Silverstone GP circuit. SOPSO set to 50 iterations, 200 particles.

The full lap optimisation fares much better than of that for shortest path, with regards to expected trajectory plot, however, during the 200 particles experiment the straight aways tend to have an erratic response instead of a straight line where curvature should tend to infinity. This is also visible in the 12 x 30 sector tests, Figure 6.26, National Pit Straight and Figure 6.27, Hangar Straight for instance. However, it is much more pronounced over the full lap simulation.

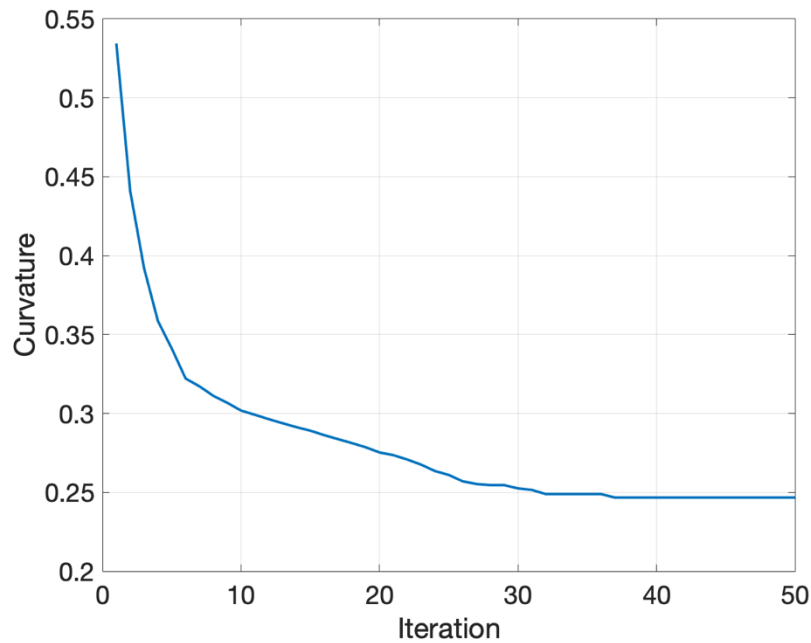


Figure 6.29 Minimum curvature fitness function versus iteration number (Test 15) with 1 by 360 segmentation sector of the Silverstone GP circuit. SOPSO set to 50 iterations, 200 particles.

To ensure consistency with the test steps of shortest path SOPSO, the particles count was increased to 800 and this increase almost eradicated the issue except in the straight prior to Maggotts and Becketts (similar to that in 12 x 30 sector tests), and along Hangar straight. This was totally eradicated in the 12 x 30 sector tests. All fitness functions from the 12 x 30 segment tests returned a result lower than the inside or outside trajectory curvature, as expected, since the optimisation should find a straighter path than that of just the outside or inside line. In the case of full lap optimisation as per Table 6.6 the fitness function did not find the minimum curvature from the outside or inside path.

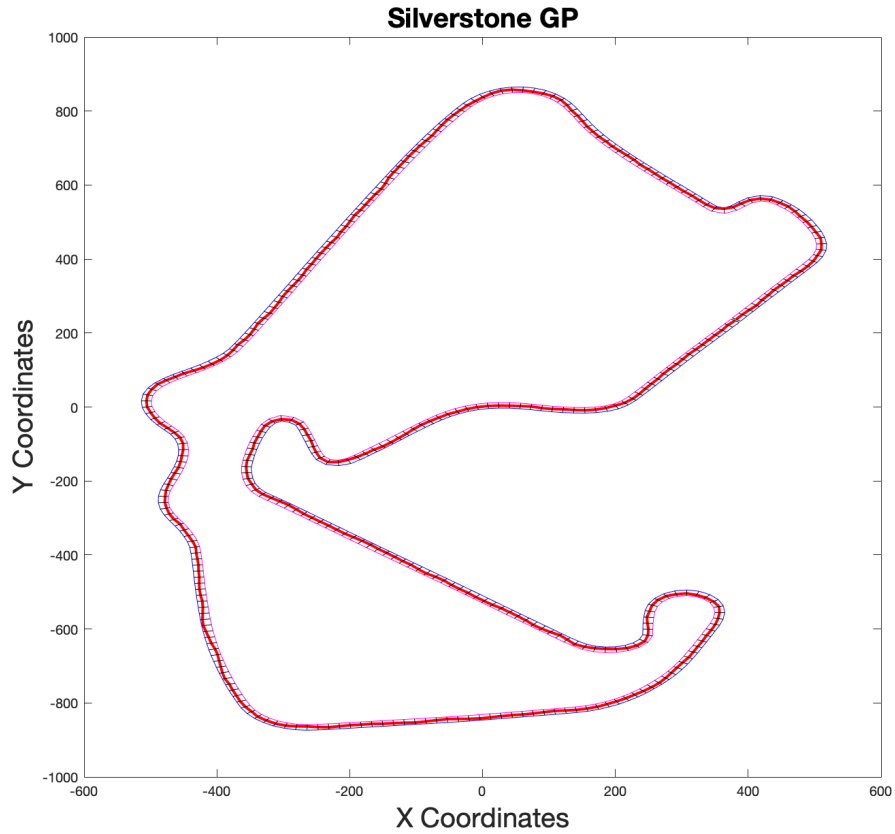


Figure 6.30 Minimum curvature trajectory (red line) with 1 by 360 segmentation sector of the Silverstone GP circuit. SOPSO set to 50 iterations, 800 particles.

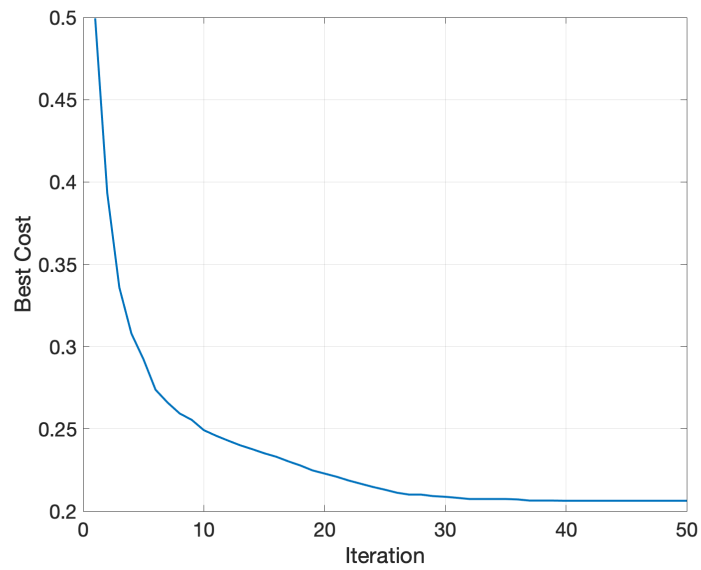


Figure 6.31 Minimum curvature fitness function vs iteration number (Test 16) with 1 by 360 segmentation sector of the Silverstone GP circuit. SOPSO set to 50 iterations, 800 particles.

Table 6.6 SOPSO curvature result, iteration number at best fitness function, number of variables (segments), sector number, outside and inside path curvature and run time for a full lap of the Silverstone GP circuit.

Minimum Curvature SOPSO Results						
Test	Curvature	Iteration	nVar	Sector	Out/In Curvature	Run Time(m)
15	0.2467	37	360	All	0.18681/0.18895	24.84
16	0.20634	40	360	All	0.18681/0.18895	108.61

6.9 Multi Objective PSO

Using a multi-objective algorithm, the simulation can be set to test several objectives simultaneously. The MOPSO can be used to optimise all twelve sectors at once, to determine the pareto front and therefore best trajectories as a trade-off between shortest path and minimum curvature, and also to include further optimisation outputs such as minimum best lap time, vehicle dynamic performance and energy management of a hybrid system. As is the case in Chapter 5, MOPSO does not necessarily save much time in simulation processing and therefore the determined appropriate first instance of using MOPSO would be to compare shortest path against minimum curvature for individual sectors rather than testing all sectors simultaneously for shortest path or minimum curvature.

The optimisation algorithm is set to find the best cost for both of the two conflicting fitness function parameters; shortest path (most likely the highest curvature and smallest radius around a corner) and minimum curvature (a longer but straighter path around a corner) and compare these results along a pareto front.

6.9.1 MOPSO vs SOPSO Results

With the MOPSO algorithm set for trajectory a true minimum curvature or shortest path trajectory cannot be found but a compromise between the two. The nature of a MOPSO means that inevitably there are iterations where minimum curvature or shortest path dominates. The overall fitness functions of each iteration where both results cannot be dominated yields a pareto front

curve as shown in Figure 6.32. All results in this figure are ranked as number one in a hierarchy results table.

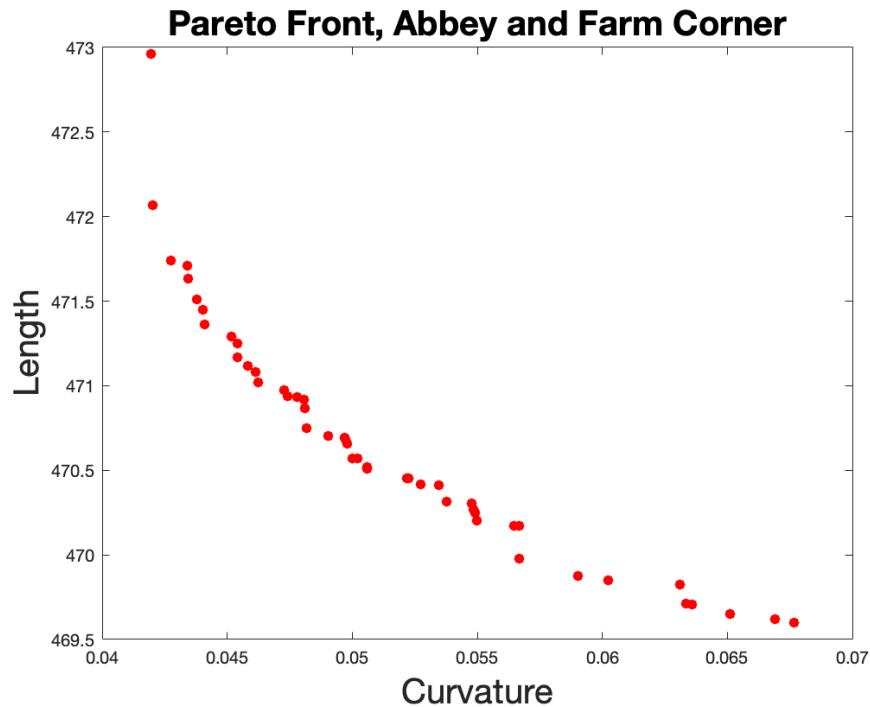


Figure 6.32 MOPSO pareto front for Abbey and Farm corners.

The optimum solution across the pareto front is a compromise between shortest path and least curvature, choosing a trajectory from either the lowest curvature result or shortest path result shows a trajectory curve tending towards that of the SOPSO but as expected the true minimum is never found whilst the conflict exists. A mid pareto point where neither minimum curve nor shortest trajectory is at the lowest found the output in some instance produced a trajectory close to what would be known as the racing line within the Motorsport Industry. The racing line trajectory normally follows a path closer to minimum curvature, but it can also be of a path that resembles that of shortest path, minimum curvature or of a compromise between the two, dependant on vehicle dynamic ability and extracting the maximum performance from the tyre, which ultimately will determine lap time as detailed in Sections 6.9 to 6.11

Table 6.7 details each individual 30-segement sector and shows the resulting minimum curvature and shortest path results for the Best Minimum Curvature, Best Shortest Path and a Mid Pareto

point, the individual Best minimum Curvature and Best shortest path results are also included from the SOPSO as a comparison.

Table 6.7 MOPSO and SOPSO results including minimum curvature result and shortest path result for best minimum curvature, best shortest path and mid-pareto point.

Sector	Best Minimum Curve	Best Shortest Path	Mid Pareto	SOPSO Results	MOPSO Run Time (m)
Results = Minimum Curvature, Shortest Path					
1	0.0419, 472.96	0.0676, 469.59	0.0500, 470.57	0.0267, 465.66	20.55
2	0.1077, 470.46	0.1694, 447.11	0.1343, 456.76	0.0723, 437.87	20.99
3	0.0468, 472.61	0.0724, 468.44	0.0585, 470.26	0.0240, 465.49	20.45
4	0.0736, 469.52	0.0958, 461.65	0.0823, 464.69	0.0467, 457.13	20.43
5	0.1080, 462.28	0.1200, 456.05	0.112, 457.92	0.0639, 441.81	20.51
6	0.0180, 472.78	0.0274, 472.57	0.0217, 472.60	0.0066, 470.73	20.39
7	0.0384, 471.39	0.0603, 468.44	0.0453, 469.63	0.0162, 465.84	18.68
8	0.0840, 467.41	0.1028, 462.79	0.0919, 464.53	0.0336, 456.81	18.77
9	0.0384, 471.15	0.0595, 470.26	0.0406, 470.58	0.0192, 468.94	18.77
10	0.0303, 471.66	0.0428, 471.23	0.0325, 471.37	0.0113, 469.71	18.86
11	0.0459, 470.54	0.0674, 466.93	0.0522, 468.05	0.0268, 462.26	18.85
12	0.0749, 473.48	0.1280, 460.64	0.0973, 464.68	0.0505, 451.62	19.19

The values of minimum curvature and shortest path show that the two paths are in conflict, as minimum curvature decreases, shortest path increases, allowing for a reasonable sized pareto front and several options for analysis of best path. The numerical size variation of minimum curvature to shortest path, ($1e-02$ Minimum Curvature result as opposed to the shortest path numerical result of $1e+02$) show that the error between the best result within the MOPSO when compared to the best result of the SOPSO results in a larger percentage for minimum curvature trajectory.

Table 6.8 Error of MOPSO results versus SOPSO results. Best minimum curvature and best shortest path.

Sector	Minimum Curvature			Shortest Path		
	MOPSO	SOPSO	% Error	MOPSO	SOPSO	% Error
1	0.0419	0.0267	56.93%	469.59	465.66	0.84%
2	0.1077	0.0723	48.96%	447.11	437.87	2.11%
3	0.0468	0.024	95.00%	468.44	465.49	0.63%
4	0.0736	0.0467	57.60%	461.65	457.13	0.99%
5	0.108	0.0639	69.01%	456.05	441.81	3.22%
6	0.018	0.0066	172.73%	472.57	470.73	0.39%
7	0.0384	0.0162	137.04%	468.44	465.84	0.56%
8	0.084	0.0336	150.00%	462.79	456.81	1.31%
9	0.0384	0.0192	100.00%	470.26	468.94	0.28%
10	0.0303	0.0113	168.14%	471.23	469.71	0.32%
11	0.0459	0.0268	71.27%	466.93	462.26	1.01%
12	0.0749	0.0505	48.32%	460.64	451.62	2.00%

Sector	Minimum Curvature			Shortest Path		
	MOPSO	SOPSO	Numerical Error	MOPSO	SOPSO	Numerical Error
1	0.0419	0.0267	0.0152	469.59	465.66	3.9300
2	0.1077	0.0723	0.0354	447.11	437.87	9.2400
3	0.0468	0.024	0.0228	468.44	465.49	2.9500
4	0.0736	0.0467	0.0269	461.65	457.13	4.5200
5	0.108	0.0639	0.0441	456.05	441.81	14.2400
6	0.018	0.0066	0.0114	472.57	470.73	1.8400
7	0.0384	0.0162	0.0222	468.44	465.84	2.6000
8	0.084	0.0336	0.0504	462.79	456.81	5.9800
9	0.0384	0.0192	0.0192	470.26	468.94	1.3200
10	0.0303	0.0113	0.0190	471.23	469.71	1.5200
11	0.0459	0.0268	0.0191	466.93	462.26	4.6700
12	0.0749	0.0505	0.0244	460.64	451.62	9.0200

The numerical error of course is much smaller for minimum curvature. The resultant fitness function results are therefore not just the only means of scrutiny and the trajectory paths must be plotted.

Based on trajectory plots, the error is not as unacceptable as first appears, when comparing trajectories to those from the SOPSO simulations both trajectories are a compromise between the two output functions (Figure 6.33 – 6.34). All Pareto front and vehicle trajectories for MOPSO

versus SOPSO can be found in Appendix 6. Whereby the middle pareto point is chosen and compared to the best minimum curvature result and best shortest path results from the MOPSO.

In some instances, as per Sector 8, shown in Figure 6.34, the MOPSO best minimum curvature trajectory from the Pareto front is closer to that of the SOPSO minimum curvature. The MOPSO best shortest path from the pareto front does not follow the true shortest path and is worse off than that of the shortest path SOPSO, even though a 150% error is calculated for MOPSO minimum curvature as opposed to 1.31%. For this reason, visual analysis has to be included in the result conclusion.

It is also paramount to conclude that although the MOPSO is working effectively and finding a compromise a lap time should be optimised to find the ideal line. With the inclusion of lap time, vehicle dynamic behaviour and thus vehicle speed and lateral and longitudinal accelerations should be modelled.

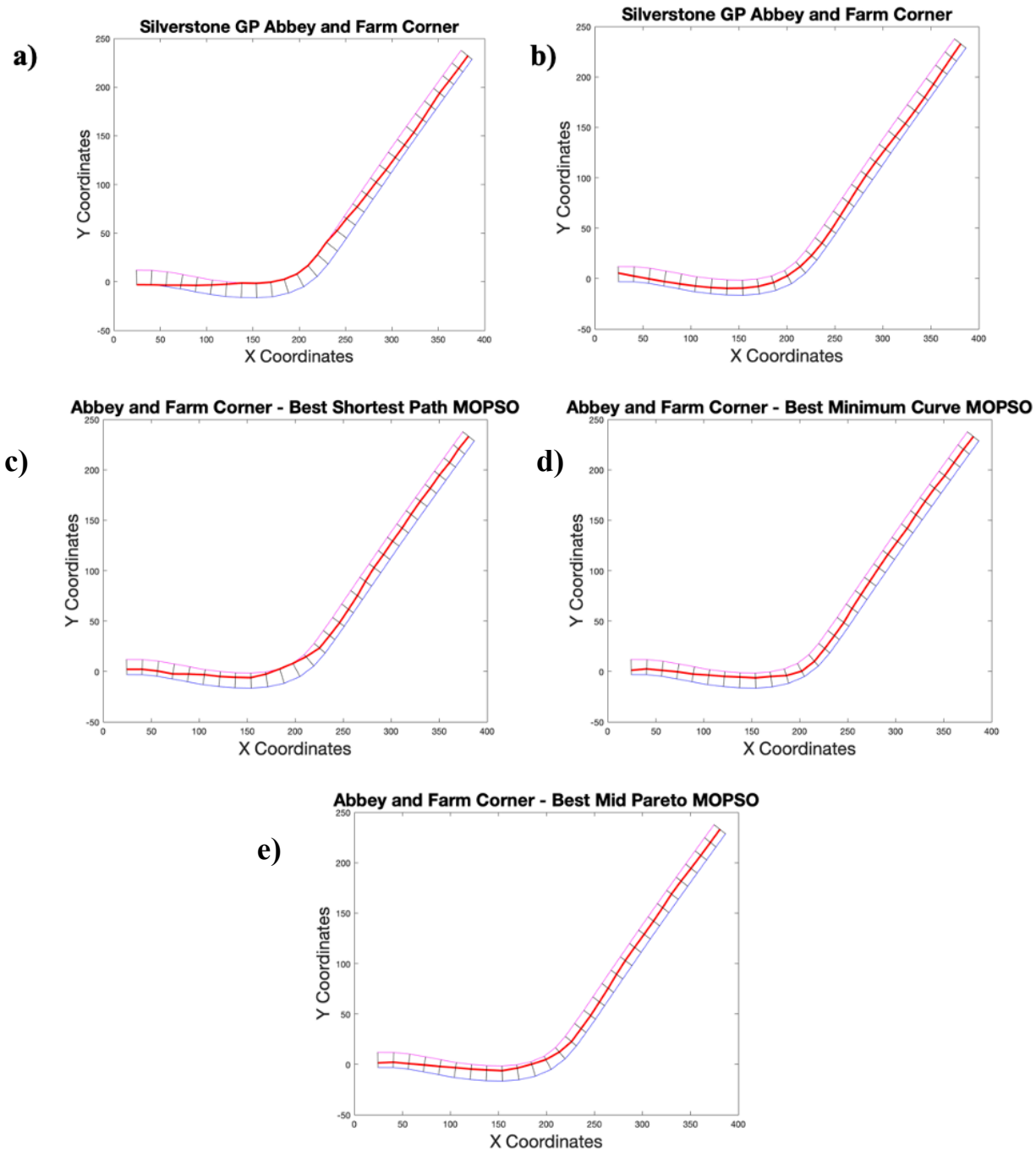


Figure 6.33 a) SOPSO shortest path and b) SOPSO minimum curvature trajectory comparison with c) MOPSO best shortest path trajectory result, d) MOPSO best minimum curvature result and e) mid-pareto trajectory result for Sector 1.

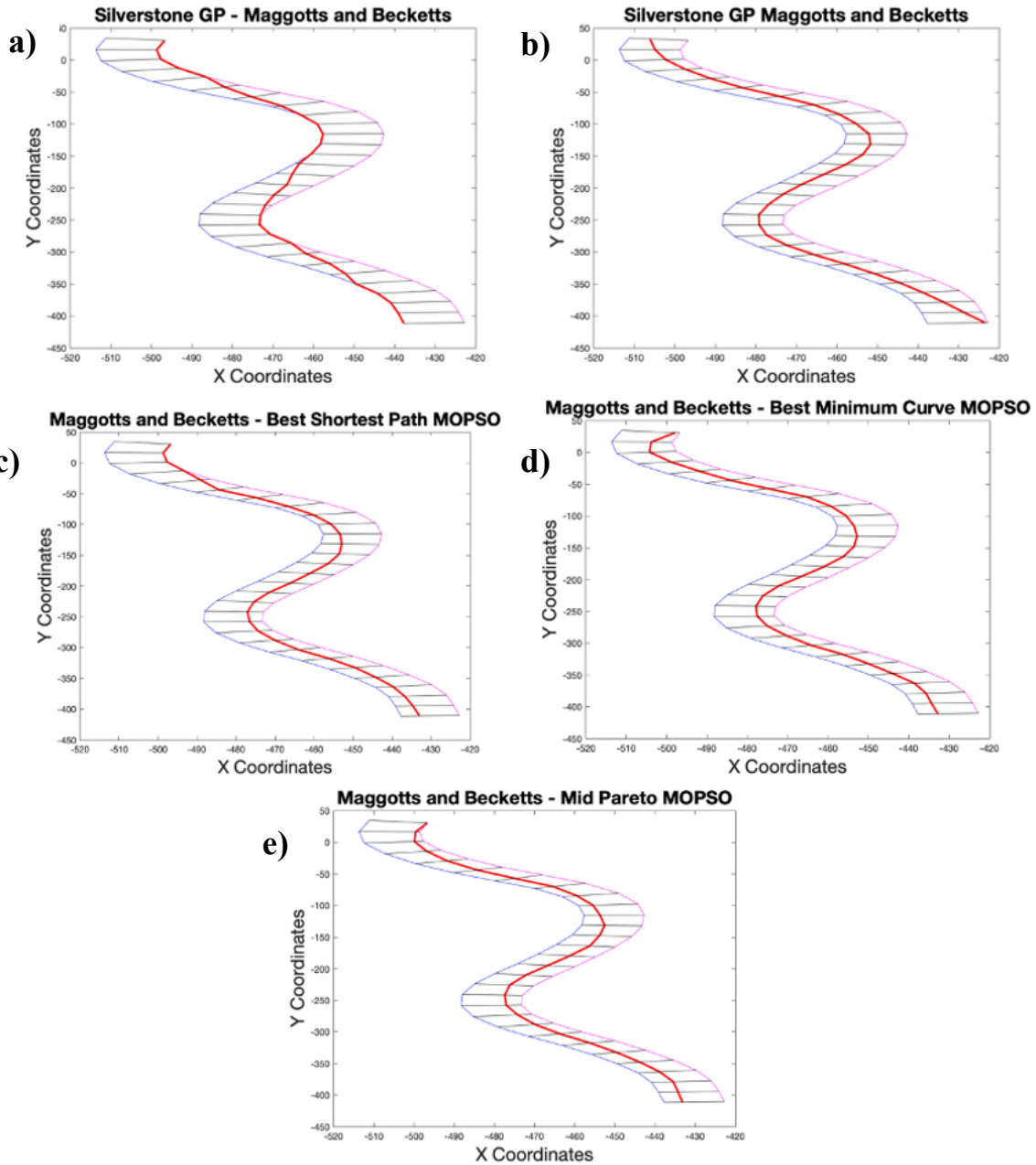


Figure 6.34 a) SOPSO shortest path and b) SOPSO minimum curvature trajectory comparison with c) MOPSO best shortest path trajectory result, d) MOPSO best minimum curvature result and e) mid-pareto trajectory result for Sector 8.

6.10 Dynamic Constraints

The next stage is to define mechanical grip limits for the race vehicle. Although the tyre determines the maximum grip levels in a longitudinal and lateral direction, the lateral maximum G-Forces are used as per [92, 96]. However further in this study a concept GT Hybrid vehicle will be introduced, and so maximum longitudinal dynamics cannot be utilised once the Hybrid model is incorporated, as maximum acceleration may not always be available dependant on battery charge and use of the motor. This ensures this work differs from other published material by incorporating the dynamic model from Chapter 3. Maximum deceleration is modelled as per the vehicle dynamic ability and assumed that regeneration is occurring in all instances within the Hybrid model; where additional braking force (above the regeneration capabilities) is required, it is assumed the hydraulic brake fulfils the discrepancy between motor regeneration capabilities and maximum braking ability.

Firstly, prior to including the dynamic model for optimisation of a Hybrid model, vehicle constraints are included into the MOPSO via the validated GT model from the Particle Swarm Optimisation model in Chapter 5. The vehicle dynamic model is set to sweep through the full range of steering angles physically permissible by the car and so simulations were carried out whereby the steering is slowly increased at a specific longitudinal speed. This is then repeated over several speeds that represent the minimum and maximum corner speeds (20 – 65 m/s) as observed from the measured data of a flying lap of the Silverstone GP circuit. This results in a surface plot from the two inputs imposed on the model; steering angle and longitudinal velocity and the calculated output; lateral acceleration. (Figure 6.35 – 6.36).

A +/- 10 % speed range was also included above and below the original physical vehicle measured data to allow slower and faster corner speeds to be optimised and finally the results from the test were smoothed to eradicate anomalies. The longitudinal velocity and steering angle (at the wheels) vs lateral acceleration are then plotted in Figures 6.37 and 6.38. This data is discretised and interpolated into finer increments to the magnitude of velocity = [0: 0.1: 70], steering = [-0.1745: 0.001: 0.1745] with lateral velocity interpolated between all points.

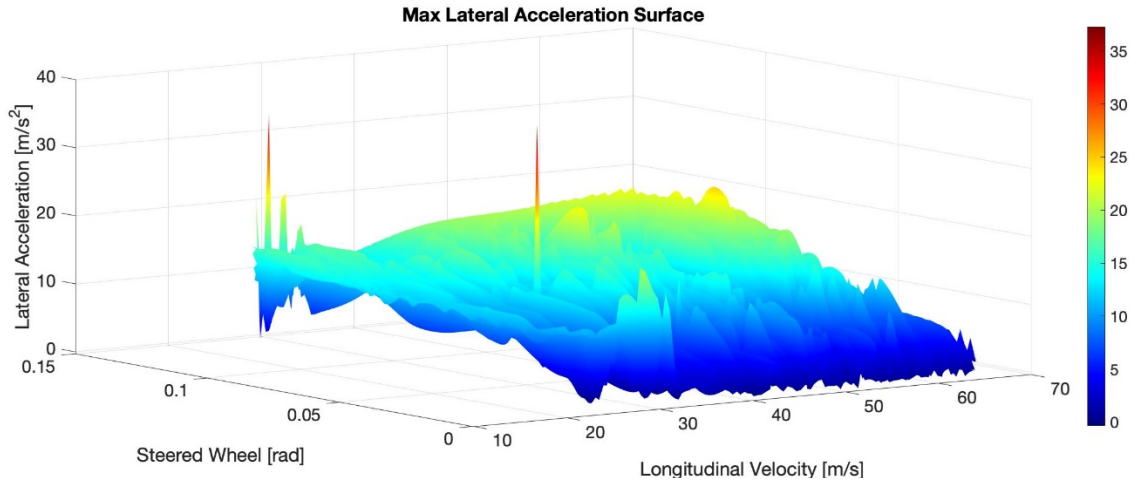


Figure 6.35 Velocity(m/s) vs steering angle (rad), at the wheels, vs lateral acceleration (m/s²).

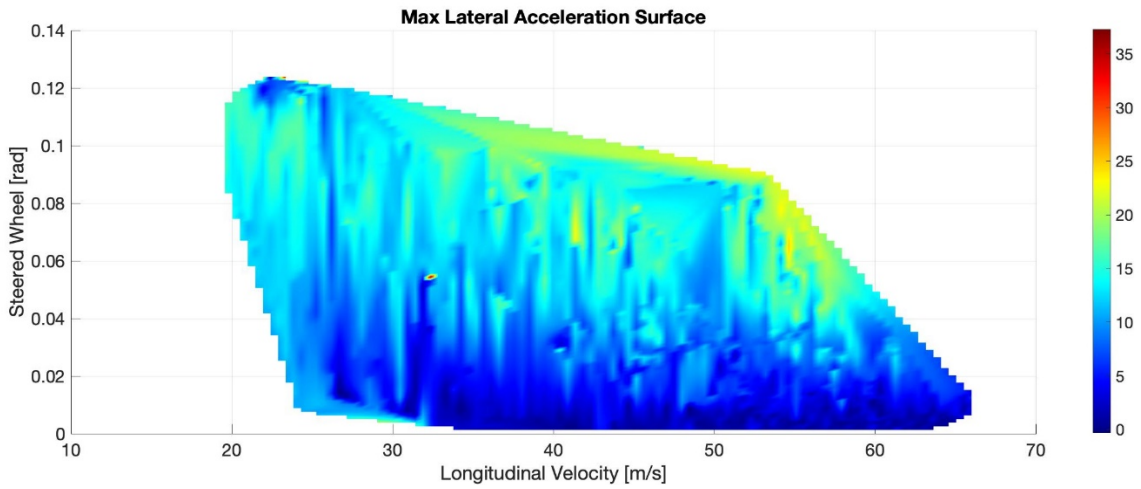


Figure 6.36 Plan view of velocity(m/s) vs steering angle (rad), at the wheels, vs lateral acceleration (m/s²).

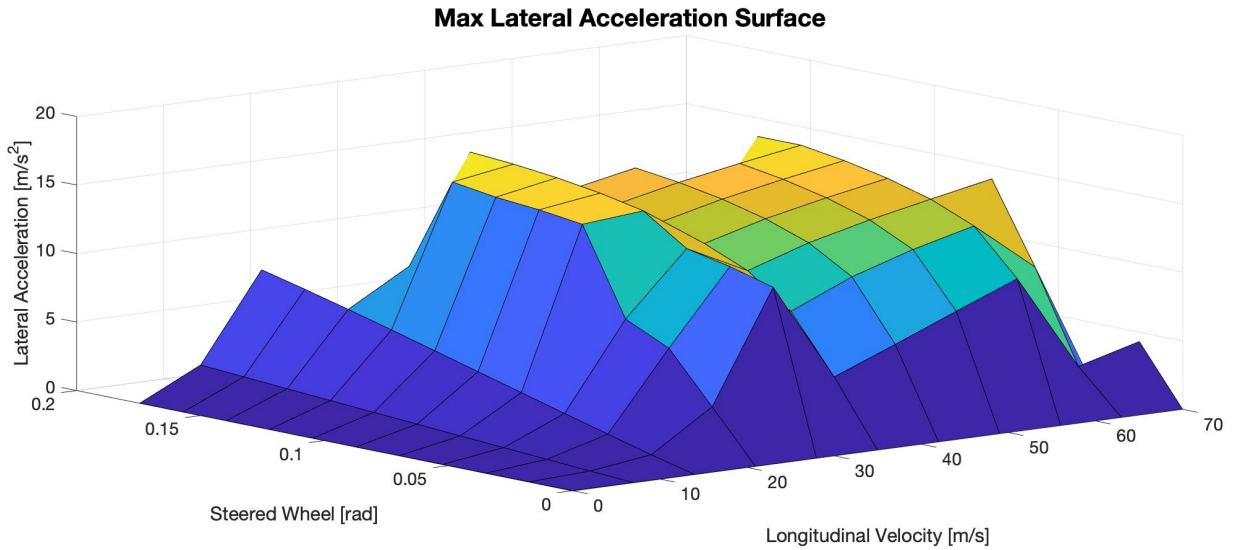


Figure 6.37 Velocity(m/s) vs steering angle (rad), at the wheels, vs lateral acceleration (m/s^2) smoothed data.

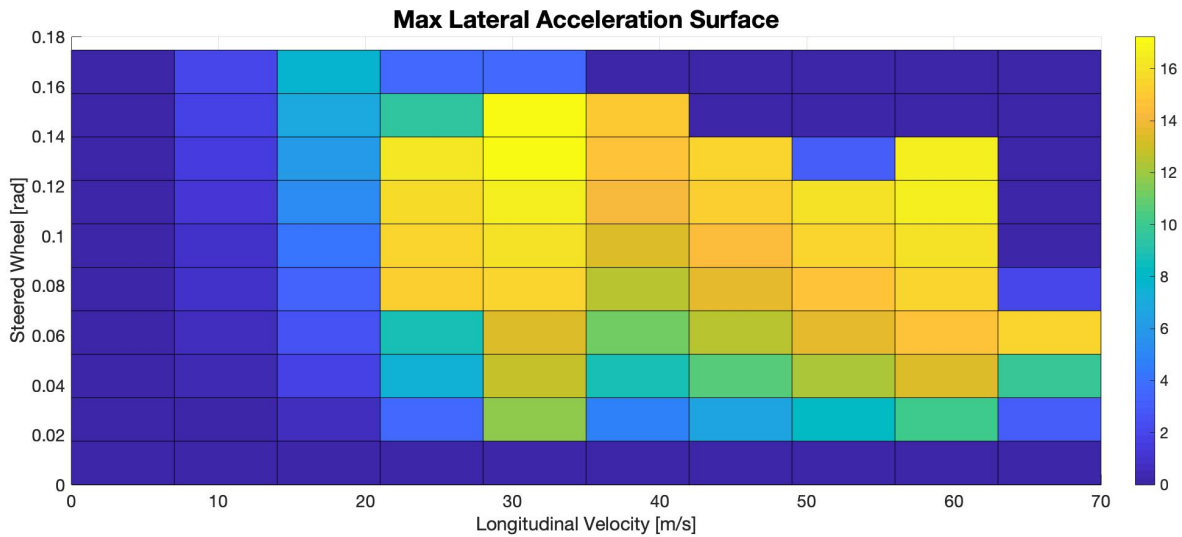


Figure 6.38 Plan view of velocity(m/s) vs steering angle (rad), at the wheels, vs lateral acceleration (m/s^2).

The dynamic model as described in chapters three, four and five are also utilised to determine the maximum acceleration and deceleration to and from maximum velocity, whereby $V_{max} = 70m/s$ due to transmission and final drive gearing and aerodynamic drag of the vehicle. Data from the measured race vehicle again only extends to a maximum of 65m/s due to acceleration and track

constraints and has the lowest speed of 20m/s, since the vehicle never arrives at a complete stop on circuit unless in the pit lane whereby maximum deceleration is not utilised. Therefore, the validated dynamic model was simulated to accelerate from 0 – 70m/s as plotted in Figure 6.39, and then decelerate as fast as possible as can be seen from Figure 6.40. This data is transposed into a look up table within the vehicle dynamic constraints parameter for the trajectory MOPSO. The maximum acceleration parameter was set within the trajectory model for all speeds greater than 70 m/s so that acceleration = 0 m/s², therefore restricting the top speed of the vehicle to 70 m/s as per the actual race vehicle.

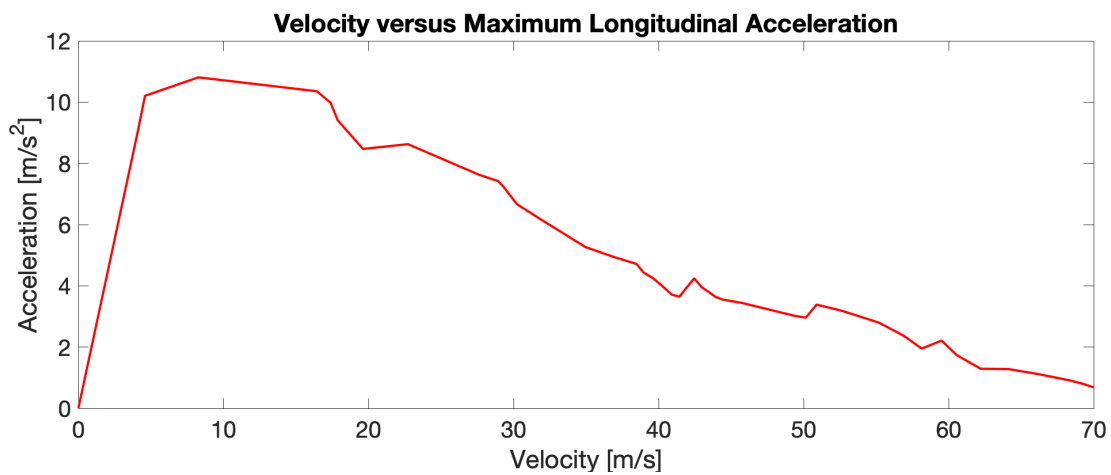


Figure 6.39 Maximum acceleration from 0 to 70 m/s with zero radians of steering through all 6 gears.

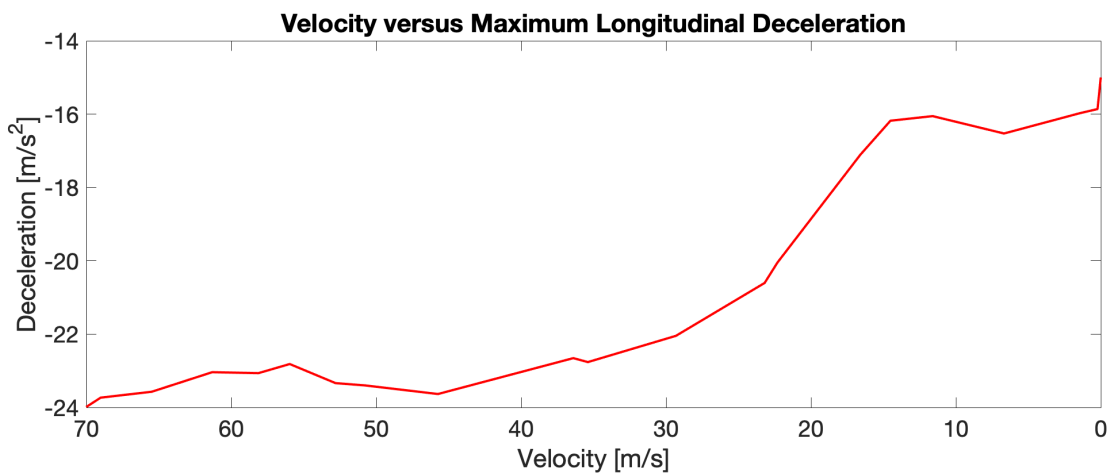


Figure 6.40 Maximum deceleration from 70 to 0 m/s with zero radians of steering.

6.11 Optimum Trajectory and Lap Time

The problem posed for fastest lap time is via a hierarchical order ultimately based on the vehicle dynamic behaviour and the peak operating range of the vehicle and powertrain. The vehicle dynamic operating range is explored to locate minimisation of the curvature or minimisation of the length of the trajectory. An optimisation algorithm must be identified to satisfy these two conflicting objectives whilst optimising the vehicle dynamic behaviour for lap time reduction.

As proposed earlier the ideal trajectory for best lap time lies somewhere between shortest path and the minimum curvature trajectories determined also by the vehicle dynamic constraints allowing for tyre grip (traction circle), available power and aerodynamic efficiency. Therefore, the optimum MOPSO solution for a track segment is:

$$\min_{i=1:n} [\Gamma, L, LT] \quad (6.36)$$

where lap-time is calculated from (6.37) and $h(i)$ is the distance of the trajectory path for a segment

$$\sum_{i=0}^n h(i)/vx(i) \quad (6.37)$$

An optimum lap time around the Silverstone circuit for a GT3 car is currently circa 1.59.50 (m.s.ms) in qualifying trim and 2.01.40 in race trim (with fuel) for professional gold standard drivers [101] and a 2.02.50 (qualifying trim) to 2.04.00 (race trim) for amateur drivers [102]. As discussed previously the optimum trajectory and therefore ideal lap time lies somewhere between the least curvature and shortest path and is determined by the vehicle dynamic limitations. The measured data as detailed in Chapter 5 and utilised for the dynamic constraints modelling is taken from a 2011 GTE car with lower power than the latest GT3 cars and less aerodynamic force. The Evora GTE in low weight qualifying trim (low fuel) can circulate Silverstone GP in 2.05.143 and in Race Trim, a fastest lap of 2.08.626 with a slowest race trim lap of 2.09.502 [103].

6.11.1 Shortest Path MOPSO including Dynamic Constraints

Initially for comparison analysis, MOPSO optimisation simulations were conducted to understand the lap time output against shortest path and minimum curvature trajectories individually with the addition of the vehicle dynamic constraints. The SOPSO as per Section 6.6 and 6.7 is modified to optimise for a specific trajectory path but are now also optimising Lap time and constrained within each sector by maximum steering and accelerations as shown in Figures 6.37 to 6.40.

For the shortest path trajectory as the vehicle is negotiating low radius corners so as to follow the inner radii of any given corner the speed is reduced and therefore lap time is increased. Nevertheless, at the same time accelerations and thus velocities are attempting to maximise so as to decrease lap time. The ideal shortest path trajectory result returned a length of 5923.6 with the second fitness function returning a lap time of 2.10.591, however the fastest lap time fitness function returned a time of 2.08.979 with a trajectory length of 5966.5m, 42.9m longer than the shortest length best cost and 1.612 seconds faster (Figure 6.41). As a comparison the SOPSO for shortest path with the same population size and iteration count as detailed in Section 6.6, Table 6.4 returned a best cost result of 5844.48m highlighting that the dynamic constraint is working against the minimum curvature to optimise lap time.

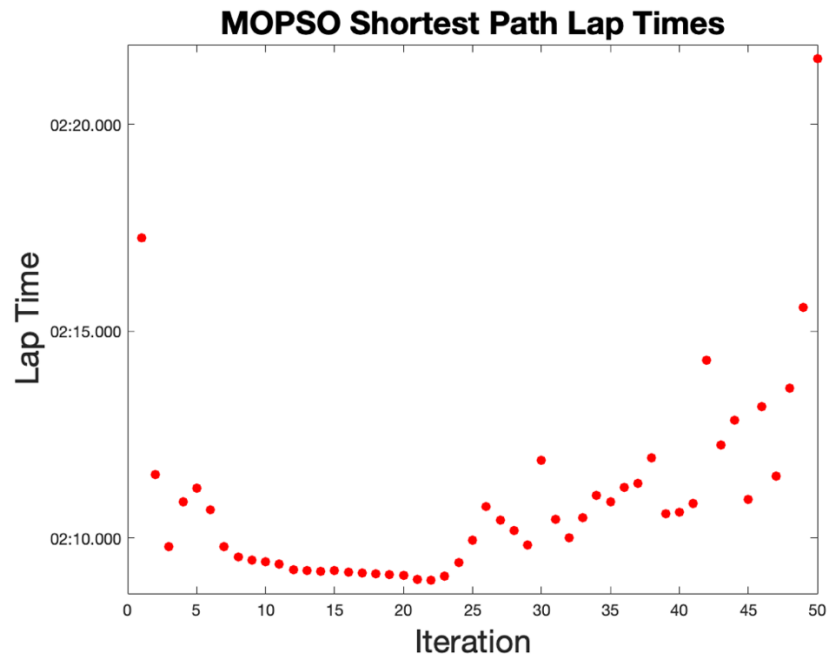


Figure 6.41 Lap time vs iteration for shortest path SOPSO.

Figure 6.41 depicts that the fastest lap generated during the shortest distance SOPSO was recorded at iteration 22 where a length of 5966.5m was recorded suggesting a further distance (and potentially higher curvature) will yield the best lap time whereas the shortest path best cost was recorded at Iteration 39.

As can be seen in Figure 6.42, the vehicle has to slow dramatically for certain corners, less than 20m/s, whereas the measured, simulated and PSO data presented in Chapter 5 never falls below 20m/s. This is much more noticeable through the Luffield Corner (2200m) and the Maggotts and Becketts complex (3500m to 3750m) for the vehicle to maintain the shortest path.

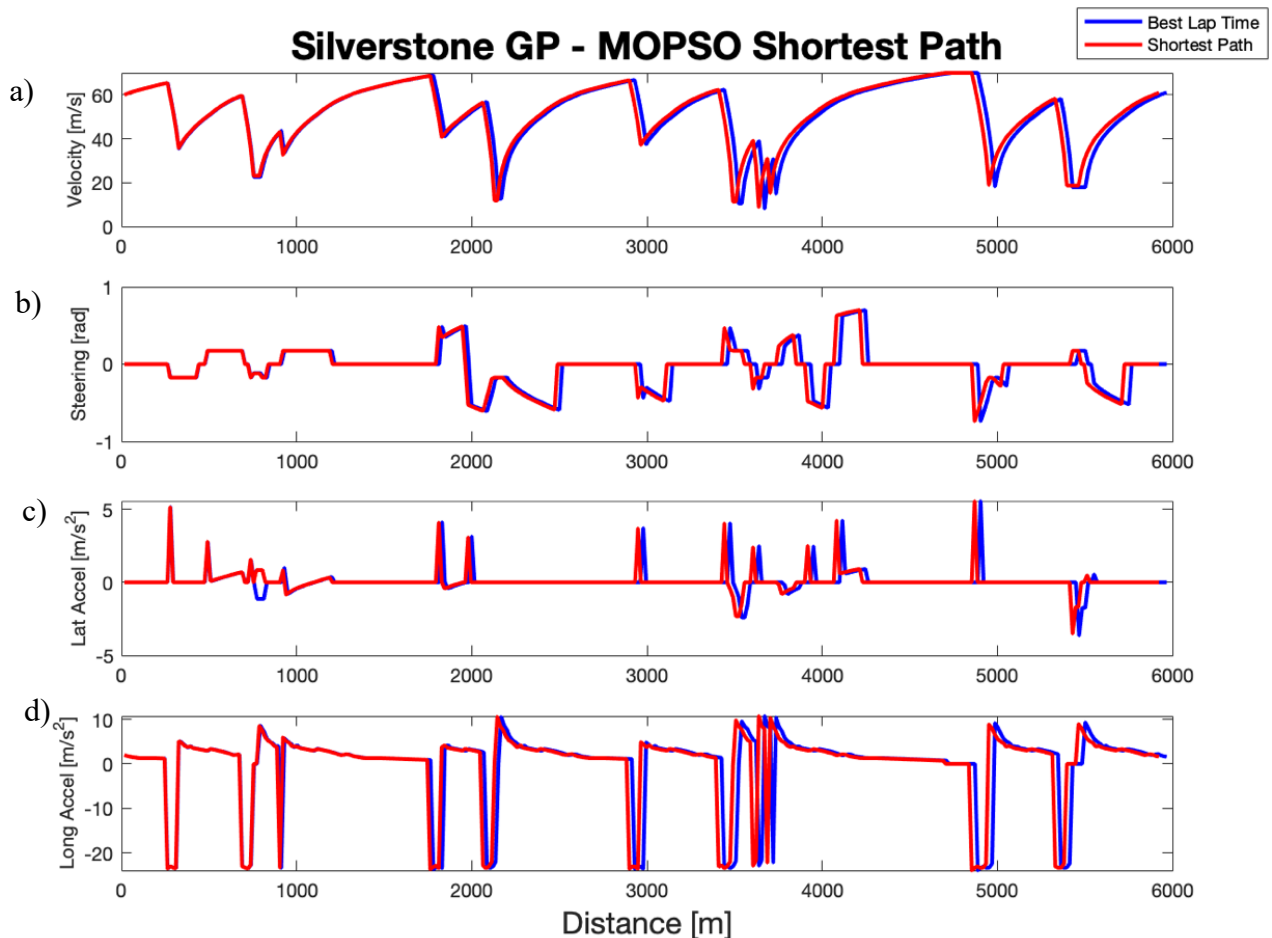


Figure 6.42 The vehicle dynamic output for a) Vehicle velocity, b) steering input, c) lateral acceleration and d) longitudinal acceleration vs distance for an ICE only race vehicle around Silverstone GP circuit (shortest path trajectory). Best lap time (blue line) versus best shortest path length (red line)

The steering angles although very similar occur at different distances into the lap. The peak figures are very similar suggesting the fastest lap is generated by traveling further on a straight before braking and turning into the corner, ensuring higher speeds. Figure 6.43 shows the delta difference between the best lap time and shortest distance plots (Best Shortest Distance Data – Best Lap Time Data), depicted in Figure 6.42 plotted over segments rather than distance to show a comparison within each segment. As can be seen for all straight aways the best lap time vehicle returns a higher velocity, however in some cases the velocity mid corner is lower suggesting the late turn in means the car has to slow down further to make the later apex of the corner.

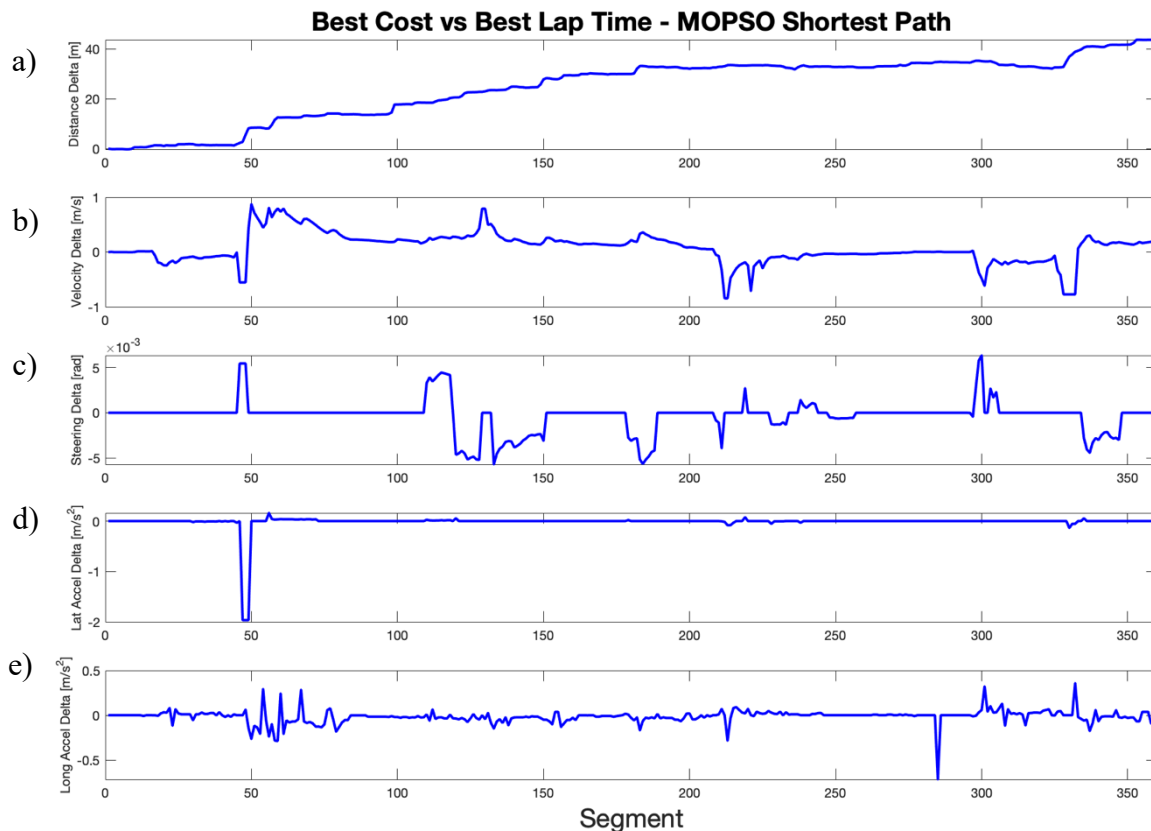


Figure 6.43 a) Distance variation and error variance between best lap fitness function versus trajectory length fitness function for b) vehicle velocity, c) steering input, d) lateral acceleration and e) longitudinal acceleration for an ICE only race vehicle around Silverstone GP.

6.11.2 Minimum Curvature MOPSO with Dynamic Constraints

Within the minimum curvature trajectory, the vehicle should open up the corner and utilise more longitudinal acceleration by reducing lateral acceleration due to the constraints within the traction circle. The minimum curvature trajectory yields a best curvature of 0.357 and returned a lap time of 2.07.551, however, the fastest lap time was a 2.05.592 also with a minimum curvature fitness function (best cost) of 0.363.

The slower lap time generated a total length of 5902.4 whilst the faster lap times total distance travelled was 5956.1. This again shows that the faster lap time travels farthest by 53.7m showing that shortening a distance around a corner has a negative effect on lap time but also the fastest lap was not found with the fitness function of the minimum curvature at the best cost.

Figure 6.44 depicts that the fastest lap generated during the minimum curvature SOPSO falls at iteration 45 where the curvature was higher but the best cost for minimum curvature was found at iteration 34 with a curvature of 0.357 suggesting the distance, as shown in Figure 6.47, has a role to play in lap time also and the fastest lap time is somewhere between minimum curvature and shortest path. This is inevitably ensuring a combined shortest path, minimum curvature and vehicle dynamic MOPSO would be a preferred method to find ultimate lap time.

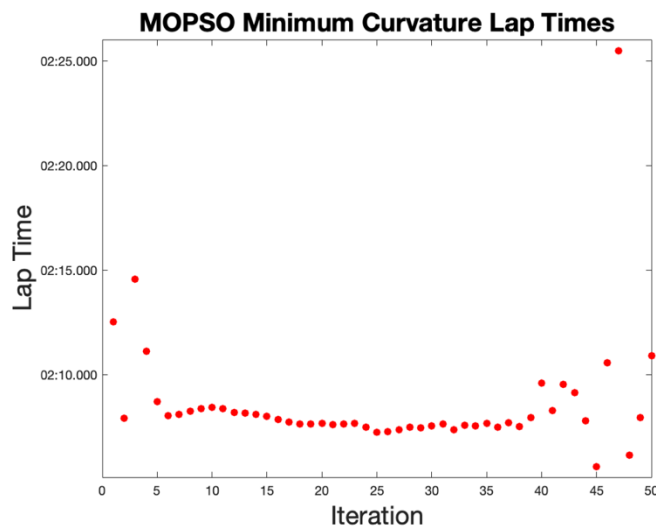


Figure 6.44 Lap time vs iteration for the minimum curvature SOPSO.

Figure 6.45 shows that the vehicle generated a minimum curvature best cost although the steering input during certain corners were higher. This is suggesting a higher curvature, although the steering input is less than those in the shortest path optimisation. This enables a shorter distance but explains that the transition between corners (straight aways) are important also and the path along the straight away can be much shorter if the vehicle does not transition from one side of the track to the other. It is acknowledged that the minimum curvature results found in this study are much higher than that of the SOPSO, and therefore the vehicle dynamic behaviour once again has a dramatic effect on results.

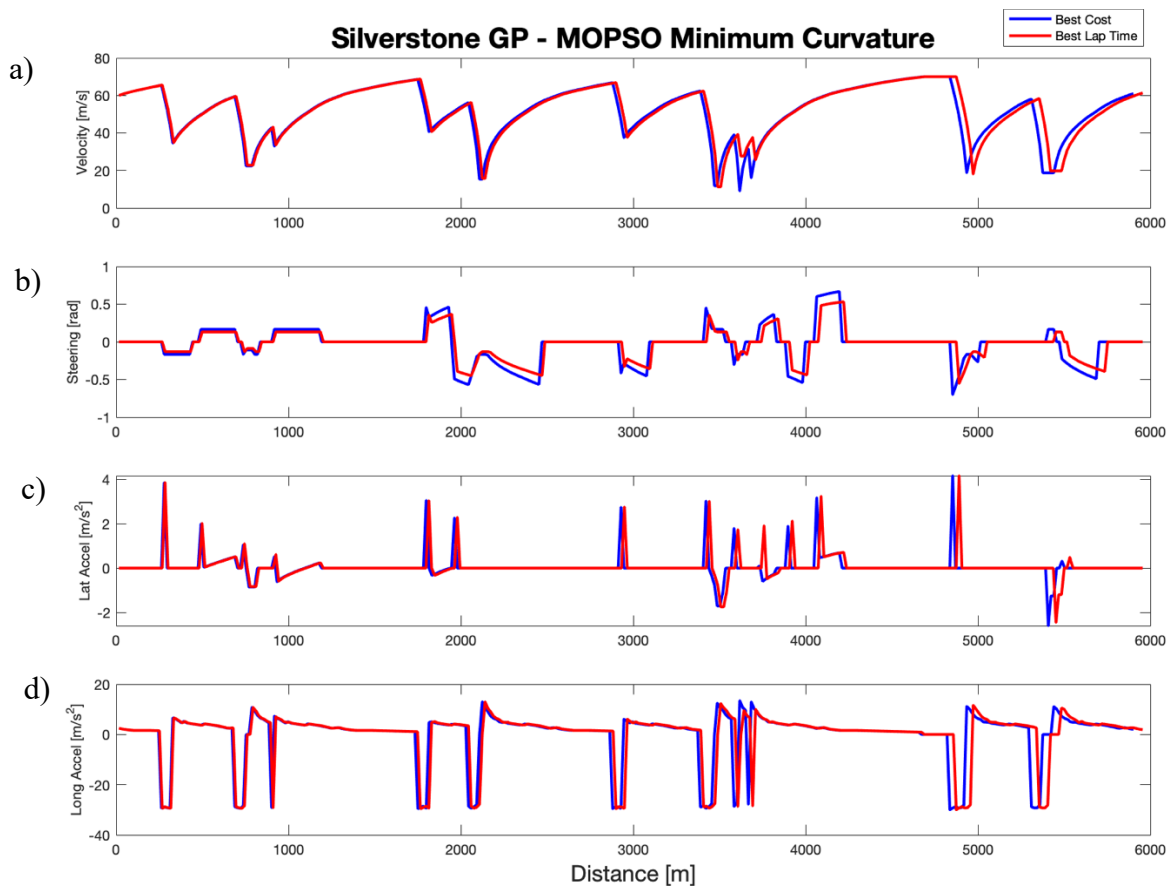


Figure 6.45 a) Vehicle velocity, b) steering input, c) lateral acceleration and d) longitudinal acceleration vs distance for an ICE only race vehicle around Silverstone GP circuit (minimum curvature trajectory).

The delta difference between the two best costs, i.e., minimum curvature and lap time show that the best lap time is generated from higher speeds and improved accelerations (Figure 6.46). The delta plots show that the best lap time accelerates harder within the range of 0.25 to 0.5ms^2 and decelerates later by on average 0.6ms^2 , in turn not needing as much steering angle to negotiate a corner by opening the corner up.

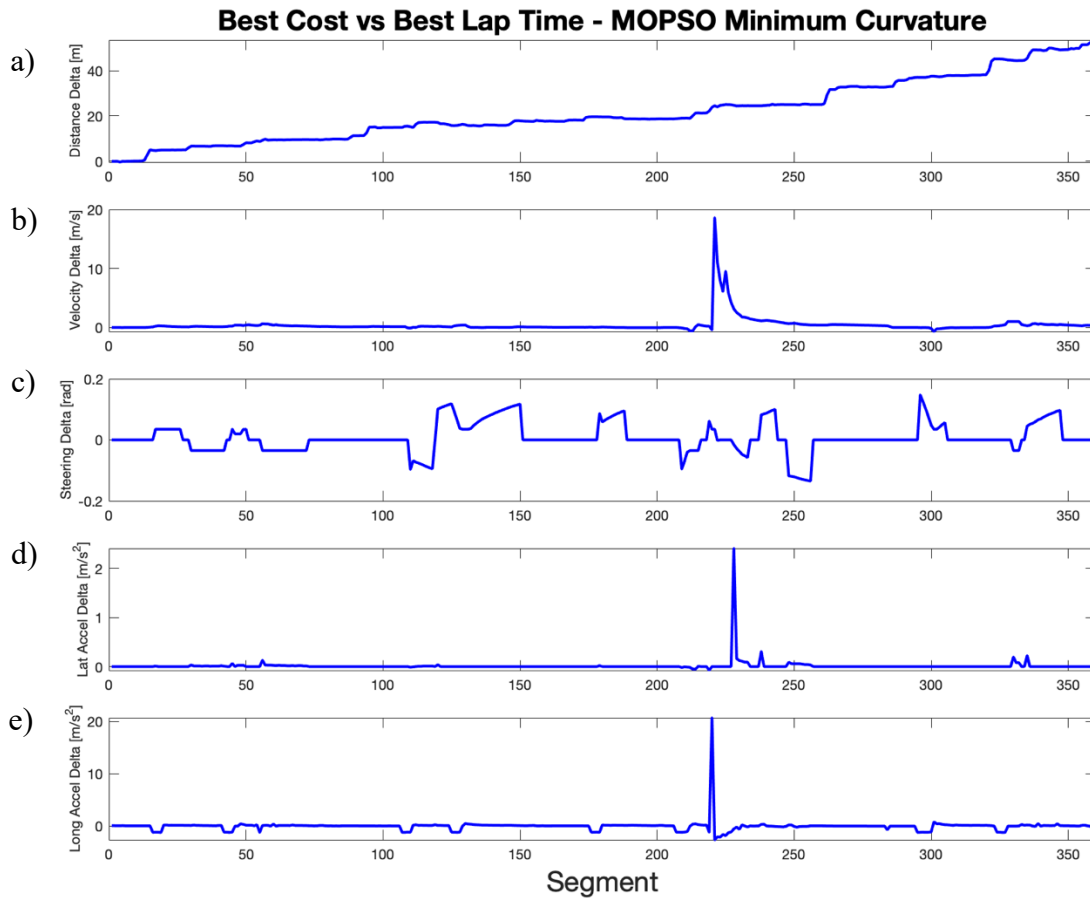


Figure 6.46 a) Distance variation and error variance between best lap fitness function versus trajectory curvature fitness function for b) vehicle velocity, c) steering input, d) lateral acceleration and e) longitudinal acceleration for an ICE only race vehicle around Silverstone GP.

Maintaining vehicle speed over a longer distance, steering inputs and vehicle acceleration in Figure 6.45, all confirm that certain sections of the track are more detrimental to lap time than others. Alongside the physical vehicle constraints, the minimum curvature or shortest path alone cannot produce the best lap time as confirmed by the best lap times not falling at shortest path or minimum curvature in the previous experiments. By plotting the shortest path MOPSO and minimum

curvature MOPSO against total length as in Figure 6.47, it is clear that a combined MOPSO as per equation (6.36) is required. Nonetheless, it is important to add that the minimum lap time for the least curvature SOPSO generated a time within 0.45s of the physical vehicle and the measured data presented in Chapter 5.

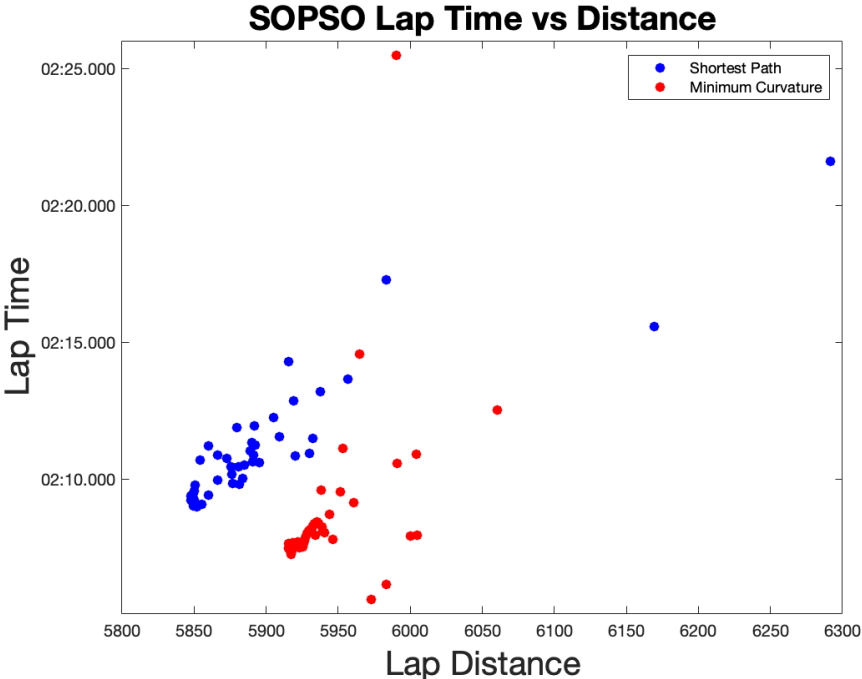


Figure 6.47 Lap time vs distance for shortest path and minimum curvature SOPSO.

When comparing similar lap times, the minimum curvature and shortest path tend to yield similar vehicle dynamic performance, however, the optimum dynamic behaviour of the vehicle is not being extracted as the MOPSO is not set to optimise a combined path.

The vehicle dynamic model for the MOPSO presented in Sections 6.10.1 and 6.10.2 utilises the equation (6.38) to calculate curvature (k) that works well for steady state situations, but not always producing desired results in transient situations [9]. This results in a very square wave pattern for some steering inputs (start of the lap) and a lack of exploitation for high lateral acceleration and steering parameters. As seen in Figures 6.42 and 6.45 the steering input (at the steering wheel) results in a maximum 0.7 radians as opposed to a maximum steering input of 2.443 radians at the

steering wheel, or 0.1745 radians at the wheels. This limitation due to the dynamic constraints then limits the lateral acceleration of the vehicle.

$$k = \frac{1}{C_{friction}/V_x} \quad (6.38)$$

where

$$C_{friction} = C_{fric} + \mu \times DF_A \quad (6.39)$$

and

$$C_{fric} = \mu \times (m \times g) \quad (6.40)$$

Steering is derived from curvature by Equation 6.41.

$$\delta = wb \times k \quad (6.41)$$

In (6.41), wb is referring to the vehicle wheelbase.

As a further evidence for utilising a combined trajectory MOPSO it can be concluded that the curvature calculation from the minimum curvature algorithm can be utilised as the actual curvature at any dynamic point on the circuit. This is eradicating any anomaly between PSO curvature (Γ) and calculated curvature (k). As both minimum curvature and shortest path algorithms utilise the same α input variable for the track location, the calculated dynamic curvature can be included in the dynamic constraint model and for a combined trajectory MOPSO optimisation. The minimum curvature algorithm is incorporated into the vehicle dynamics model and replaces equations 6.38 to 6.40 for the dynamic constraint steering calculation to determine the transient curvature and therefore steering angle.

6.11.3 MOPSO including Dynamic Constraints

The multi-objective PSO returns much improved lap times and appropriate expected vehicle dynamic results. The best cost results congregate around the 2 minute, 5 seconds to 2-minute, 6 seconds lap times as expected from this vehicle. The results are shown in Figure 6.48. These are similar to the results presented in the SOPSO. However, there are samples whereby 2 minute 2 second and 2 minute 3 seconds are found as best lap time with a 2.02.106 as the best recorded lap time.

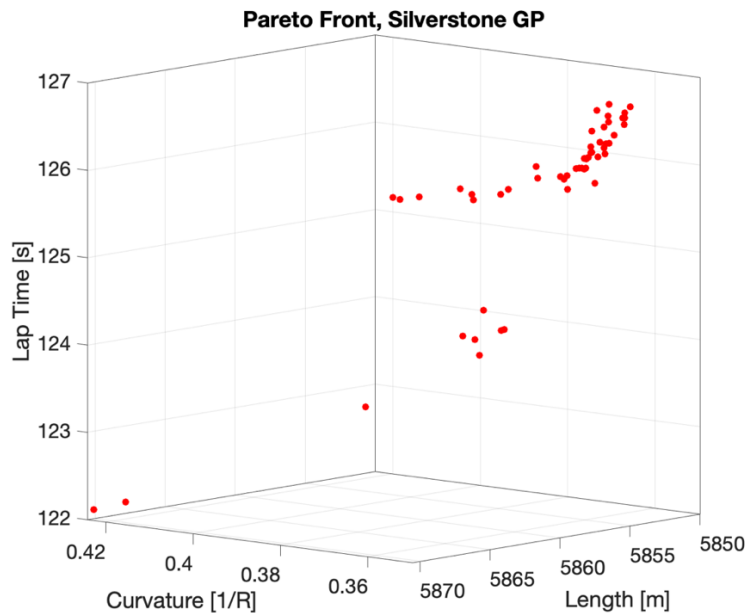


Figure 6.48 Three-dimensional pareto front, MOPSO.

The best lap time of 2.02.106 is recorded with a slightly longer length (20m) and a higher curvature (0.06) than the cluster around the 2-minute, 5 seconds mark (Figure 6.49). This lends itself to much better lap time due not only to the curvature of the corner sections but also to the improved straight away sections and how those sections are entered with improved acceleration (Figures 6.50, 6.51). It can also be seen with the improved curvature calculation implemented into steering angle, the steering angle range is greatly improved and hence lateral accelerations.

The vehicle dynamic properties are improved with the inclusion of the transient curvature algorithm allowing for a much broader search space and usage of the dynamic constraints.

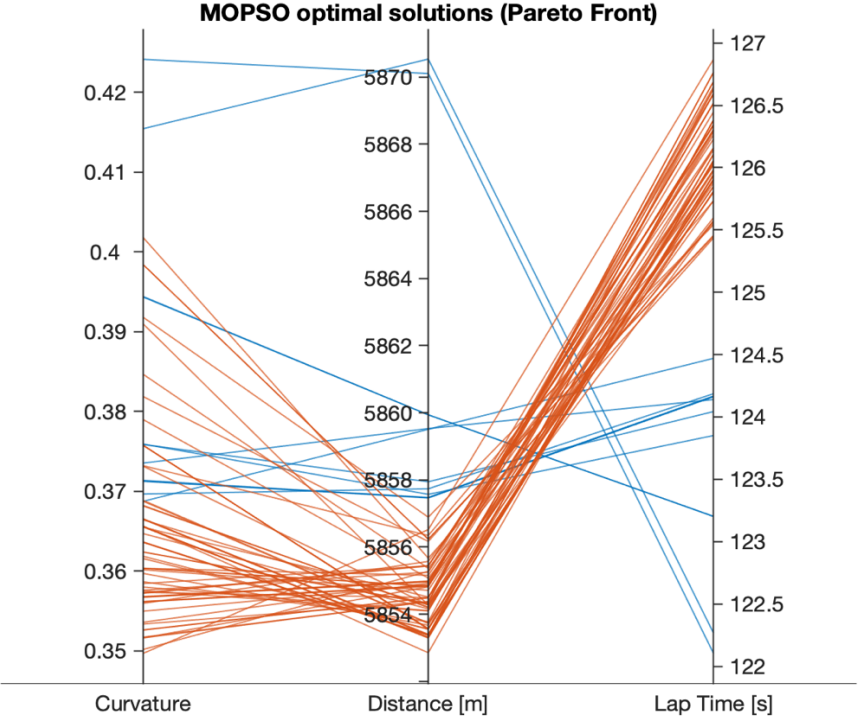


Figure 6.49 Parallel plot results - curvature vs distance vs lap time (Blue = Best 10%).

The resultant output from the vehicle follows more closely what is expected from a vehicle (Figure 6.50) and less like a digital signal (Figure 6.45) as resulted from the single trajectory MOPSO. This enables the vehicle to accelerate earlier, brake later and corner with higher forces than the previous MOSPO simulations and enables much better lap times for given sector lengths as illustrated in Figures 6.50, 6.51. The lateral acceleration is now producing results that explore the full range of lateral acceleration up to 18m/s^2 as opposed to 5m/s^2 within the previous MOPSO results. However, with the sensitivity of the steering input the final trajectory (Figure 6.50) has some very minor abnormal paths more noticeably at the lead straight away into the Maggotts and Becketts complex.

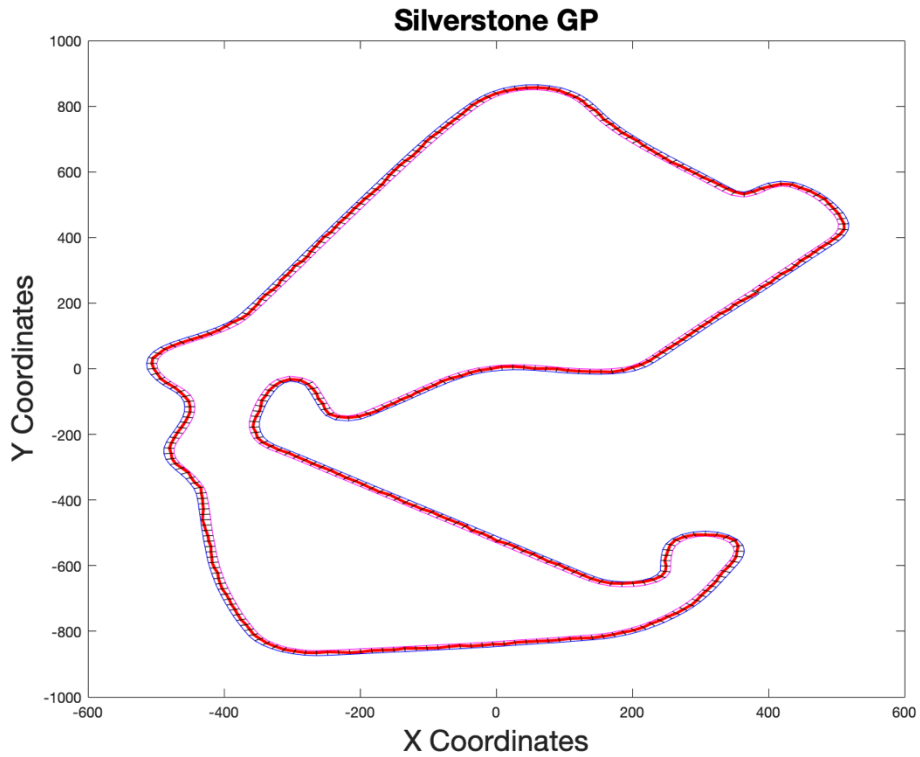


Figure 6.50 MOPSO trajectory (red line) with 1 by 360 segmentation sector of the Silverstone GP circuit.

Spline interpolation can produce a smoother more accurate trajectory and smoothing of the data can assist the final vehicle dynamic data. As the vehicle dynamic constraints are based on the α input from the trajectory the constraints algorithms can be independently simulated without the need for PSO by utilising a trajectory as the input. This allows the spline interpolated trajectory to be used as an input after the MOPSO has found the preferred trajectory and make small variations to the vehicle dynamic output to coincide with the smoothed trajectory. The final smoothed trajectory and data are shown in Figures 6.51 and 6.52.

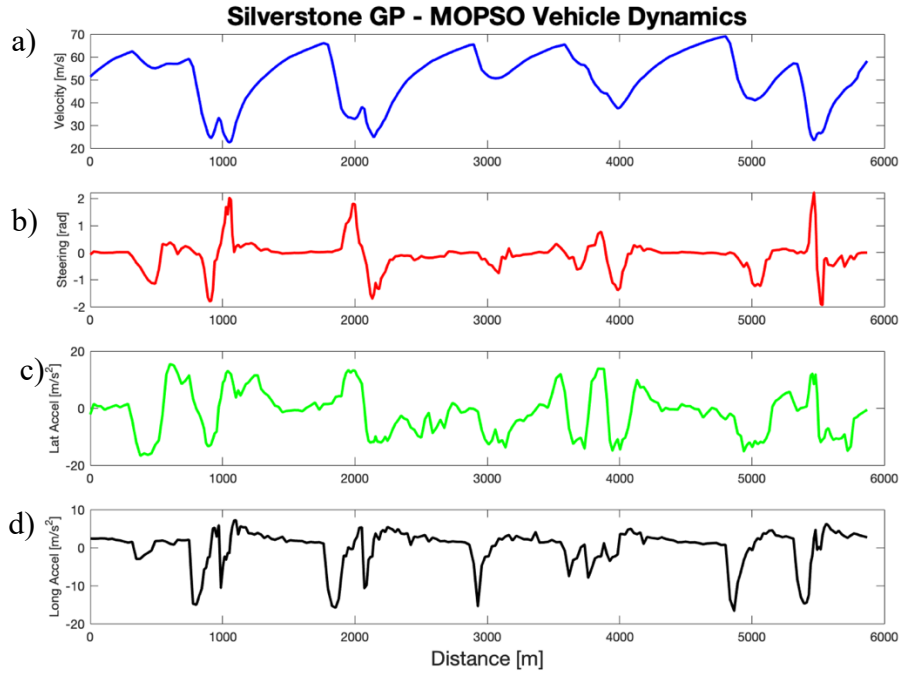


Figure 6.51 a) Vehicle velocity, b) steering input, c) lateral acceleration and d) longitudinal acceleration vs distance for an ICE only race vehicle around Silverstone GP circuit.

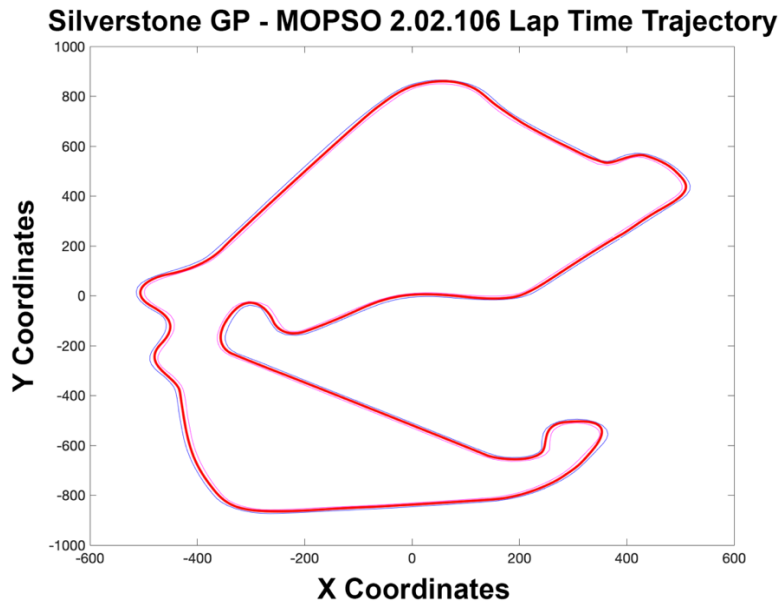


Figure 6.52 Spline interpolated and smoothed trajectory for the combined trajectory MOPSO.

6.12 Conclusion

The particle swarm optimisation algorithm has been experimented with until failure. Limitations have been sought to satisfactory performance of results. It is apparent that the PSO does perform better as particle population increases but this has an adverse effect on simulation time and in some cases with the shortest path SOPSO, yielded very little gains in results.

Where results can be similar, in the instance of shortest path whereby two almost linear paths could be very close in length in a single section, especially on a straight away. The PSO could not determine the best overall path on said straights as the variation in some paths could be in the range of 0.1, and therefore unless the simulation was to employ large population counts for much longer simulation times, some possibilities cannot be explored and the best path is not always found. This can then have a negative effect on overall trajectory as one path connects to the next segment path which again may find several optimums of the same length, creating a non-linear line concluding with erratic trajectories on straight aways.

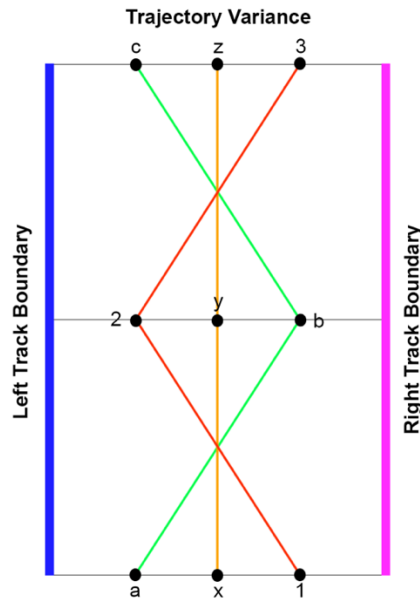


Figure 6.53 Trajectory variation with $\alpha = rand$ (to 4d.p).

As an exaggerated example, Figure 6.50 depicts three potential trajectories for shortest path across 2 segments of the circuit. The PSO determines the location of a, x or 1 via alpha, and alpha is a random number to an accuracy to four decimal places. As the next segment is calculated b, y or 2 is the returned positional result for alpha. As the track width is 15m, the distance between any

points across the width of the track could be 0.15mm. This results in various trajectories returning results as per the line depicted by a, b and c, x, y and z or 1, 2 and 3. These trajectories can be very similar in length whereby line a-b-c is very similar to x-y-z due to the very nature of the accuracy of the random number generator. Hence why smoothing is essential after the results are produced.

SOPSO and MOPSO fared much better for minimum curvature as the curve is always expanding and produced excellent results. The MOPSO algorithm with the inclusion of vehicle dynamics and lap time objectives certainly found acceptable results that can be closely compared to actual measured vehicle behaviour and lap time. Figure 6.52 overlays two similar lap times, one from the MOPSO (2.05.437) and one from the physical measured Lotus race vehicle data (2.05.143). The MOPSO travels 112m further but carries more speed through all corners and minimises steering angle however the MOPSO vehicle dynamics are very similar to a physical vehicle and produces results within 0.3s.

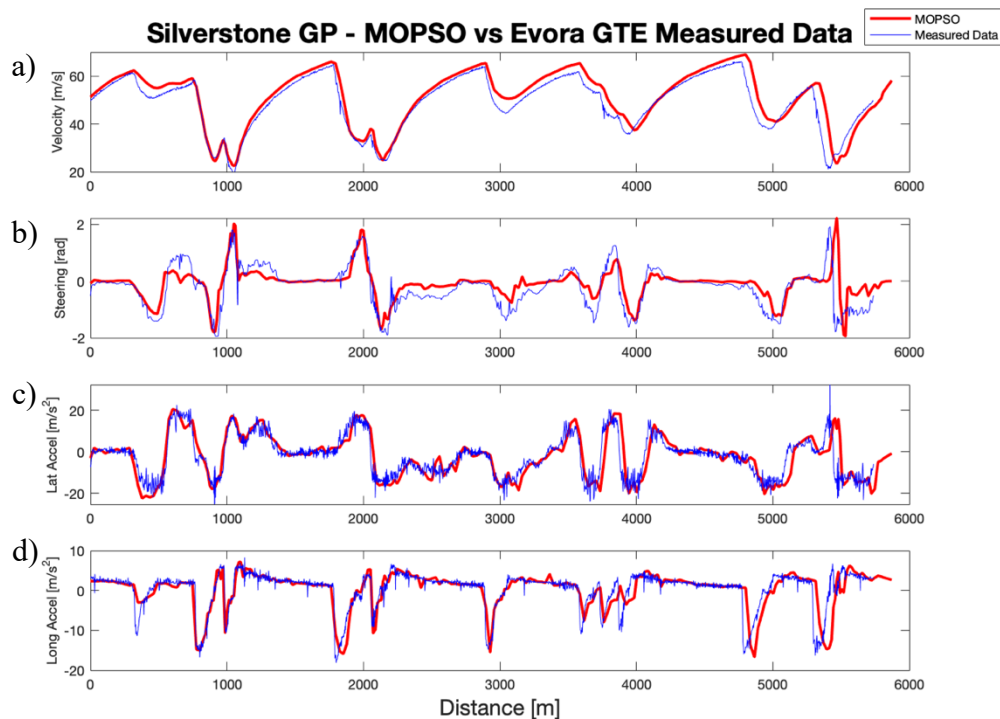


Figure 6.54 MOPSO vs Measured Evora GTE Data. a) Vehicle velocity, b) steering input, c) lateral acceleration and d) longitudinal acceleration vs distance for an ICE only race vehicle around Silverstone GP circuit. MOPSO vehicle dynamic output (red line) versus physical measured race car data (blue line)

7. Race Car Hybrid Energy Management

7.1 Introduction

In this chapter a hybrid electric vehicle is proposed based upon the modifications to the vehicle discussed in the previous chapters. Energy management strategies are studied, and hybrid energy deployment strategies are compared to the best lap time of the MOPSO presented in Chapter 6. The results are analysed by using the vehicle parameters estimated for the transient vehicle dynamic model presented in Chapter 3. The hybrid electric vehicle includes the powertrain model developed in Chapter 4 and is used to determine the fuel saving of a hybrid vehicle to its ICE only counterpart. The chapter concludes with a MOPSO algorithm which considers an electrified version of the developed vehicle dynamic model as an additional constraint to determine the fastest lap time alongside the best trajectory.

7.2 Hybrid Race Car Power Balance

Current trends dictate that race series such as such as World Rally, Touring Cars, World Endurance and the Formula One world championship introduce electric only or hybrid vehicles as their racing category and many have implemented or are due to launch hybrid electric vehicle inclusion for the 2021 race season. It is inevitable that GT racing will follow suit sooner rather than later. The final optimisation scenario for this thesis is to determine the validity of a hybrid vehicle category for GT and endurance racing in the form of a case study. As a hybrid vehicle is yet to be conceived, the analysis will be based upon creating a hybrid package with appropriate battery capacity and motor power to assess fair competition with the view that GT racing will adopt the hybrid race cars into their current plethora of ICE only vehicles, especially in GT4, GT3 and GTE. For comparison analysis several hybrid energy deployment strategies are simulated for a hybrid electric race vehicle and compared against an internal combustion engine vehicle.

All vehicles that compete in a GT series must undergo the FIA balance of performance (BOP) tests [100] to assign performance levels of the vehicle. Furthermore, vehicles competing in the LMP1

category contains hybrid and ICE only vehicles so an equivalence of technology (EoT) [106] is also implemented as a way to handicap power. Both handicap systems enable the event organisers, the possibility to limit or improve performance on a race-to-race basis, thus creating similar lap times for all vehicles. It is fair to assume any hybrid vehicle proposed in future rules and regulations, entering such a series would be scrutiny to similar constraints.

As the work is for a hypothetical race car, the analysis will be based upon both hybrid and non-hybrid version of the race car with an identical vehicle mass and similar torque output. It is proposed that if a hybrid vehicle uses a smaller capacity ICE then the motor can be larger or vice versa, and hence the torque profiles can be matched with ICE only vehicles. Another alternative for hybrid vehicles is that the ICE can be switched off or ‘pegged’ at certain sites so the additional motor output can create equal torque outputs to that of an ICE only vehicle, and therefore fuel can be utilised as an optimisation metric. These options enable a study of an appropriate hybrid package to be assessed and utilised to identify the appropriate hybrid powertrain on/off ratio. Power from the motor can be analysed and optimised, thus allowing balance of performance of the torque from the powertrain and equalising lap times through acceleration performance. Acceleration and torque profiles for all hybrid powertrain concepts were generated as detailed in Chapters 4 and 6.

7.3 Hybrid Race Car Power Characteristics for Deployment

To enable fair usage of the hybrid electric powertrain, the regeneration power will be set to maximum regeneration for all braking events and power deployment limited. In a deceleration zone, if the braking force required does not exceed the power of the generator unit, the energy harvested will be through electric only regeneration and the MGU-K will be the sole braking force applied to the vehicle; a fast corner for instance where very little braking is applied. When required deceleration forces exceed the motor power, it is assumed maximum regeneration will be harvested from the generator unit and the remaining deficit in braking power retardation and deceleration of the car is from the hydraulic braking system. This scenario allows all possible electrical energy to be harvested in all braking zones.

Energy deployment will be optimised via a change in variables through the management strategy logic.

For clarity, regeneration will be calculated as a negative number and motor usage as a positive number added to the ICE power, generating the required power to propel the car. Required vehicle power (P_d) is calculated through equation (7.1).

$$P_d = \frac{v_x}{1000}(mgf_r + DF_A + mIa_x) \quad (7.1)$$

where

v_x is the longitudinal velocity

DF_A is the aerodynamic drag force

f_r is the rolling resistance of the tyre

I is the rotational inertia factor.

The controller parameters for MGU-K systems and MGU-K/MGU-H combined systems are as presented in Figures 7.1 and 7.2 and Appendix 7. For clarity to the rules and regulations, the MGU-H is for namesake only, however it will be used only as a generator and will not provide motoring power. The parameters defined on the arrows in Figures 7.1 and 7.2 are an illustration of the variables used to control the power transfer and will be subject to scrutiny and optimisation.

As an initial analysis to test the effect of the parameters listed in Table 7.1 for the energy management purposes, the trajectory and lap time (2.08.979) results from the MOPSO as described in Section 6.11.1 are utilised to test for appropriate functioning of the energy management model. After this test the results for best lap time (2.02.106) combined trajectory MOPSO from Section 6.11.3 are utilised to ascertain a balance of performance. The nature of this chapter is to analyse electric power usage as a means to reduce ICE usage for the same dynamic results and lap time produced by the ICE only car in 6.11.3.

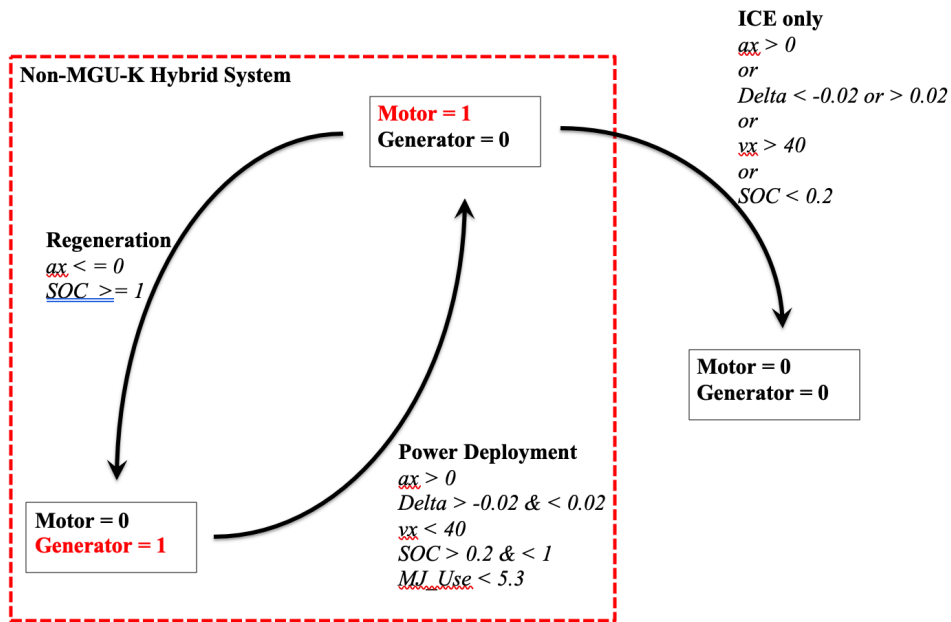


Figure 7.1 Example controller parameters for regeneration and hybrid power deployment, single MGU-K (non-MGU-H).

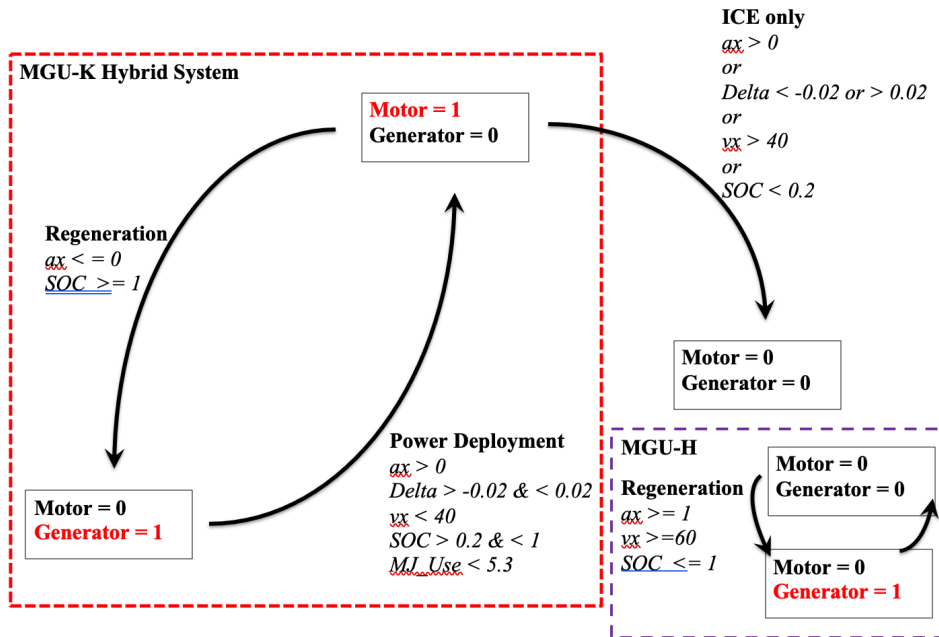


Figure 7.2 Example controller parameters for regeneration and hybrid power deployment, MGU-K/MGU-H system.

Table 7.1 Initial scenario used for energy management evaluation.

	Steering Wheel	Steered Wheels	Velocity	Acceleration	SOC
Deployment	0 +/- 0.28 rads	0 +/- 0.02 rads	<= 70 m/s	Positive	N/A
Regeneration (MGU-K)	0 +/- 2.44 rads	0 +/- 0.1745 rads	<= 70 m/s	Negative	N/A
Regeneration (MGU-H)	N/A	N/A	N/A	N/A	N/A

The test was carried out, allowing the vehicle to deploy energy at all acceleration zones up to maximum velocity, but limited to low steering angle inputs only, negating deployment within a corner. Regeneration was set during all deceleration zones from the MGU-K, while the MGU-H was switched off and all steering inputs were permissible during regeneration. This ensures all deceleration events within a corner are captured. The hybrid battery was assumed to be fully charged from the previous lap(s).

With the aim to test and identify the extremities of the power deployment and regeneration and also understand how much energy could be deployed, if the available battery power was to be utilised for a 120kW motor during all straight aways. Based upon the Formula One powertrains, 120kW motors are utilised and as this power is close to 30% of the ICE power output of a modern GT3 car, this power output for the motor appears to be appropriate as it is utilised within the motorsport industry already. Reducing ICE power by 30% has the potential to generate results that can be appropriately analysed and scrutinised for the proposal of a hybrid vehicle.

By having the energy management constraints described above, the aim is to repeat the vehicle dynamic results for a full lap single trajectory MOPSO (section 6.11.1), by including the energy management constraints along with the dynamic constraint investigated in Chapter 6. As explained in Chapter 4, the maximum deployment limit of the world endurance vehicle around Silverstone is 5.3MJ per lap. However, Figure 7.3 shows that the total energy flow over a lap both from harvesting and power deployment is 6.37MJ. Whilst 5.59MJ of energy was deployed, only 0.78MJ

has been harvested. These results suggest a full lap deployment would not be possible as it breaches the rules. In fact, the black line in Figure 7.3 depicts the maximum permissible deployment. This scenario suggests the parameters in Table 7.1 would not be an ideal for a race set-up as several laps would be required to recharge the batteries to full.

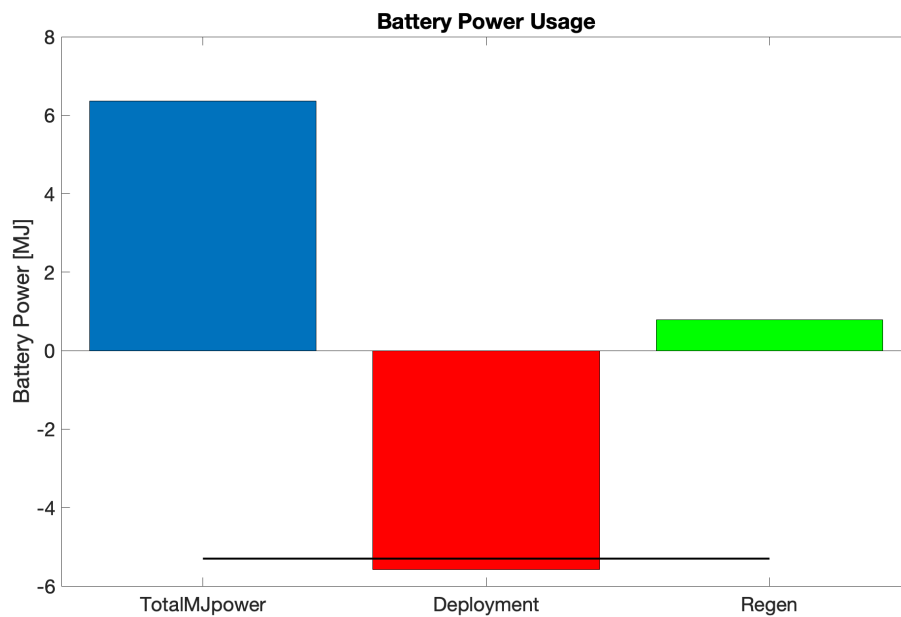


Figure 7.3 Battery usage during the best lap time (2.08.979) shortest path trajectory, (the black line depicts the maximum power deployment usage allowed).

Within this scenario, with the battery fully charged at the start of a qualifying lap, there is a potential, through optimisation of the deployment strategy, to limit the deployment to 5.3MJ. In this case, the battery power can be consumed for almost an entire lap using the same dynamics as presented in Section 6.11.1, Figure 6.42 of the shortest path trajectory, dynamic constraint MOPSO.

The motor was set to deploy at 100% during all acceleration zones and use 100% harvesting power during braking events. This can be clearly seen in Figure 7.4 in the motor power and regeneration power plots. Equation 7.2 determines the state of charge (SOC) of the battery and from Figure 7.4, it can be concluded as there is no limitation to usage in the initial test parameters that either SOC or Charge status (MJ) will need to be assigned to the control strategies and appropriate parameters

set to establish a suitable complete MOPSO simulation for one lap qualifying events and multi-lap race sessions.

As analysed in Section 6.11.3, the vehicle dynamic behaviour from the combined trajectory, dynamic constraints MOPSO, generates improved longitudinal acceleration/deceleration profiles (Figure 6.51), and is a much-preferred method for testing the hybrid capabilities. This is due to the fact that the deceleration events should enable a substantial improvement on energy harvesting. The results from section 6.11.3 will be utilised for analysis of energy management strategies. Although the initial test using the data from section 6.11.1 ensures the hybrid energy system is working as expected with regards to power deployment and harvesting as shown in Figure 7.4.

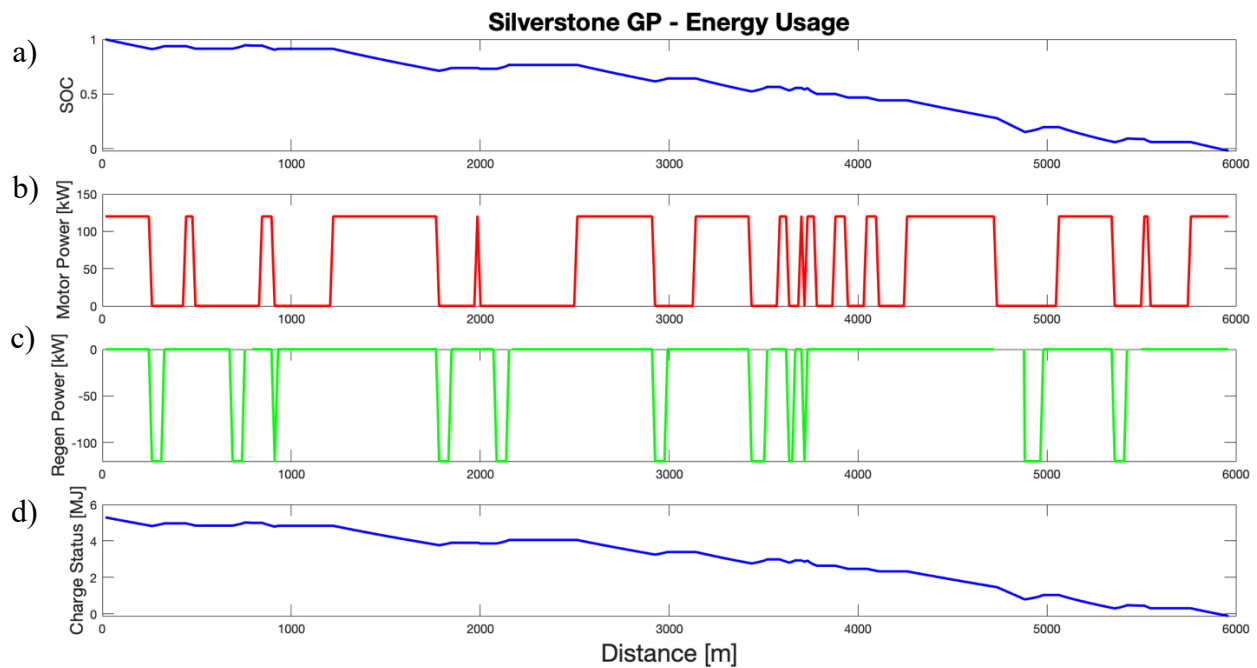


Figure 7.4 a) SOC, b) Motor Power (kW), c) Regen Power(kW) and d) Charge Status (MJ) usage during the best lap time (2.08.979) using trajectory results from the shortest path MOPSO presented in section 6.11.1.

7.4 Hybrid Energy Management Scenarios

In this section, the aim is to optimise the variables involved in different power deployment strategies and investigate the typical modes of a hybrid vehicle battery energy, i.e., 1. charge depleting, 2. charge sustaining, and 3. maximum deployment.

For this purpose, the energy management strategy is combined with the vehicle dynamic constraints, and trajectory path created for the best lap time of 2.02.106 from Chapter 6, Section 6.11.3.

The SOC is determined from maximum power deployment as set by the rules and regulations (5.3MJ). However, as charge is unlimited (Appendix 7), the SOC is allowed to mathematically go beyond one so as to determine an appropriate battery sizing after the initial simulations. The instantaneous SOC is determined by charge at the vehicle position at any given track segment and the maximum charge capacity of the battery. As the maximum deployment is 5.3MJ, the max charge is set identical to this value as can be inferred from (7.2).

$$SOC_{(i)} = \frac{Charge_{(i)}}{Charge_{max}} \quad (7.2)$$

where

i refers to any given segment of the track

By considering the dynamic and energy management constraints as explained just now, the analysis of the energy management problem for each scenario is determined by two measures written in (7.3).

$$\text{Charge Depleting} = \min_{1 \leq i \leq k} SOC_i$$

$$\text{Charge Sustaining} = \frac{SOC_n}{SOC_1} \quad (7.3)$$

here

SOC_i is the state of the charge at segment i of the track.

k is the current segment of the track during one lap which is always less than the number of segments in the track (n).

In the charge depleting scenario, the minimum battery state of the charge is found from the beginning of the lap up to the current segment travelled by the vehicle. While in the charge sustaining scenario the ratio of the battery state of the charge between the last segment and the last segment is evaluated.

The trajectory and vehicle dynamic data results are used as a means to produce the same lap time as the ICE only vehicle, however, the inclusion of the hybrid management strategy is included to enable analysis and exploration of control parameters so as to design effective strategies to be utilised within the transient vehicle dynamic model presented in Chapters 4 and 5. The following energy management strategy scenarios are to estimate battery usage and tune the energy management parameters.

7.4.1 Charge Depleting Scenario

In the first examination, the parameters presented in Section 7.3, (Table 7.1), are utilised with the addition of electrical harvesting from the MGU-H, allowing for unlimited discharge to determine energy usage over a lap with very little restrictions. The parameters listed in Table 7.2, clarifies that the regeneration through the MGU-K will be during all deceleration events, and contains the inclusion of MGU-H regeneration during low acceleration events. As previously discussed in Chapter 4, this limits the power taken away from the engine when the MGU-H is operating. The SOC is ignored at this stage.

Table 7.2 Charge depleting scenario used for energy management evaluation.

	Steering Wheel	Steered Wheels	Velocity	Acceleration	SOC
Deployment	0 +/- 0.28 rads	0 +/- 0.02 rads	≤ 70 m/s	Positive	N/A
Regeneration (MGU-K)	0 +/- 2.44 rads	0 +/- 0.1745 rads	≤ 70 m/s	Negative	N/A
Regeneration (MGU-H)	0 +/- 2.44 rads	0 +/- 0.1745 rads	≥ 65 m/s	≤ 1.5 m/s ² >0 m/s ²	N/A

The improved vehicle dynamic data as presented in Chapter 6; Figure 6.51 ensures the maximum deceleration performance of the vehicle is exploited for maximum regeneration. The vehicle begins the lap with a full charge (5.3MJ) available at the start of the lap as would be the case for a qualifying lap. Here, the car would charge up the batteries on the out-laps prior to a qualifying lap. As listed in Table 7.3, in this charge depleting scenario, the energy usage is within the maximum deployment parameters set by the rules. Moreover, as depicted in Figures 7.6, 7.7 and 7.8, the vehicle regenerates enough energy so that almost an entire second lap could deploy energy. This can be inferred from Figure 7.5 that the state of charge at the end of one lap contains 44.6% of the initial charge. With the additional benefit of the MGU-H, some energy is harvested whilst the vehicle is still increasing speed towards the maximum velocity of the vehicle. The motor and combined MGU-H/MGU-K generator usage are plotted in Figure 7.6 along with the vehicle velocity. It can be clearly seen in Figure 7.6 that, the sections at the end of long straights, especially the ones at 310m, 1760m, 2860m and 4800m (circled), where regeneration power has started to be harvested whilst power is being deployed from the motor and velocity is towards its maximum. This additional recharge from the MGU-H at the end of certain straights when speed is high and acceleration is low, adds an additional 0.23MJ of harvested energy as listed in Table 7.3.

Table 7.3 The result of energy charge depletion over one lap of Silverstone GP circuit.

MOPSO Energy	Deployed (MJ)	MGU-K Regen (MJ)	MGU-H Regen (MJ)	Net Deployment (MJ)	SOC end of Lap
	5.0303	1.8633	0.23	2.9370	0.446

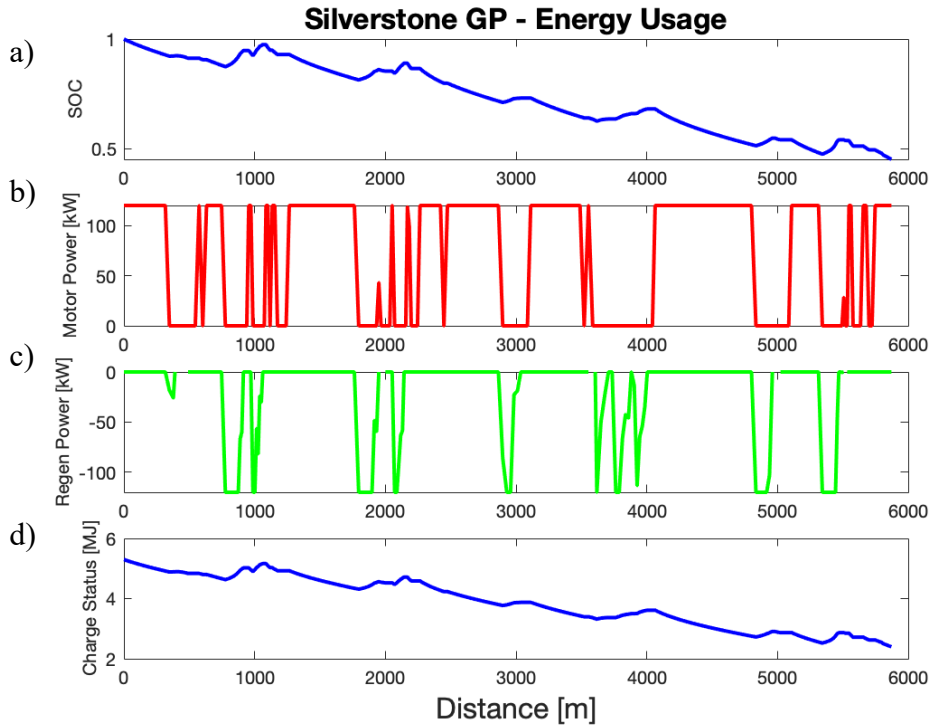


Figure 7.5 a) SOC, b) motor power (kW), c) regeneration power (kW) and d) charge status (MJ) usage during the charge depletion strategy utilising the 2.02.10s lap-time trajectory results.

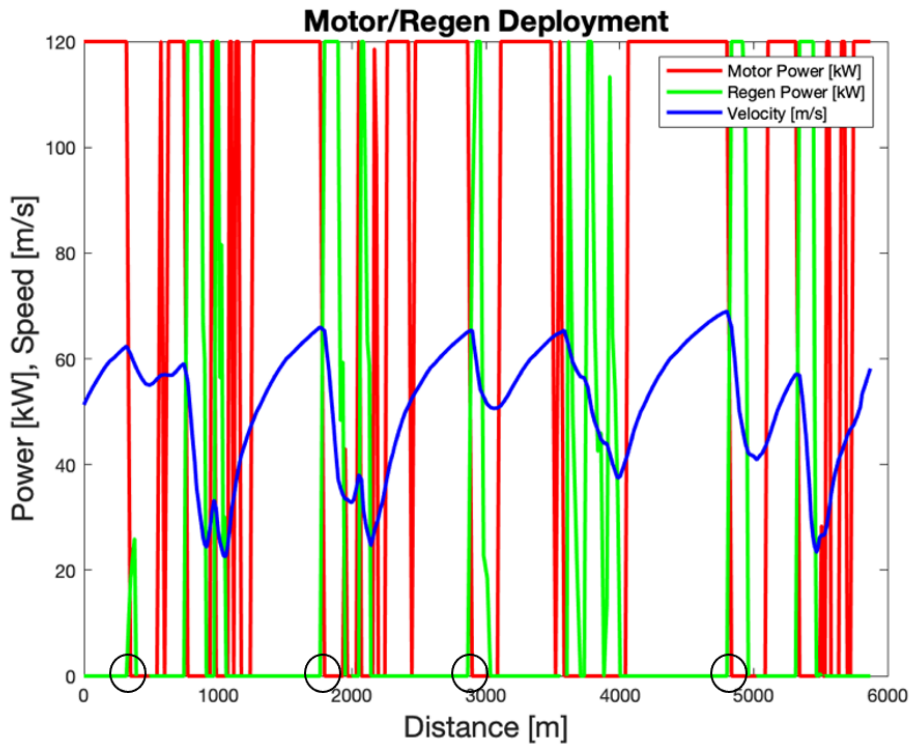


Figure 7.6 Motor power (red) and regeneration power (green) along with the vehicle velocity.

The regeneration has been drastically improved from the results found in Section 7.3. In the energy management scenario using the results from section 6.11.1, all of the battery power was depleted, and the rule parameters of maximum deployment usage were breached (Figure 7.3), due to lower maximum deceleration results (Figure 6.42).

As shown in Figure 7.7, by improvement in harvesting, the net energy used is 2.937MJ. with a total energy deployment of 5.03MJ, allowing 0.3MJ to be deployed during cornering if traction is available. This information can be carried forward into a MOPSO so that the dynamic constraints of the traction circle can be explored within the dynamic vehicle model presented in Chapters 3 and 5.

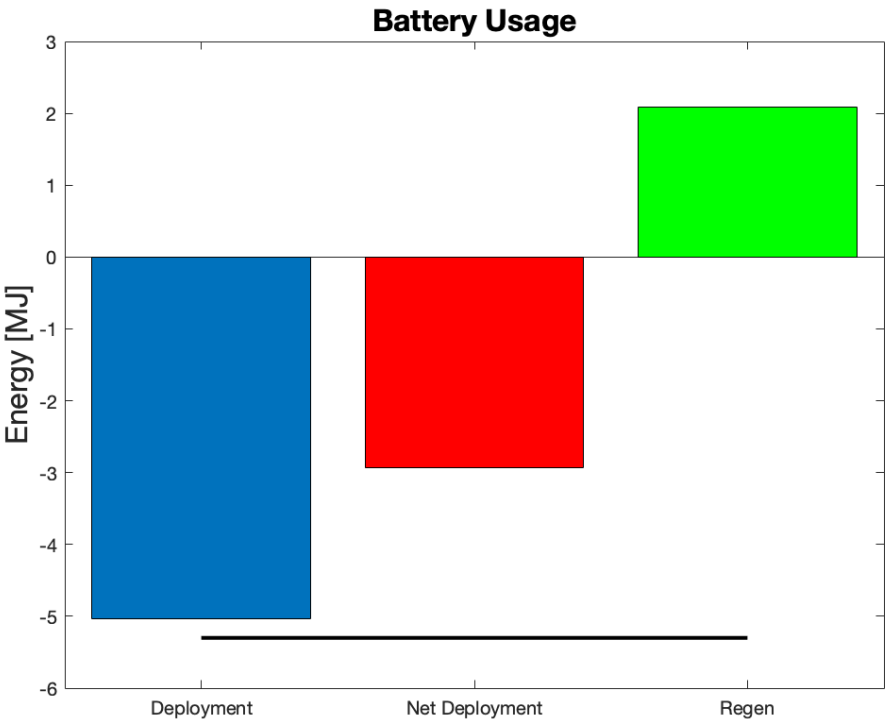


Figure 7.7 Total energy, Net energy deployment and regenerated energy.

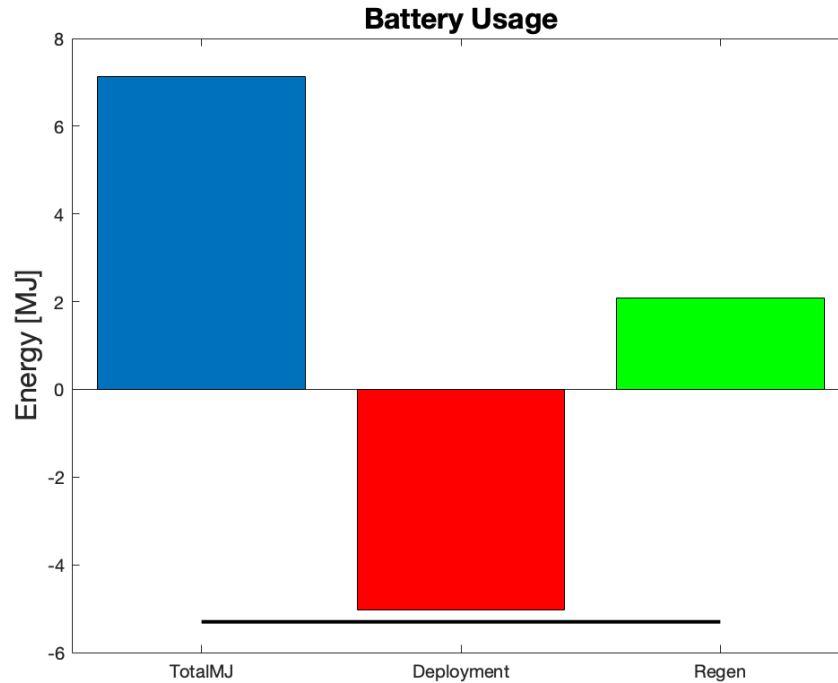


Figure 7.8 Total energy flow, total energy deployment and regenerated energy. (The black line depicts total permissible energy deployment over a single lap).

From the total deployed energy in this scenario, it can be deduced that for a qualifying lap, where charge is only required for one full lap, a larger motor could be utilised. as there is additional charge left in the batteries at the end of the lap. Potentially allowing a larger deployment power to regeneration power MGU-K strategy. However, as a race vehicle has to contend with longer race distances and not just one lap qualifying, the power deployment and regeneration has to be strategised to ensure power is available to maintain a balance of performance with ICE only vehicles each lap. Therefore, for all energy scenarios a 120kW motor will be utilised for the remainder of the study.

7.4.2 Charge Sustaining

The charge sustaining energy management scenario dictates that the battery level at the end of a lap must be equal to the battery level at the start of the lap. Therefore, the net energy usage across one lap of Silverstone GP circuit is zero.

Table 7.4 Charge sustaining scenario used for energy management evaluation.

	Steering Wheel	Steered Wheels	Velocity	Acceleration	SOC
Deployment	+/- 0.28 rads	+/- 0.02 rads	≤ 70 m/s	Positive	≥ 1
Regeneration (MGU-K)	+/- 2.44 rads	+/- 0.1745 rads	≤ 70 m/s	Negative	≥ 0
Regeneration (MGU-H)	+/- 2.44 rads	+/- 0.1745 rads	≥ 65 m/s	≤ 1.5 m/s ² >0 m/s ²	≥ 0

As the braking zones are used for full regeneration of the MGU-K, the total amount of regenerative energy for a given scenario with identical control parameters remains the same when comparing the energy strategies. The MGU-H regeneration takes power away from the engine (Chapter 4, Figure 4.1), and the acceleration and speed loss resulting from additional MGU-H may directly affect the braking zones lengths. The MGU-H regeneration, therefore, during these preliminary tests must maintain the same parameters as the initial charge depleting test, so that it is not affecting the acceleration and speed of the vehicle.

Figure 7.9 details how the battery constantly tops up the SOC level prior to usage aside from the initial start to the lap during the initial acceleration zone and prior to a braking section. The SOC is allowed to go numerically above 1, however, in reality this energy management strategy would have to be utilised below 96.5% of SOC. This is due to the fact that the peak regeneration causes a SOC of 103.5%, or the energy store would need to have a maximum capacity of 5.49MJ. Figure 7.10 overlays the energy deployment and harvesting along with the vehicle velocity profile. In this scenario, the power deployment is only utilised after each braking zone, when the SOC is above the initial SOC. Once the initial SOC is breached, the energy is no longer deployed during that acceleration zone. The end of the lap is utilised to deplete any excess energy stored above the initial SOC.

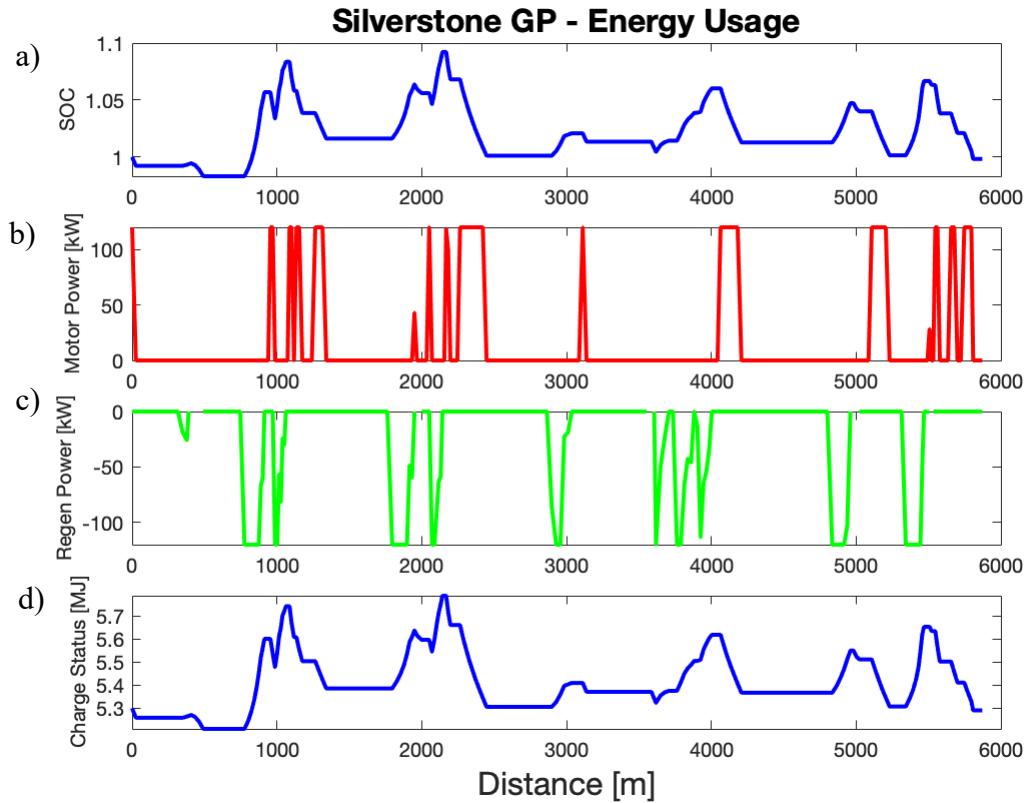


Figure 7.9 a) SOC, b) motor power (kW), c) regeneration power (kW) and d) charge status (MJ) for charge sustaining control utilising the 2.02.10s lap-time trajectory results.

Table 7.5 The energy usage and regeneration results for the charge sustaining scenario over one lap of Silverstone GP circuit.

MOPSO				
Energy				
Deployed (MJ)	MGU-K Regen (MJ)	MGU-H Regen (MJ)	Net Deployment (MJ)	SOC end of Lap
2.1026	1.8633	0.23	0.0093	0.9982

In general, with any controlled additional power deployment within the powertrain, the low speed, high acceleration zones always yield the best lap time improvements. This is because the aerodynamic drag is at a minimum and the motor torque is high. Early deployment after the braking zones is a preferred hybrid strategy for a race vehicle to improve the lap times. The scenario

presented for the charge sustaining case would be an ideal solution to maintain the energy and deploy that energy at the most effective acceleration zones.

Figures 7.11 and 7.12 show the energy used and regenerated for the charge sustaining scenario. The results open the scope for a race vehicle to change to charge depleting for a lap and recover almost instantly the energy used. Here, the charge depleting lap used 2.937MJ, then by changing to charge sustaining mode it enables the car to still accelerate at appropriate times and maintain a charge for any consecutive laps. The regeneration only mode would allow 2.093MJ to be harvested during a lap with no deployment.

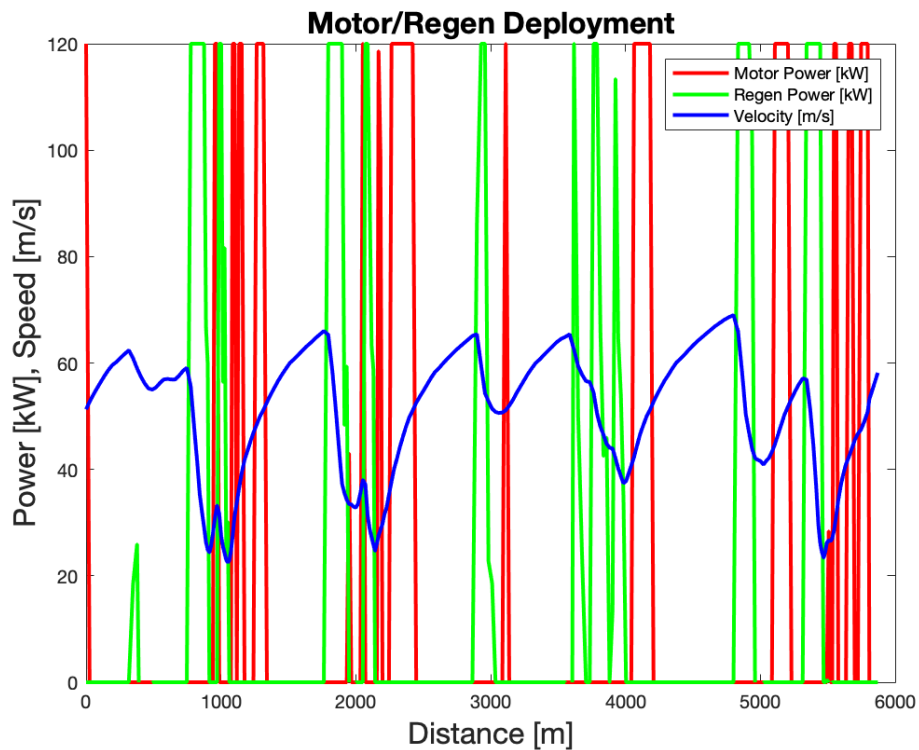


Figure 7.10 Charge sustaining motor power (red) and regeneration power (green) along with the vehicle velocity.

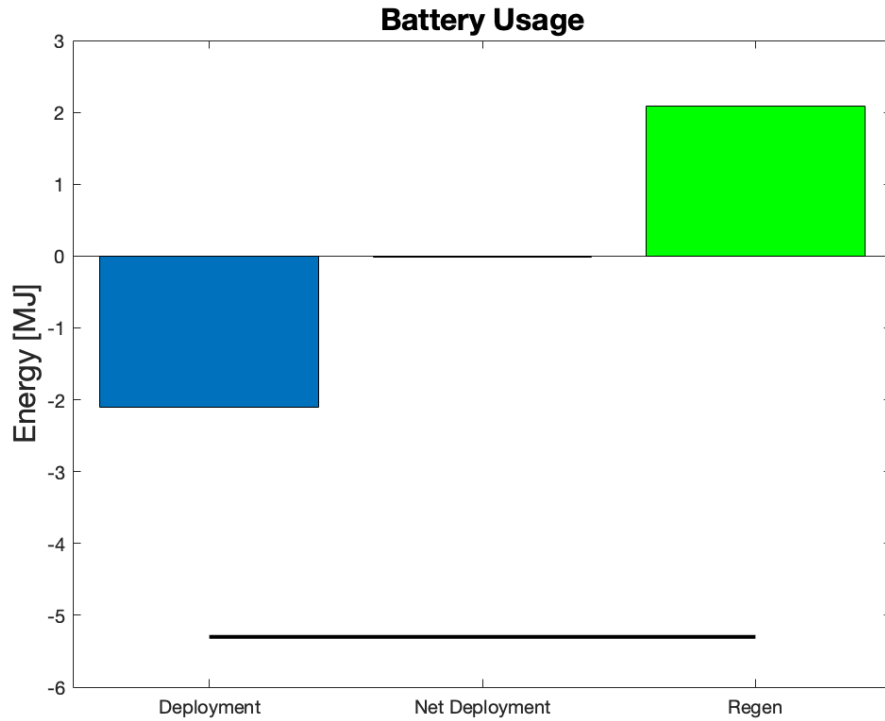


Figure 7.11 Total energy, net energy deployment and regenerated energy for the charge sustaining scenario.

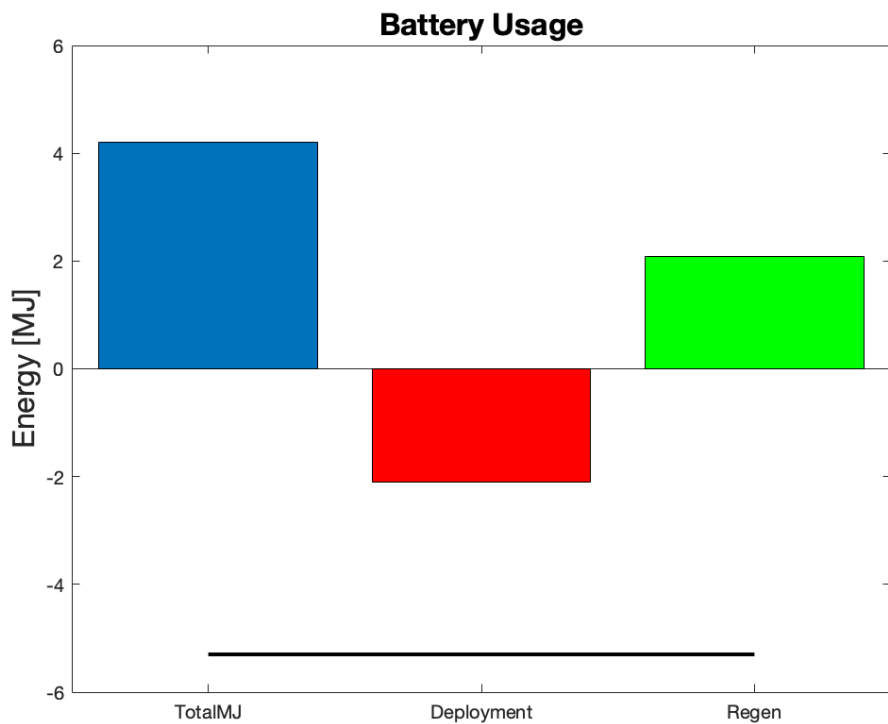


Figure 7.12 Total energy flow, total energy deployment and regenerated energy for the charge sustaining scenario (the black line depicts total permissible energy deployment over a single lap).

7.4.3 Maximum Deployment

In this scenario, all battery energy will be deployed with no limitation to maximum energy deployment. The battery is charged to 5.3MJ at the start of the lap, and the optimisation variables were changed to those shown in Table 7.6. In this case, the SOC has no influence over deployment.

Table 7.6 Maximum depletion scenario used for energy management evaluation.

	Steering Wheel	Steered Wheels	Velocity	Acceleration	SOC
Deployment	+/- 2.1 rads	+/- 0.15 rads	≤ 70 m/s	Positive	≥ 0
Regeneration (MGU-K)	+/- 2.44 rads	+/- 0.1745 rads	≤ 70 m/s	Negative	≥ 0
Regeneration (MGU-H)	+/- 2.44 rads	+/- 0.1745 rads	≥ 65 m/s	≤ 1.5 m/s ² >0 m/s ²	≥ 0

As shown in Figure 7.13 and Figure 7.14, the energy is deployed in all acceleration zones for the entirety of the lap. This includes higher steering angles to exploit the full potential of the traction circle. As shown in Figures 7.15 and 7.16, the total energy deployed is 7.38MJ, and the total energy flow through the deployment and regeneration system is 9.473MJ. As listed in Table 7.7, a similar regeneration strategy to that of charge sustaining mode ensures 2.093MJ of energy has been harvested between the MGU-K and MGU-H. As depicted in Figure 7.16, the 7.38MJ breaches the rules and regulations of the total deployment, set out by the WEC regulations. Nevertheless, for testing parameters purposes this scenario shows that all of the energy available can be utilised across a lap, if required and permitted, and as can be seen from Figure 7.15, the net energy deployment usage is 5.2864MJ. Interestingly, if the net usage (rather than total usage) was the regulated limit, this scenario would be within the proposed rules and regulations. This dictates that a smaller capacity ICE engine could be offset against hybrid higher-powered electric motors and permissible electric energy usage to maintain an equilibrium of torque profiles against ICE only vehicles. However, for the energy management parameter analysis, the maximum energy as per rules and regulations need to be adhered to.

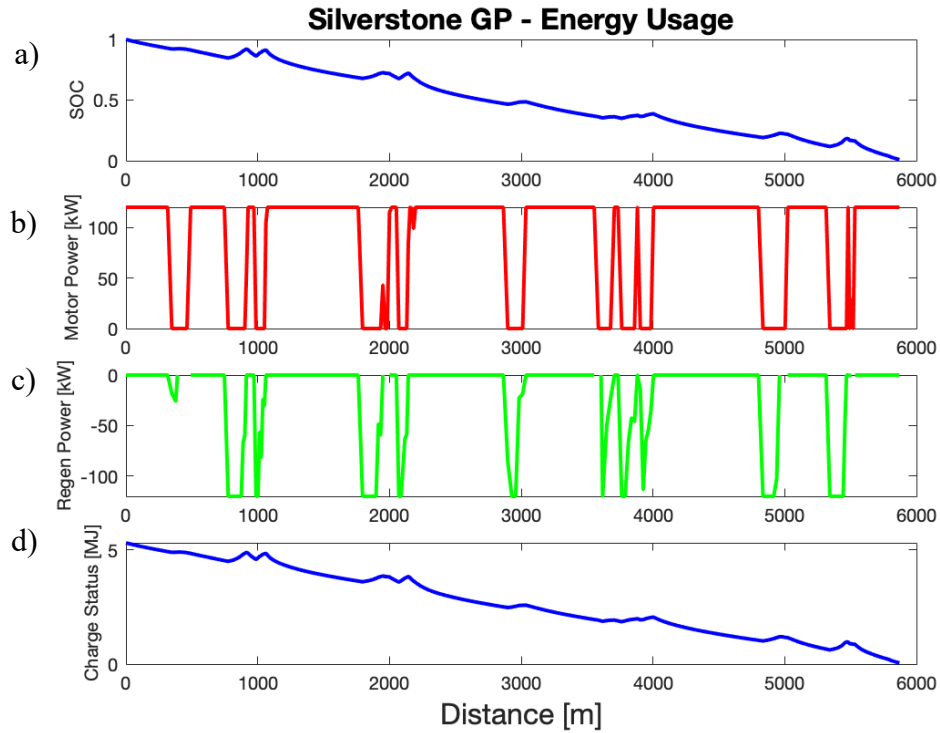


Figure 7.13 a) SOC, b) motor power (kW), c) regeneration power (kW) and d) charge status (MJ) usage for charge depletion during a lap time of 2.02.106.

Table 7.7 Energy usage, one lap of Silverstone GP circuit - charge depleting.

MOPSO				
Energy				
Deployed (MJ)	MGU-K Regen (MJ)	MGU-H Regen (MJ)	Net Deployment (MJ)	SOC end of Lap
7.3797	1.8633	0.23	5.2864	0.0026

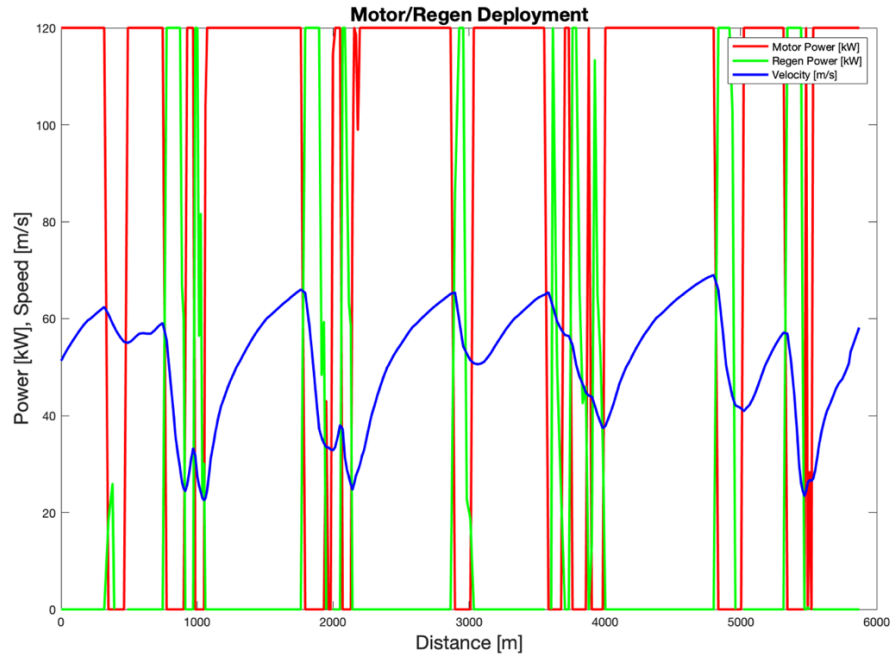


Figure 7.14 Motor power (red) and regeneration power (green) for the charge depleting scenario along with the vehicle velocity.

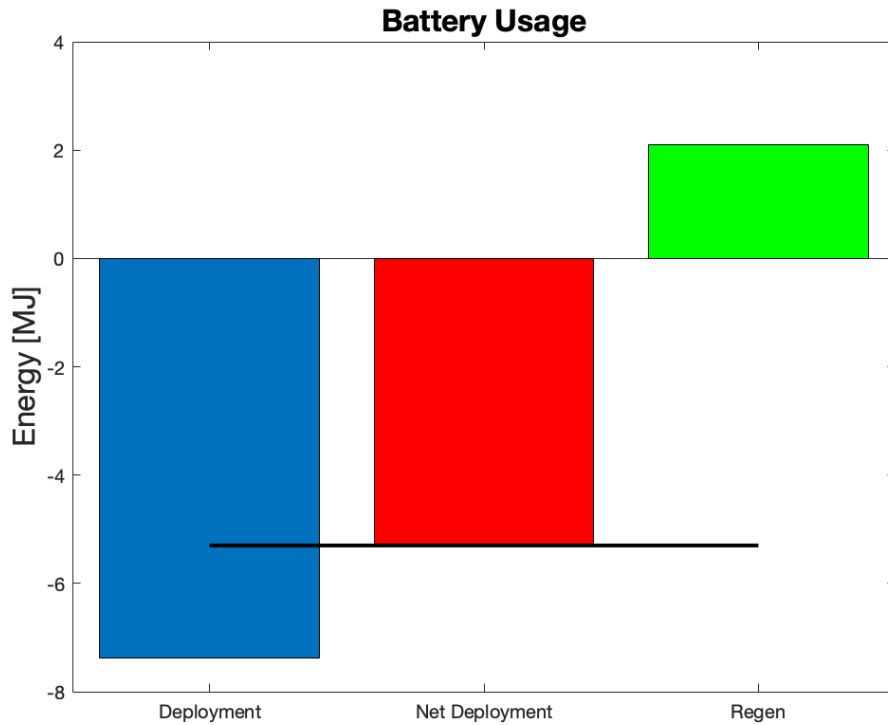


Figure 7.15 Total energy, net energy deployment and regenerated energy for the charge depleting scenario.

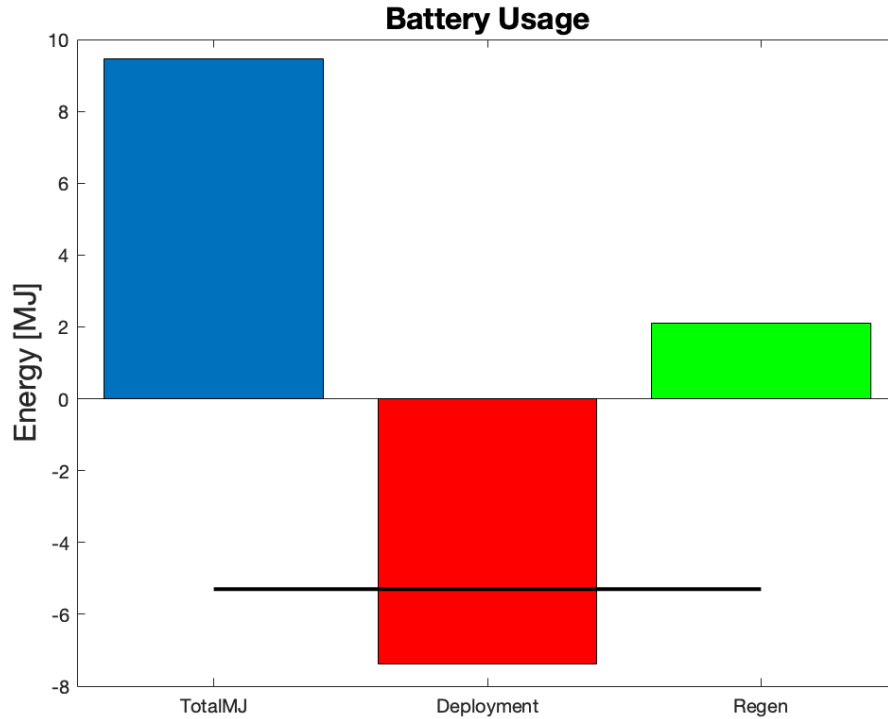


Figure 7.16 Total energy flow, total energy deployment and regenerated energy for the charge depleting scenario (the black line depicts total permissible energy deployment over a single lap).

7.4.4 Maximum Permissible deployment

The final scenario to determine specific set of optimisation variables is for maximum deployment to the FIA rules and regulations at the Silverstone GP for the LMP1 category (5.3MJ per lap). The list of optimisation variables for this scenario are listed in Table 7.8.

Table 7.8 5.3MJ depletion scenario used for energy management evaluation.

	Steering Wheel	Steered Wheels	Velocity	Acceleration	MJ Deploy
Deployment	+/- 0.80 rads	+/- 0.05 rads	≤ 60 m/s	Positive	≤ 5.3
Regeneration (MGU-K)	+/- 2.44 rads	+/- 0.1745 rads	≤ 70 m/s	Negative	SOC ≥ 0
Regeneration (MGU-H)	+/- 2.44 rads	+/- 0.1745 rads	≥ 65 m/s	≤ 1.5 m/s ² > 0 m/s ²	SOC ≥ 0

The controller is enabled to deploy energy earlier within a corner whilst a higher rate of steering angle is applied but limits the maximum velocity allowed for deployment. This is to exploit the lap time improvements associated with additional power at lower speeds as described in Section 7.4.2. This energy management strategy allows the energy across a lap to be depleted by 5.3MJ (Figures 7.17 and 7.20), with the regenerated energy this equates to a net deployment of 3.2MJ (Figure 7.19), and with top speed deployment reduced to less than 60m/s this again allows for a bias towards lower speed, corner exit deployment (Figure 7.18).

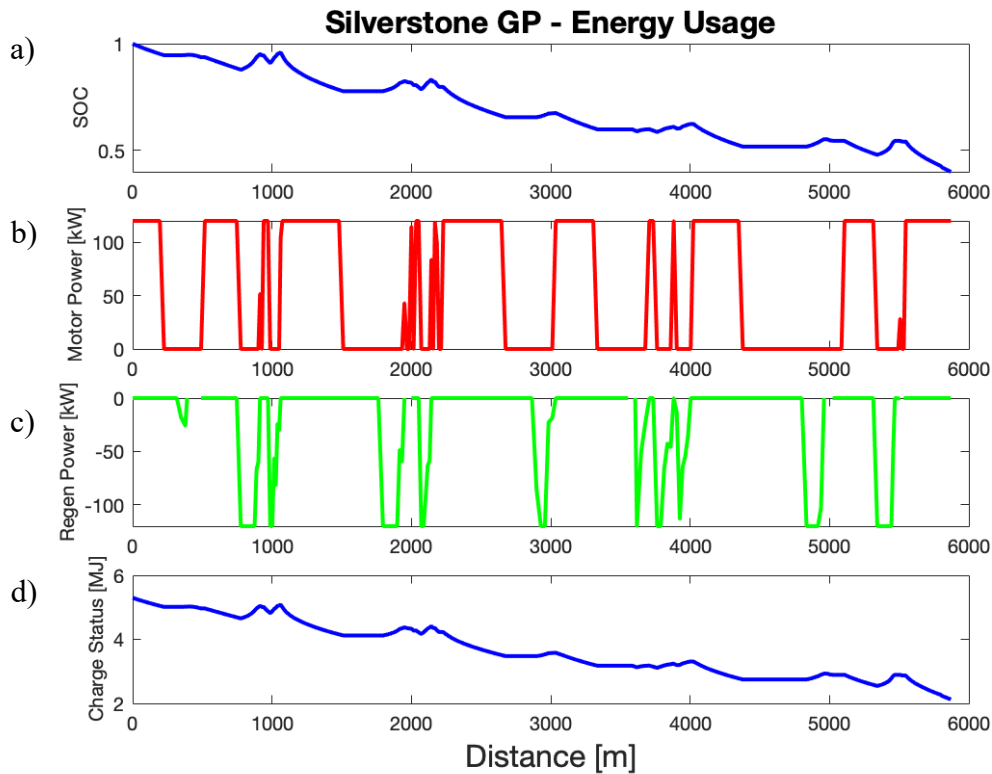


Figure 7.17 a) SOC, b) motor power (kW), c) regeneration power(kW) and d) charge status (MJ) for maximum deployment scenario during the best lap time (2.02.106).

Table 7.9 Energy usage, one lap of Silverstone GP circuit - 5.3MJ charge depleting.

MOPSO				
Energy				
Deployed (MJ)	MGU-K Regen (MJ)	MGU-H Regen (MJ)	Net Deployment (MJ)	SOC end of Lap
5.296	1.8633	0.23	3.2027	0.396

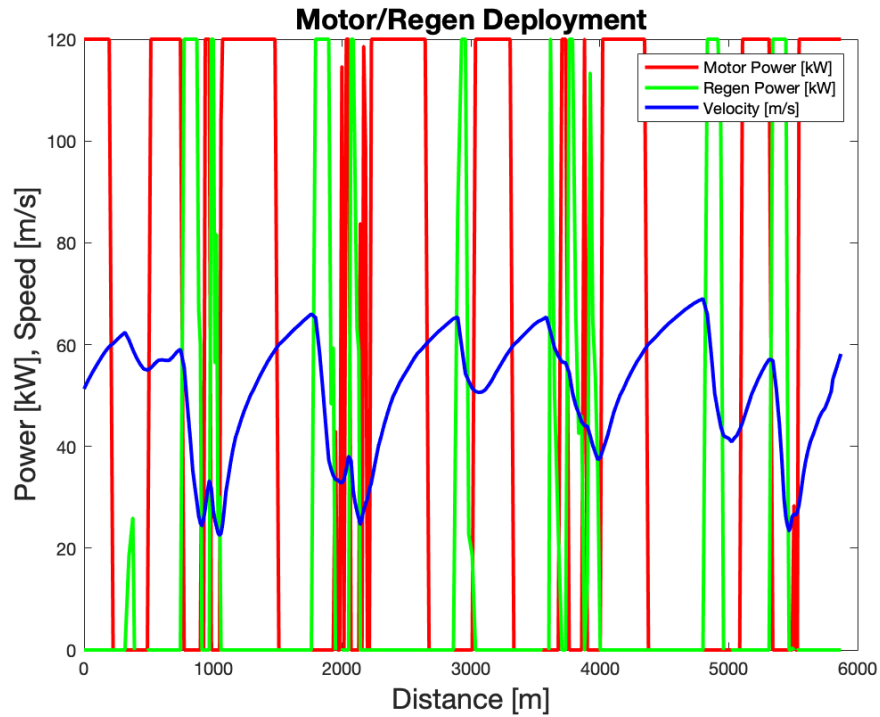


Figure 7.18. Motor power (red) and regeneration power (green) for the maximum deployment scenario along with the vehicle velocity.

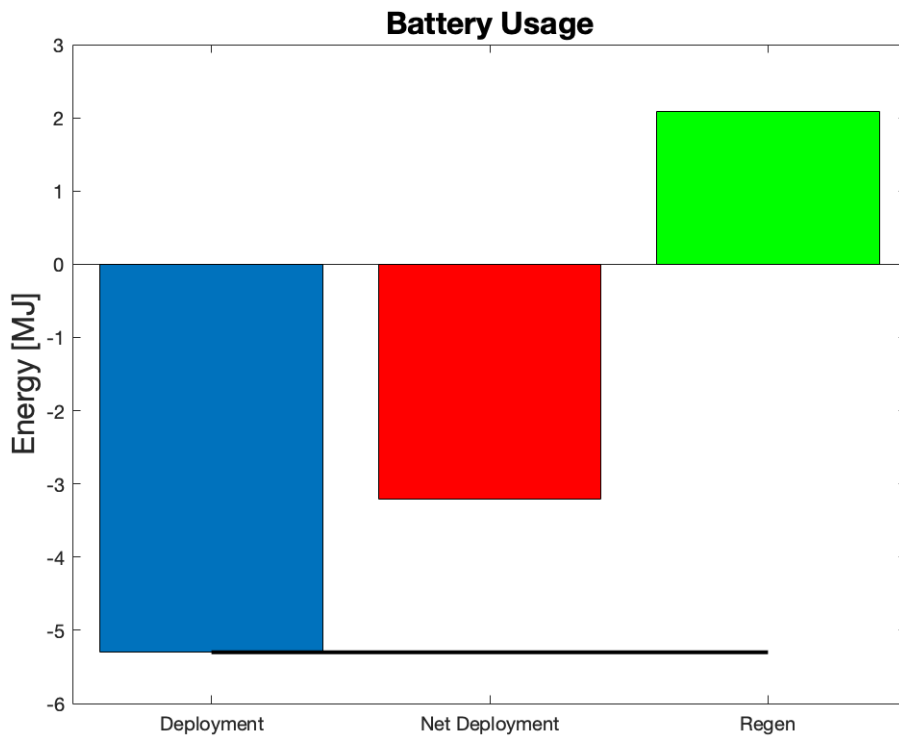


Figure 7.19 Total energy, net energy deployment and regenerated energy for the maximum permissible deployment scenario.

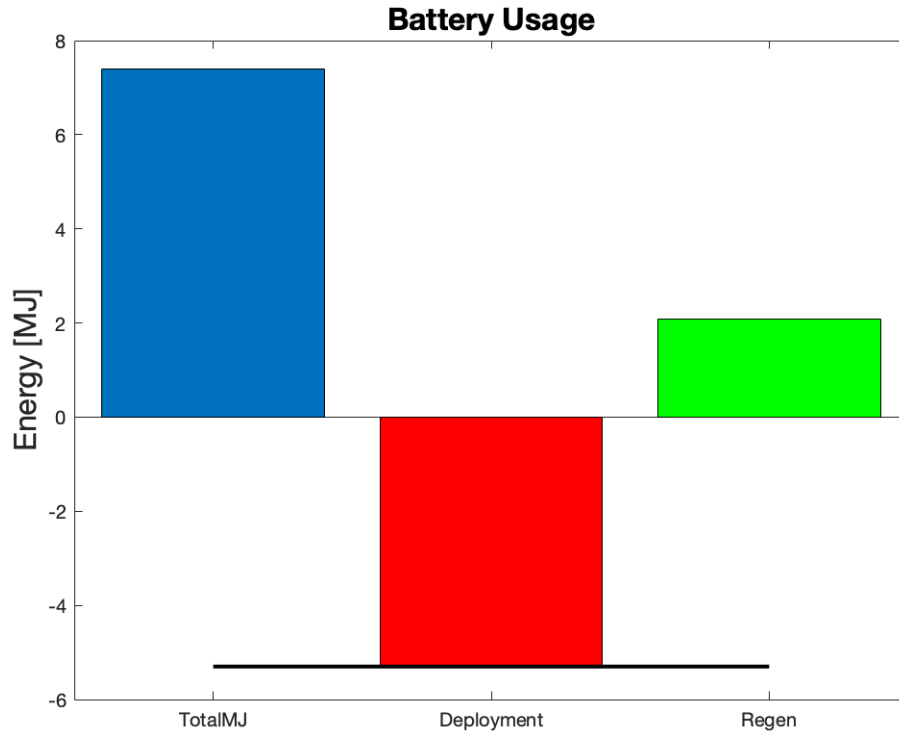


Figure 7.20 Total energy flow, total energy deployment and regenerated energy for the maximum permissible deployment scenario (the black line depicts total permissible energy deployment over a single lap).

7.5 Fuel Use Analysis of the Hybrid Race Vehicle

Utilising the vehicle data acquired from the vehicle trajectory MOPSO in Chapter 6 Section 6.11.3 the steering and vehicle velocity results can be set as input data for the dynamic model as detailed in Chapter 5 (Appendix 8). Considering the hybrid race car powertrain model developed in Chapter 4, it is possible to calculate the fuel consumption profile per lap. Adding the hybrid constraints outlined in Section 7.4, the optimum fastest lap time problem can be formulated and solved using the techniques proposed in Chapter 5. The speed data (Figure 6.51) from the MOPSO results in section 6.11.3 would be used to optimise the powertrain as detailed below.

The wheel speed is a function of the engine RPM and therefore can be calculated from equation (7.4) as

$$W_{RPM} = \frac{ICE_{RPM}}{DR} \Rightarrow V_x = \frac{W_{RPM} \times W_C}{60000} \quad (7.4)$$

where

W_{RPM} is the wheel speed in revolutions per minute.

ICE_{RPM} is the engine speed in revolutions per minute.

DR is the total drive ratio of the gearbox and final drive.

W_C is the wheel circumference (including tyre).

As a race vehicle is in the most efficient gear at all times, based upon the engine RPM, the gear and drive ratio can be calculated for the maximum power delivery. Throttle position (TPS) is derived from the power demand calculated from Equation 7.1 and the engine power look up table generated by the GT Suite model described in Section 4.5. This look up table was produced by setting the engine model to run at 5% increments of throttle position (0 to 100%) and the results stored similar to that as shown in Figure 4.3 albeit in a table format of RPM vs TPS vs Power. Due to the non-disclosure agreement the table of results is omitted. Having the RPM and power demand calculated, the TPS is therefore derived from this 3D look up table containing TPS and RPM vs Power.

For the non-hybrid vehicle studied in Chapter 6, the optimised lap time of 2.02.106 was achieved. The dynamic constraint included in the optimisation were rooted in the engine and power train described in Chapter 4 as well as the range of throttle position and RPM fuel usage sites from the GT Suite model described in Section 4.5. Having the vehicle velocity profile along with the TPS and RPM sites, fuel usage can be found off the brake specific fuel consumption (BSFC) (g-kW/hr) table, shown in Figure 7.21. The vehicle velocity profile achieved as a result of the MOPSO algorithm in Section 6.11.3 and using the TPS and RPM values derived from equations (7.1) and (7.4) the fuel consumption is determined and highlighted with blue dots in Figure 7.21. The fuel used for such vehicles is high octane race fuel. For the engine performance measured data, shown in Figure 4.3, the engine used Sunoco fuel, given as 0.748kg/l [105].

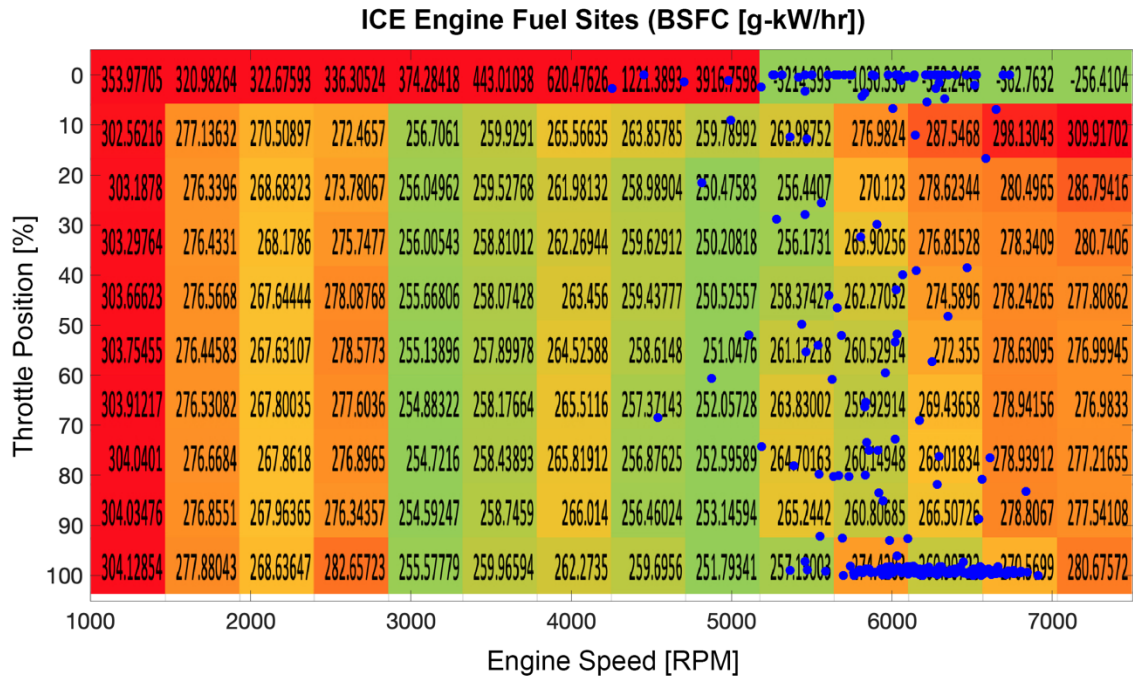


Figure 7.21 Transient engine RPM and throttle sites vs brake specific fuel consumption.

Integrating the brake specific fuel consumption usage data for each segment of track, over the segment time and multiplying by engine power results in the isolation of fuel mass from BSFC which is measured in g-kW/hr. The sum of the mass of fuel used for all segments equates to the mass of fuel used over one lap. In this scenario with a fuel mass of 0.748g per litre, the fuel usage equates to 2.885 litres per lap.

In the previous cases of assuming identical dynamic constraints (maximum acceleration and deceleration) for the race car hybrid engine vehicle (Section 7.4), the vehicle dynamic parameters for the algorithm remain the same as ICE only engine. As such, the optimum lap time achieved as a result of optimisation will be the same as before through all hybrid deployment strategies. Consequently, for all hybrid energy deployment strategies, the throttle sites will be the same for all simulations, however, the deployment time will be different for the hybrid system dependant on energy management strategy.

Integrating the total time of hybrid deployment for each of the energy strategies discussed in section 7.4 and removing the 120kW power and equivalent torque at a given speed from the engine,

the BSFC data can be utilised to analyse the fuel saving for the same total power deployment (reduced ICE output + motor output). Figure 7.22 shows the normalised measured total engine power and torque, simulated engine power and torque, and motor power and torque. When the motor is in use, the power generated from the motor at that point will be taken away from the engine power to maintain equilibrium with the ICE only power and torque.

This offsetting of the engine torque and power against motor torque and power as illustrated in Figure 7.23, confirms a reduction on ICE power between 40% and 85%, permitting the vehicle to generate the equivalent acceleration. Since the force at the driven wheels and the vehicle mass are equal for both non-hybrid and hybrid vehicles, a balance of performance and equivalence of technology is created with this scenario.

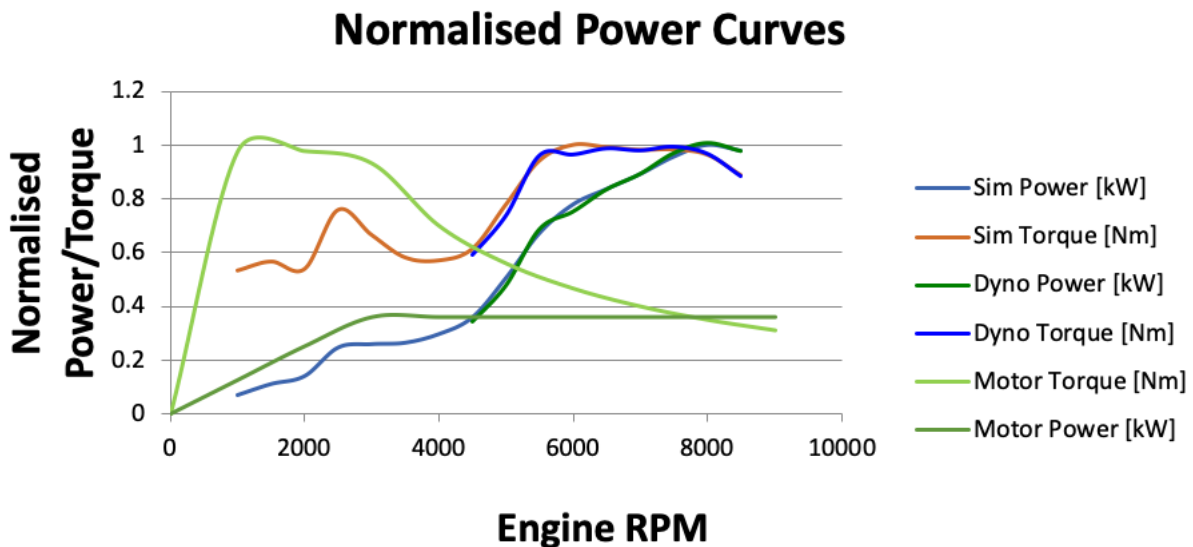


Figure 7.22 Hybrid Powertrain - normalised power and torque deployment.

Normalised Engine Power Usage - Hybrid Motor ON

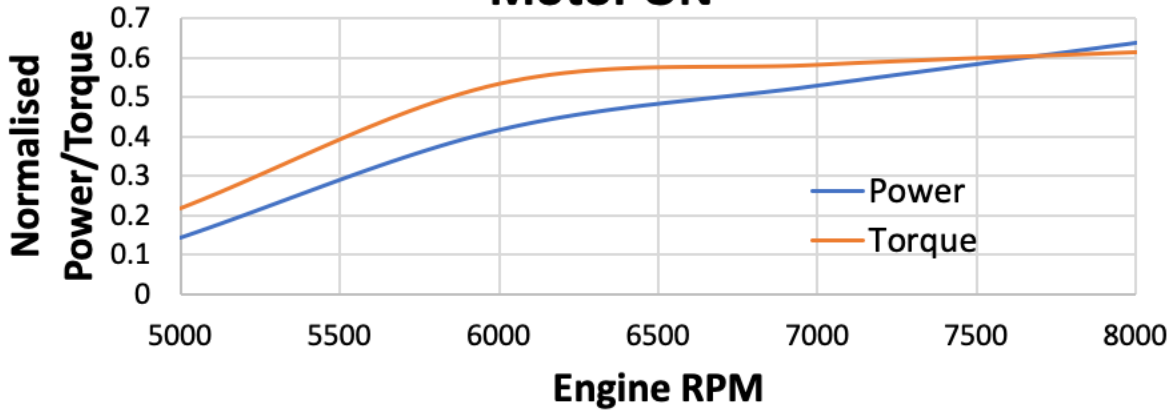


Figure 7.23 Engine power and torque; normalised total use with hybrid Motor ON = Normalised Engine Power - Normalised Motor Power.

Utilising a throttle histogram based on Figure 7.21 the fuelling can be calculated and a reduction in BSFC, and thus fuel saving, can be established per kilowatt-hour. By integrating this over the lap-time, the summation of the fuel usage for each hybrid energy strategy yields a fuel usage between 39.04% to 83.54% of that when the hybrid system is not utilised. The fuel saving results achieved over one lap for various hybrid strategies are listed in Table 7.10.

Table 7.10 Fuel saving over one lap of Silverstone GP for various hybrid strategies.

	Motor Power Deployment time per lap [%]	Fuel Usage per lap [L]	Fuel Usage Difference [% , L]
ICE Only	0	2.885L	N/A
Charge Sustaining	18.45%	2.41L	-16.46%, -0.475L
Charge Depleting (Full)	68.29%	1.127L	-60.94%, -1.758L
Charge Depleting 5.3MJ	54.07%	1.493L	-48.25%, -1.392L

7.6 Fastest Lap Time of the Hybrid Vehicle

A final MOPSO was carried out to determine the lap time with the hybrid energy strategy set to that of maximum permissible usage as per the charge depleting scenario but constrained to 5.3MJ. The cost function for this scenario is the same as presented in (6.36). However, the dynamic constraints presented in Section 6.10; Figure 6.39 has been changed for a harder accelerating vehicle (Figure 7.24). The new dynamic constraint is based upon the engine and hybrid deployment at full deployment rather than offsetting electrical power against mechanical power by once again as in Chapter 5 allowing the vehicle dynamic model presented in Chapter 3 to accelerate at 100% throttle create a new acceleration profile, albeit in this case with the MGU-k set to 100% power as an addition to ICE power.

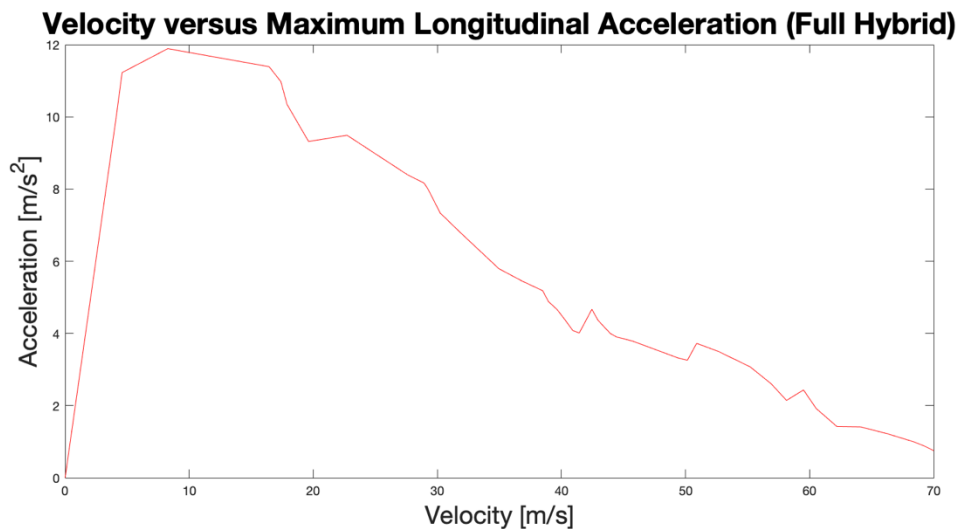


Figure 7.24 Maximum longitudinal acceleration for 100% ICE and Motor deployment.

The aim is to understand the possible gains if the ICE power and torque were maintained and the hybrid system is used as an additional power with a maximum possible additional power of 120kW. By having the increase in torque during the acceleration zones due to the deployment strategy as listed in Table 7.8, the vehicle can accelerate quicker and therefore the higher speeds on the straight aways promote a faster lap time. The results shown in Figure 7.28 clearly confirms an increase in longitudinal acceleration and speed, producing the fastest lap times from the pareto

front ranging between 118.371 seconds (1.58.371 [m.s.ms]) and 118.451 seconds (1.58.451), conferring from Figures 7.25 and 7.26.

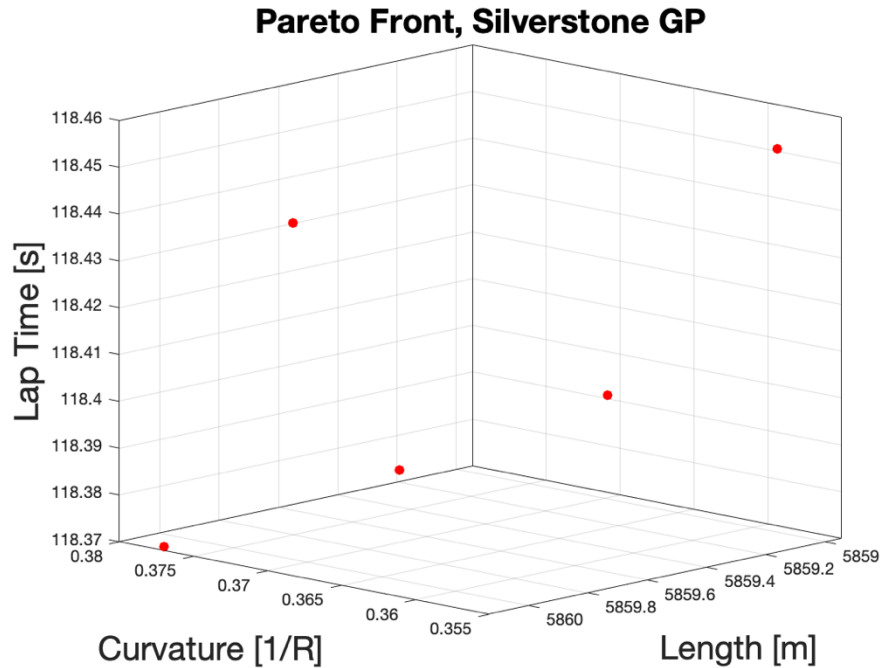


Figure 7.25 Three-dimensional pareto front achieved by running MOPSO algorithm under the maximum permissible deployment scenario.

This fastest lap time is 3.74 seconds faster than the best MOPSO when ICE only or combined hybrid power is utilised and 1.13 seconds faster than a professional driver in a GT3 car. As the hybrid usage was set to utilise 5.3MJ and from the energy management case study detailed in section 7.3.4 the energy can only be deployed at this rate for 2 laps before a recharge is required. Nonetheless, it is inevitable to see that a hybrid category in the WEC GT series would be possible with balance of performance and equivalence of technologies employed. Simple changes to energy deployment limits and weight additions would allow a competitive race series.

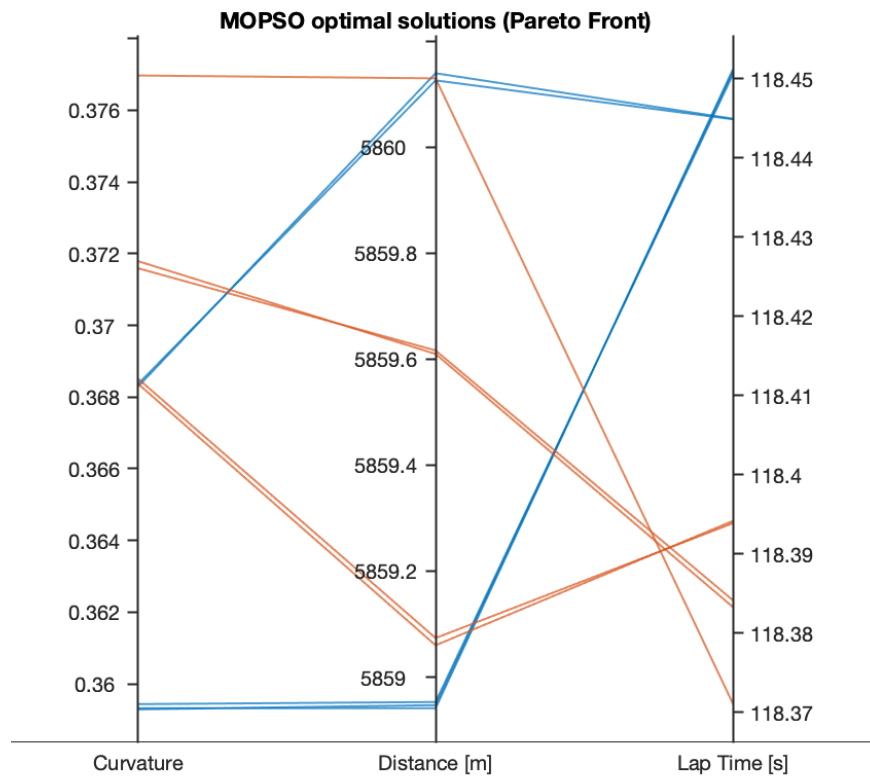


Figure 7.26 Parallel plot results for 5.3MJ deployment, curvature vs distance vs lap time (Orange = Best 50%).

Figure 7.27 depicts the final trajectory for the 1.58.371 lap after smoothed and spline interpolation has taken place. A detailed view of the race car trajectory performance for all corners with both the optimal ICE only and the hybrid race vehicle is provided in Appendix 9. These final trajectories can be utilised as a driving aid to assist drivers with their racing lines, knowing that the vehicle dynamic limits would not be breached.

Silverstone GP - 5.3MJ Hybrid Deployment Trajectory

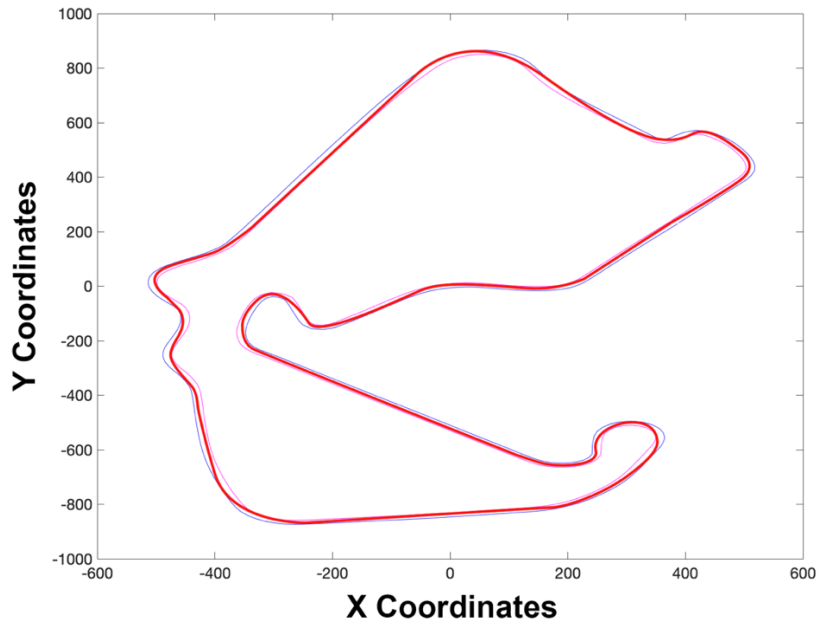


Figure 7.27 The final trajectory achieved after optimisation via MOPSO algorithm and smoothed via the spline method (1.58.371 lap time).

Silverstone GP - Additional Hybrid Deployment

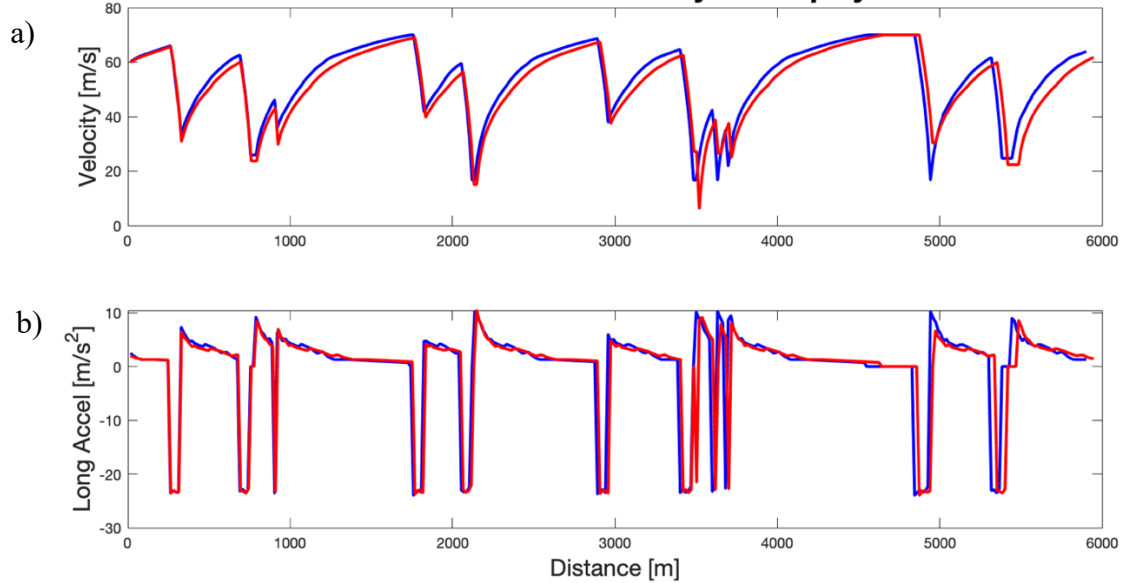


Figure 7.28 Vehicle dynamic outputs, a) vehicle velocity and b) longitudinal acceleration, utilising additional hybrid power (blue line) vs integrated hybrid power (red line).

7.7 Conclusion

A hybrid GT conceptual car has been introduced and tested as a case study to utilise all various simulation and optimisation models produced during this thesis. Such models were produced as a sole necessity to test particle swarm optimisation algorithms for validation of simulation data to physical results. The initial ‘real world’ data ensured a validated model that was produced and used as a basis to inform the next stage (trajectory planning) of the optimisation. It is an excellent conclusion to finalise the thesis by completing each stage of optimisation and utilising the results to inform the next step of modelling and optimisation. The results from one model can inform the next, dynamic model results into trajectory results or vice versa for instance. These trajectory MOPSO results are eventually feeding back into the initial dynamic model, allowing for the fuel analysis to start an iterative process of simulation and optimisation to take place. Moreover, the resultant vehicle dynamic behaviour from the dynamic model can be used to create dynamic constraints for the trajectory and lap time optimisation MOPSO. The results presented in this chapter show the trajectory, lap time, and vehicle dynamic behaviour can be optimised for a vehicle simulation model and produce an output of that of modern-day GT cars, resulting in a realisation that a robust model has been produced enabling PSO to be fully scrutinised and assessed as an alternative to other optimisation algorithms.

8. Conclusion and Future Work

8.1 Conclusion

A suite of simulation models and optimisation packages has been presented. The suite of programmes has proven to be robust with coherent validated results produced against ‘real world’ physical measured data taken from logged race vehicle data. The problems posed have been confronted from an academic, empirical and practical stance to ensure vigorous critical analysis of the simulation models and optimisation techniques. With limitation to a 2.3 GHz Quad-Core Intel Core i7, 16GB RAM personal computer an optimisation suite has proved to produce accurate results in reasonable simulation times and with the development of algorithms for optimisation tuning parameters, improvements to mutation algorithms and the use of sensitivity analysis, the accurate and validated results have been produced within a sensible computing time constraint.

Sensitivity analysis provides an insight into the parameter estimation problem and assists with generating appropriate search spaces for the PSO algorithm. Tuning of the PSO is inevitable as the crowd population size, and weighting and acceleration coefficients can affect the PSO considerably. However, once a robust optimisation model has been produced, the results can be very effective and achieved in suitable time constraints.

Although an initial aim was to produce a one-stop simulation process the complexity of the modelling and inevitable development of succinct and accurate models, the computing time took precedence over a complete simulation programme. However, the simulation and optimisation package produced, dissects the required model validation and optimisation algorithms into three clear areas; 1. Model correlation and validation – simulated vehicle parameters and vehicle dynamic behaviour validation through optimisation. 2. Optimisation - trajectory planning, racing line optimisation, vehicle dynamic optimisation and lap time optimisation, 3. Simulation - modelling of vehicle and engine transient behaviour. This process allows a continuous research and development loop to be established.

As discussed in the literature review there are conflicting theories for particle swarm optimisation accuracy and convergence time. Sensitivity analysis assists with reducing errors of search space parameters and aids with the reduction in accuracy and convergence time. The main observations taken from the results presented over the past three chapters are

- Large search space parameters and incorrectly tuned acceleration and velocity coefficients can generate local best costs restricting the final solution.
- Large population sizes can assist in finding an area of global best costs, enabling secondary PSO algorithms to be used with a tighter search space ensuring global best fixation.
- PSO input parameter size can affect output results. Trajectory planning highlighted this when 360 input parameters were utilised. Reducing this amount produced sensible and realistic results in a preferred simulation time.
- Accurate results are obtained when population size is appropriate to input parameter size
- Increasing iteration or population size increases simulation time by a factor of 2, increasing both population and iteration size results in a time multiplication of a factor of 4.
- Appropriately tuned parameters and population sizes ensure fast, accurate convergence.

The optimisation presented addresses one of the major issues with simulation models, the adage attached to simulation; results that are produced are only as good as the inputs entered.

Validation of model outputs, and therefore input parameters is a must within the motorsport industry as simulation continues a meteoric rise, borne from the testing embargo in race series such as WEC, IMSA and F1. The use of the MOPSO to reduce the error between measured data and simulation results enables a fast (49 minutes with a standard computation power), accurate, fully validated, simulation model to be developed. From this point forward further analysis of vehicle dynamic changes, component changes or race strategies can be optimised and assess again in fast time frames.

In the endeavour to robustly test PSO algorithms, a suite of motorsport engineering simulation models has been produced and a cycle of optimisation has been created, closing of the loop feels like the story has reached its conclusion.

The novelty of the thesis was to develop:

1. *A simulation product within Matlab® and Simulink® that includes the validation of vehicle dynamic models through particle swarm optimisation algorithms.*

A transient dynamic model has been developed and both SOPSO and MOPSO has been implemented to generate appropriate results to aid in the validation of industry simulation models.

2. *Trajectory planning and race line optimisation using particle Swarm Optimisation*

Trajectory planning, race line optimisation and lap time analysis has been performed through the development of SOPSO and MOPSO algorithms.

3. *The integration of energy management optimisation and vehicle dynamic behaviour for any race circuit or road orientation*

Integrated energy management control and optimisation has been implemented however the simulations are not integrated together. Due to computer performance and a search for balance of simulation time, aim 1 is utilised to inform the optimisation and vehicle simulations in aim 2. Aim 3 has been integrated with simulation models detailed in aims 2 and 3, independently. This thesis was carried out on a 2.3 GHz Quad-Core Intel Core i7, 16GBRAM personal Mac computer. Future work would include a complete integration of all 3 simulations with powerful computing or cloud-based computing so as to maintain reasonable simulation times.

In the endeavour of these novelties the aims and objectives of this thesis were

- i. *Determine appropriate degrees of freedom model for optimal balance of accuracy of results and computing speed.*

Through validation of measured results versus simulated results, the use of PSO algorithms and analysis of data, a balance of vehicle dynamic degrees of freedom model versus computation time and simulation result error output has been created that produces appropriate and reasonable results.

ii. Design and develop vehicle dynamics model in Matlab® and Simulink®.

Vehicle dynamic and lap time simulation models have been created in Matlab and Simulink

iii. Design and develop power-train and drive-train model in GT-Power, Matlab® and Simulink®.

Engine simulation models validated to measured data from a dynamometer have been created and results utilised in an integrated transient vehicle dynamic model.

iv. Design and develop hybrid electrical system model in Matlab® and Simulink®.

A Hybrid Energy system has been modelled and integrated independently into a transient vehicle dynamic model and lap time simulation and trajectory model.

v. Establish system input and output functions for control system design and optimisation for energy management

A control system was created for a vehicle dynamic model and published in [26], further control parameters were developed to integrate into the energy management algorithms within the MOPSO.

vi. Develop race circuit modelling algorithm.

Algorithms and mathematical models for Trajectory planning, race line optimisation and lap time optimisation have been created and results validated.

vii. Evaluate through simulation and model analysis appropriate control and optimisation solutions.

Simulation and analysis of Energy optimisation, vehicle dynamic behaviour validation and lap time optimisation has produced appropriate vehicle dynamic and energy control modelling.

8.2 Future Work

Several areas of exploration are envisaged for future work, with such an elaborate set of simulation tools and models this work was too large to analyse other forms of optimisation and the aims of work was to fully explore particle swarm optimisation and its benefits and limits. A similarly sized study utilising other optimisation techniques and algorithms, NSGA-II for instance, would be complementary to this research. Detailed control strategies would also be a deep exploratory exercise that could aid the models. Furthermore, as computing power continues to progress the introduction of artificial intelligence and enhance machine learning would be a future exploratory research possibility whereby the algorithms could learn appropriate optimisation algorithms and trends for engineering problems. Software in the loop and Driver in the loop simulation could also be a next step to enhance the software suite presented in this research. With improvements in computing power inevitable the vehicle dynamics model can be developed with the inclusion of full suspension systems to create complex multi-degrees of freedom models.

One area particularly of note and one that has been identified by the author as the next steps is to couple the PSO algorithms set out in this work to Industry Standard software to limit the error when generating models that require thorough validation.

Bibliography

- [1] Lot, R. Biral, F. (2014). A Curvilinear Abscissa Approach for the Lap Time Optimization of Racing Vehicles. *Proceedings of the 19th World Congress. The International Federation of Automatic Control*. p7559-7565.
- [2] Fédération Internationale de l'Automobile (2017). *2017 F1 Technical Regulations*. 6th ed. France: Fédération Internationale de l'Automobile. p37-45, p102.
- [3] Ehsani, M. Gao, Y. and Emadi, A. (2009). *Modern Electric, Hybrid Electric and Fuel Cell Vehicles. Fundamentals, Theory and Design*. 2nd ed. Florida: CRC Press, Taylor and Francis Group. p126-149.
- [4] Schofield, B. (2006). *Vehicle Dynamics Control for Rollover Prevention* Department of Automatic Control, Lund Institute of Technology, Lund University.
- [5] Newton, I (Sir) (1848). *The Principia*. New York: Republished 1995 Prometheus Books. p1.
- [6] Pacejka, H.B (2012). *Tyre and Vehicle Dynamics*. 3rd ed. Oxford: Butterworth-Heinemann. p8-17.
- [7] Sugiyama, H. Suda, Y. (2009). Non-linear elastic ring tyre model using the absolute nodal coordinate formulation. *Proceedings of the Institution of Mechanical Engineers, Journal of Multi-body Dynamics*. 223 (K), p211-219.
- [8] Maniowski, M. (2016). Optimisation of driver actions in RWD race car including tyre thermodynamics. *Vehicle System Dynamics International Journal of Vehicle Mechanics and Mobility*. 54 (4), p526-544.
- [9] Nowlan, D. (2010). Characterising the performance of the racing tyre. In: Nowlan, D. *The Dynamics of the Race Car*. Sydney: University of Sydney. p.13 - 44.
- [10] Lundahl, K. Aslund, J. and Nielsen, L. (2013). Vehicle Dynamics Platform, Experiments and Modelling, Aiming at Critical Manoeuvre Handling. *Technical report: LiTH-ISY-R-3064*. 1 (1), p1-19.
- [11] Reeves, K. Taylor, C.J, Montazeri, A. (2016). Validation of a Hybrid Electric Vehicle dynamics model for energy management and vehicle stability control. *2016 IEEE 25th International Symposium on Industrial Electronics (ISIE)*. 1 (1), p. 1-6.

- [12] Timings, J. and Cole, D. (2011). Efficient minimum manoeuvre time optimisation of an oversteering vehicle at constant forward speed. *American Control Conference*. 1 (1), p. 5267 - 5272
- [13] Limebeer, D.J.N. Perantoni, G and Rao, A.V. (2014). Optimal control of formula one car energy recovery systems. *International Journal of Control*. 87 (10), p2065-2080. Rev. 2016-03-07.
- [14] Kelly, D.P. and Sharp, R.S. (2010). Time-optimal control of the race car: a numerical method to emulate the ideal driver. *International Journal of Vehicle Mechanics and Mobility*. 48 (Vehicle System Dynamics), p1461-1474.
- [15] Milliken, W.F & Milliken, D.L W.F. & Milliken, D.L. (1995). *Race Car Vehicle Dynamics*. London: SAE International. p.129-143
- [16] Society of Automotive Engineers. (2008). Vehicle Dynamics Terminology. *SAE International Surface Vehicle Recommended Practice J670*. Rev. 2008-01-24.
- [17] Hong, J. Kim, S and Min, B. (2009). Drivability Development Based on CoSimulation of AMESim Vehicle Model and Simulink HCU Model for Parallel Hybrid Electric Vehicle. *SAE Technical Paper*. 2009-01-0725 (10.4271/2009-01-0725), p2.
- [18] Ehsani, M. Gao, Y. and Miller, M. (2007). Hybrid Electric Vehicles: Architecture and Motor Drives. *Proceedings of the IEEE*. 95 (4), p79-728.
- [19] Moura, S.J. Fathy, H.K. Callaway, D.S. and Stein, J.L. (2011). A Stochastic Optimal Control Approach for Power Management in Plug-In Hybrid Electric Vehicles. *IEEE Transaction on Control Systems Technology*. 19 (3), p.545-555.
- [20] Wirasingha, S.G. and Emadi, A. (2011). Classification and Review of Control Strategies for Plug-In Hybrid Electric Vehicles. *IEEE Transactions on Control Systems Technology*. 60 (1), p.111-122.
- [21] MSC Software Corporation. (2017). *Adams: The Multibody Dynamics Simulation Solution*. Available: <http://www.mscsoftware.com/product/adams>. Last accessed 26th June 2017.
- [22] AVL GmbH. (2017). *Balance Performance, Fuel Economy and Emissions*. Available : <https://www.avl.com/-/avl-cruise->. Last accessed 26th June 2017.
- [23] Lapsim. (2017). *Lapsim Hybrid*. Available: <http://www.lapsim.nl/hybrid-license.html>. Last accessed 26th June 2017.

- [24] Gamma Technologies (2017). *GT Drive 2017 User Manual*. Chicago: Gamma Technologies. p6.
- [25] Hotten, R. (2015). *Volkswagen: The scandal explained*. Available: <http://www.bbc.co.uk/news/business-34324772>. Last accessed 26th June 2017.
- [26] Reeves, K. Montazeri, A. and Taylor, C.J. (2016). Model development and energy management control for hybrid electric race vehicles. *11th International Conference on Control (CONTROL), 2016 UKACC*. 1 (1), p. 1-6.
- [27] Mizuno, M. (2003). Development of Tire Side Force Model Based on “Magic Formula” with the influence of Tire Surface Temperature. *R & D Review of Toyota CRDL: Modelling, Analysis and Control Methods for Improving Vehicle Dynamic Behaviour*. 38 (4), p.17-22.
- [28] Février, P., & Fandard, G. (2006, December). Thermal and mechanical tyre force and moment modelling. In *Tire. Wheel. Tech, TÜV SÜD Automotive GmbH Congress, Munich December* (pp. 5-6).
- [29] Ellis, J.R. (1994). *Vehicle Handling Dynamics*. Hoboken: Wiley-Blackwell. p 100 - 108
- [30] Lundahl, K. Aslund, J. and Nielsen, L. (2012). Investigating vehicle model detail for close to limit manoeuvres aiming at optimal control. *Technical report*. 1 (1), p.2.
- [31] Berntorp, K. (2013). Derivation of a Six Degrees-of-Freedom Ground-Vehicle Model for Automotive Applications. *Technical Paper ISSN 0280-5316*. 1 (1), p.13-15.
- [32] Nowlan, D. (2012). *Deriving a Tyre Model from Nothing*. Available: http://www.chassissim.com/blog/wp-content/uploads/2011/10/DN_RCE_Tyre_Model_basics.pdf. Last accessed 27th June 2016.
- [33] Feverier, P and Fandard, G. (2008). Thermal and mechanical tyre modelling for handling simulation. *ATZ Worldwide: Designing Brake and Steering*. 110 (26), p26-31.
- [34] Segers, J (2014). *Analysis Techniques for Racecar Data Acquisition*. 2nd ed. Warrendale: SAE International. p83-87.
- [35] Perantoni, G and Limebeer, D. J. (2014). Optimal control for a formula one car with variable parameters. *Vehicle System Dynamics*. 52 (5), p.1–27.
- [36] Nowlan, D. (2010). Stability and Control. In: Nowlan, D. *The Dynamics of the Race Car*. Sydney: University of Sydney. p.112 - 138.
- [37] Limebeer, D.J.N. and Rao, A.V. (2015). Faster, Higher and Greener. *IEEE Control Systems Magazine*. April 2015 (1), p.36-56.

- [38] Limebeer, D.J.N. (2015). *Reducing lap times and fuel consumption in F1*. Available: <https://tv.theiet.org/?videoid=7599>. Last accessed 28th June 2017.
- [39] Smith, D. E and Starkey, J.M. (1995). Effects of Model Complexity on the Performance of Automated Vehicle Steering Controllers: Model Development, Validation and Comparison. *Vehicle System Dynamics: International Journal of Vehicle Mechanics and Mobility*. 24 (2), p.163-181.
- [40] Wirasingha, S.G. and Emadi, A. (2011). Classification and Review of Control Strategies for Plug-In Hybrid Electric Vehicles. *IEEE Transactions on Vehicular Technology*. 60 (1), p111-122.
- [41] Aghaali, H. and Ångström, H. E. (2015). A review of turbo compounding as a waste heat recovery system for internal combustion engines. *Renewable and Sustainable Energy Reviews*. 49 (1), p.813-824.
- [42] Limebeer, D.J.N. Perantoni, G and Rao, A.V. (2014). Optimal control of formula one car energy recovery systems. *International Journal of Control*. 87 (10), p2065-2080. Rev. 2016-03-07.
- [43] Canale, M. Fagiano, L. and Razza, V. "Vehicle lateral stability control via approximated NMPC: real-time implementation and software-in-the-loop test," *Proceedings of the 48th IEEE Conference on Decision and Control (CDC) held jointly with 2009 28th Chinese Control Conference*, Shanghai, 2009, pp. 4596-4601.
- [44] Vyas, M. Sarath, H. Smitha, K. and Bagubali, A. "A strategy and framework for analysis of operational data of automotive radars for development of active safety systems," *2017 2nd IEEE International Conference on Recent Trends in Electronics, Information & Communication Technology (RTEICT)*, Bangalore, 2017, pp. 2176-2181.
- [45] Zulkifli, Saiful & Dali, Muhd. (2017). Development of vehicle powertrain simulation module by interfacing Matlab-ADVISOR to LabVIEW. 128-133.
- [46] Khastgir, S. Birrell, S. Dhadyalla, G. and Jennings, P. "Development of a Drive-in Driver-in-the-Loop Fully Immersive Driving Simulator for Virtual Validation of Automotive Systems," *2015 IEEE 81st Vehicular Technology Conference (VTC Spring)*, Glasgow, 2015, pp. 1-4.

- [47] Khosravani, S. Khajepour, A. Fidan, B. Chen, S. and Litkouhi, B. "Development of a robust vehicle control with driver in the loop," *2014 American Control Conference*, Portland, OR, 2014, pp. 3482-3487.
- [48] Yang, Z. Zhou, Y. and Liang, S. "Sliding mode control of chaos vibrations in 7-DOF nonlinear active vehicle suspension," *2017 International Conference on Advanced Mechatronic Systems (ICAMechS)*, Xiamen, 2017, pp. 467-471.
- [49] Yakub, F. Muhammad, Daud, P. Z. H. C. Fatah, A. Y. A. and Mori, Y. "Ride comfort quality improvement for a quarter car semi-active suspension system via state-feedback controller," *2017 11th Asian Control Conference (ASCC)*, Gold Coast, QLD, 2017, pp. 406-411.
- [50] Zhang, J. Sun, W. and Jing, H. "Nonlinear Robust Control of Antilock Braking Systems Assisted by Active Suspensions for Automobile," 2019, in *IEEE Transactions on Control Systems Technology*, vol. 27, no. 3, pp. 1352-1359.
- [51] Sanchez, E. and Nazari, M. H. "Component validation process for high performance hybrid electric race vehicle," *2016 IEEE Green Energy and Systems Conference (IGSEC)*, Long Beach, CA, 2016, pp. 1-8.
- [52] Reeves, K. Montazeri, A. and Taylor, C.J. (2016). Model development and energy management control for hybrid electric race vehicles. *11th International Conference on Control (CONTROL), 2016 UKACC*. 1 (1), p. 1-6.
- [53] Ebbesen, S. Salazar, M. Elbert, P. Bussi, C. and Onder, C.H. "Time-optimal Control Strategies for a Hybrid Electric Race Car," in *IEEE Transactions on Control Systems Technology*, vol. 26, no. 1, 2108, pp. 233-247.
- [54] Lot, R. Biral, F. (2014). A Curvilinear Abscissa Approach for the Lap Time Optimization of Racing Vehicles. *Proceedings of the 19th World Congress. The International Federation of Automatic Control*. p7559-7565.
- [55] Altché, F. Polack, P. and de La Fortelle, A. "High-speed trajectory planning for autonomous vehicles using a simple dynamic model," *2017 IEEE 20th International Conference on Intelligent Transportation Systems (ITSC)*, Yokohama, 2017, pp. 1-7.
- [56] Cowlagi, R. V. and Zhang, Z. "Motion-planning with linear temporal logic specifications for a nonholonomic vehicle kinematic model," *2016 American Control Conference (ACC)*, Boston, MA, 2016, pp. 6411-6416.

- [57] Subroto, R. K. "Vehicle stability control of 4WD electric vehicle using combined adaptive sliding mode controller and control allocation method," *2017 IEEE 3rd International Future Energy Electronics Conference and ECCE Asia (IFEEEC 2017 - ECCE Asia)*, Kaohsiung, 2017, pp. 812-817.
- [58] Zhang, W. Li, D. Wang, W. Wang, J. and Peng, H. "A rollover warning algorithm for vehicles based on dangerous speeds considering the suspension and dynamic characteristics," *2017 IEEE International Conference on Cybernetics and Intelligent Systems (CIS) and IEEE Conference on Robotics, Automation and Mechatronics (RAM)*, Ningbo, 2017, pp. 411-416.
- [59] Galpin, M. (2018). *F1 Simulators revealed*. Available: <https://www.racecar-engineering.com/articles/f1/f1-simulators-revealed/>. Last accessed 02 Feb 2020.
- [60] Federation Internationale de l'Automobile. (2019). LMP1-H Hybrid Systems. *WEC 2019 Technical Regulations*. 1 (7), 42.
- [61] Federation Internationale de l'Automobile. (2019). *Formula 1 2019 Technical Regulations*.
- [62] Federation Internationale de l'Automobile. (2019). *Formula-e 2019 Technical Regulations*.
- [63] Joint Air Quality Unit. (2017). Principles for setting up Clean Air Zones in England. *Clean Air Zone Framework*. 1 (1), 23.
- [64] Bloomberg NEF. (2019). *New Energy Outlook 2019*. Available: <https://bnef.turtl.co/story/neo2019/?teaser=true>. Last accessed 02 Feb 2020.
- [65] Reeves, K. Taylor, C.J, Montazeri, A.. (2016). Validation of a Hybrid Electric Vehicle dynamics model for energy management and vehicle stability control. *2016 IEEE 25th International Symposium on Industrial Electronics (ISIE)*. 1 (1), p. 1-6.
- [66] Kirli, A. "Design and application of an active suspension system on a 6 DOF half vehicle model," *2015 XXV International Conference on Information, Communication and Automation Technologies (ICAT)*, Sarajevo, 2015, pp. 1-6.
- [67] Timings, J. and Cole, D. (2011). Efficient minimum manoeuvre time optimisation of an oversteering vehicle at constant forward speed. *American Control Conference*. 1 (1), p. 5267-5272
- [68] Schofield, B. (2006). *Vehicle Dynamics Control for Rollover Prevention* Department of Automatic Control, Lund Institute of Technology, Lund University.

- [69] Kelly, D.P. and Sharp, R.S. (2010). Time-optimal control of the race car: a numerical method to emulate the ideal driver. *International Journal of Vehicle Mechanics and Mobility*. 48 (Vehicle System Dynamics), p1461-1474.
- [70] Reyes-Sierra, M. and Coello, C.A. (2006). Multi-Objective Particle Swarm Optimizers: A Survey of the State-of-the-Art. *International Journal of Computational Intelligence Research*. Vol. 2 (3), 287–308.
- [71] Sheng, L.K et al. Multi-Objective Particle Swarm Optimization Algorithms – A Leader Selection Overview. *International Journal of Simulation: Systems, Science & Technology*. 6 – 19.
- [72] van den Bergh, F. (2006). Empirical Analysis of PSO Characteristics. In: *An Analysis of Particle Swarm Optimisers*. Pretoria: University of Pretoria. 134-143.
- [73] Parsopoulos, K & Vrahatis, N. (2010). Established and Recently Proposed Variants of Particle Swarm Optimization. In: Klingler, K *Particle Swarm Optimization and Intelligence: Advances and Applications*. New York: Information Science Reference. 116-119.
- [74] Federation Internationale de l'Automobile. (2009). LMP1-H Hybrid Systems. *WEC 2014 Technical Regulations*. 1 (7), 42.
- [75] Federation Internationale de l'Automobile. (2014). Equivalence Systems. *WEC 2014 Technical Regulations*. 1 (6), 36.
- [76] Federation Internationale de l'Automobile. (2014). Powertrain & Energy Recovery Systems. *Formula 1 Technical Regulations*. 1 (1.21 - 1.27), 6-8.
- [77] Federation Internationale de l'Automobile. (2018). *New 2020 Hypercar Regulations approved*. Available: <https://www.fiawec.com/en/news/new-2020-hypercar-regulations-approved/6186>. Last accessed 31st January 2020.
- [78] British Touring Car Championship. (2018). *Hybrid Energy coming to the BTCC*. Available: <http://www.btcc.net/2018/08/01/hybrid-energy-coming-to-the-btcc/>. Last accessed 31st January 2020.
- [79] Mahmoodabadia, M.J. Safaieb, A. Bagheric, A. & Nariman-zadeh, N. (2013). A novel combination of Particle Swarm Optimization and Genetic Algorithm for Pareto optimal design of a five-degree of freedom vehicle vibration model. *Applied Soft Computing*. 13 (1), 2577-2591.
- [80] F. Klück, M. Zimmermann, F. Wotawa and M. Nica, "Genetic Algorithm-Based Test Parameter Optimization for ADAS System Testing," *2019 IEEE 19th International Conference*

on Software Quality, Reliability and Security (QRS), Sofia, Bulgaria, 2019, pp. 418-425.

doi: 10.1109/QRS.2019.00058

[81] L. Zhang, C. Lin and X. Niu, "Optimization of Control Strategy for Plug-in Hybrid Electric Vehicle Based on Differential Evolution Algorithm," *2009 Asia-Pacific Power and Energy Engineering Conference*, Wuhan, 2009, pp. 1-5.

[82] J. Kennedy and R. Eberhart, "Particle swarm optimization," *Proceedings of ICNN'95 - International Conference on Neural Networks*, Perth, WA, Australia, 1995, pp. 1942-1948 vol.4.

doi: 10.1109/ICNN.1995.488968

[83] Montazeri, A West, C Monk, S.D. & Taylor, C.J.. (2017). Dynamic modelling and parameter estimation of a hydraulic robot manipulator using a multi-objective genetic algorithm. *International Journal of Control*. 90 (4), 661-683.

[84] Zheng, W. (2017). A Multi-Objective Particle Swarm Optimization Algorithm Approach for Parameter Optimization of a 7 DOF Robotic Manipulator. *Masters Thesis*. 1 (1), 52-63.

[85] Fan, Z Wang, T Cheng, Z Li, G & Gu, F. (2017). An Improved Multiobjective Particle Swarm Optimization Algorithm Using Minimum Distance of Point to Line. *Shock & Vibration*. 1 (1), 1-16. Drehmer, L.R.C. Casas, W. J. P. & Gomes, H.M. "Parameters

[86] Drehmer, L.R.C. Casas, W. J. P. & Gomes, H.M. "Parameters optimisation of a vehicle suspension system using a particle swarm optimisation algorithm," *Vehicle System Dynamics*, vol. 53, no. 4, pp. 449–474, 2015.

[87] Bouazara, M. Richard, M. J. (2001) "An optimal design method to control the vibrations of suspensions for passenger cars," *International Mechanical Engineering Congress and Exposition: The Winter Annual Meeting of ASME*, pp. 61–68.

[88] Jamali, A. Hajiloo, A. Nariman-zadeh, N. (2010) "Reliability-based robust Pareto design of linear state feedback controllers using a multi-objective uniform-diversity genetic algorithm (MUGA)," *Expert Systems with Applications* 37 (1), pp. 401–413.

[89] Wang, C.Y. Xu, Z. J. & Zhao, W. Z. (2016). "Parameter optimization of automotive suspension system based on particle swarm algorithm." *WSEAS transactions on systems and control*. 1 (1), 608-615.

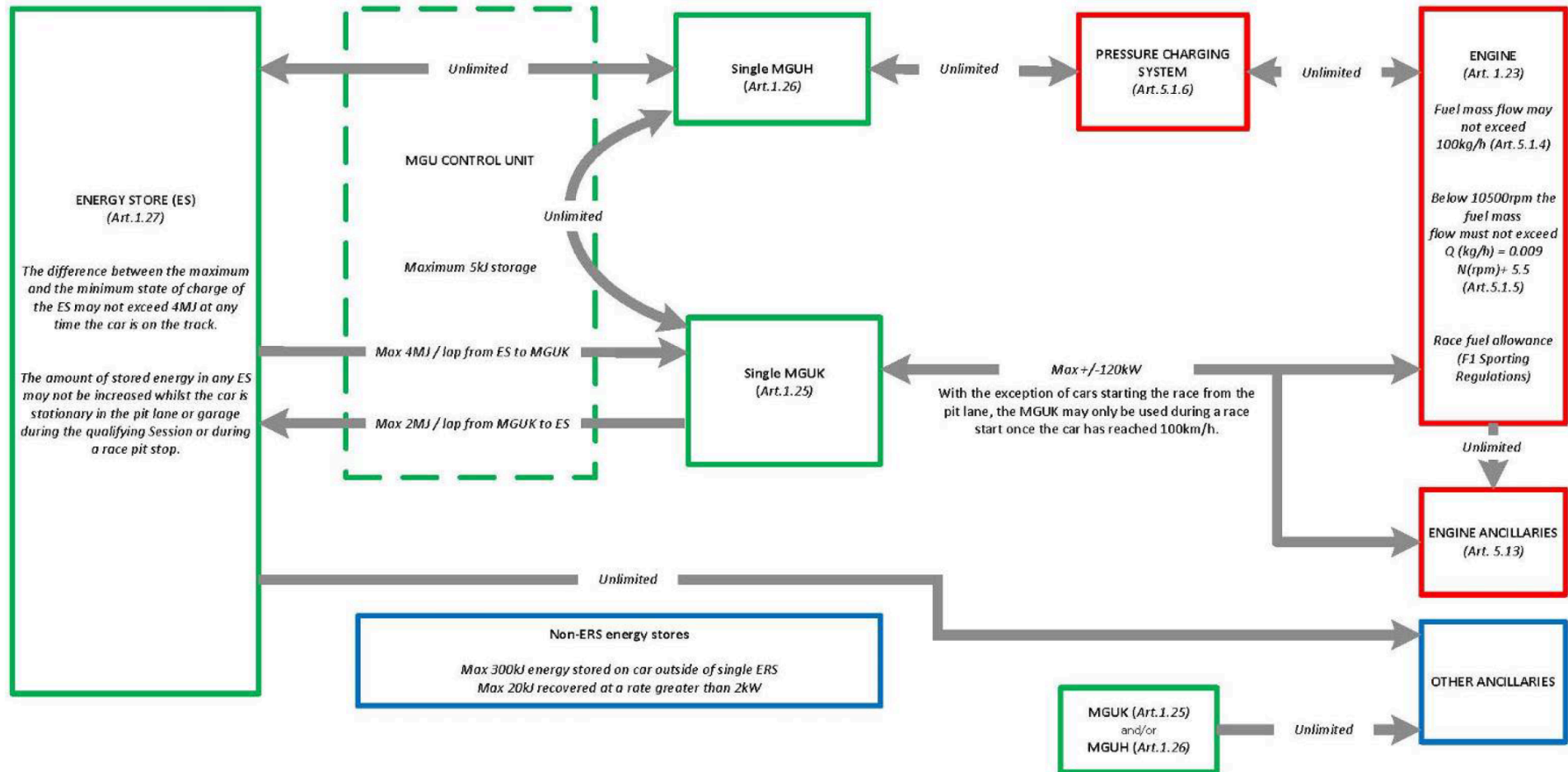
[90] Alagappan, A.V. Narasimha Rao, K.V. & Kumar, R. K. (2015) "A comparison of various algorithms to extract Magic Formula tyre model coefficients for vehicle dynamics simulations", *Vehicle System Dynamics*, 53:2, 154-178.

- [91] Nariman-Zadeh, N. Salehpour, M Jamali, A. & Haghgoo, E (2010). "Pareto optimization of a five-degree of freedom vehicle vibration model using a multi-objective uniform-diversity genetic algorithm (MUGA)." *Engineering Applications of Artificial Intelligence*. 23 (1), 543-551.
- [92] Fu, M. Ni, J. Li, X & Hu, J. (2018). "Path tracking for autonomous race car based on g-g diagram." *International Journal of Automotive Technology*. 19 (4), 659-668.
- [93] Timings, J & Cole, D (2014). Robust lap-time simulation. *Journal of Automobile Engineering*. 228 (10), 1200-1216.
- [94] Rizano, T. Fontanelli, D. Palopoli, L. Pallottino, L. & Salaris, P. "Local motion planning for robotic race cars " in Conference on Decision and Control (CDC) 2013 submitted.[Online]. Available: <http://www.centropiaggio.unipi.it/sites/default/files/CDC13-LocalPlanning.pdf>.
- [95] Jacob, J. Colin, J. A. Montemayor, H. Sepac, D. Trinh, H. D. Voorderhake, S. F. & Lomonova, E. A. (2015). InMotion hybrid racecar : F1 performance with LeMans endurance. *COMPEL: The International Journal for Computation and Mathematics in Electrical and Electronic Engineering*, 34(1), 210-233.
- [96] Braghin, F. Melzi, S. Sabbioni, E. & Poerio, N. (2011). Identification of the optimal trajectory for a race driver. *Proceedings of the ASME 2011 International Design Engineering Technical Conferences & Computers and Information in Engineering Conference*. 1 (1), 1-8.
- [97] Cardamone, L. Loiacono, D. Lanzi, P.L. and Bardelli, A.P. "Searching for the optimal racing line using genetic algorithms," *Proceedings of the 2010 IEEE Conference on Computational Intelligence and Games*, Dublin, 2010, pp. 388-394.
- [98] Beelitz, W.D. (2017). *TORCS Robot Development*. Available: <http://torcs.sourceforge.net/index.php?name=News&topic=3>. Last accessed 31st January 2020.
- [99] Marques, L. H. V. B.. (2016). Optimal Lap Time for a Race Vehicle. *Masters Thesis*. 1 (5), p. 63-75.
- [100] Federation Internationale de l'Automobile (2019). *Balance of Performance for 2019 FIA GT3 specifications*. France: Federation Internationale de l'Automobile. p1.
- [101] SRO Motorsports Group. (2019). *2019 Race Results – Silverstone*. Available: <https://www.gt-world-challenge-europe.com/results/2019/blancpain-gt-series-endurance-cup-silverstone>. Last accessed 9th June 2020.

- [102] Daley, P. (2019). *British GT Championship - Round 5 - 8th/9th June - Silverstone - 2019*. Available: <https://www.tsl-timing.com/event/192305>. Last accessed 9th June 2020.
- [103] Alkamel Systems. (2011). *WEC 6 Hours of Silverstone*. Available: <http://fiawec.alkamelsystems.com>. Last accessed 27/08/20.
- [104] Mavros, G. (2010). Contact mechanics of tyre–road interactions and its role in vehicle shuffle. *Tribology and Dynamics of Engine and Powertrain Fundamentals, Applications and Future Trends*. 1 (1), p703-734.
- [105] Sunoco Race Fuels. (2020). *260GT 105 RON Race Fuel Data Sheet*. Available: <https://www.sunocoracefuels.com/fuel/260-gt>. Last accessed 21st Sept 2020.
- [106] Federation Internationale de l'Automobile. (2019). Equivalence Systems (Technologies and Performance). In: *Federation Internationale de l'Automobile 2019-2020 FIA World Endurance Championship Sporting Regulations*. France: Federation Internationale de l'Automobile. p35-36.
- [107] A Montazeri, J Poshtan, “GA-based optimization of a MIMO ANC system considering coupling of secondary sources in a telephone kiosk,” *Applied Acoustics* 70 (7), 945-953.
- [108] A Montazeri, J Poshtan, “Optimizing a multi-channel ANC system for broadband noise cancellation in a telephone kiosk using genetic algorithms,” *Shock and Vibration* 16 (3), 241-260.
- [109] C West, A Montazeri, SD Monk, CJ Taylor, “A genetic algorithm approach for parameter optimization of a 7DOF robotic manipulator,” *IFAC-PapersOnLine* 49 (12), 1261-1266.
- [110] C West, A Montazeri, SD Monk, D Duda, CJ Taylor, “A new approach to improve the parameter estimation accuracy in robotic manipulators using a multi-objective output error identification technique,” *26th IEEE International Symposium on Robot and Human Interactive*, pp. 1406-1411, Lisbon, Portugal, 2017

Appendices

Appendix 1 – Formula One Hybrid Powertrain Energy Flow



Appendix 2. Comparison of Single objective PSO results versus simulated baseline data

Table A2.1. Specific corner and a full lap results comparison for tyre and chassis parameters and their relative error compared to the baseline for the longitudinal velocity SOPSO including sum of all parameter errors.

SOPSO comparison of baseline variables to simulated data (Longitudinal Velocity)																							
	Tyre Parameters																		Chassis Parameters				
	rBx1	rBx2	rCx1	rEx1	rEx2	rHx1	rBy1	rBy2	rBy3	rCy1	rEy1	rEy2	rHy1	rHy2	rVy1	rVy2	rVy3	rVy4	rVy5	rVy6	kroll	croll	
Baseline	13.200	-13.900	1.140	0.317	0.109	-0.009	14.600	10.900	0.016	1.140	0.389	0.358	-0.064	-0.049	0.560	18.500	0.019	0.020	1.900	19.200	100000.00	19000.00	
Abbey	11.729	-15.000	0.000	1.000	0.720	-0.020	14.396	10.232	0.049	2.661	0.450	0.000	-0.200	-0.200	1.089	16.572	0.100	0.008	1.496	20.481	115000.00	15000.00	
The Loop	14.711	-15.000	2.000	0.628	0.973	-0.020	11.707	12.977	0.037	1.243	0.540	0.000	-0.200	-0.200	2.241	18.835	0.077	0.015	0.064	23.758	115000.00	15000.00	
Luffield	11.530	-15.000	1.764	0.907	0.659	-0.020	14.204	10.000	0.008	1.978	0.744	0.000	-0.200	-0.200	3.000	16.143	0.076	0.080	0.916	19.055	115000.00	25000.00	
Maggots/Becketts	10.138	-15.000	0.743	0.244	0.900	-0.020	13.106	12.370	0.000	1.513	0.823	0.000	-0.200	-0.200	2.374	15.307	0.068	0.100	1.833	21.788	91474.96	19112.28	
Vale	10.000	-15.000	2.000	0.521	0.041	-0.020	13.833	10.000	0.017	3.000	0.658	0.000	-0.200	-0.200	2.358	17.476	0.000	0.009	5.000	21.945	115000.00	15783.73	
Silverstone GP	13.592	-15.000	0.664	0.423	0.223	-0.020	15.000	12.653	0.018	0.907	0.731	0.000	-0.200	-0.200	0.000	17.510	0.024	0.033	4.839	17.709	100000.04	19000.02	
Relative Error																						Sum	
Abbey	0.111	0.079	1.000	2.155	5.601	1.336	0.014	0.061	2.134	1.334	0.156	1.000	2.150	3.065	0.944	0.104	4.319	0.583	0.213	0.067	0.150	0.211	26.786
The Loop	0.114	0.079	0.754	0.981	7.931	1.336	0.198	0.191	1.371	0.091	0.388	1.000	2.150	3.065	3.001	0.018	3.112	0.253	0.966	0.237	0.150	0.211	27.597
Luffield	0.127	0.079	0.548	1.860	5.048	1.336	0.027	0.083	0.504	0.735	0.912	1.000	2.150	3.065	4.357	0.127	3.029	2.939	0.518	0.008	0.150	0.316	28.918
Maggots/Becketts	0.232	0.079	0.349	0.230	7.256	1.336	0.102	0.135	1.000	0.327	1.115	1.000	2.150	3.065	3.240	0.173	2.615	3.926	0.035	0.135	0.085	0.006	28.590
Vale	0.242	0.079	0.754	0.642	0.620	1.336	0.053	0.083	0.092	1.632	0.691	1.000	2.150	3.065	3.211	0.055	1.000	0.576	1.632	0.143	0.150	0.169	19.375
Silverstone GP	0.030	0.079	0.417	0.333	1.048	1.336	0.027	0.161	0.142	0.204	0.879	1.000	2.150	3.065	1.000	0.054	0.293	0.613	1.547	0.078	0.000	0.000	14.456

Table A2.2. Specific corner and a full lap results comparison for tyre and chassis parameters and their relative error compared to the baseline for the lateral acceleration SOPSO including sum of all parameter errors.

SOPSO comparison of baseline variables to simulated data (Lateral Acceleration)																							
	Tyre Parameters																			Chassis Parameters			
	rBx1	rBx2	rCx1	rEx1	rEx2	rHx1	rBy1	rBy2	rBy3	rCy1	rEy1	rEy2	rHy1	rHy2	rVy1	rVy2	rVy3	rVy4	rVy5	rVy6	kroll	croll	
Baseline	13.200	-13.900	1.140	0.317	0.109	-0.009	14.600	10.900	0.016	1.140	0.389	0.358	-0.064	-0.049	0.560	18.500	0.019	0.020	1.900	19.200	100000.00	19000.00	
Abbey	13.454	-15.000	0.564	0.733	0.354	-0.020	15.000	14.894	0.025	0.000	0.260	0.000	-0.200	-0.200	3.000	15.015	0.010	0.084	5.000	25.000	85000.00	25000.00	
The Loop	14.884	-15.000	2.000	0.071	0.007	-0.020	15.000	15.000	0.000	0.000	0.705	0.000	-0.200	-0.200	3.000	15.682	0.000	0.079	5.000	19.870	115000.00	20426.16	
Luffield	10.781	-15.000	0.000	0.810	0.000	-0.020	10.536	11.641	0.050	2.116	1.000	0.000	-0.200	-0.200	3.000	20.000	0.000	0.008	5.000	25.000	115000.00	25000.00	
Maggots/Becketts	11.383	-15.000	0.000	1.000	0.168	-0.020	14.784	12.989	0.031	0.890	1.000	0.000	-0.200	-0.200	1.585	16.952	0.089	0.027	5.000	16.026	85000.00	25000.00	
Vale	12.739	-15.000	1.311	1.000	0.409	-0.020	11.811	10.041	0.050	0.000	0.260	0.000	-0.200	-0.200	3.000	19.654	0.100	0.080	5.000	20.144	115000.00	25000.00	
Silverstone GP	12.318	-15.000	0.882	1.000	0.116	-0.020	12.087	13.088	0.029	3.000	0.000	0.000	-0.200	-0.200	2.786	17.307	0.028	0.061	0.000	24.307	100000.47	18999.97	
Relative Error																						Sum	
Abbey	0.019	0.079	0.505	1.311	2.251	1.336	0.027	0.366	0.586	1.000	0.331	1.000	2.150	3.065	4.357	0.188	0.457	3.123	1.632	0.302	0.150	0.316	24.552
The Loop	0.128	0.079	0.754	0.776	0.935	1.336	0.027	0.376	0.996	1.000	0.811	1.000	2.150	3.065	4.357	0.152	1.000	2.894	1.632	0.035	0.150	0.075	23.729
Luffield	0.183	0.079	1.000	1.554	1.000	1.336	0.278	0.068	2.205	0.856	1.571	1.000	2.150	3.065	4.357	0.081	1.000	0.628	1.632	0.302	0.150	0.316	24.811
Maggots/Becketts	0.138	0.079	1.000	2.155	0.538	1.336	0.013	0.192	1.016	0.219	1.571	1.000	2.150	3.065	1.830	0.084	3.759	0.320	1.632	0.165	0.150	0.316	22.727
Vale	0.035	0.079	0.150	2.155	2.750	1.336	0.191	0.079	2.205	1.000	0.332	1.000	2.150	3.065	4.357	0.062	4.319	2.961	1.632	0.049	0.150	0.316	30.372
Silverstone GP	0.067	0.079	0.227	2.155	0.064	1.336	0.172	0.201	0.884	1.632	1.000	1.000	2.150	3.065	3.975	0.064	0.499	1.993	1.000	0.266	0.000	0.000	21.828

Table A2.3. Specific corner and a full lap results comparison for tyre and chassis parameters and their relative error compared to the baseline for the yaw rate SOPSO including sum of all parameter errors.

SOPSO comparison of baseline variables to simulated data (Yaw Rate)																							
	Tyre Parameters																		Chassis Parameters				
	rBx1	rBx2	rCx1	rEx1	rEx2	rHx1	rBy1	rBy2	rBy3	rCy1	rEy1	rEy2	rHy1	rHy2	rVy1	rVy2	rVy3	rVy4	rVy5	rVy6	kroll	croll	
Baseline	13.200	-13.900	1.140	0.317	0.109	-0.009	14.600	10.900	0.016	1.140	0.389	0.358	-0.064	-0.049	0.560	18.500	0.019	0.020	1.900	19.200	100000.00	19000.00	
Abbey	14.870	-15.000	1.760	0.472	0.703	-0.020	12.305	13.367	0.042	2.279	0.378	0.000	-0.200	-0.200	0.484	17.405	0.091	0.000	3.485	21.294	85000.00	15000.00	
The Loop	10.000	-15.000	0.399	0.599	1.000	-0.020	13.520	14.132	0.050	1.861	1.000	0.000	-0.200	-0.200	0.000	16.866	0.006	0.027	0.691	25.000	85000.00	25000.00	
Luffield	14.216	-15.000	1.907	0.365	0.960	-0.020	12.034	11.881	0.049	2.395	0.776	0.000	-0.200	-0.200	1.516	16.612	0.044	0.015	0.292	15.000	85000.00	15000.00	
Maggots/Becketts	13.600	-15.000	0.107	0.686	0.067	-0.020	12.451	10.820	0.033	2.926	0.868	0.000	-0.200	-0.200	0.307	16.748	0.048	0.001	1.388	19.679	100600.58	16079.96	
Vale	12.466	-15.000	1.280	0.000	0.286	-0.020	13.951	15.000	0.050	0.541	0.867	0.000	-0.200	-0.200	3.000	17.770	0.026	0.045	0.000	15.000	115000.00	25000.00	
Silverstone GP	11.976	-15.000	0.000	0.675	0.091	-0.020	13.363	15.000	0.037	2.053	0.996	0.000	-0.200	-0.200	2.955	16.167	0.100	0.000	2.809	25.000	99999.90	18999.94	
Relative Error																					Sum		
Abbey	0.127	0.079	0.544	0.490	5.450	1.336	0.157	0.226	1.710	0.999	0.029	1.000	2.150	3.065	0.135	0.059	3.834	1.000	0.834	0.109	0.150	0.211	23.694
The Loop	0.242	0.079	0.650	0.890	8.174	1.336	0.074	0.297	2.205	0.632	1.571	1.000	2.150	3.065	1.000	0.088	0.682	0.350	0.636	0.302	0.150	0.316	25.890
Luffield	0.077	0.079	0.673	0.151	7.809	1.336	0.176	0.090	2.158	1.101	0.996	1.000	2.150	3.065	1.707	0.102	1.364	0.244	0.846	0.219	0.150	0.211	25.705
Maggots/Becketts	0.030	0.079	0.906	1.165	0.386	1.336	0.147	0.007	1.087	1.567	1.231	1.000	2.150	3.065	0.453	0.095	1.544	0.967	0.269	0.025	0.006	0.154	17.668
Vale	0.056	0.079	0.123	1.000	1.622	1.336	0.044	0.376	2.205	0.525	1.228	1.000	2.150	3.065	4.357	0.039	0.390	1.212	1.000	0.219	0.150	0.316	22.492
Silverstone GP	0.093	0.079	1.000	1.130	0.164	1.336	0.085	0.376	1.368	0.801	1.561	1.000	2.150	3.065	4.276	0.126	4.304	1.000	0.478	0.302	0.000	0.000	24.695

Appendix 3. Comparison of multi-objective PSO results versus simulated baseline data

Table A3.1. Specific corner and a full lap results comparison for tyre and chassis parameters and their relative error compared to the baseline for the MOPSO including sum of all parameter errors.

Comparison of baseline variables to simulated data (Multi-objective)																							
	Tyre Parameters																		Chassis Parameters				
	rBx1	rBx2	rCx1	rEx1	rEx2	rHx1	rBy1	rBy2	rBy3	rCy1	rEy1	rEy2	rHy1	rHy2	rVy1	rVy2	rVy3	rVy4	rVy5	rVy6	kroll	croll	
Baseline	13.200	-13.900	1.140	0.317	0.109	-0.009	14.600	10.900	0.016	1.140	0.389	0.358	-0.064	-0.049	0.560	18.500	0.019	0.020	1.900	19.200	100000.00	19000.00	
Abbey	11.207	-15.000	1.992	0.984	0.967	-0.020	10.000	15.000	0.033	2.965	0.000	0.000	-0.200	-0.200	2.963	15.377	0.002	0.027	0.000	24.984	85537.38	18438.79	
The Loop	14.736	-15.000	2.000	0.947	0.449	-0.020	10.000	13.345	0.016	1.170	0.000	0.000	-0.200	-0.200	1.329	20.000	0.000	0.100	0.691	24.195	85000.00	15539.39	
Luffield	11.298	-15.000	0.221	0.030	0.751	-0.020	15.000	14.257	0.041	1.096	0.293	0.000	-0.200	-0.200	0.244	16.646	0.056	0.055	4.765	25.000	97114.37	7955.41	
Maggots/Becketts	11.101	-15.000	1.055	0.818	0.888	-0.020	13.491	11.622	0.030	0.692	0.963	0.000	-0.200	-0.200	2.843	17.487	0.051	0.077	3.538	21.931	98990.03	6751.38	
Vale	10.188	-15.000	0.882	0.814	0.213	-0.020	15.000	10.000	0.002	0.280	1.000	0.000	-0.200	-0.200	3.000	15.003	0.026	0.000	5.000	23.985	85000.00	15000.00	
Silverstone GP	10.000	-15.000	0.000	0.325	0.226	-0.020	10.000	15.000	0.001	0.000	0.000	0.000	-0.200	-0.200	1.843	19.049	0.000	0.019	0.674	15.000	85000.00	25269.44	
Relative Error																					Sum		
Abbey	0.151	0.079	0.747	2.105	7.871	1.336	0.315	0.376	1.086	1.601	1.000	1.000	2.150	3.065	4.291	0.169	0.880	0.312	1.000	0.301	0.145	0.030	30.011
The Loop	0.116	0.079	0.754	1.988	3.121	1.336	0.315	0.224	0.020	0.027	1.000	1.000	2.150	3.065	1.373	0.081	1.000	3.926	0.637	0.260	0.150	0.182	22.805
Luffield	0.144	0.079	0.806	0.905	5.892	1.336	0.027	0.308	1.654	0.038	0.248	1.000	2.150	3.065	0.565	0.100	1.985	1.720	1.508	0.302	0.029	0.581	24.442
Maggots/Becketts	0.159	0.079	0.074	1.582	7.142	1.336	0.076	0.066	0.899	0.393	1.477	1.000	2.150	3.065	4.078	0.055	1.722	2.794	0.862	0.142	0.010	0.645	29.805
Vale	0.228	0.079	0.227	1.567	0.952	1.336	0.027	0.083	0.845	0.754	1.571	1.000	2.150	3.065	4.357	0.189	0.361	1.000	1.632	0.249	0.150	0.211	22.033
Silverstone GP	0.242	0.079	1.000	0.024	1.069	1.336	0.315	0.376	0.908	1.000	1.000	1.000	2.150	3.065	2.291	0.030	1.000	0.084	0.645	0.219	0.150	0.330	18.314

Appendix 4. MOPSO results versus SOPSO

Table A4.1. Full lap results comparison of the vehicle dynamic data error (simulated versus PSO). SOPSO results show the error and best cost for each specific dynamic optimisation algorithm (longitudinal velocity, lateral acceleration and yaw rate) as opposed to all three vehicle dynamic outputs within the MOPSO.

Comparison of Best Cost, Errors and Sum of Errors (SOPSO vs MOPSO)																								
	Abbeyy			The Loop				Luffield				Maggots/Becketts			Vale			Silverstone GP						
	SOPSO Vx	SOPSO Ay	SOPSO Yaw	MOPSO	SOPSO Vx	SOPSO Ay	SOPSO Yaw	MOPSO	SOPSO Vx	SOPSO Ay	SOPSO Yaw	MOPSO	SOPSO Vx	SOPSO Ay	SOPSO Yaw	MOPSO	SOPSO Vx	SOPSO Ay	SOPSO Yaw	MOPSO	SOPSO Vx	SOPSO Ay	SOPSO Yaw	MOPSO
Best Cost	-0.0521	-1.9596	-0.0692	-2.06	-0.0226	-1.4749	-0.0890	-1.60	-0.0688	-3.5003	-0.0230	-3.57	-0.0077	-3.5307	-0.0037	-3.55	-0.0224	-1.9265	-0.1000	-2.23	0.0000	0.0000	0.0000	-1.30
Error Vx	0.0003	0.0004	0.0003	0.0004	0.0000	0.0000	0.0001	0.0000	0.0001	0.0001	0.0001	0.0001	0.0000	0.0000	0.0000	0.0000	0.0002	0.0002	0.0002	0.0002	0.0000	0.0000	0.0000	0.0000
Error Ay	0.1853	0.1711	0.1906	0.1793	0.0806	0.0722	0.0939	0.0699	0.1056	0.1056	0.1060	0.1069	0.0811	0.0857	0.0802	0.0801	0.2605	0.2597	0.2597	0.2615	0.0000	0.0000	0.0000	0.0040
Error Yaw	0.0001	0.0001	0.0001	0.0001	0.0001	0.0001	0.0001	0.0001	0.0000	0.0000	0.0000	0.0000	0.0000	0.0000	0.0000	0.0000	0.0003	0.0003	0.0003	0.0003	0.0000	0.0000	0.0000	0.0000
Sum of Error (Vx)	26.786				27.597				28.918				28.590				19.375				14.456			
Sum of Error (Ay)		24.552				23.729				24.811				22.727				30.372				21.828		
Sum of Error (Yaw)			23.694				25.890				25.705			17.668					22.492				24.695	
Sum of Total Error																								
Sum of Total Error	SOPSO Average			MOPSO	SOPSO Average			MOPSO	SOPSO Average			MOPSO	SOPSO Average			MOPSO	SOPSO Average			MOPSO	SOPSO Average			MOPSO
Sum of Total Error	25.011			30.011	25.739			22.805	26.478			24.442	22.995			29.805	24.080			22.033	20.326			18.314

Appendix 5. Trajectory Parameters

Table A5.1. SOPSO shortest path Trajectory parameters 500 segment lap.

Test	c1	c2	w	Length	Iteration at best		Population	nVar	pm	Run Time
					length	Its				
26	3	1	linspace(0.1,1,MaxIt);	567.02	45	50	200	1 to 50	0.95	21
27	3	1	linspace(0.1,1,MaxIt);	543.86	50	50	200	51 to 100	0.95	14.17
28	3	1	linspace(0.1,1,MaxIt);	540.52	50	50	200	51 to 100	0.95	14.17
29	3	1	linspace(0.1,1,MaxIt);	543.68	65	75	200	51 to 100	0.95	21.48
30	3	1	linspace(0.1,1,MaxIt);	575	47	50	200	101 to 150	0.95	14.94
31	3	1	linspace(0.1,1,MaxIt);	541	48	50	200	151 to 200	0.95	14.91
32	3	1	linspace(0.1,1,MaxIt);	573	44	50	200	201 to 250	0.95	15.12
33	3	1	linspace(0.1,1,MaxIt);	569	47	50	200	251 to 300	0.95	14.45
34	3	1	linspace(0.1,1,MaxIt);	559	45	50	200	301 to 350	0.95	14.82
35	3	1	linspace(0.1,1,MaxIt);	575	45	50	200	351 to 400	0.95	14.86
36	3	1	linspace(0.1,1,MaxIt);	565.77	47	50	200	401 to 450	0.95	14.92
37	3	1	linspace(0.1,1,MaxIt);	555.32	48	50	200	451 to 500	0.95	14.48
38	3	1	linspace(0.1,1,MaxIt);	556.44	45	50	200	451 to 500	0.95	14.96

TableA5.2. SOPSO shortest path Trajectory parameters 360segment lap.

Test	c1	c2	w	Length	Iteration at best		Population	nVar	pm	Run Time
					length	Its				
42	3	1	linspace(0.1,1,MaxIt);	465.66	43	50	200	1 to 30	0.95	15.50
43	3	1	linspace(0.1,1,MaxIt);	437.87	45	50	200	31 to 60	0.95	15.47
44	3	1	linspace(0.1,1,MaxIt);	465.49	41	50	200	61 to 90	0.95	15.42
45	3	1	linspace(0.1,1,MaxIt);	457.13	47	50	200	91 to 120	0.95	15.23
46	3	1	linspace(0.1,1,MaxIt);	441.81	48	50	200	121 to 150	0.95	14.74
47	3	1	linspace(0.1,1,MaxIt);	470.73	46	50	200	151 to 180	0.95	14.94
48	3	1	linspace(0.1,1,MaxIt);	465.84	48	50	200	181 to 210	0.95	14.95
49	3	1	linspace(0.1,1,MaxIt);	456.81	49	50	200	211 to 240	0.95	14.91
50	3	1	linspace(0.1,1,MaxIt);	468.94	43	50	200	241 to 270	0.95	18.33
51	3	1	linspace(0.1,1,MaxIt);	469.71	43	50	200	271 to 300	0.95	15.69
52	3	1	linspace(0.1,1,MaxIt);	462.26	45	50	200	301 to 330	0.95	15.67
53	3	1	linspace(0.1,1,MaxIt);	451.62	43	50	200	331 to 360	0.95	17.13
54	3	1	linspace(0.1,1,MaxIt);	5844.48	45	50	200	1 to 360	0.95	39.44
55	3	1	linspace(0.1,1,MaxIt);	5828.98	36	50	800	1 to 360	0.95	169.72

Appendix 6. Pareto front and trajectory plots

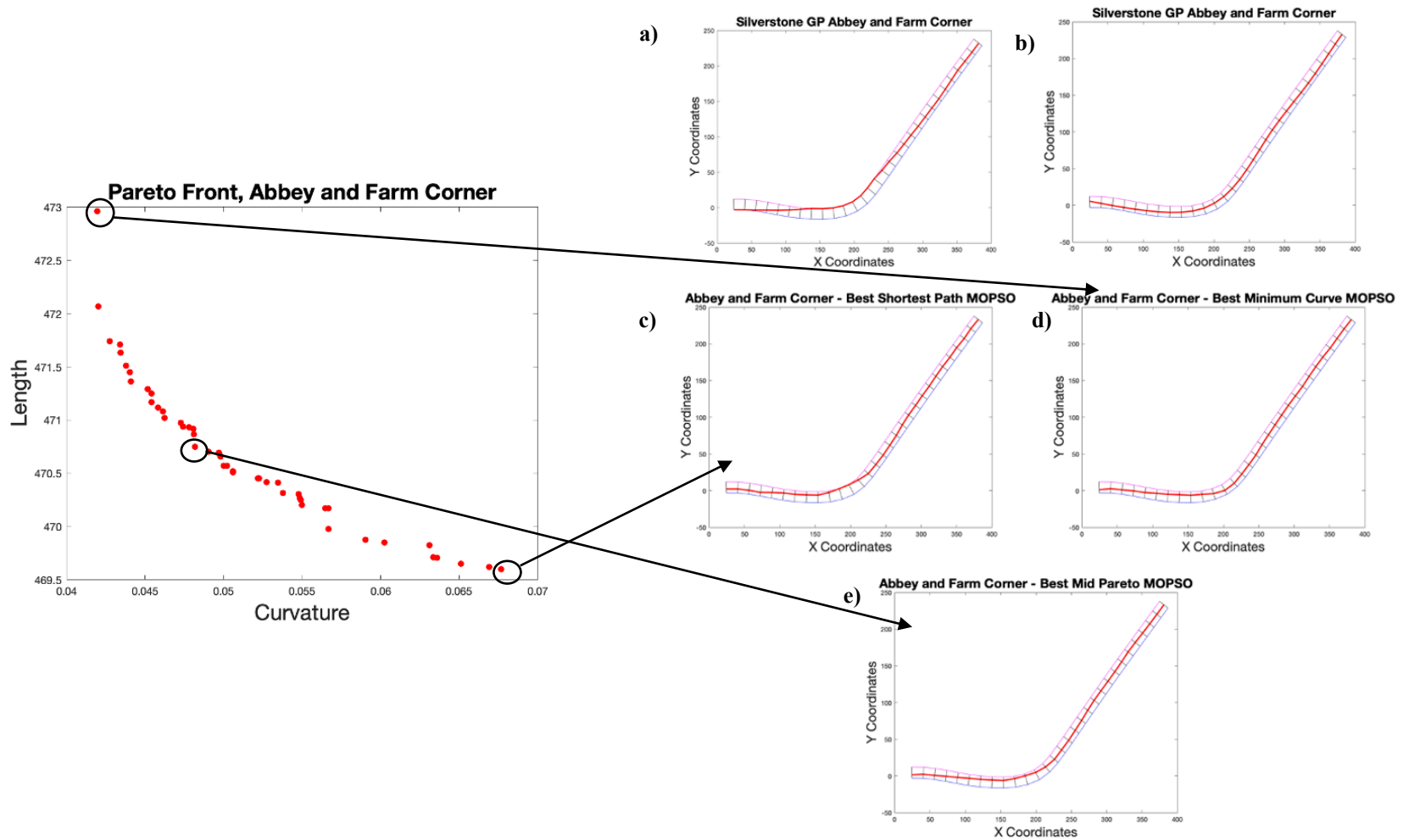


Figure A6.1. a) SOPSO Shortest Path and b) SOPSO minimum curvature vs MOPSO for Abbey and Farm Corner. c) Best shortest path, d) minimum curvature and e) mid-pareto front are presented from the MOPSO results as a comparison of trajectory path results.

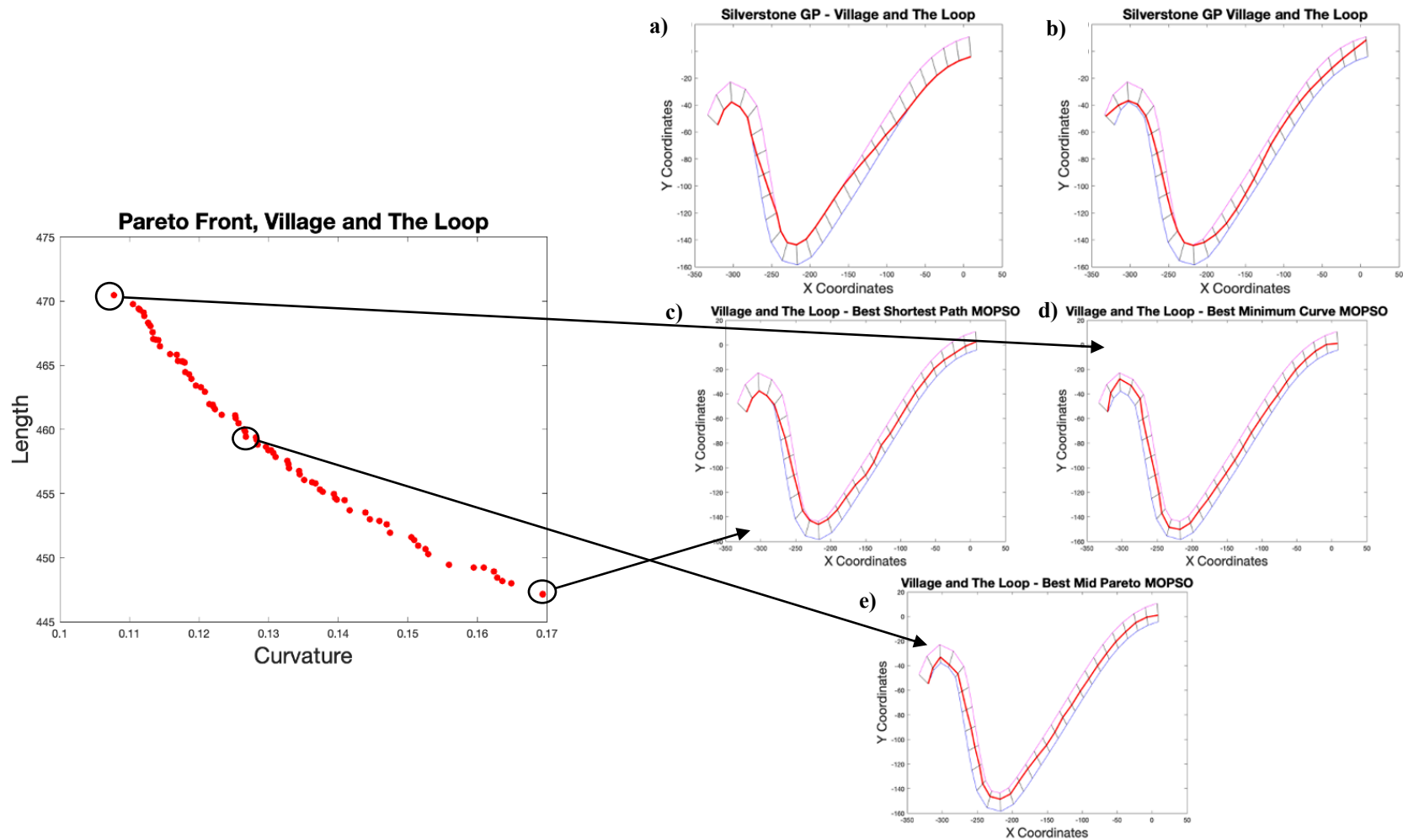


Figure A6.2. a) SOPS Shortest Path and b) SOPS minimum curvature vs MOPSO for Village and The Loop complex. c) Best shortest path, d) minimum curvature and e) mid-pareto front are presented from the MOPSO results as a comparison of trajectory path results.

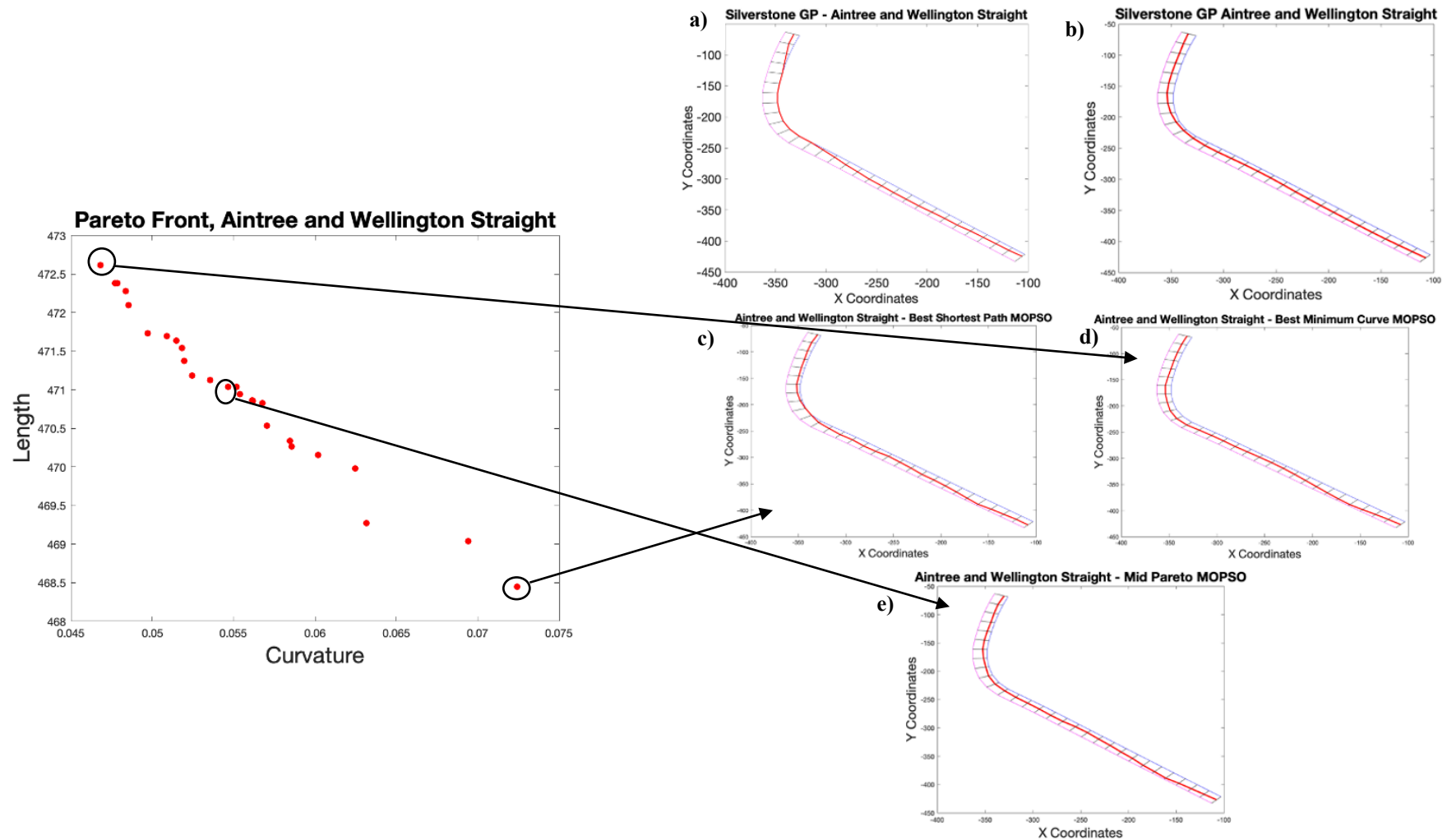


Figure A6.3. a) SOPSO Shortest Path and b) SOPSO minimum curvature vs MOPSO for Aintree and Wellington Straight. c) Best shortest path, d) minimum curvature and e) mid-pareto front are presented from the MOPSO results as a comparison of trajectory path results.

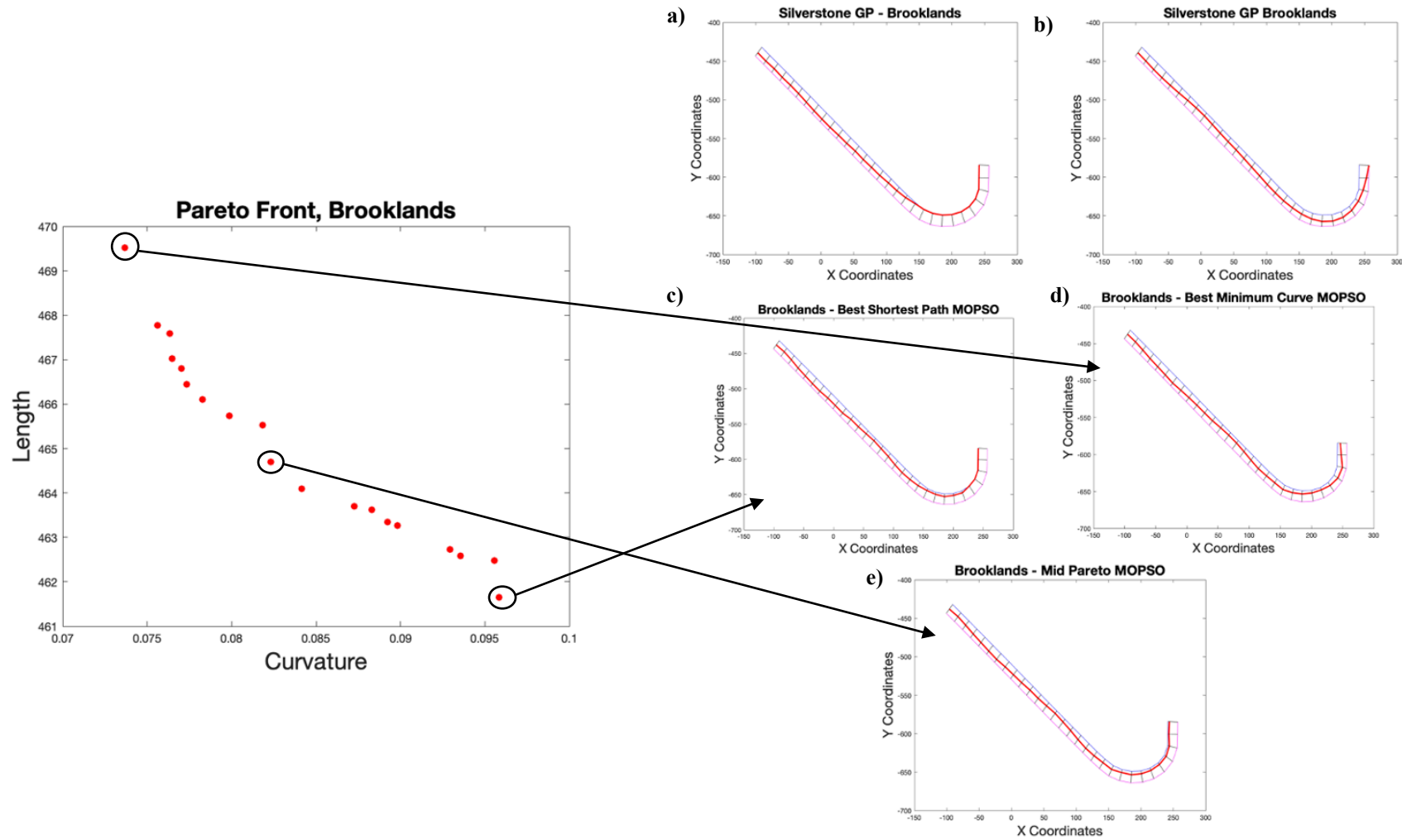


Figure A6.4. a) SOPSO Shortest Path and b) SOPSO minimum curvature vs MOPSO for Brooklands corner. c) Best shortest path, d) minimum curvature and e) mid-pareto front are presented from the MOPSO results as a comparison of trajectory path results.

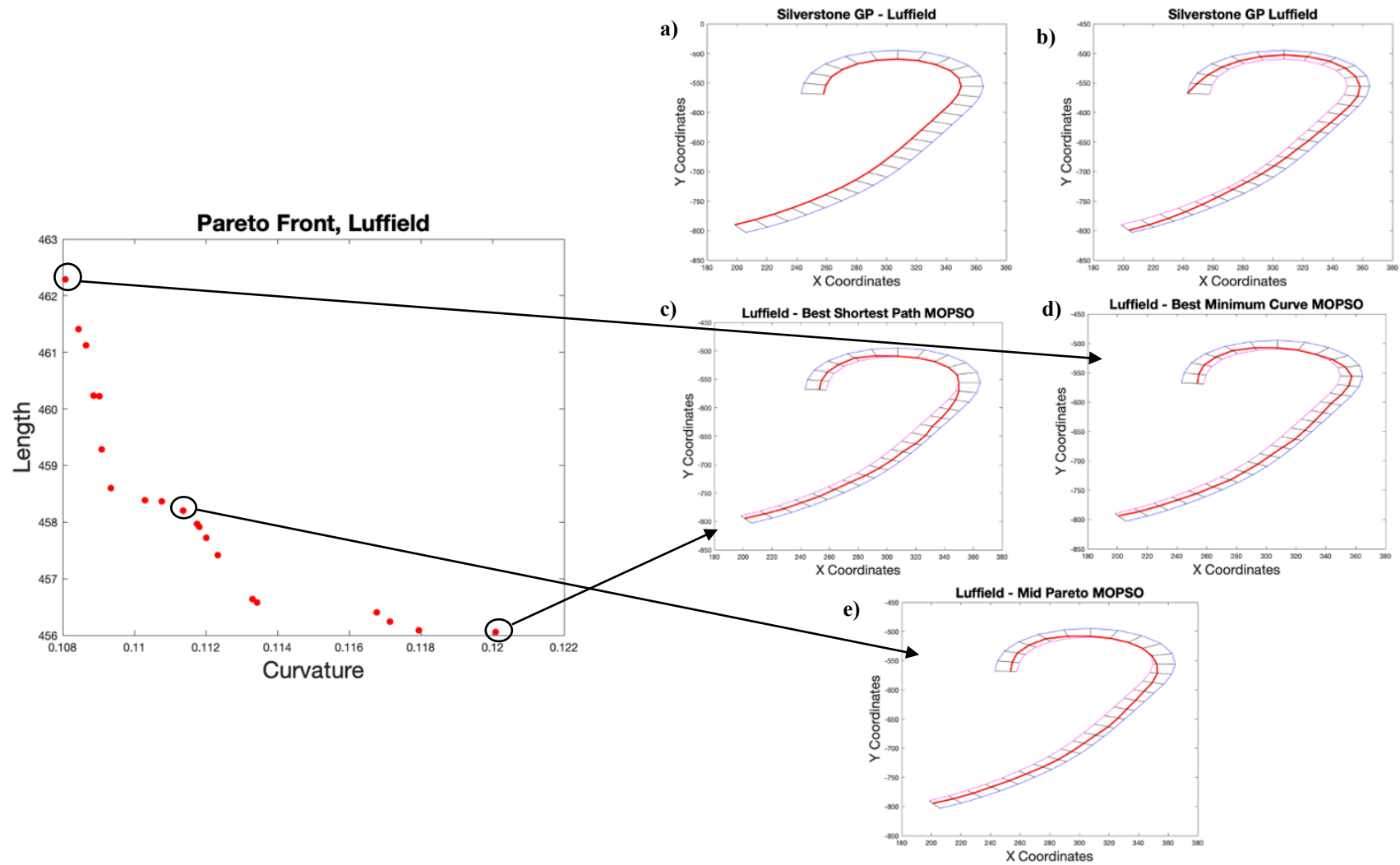


Figure A6.5. a) SOPSO Shortest Path and b) SOPSO minimum curvature vs MOPSO for Luffield corner. c) Best shortest path, d) minimum curvature and e) mid-pareto front are presented from the MOPSO results as a comparison of trajectory path results.

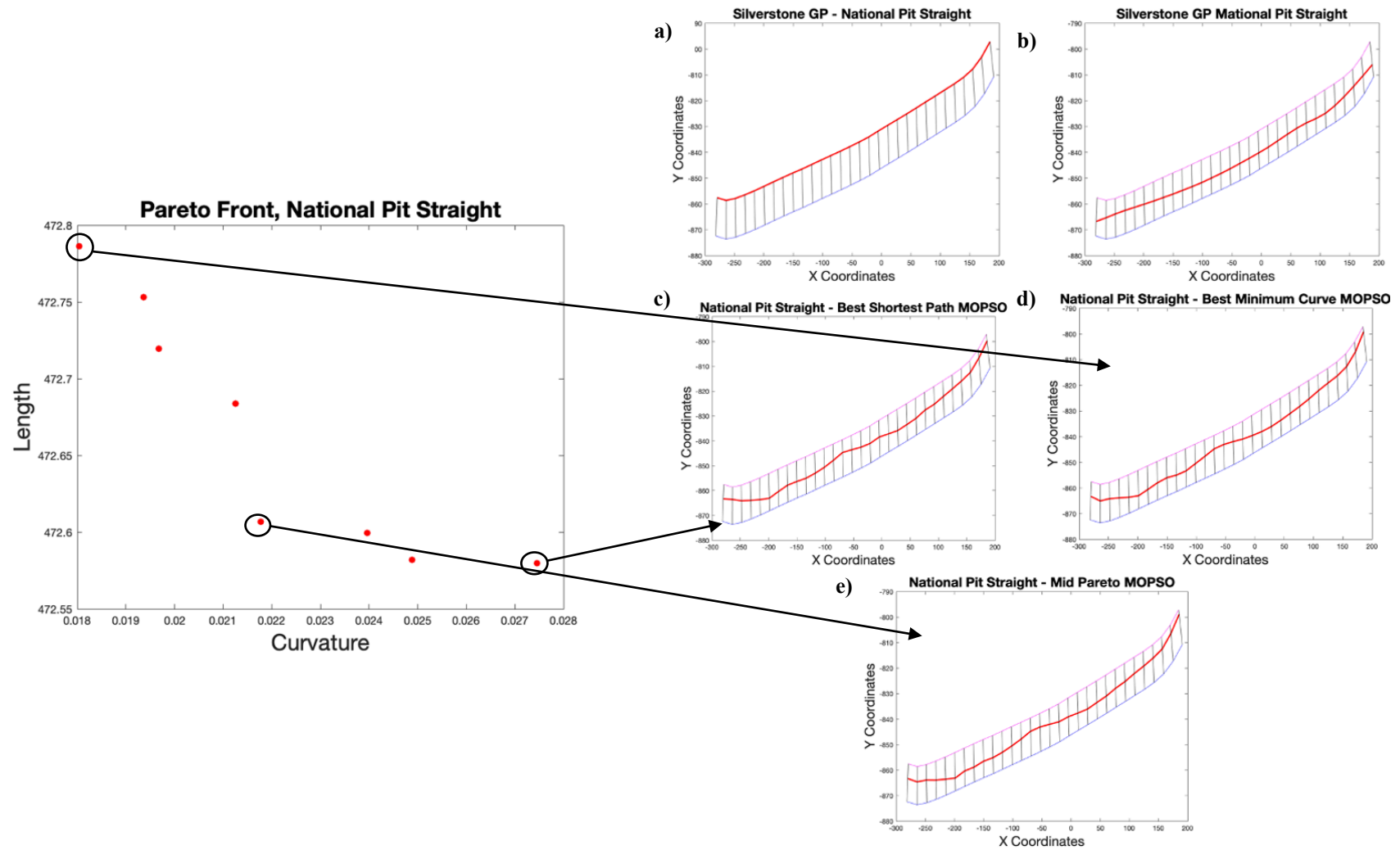


Figure A6.6. a) SOPSO Shortest Path and b) SOPSO minimum curvature vs MOPSO for National Pit Straight. c) Best shortest path, d) minimum curvature and e) mid-pareto front are presented from the MOPSO results as a comparison of trajectory path results.

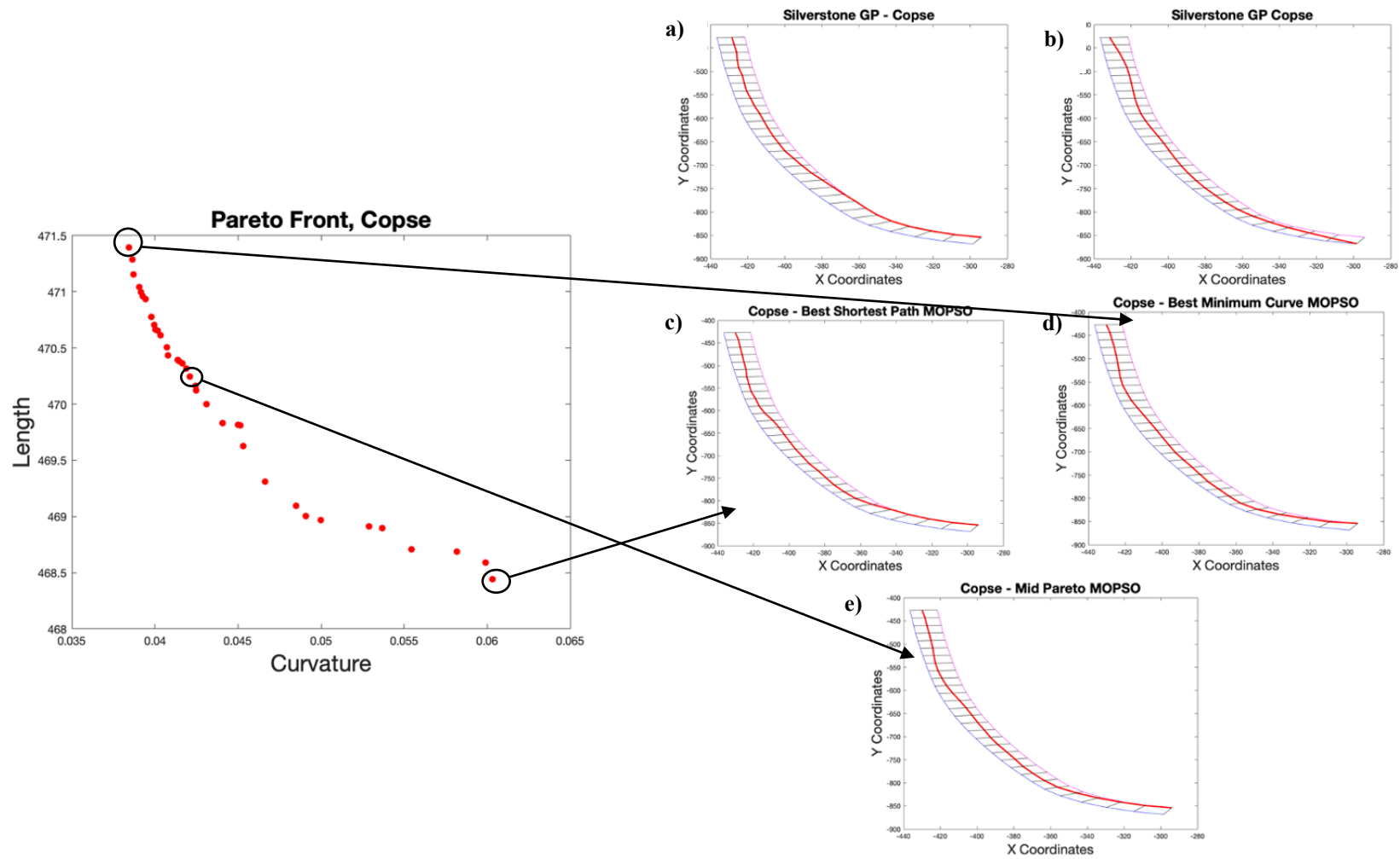


Figure A6.7. a) SOPSO Shortest Path and b) SOPSO minimum curvature vs MOPSO for Copse corner. c) Best shortest path, d) minimum curvature and e) mid-pareto front are presented from the MOPSO results as a comparison of trajectory path results.

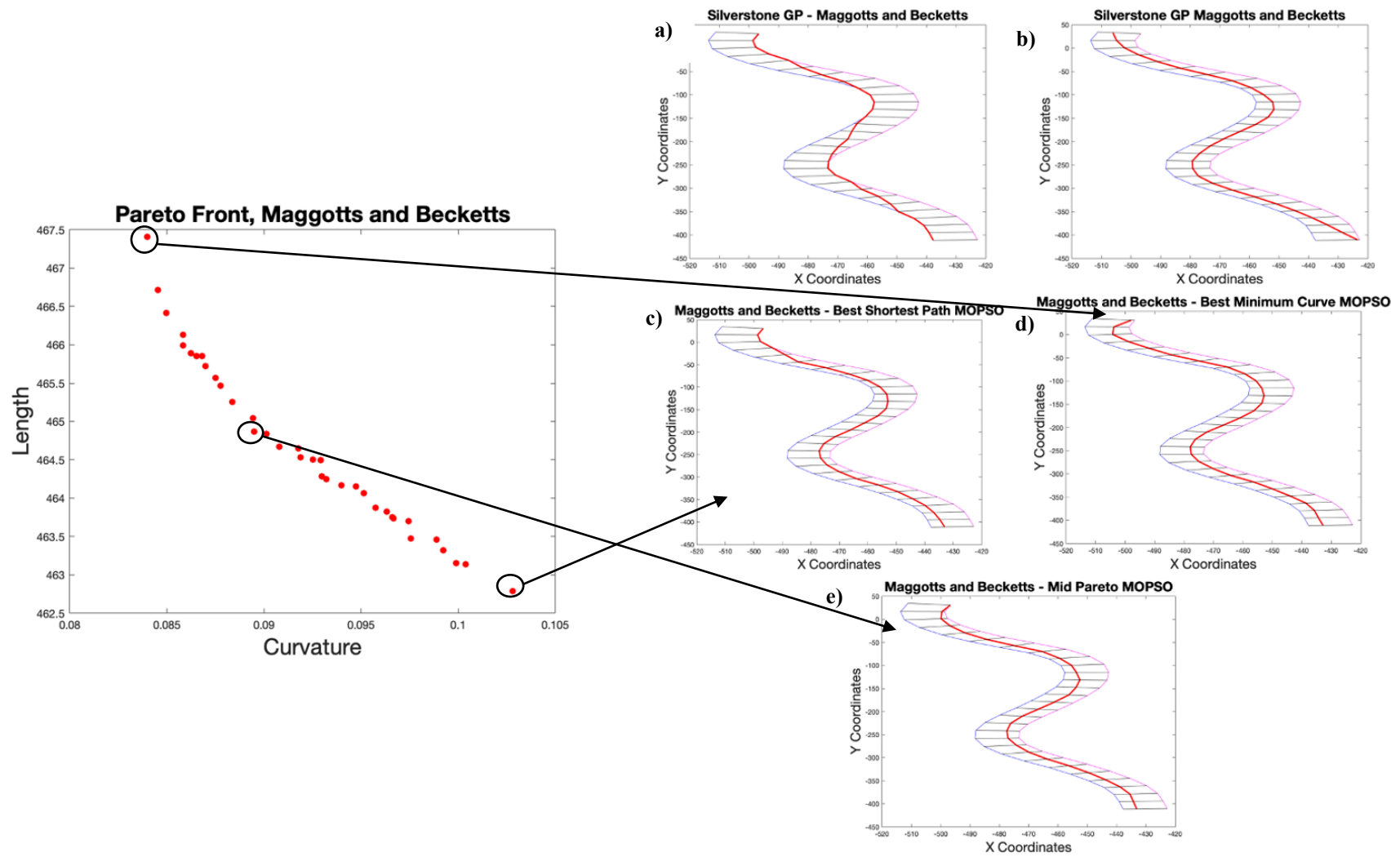


Figure A6.8. a) SOPSO Shortest Path and b) SOPSO minimum curvature vs MOPSO for the Maggotts and Becketts complex. c) Best shortest path, d) minimum curvature and e) mid-pareto front are presented from the MOPSO results as a comparison of trajectory path results.

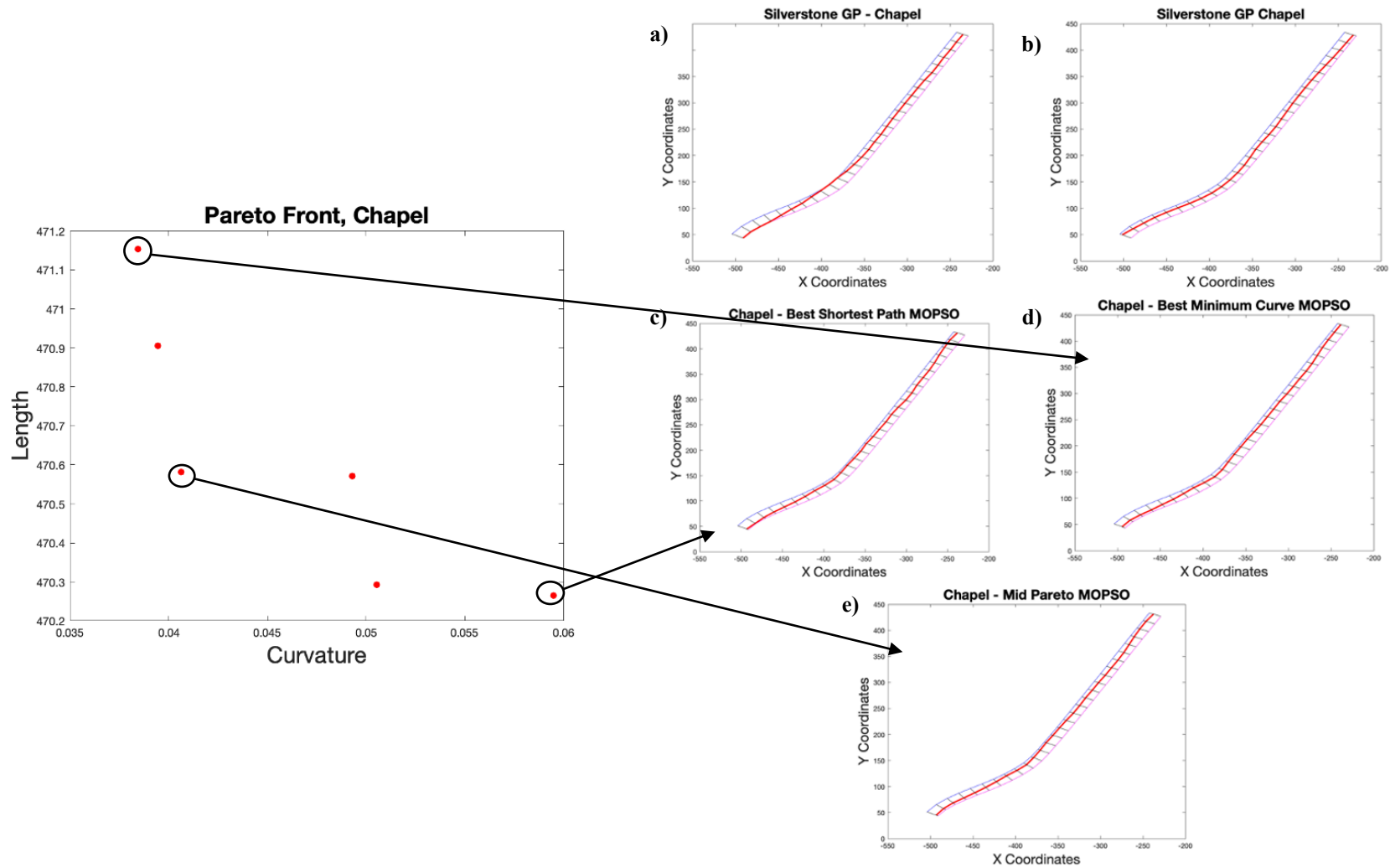


Figure A6.9. a) SOPSO Shortest Path and b) SOPSO minimum curvature vs MOPSO for Chapel corner. c) Best shortest path, d) minimum curvature and e) mid-pareto front are presented from the MOPSO results as a comparison of trajectory path results.

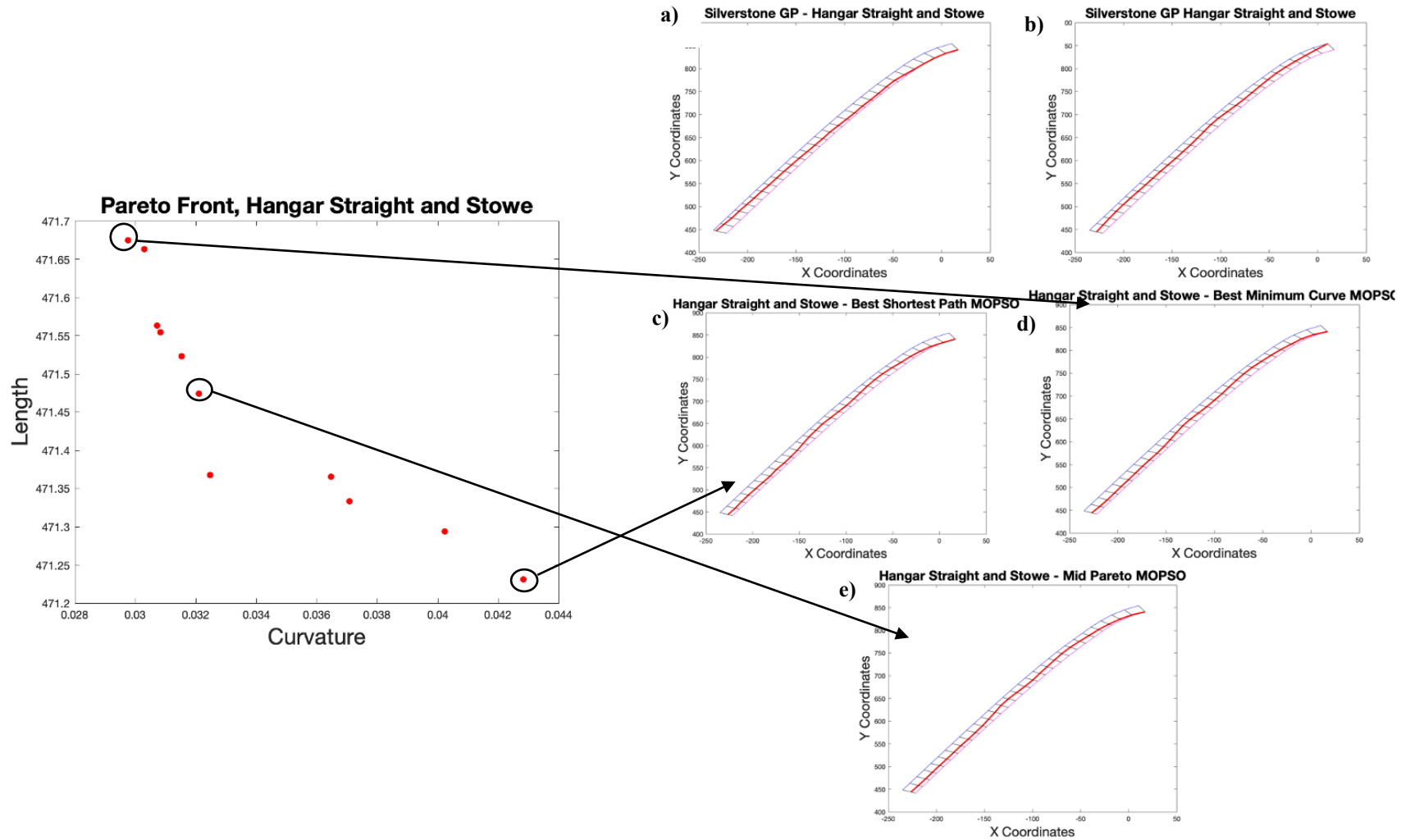


Figure A6.10. a) SOPSO Shortest Path and b) SOPSO minimum curvature vs MOPSO for Hangar Straight and Stowe corner. c) Best shortest path, d) minimum curvature and e) mid-pareto front are presented from the MOPSO results as a comparison of trajectory path results.

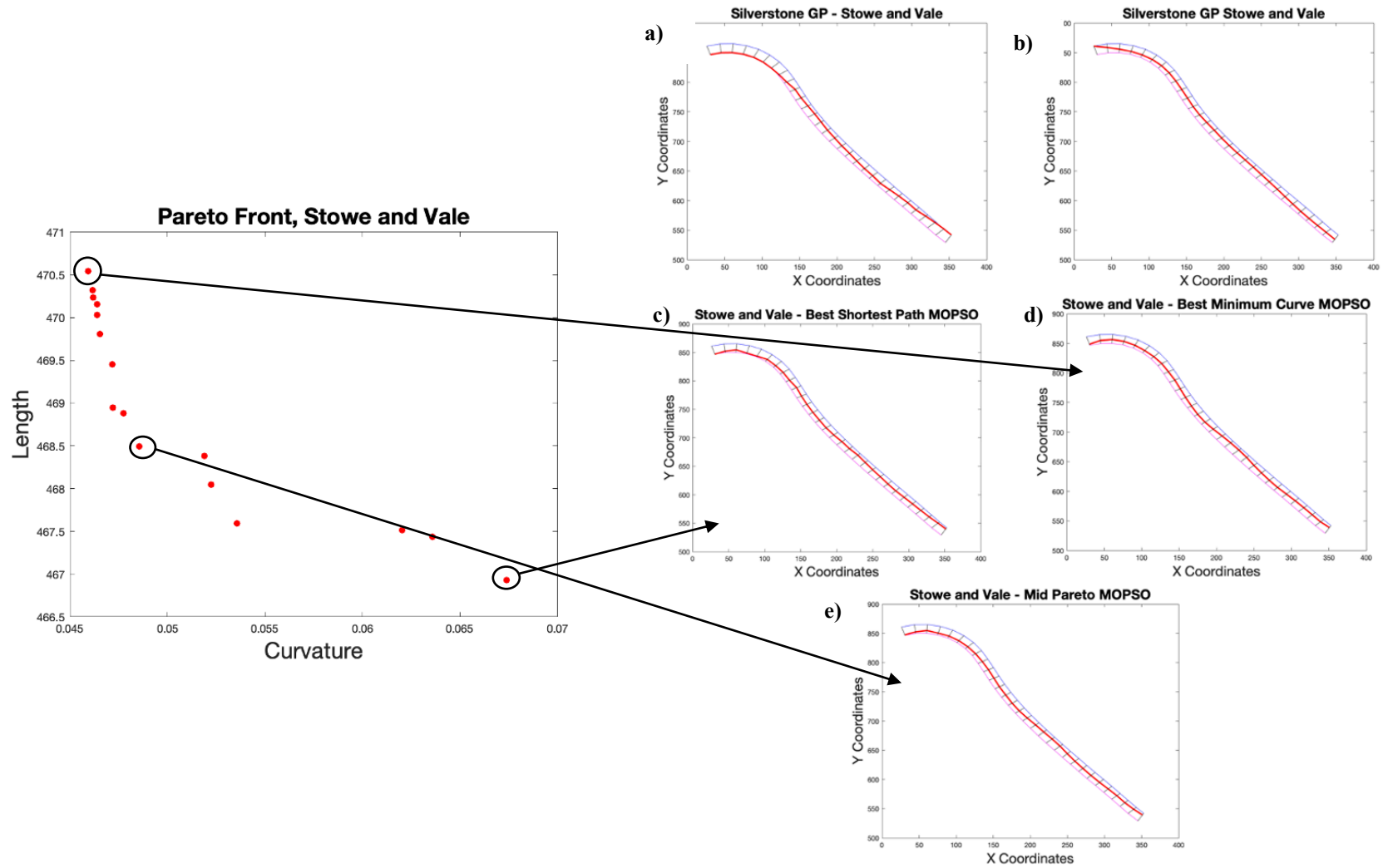


Figure A6.11. a) SOPSO Shortest Path and b) SOPSO minimum curvature vs MOPSO for Stowe and Vale corners. c) Best shortest path, d) minimum curvature and e) mid-pareto front are presented from the MOPSO results as a comparison of trajectory path results.

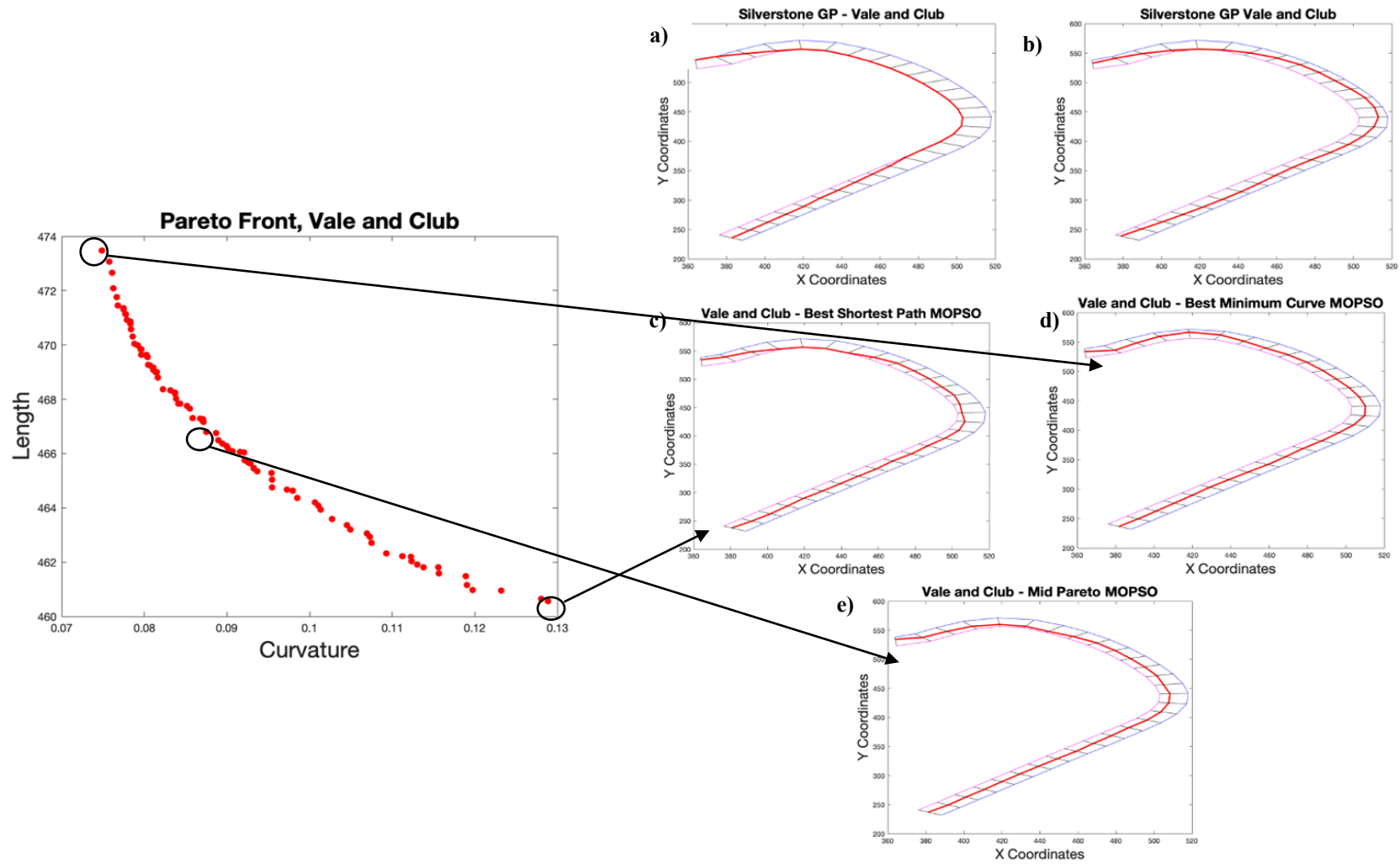


Figure A6.12. a) SOPSO Shortest Path and b) SOPSO minimum curvature vs MOPSO for Vale and Club corners. c) Best shortest path, d) minimum curvature and e) mid-pareto front are presented from the MOPSO results as a comparison of trajectory path results.

Appendix 7. Hybrid Energy Management

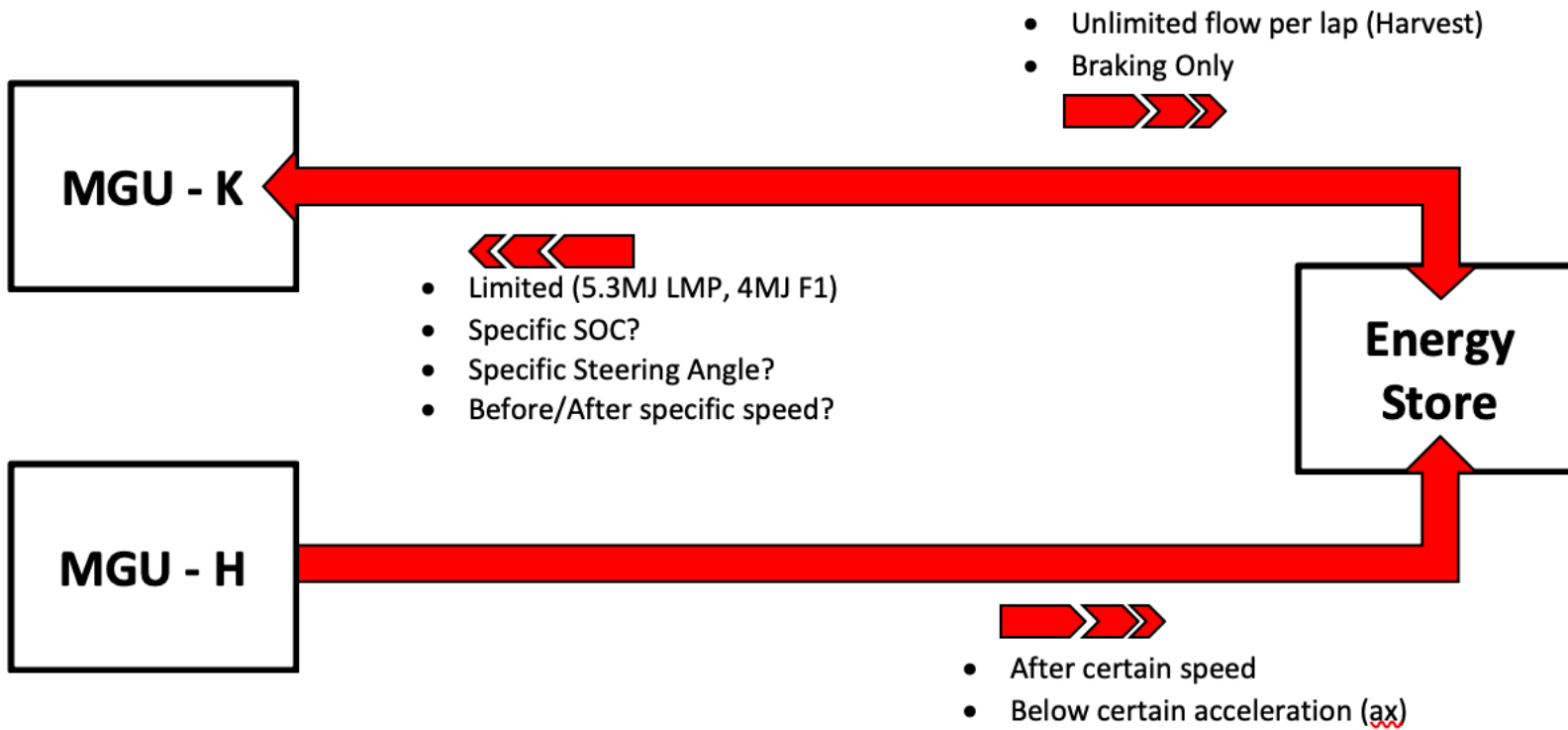


Figure A7.1. Proposed GT hybrid category - powertrain energy flow.

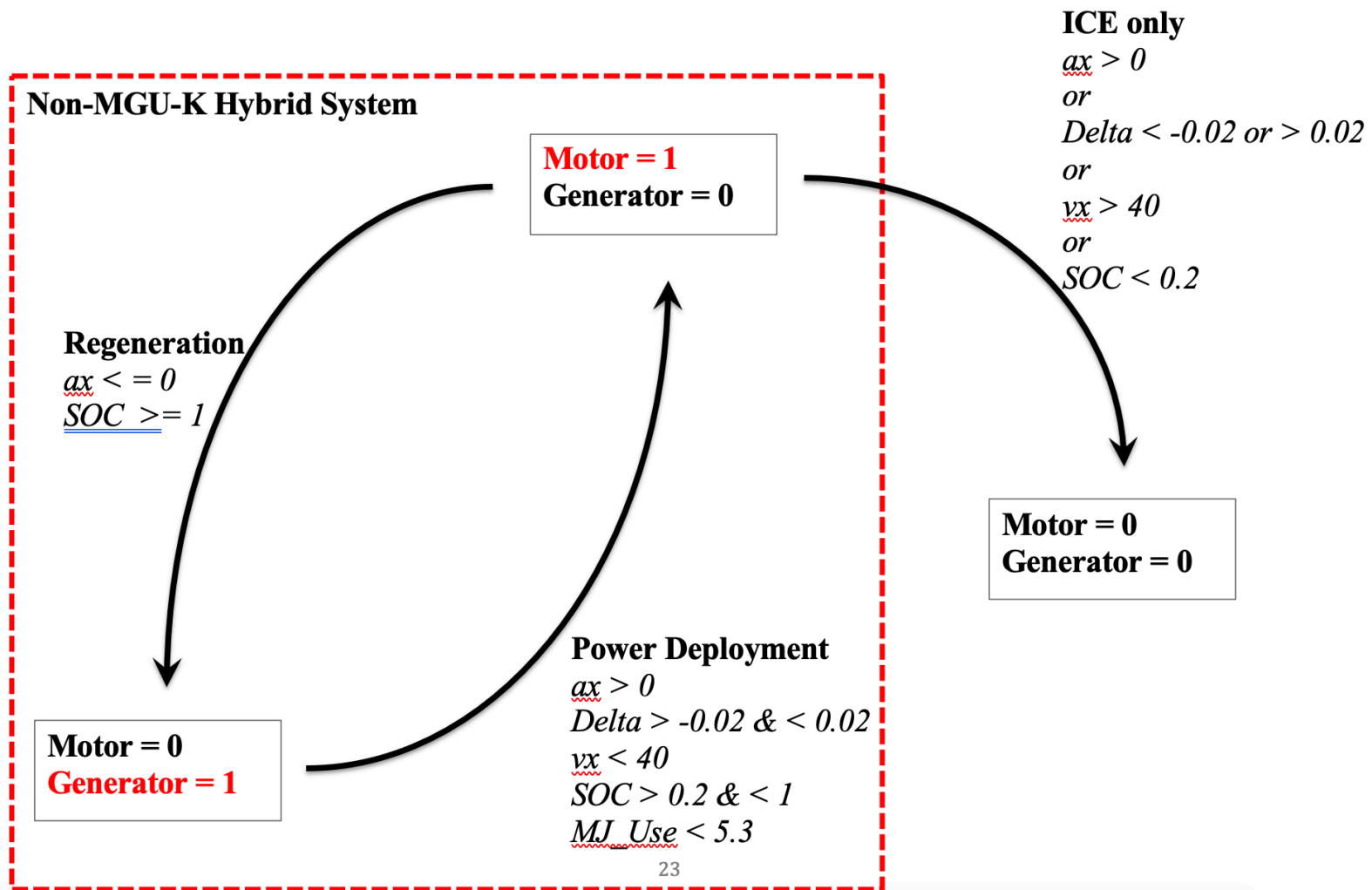


Figure A7.2. An example of variables used to control regeneration and hybrid power deployment, single MGU-K (non-MGU-H).

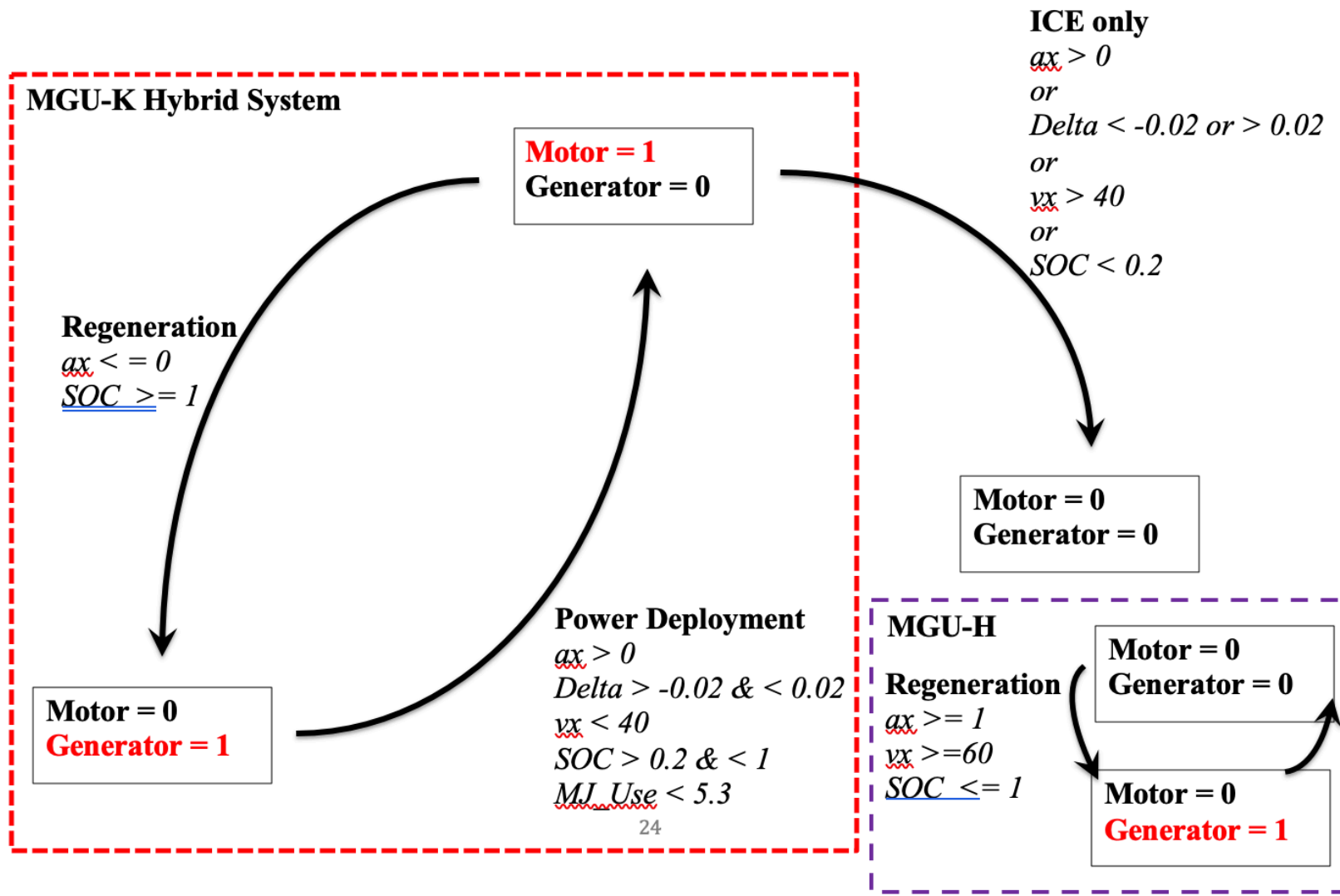


Figure A7.3. An example of variables used to control regeneration and hybrid power deployment, MGU-K/MGU-H system.

Appendix 8. Simulink Model with Hybrid Powertrain.

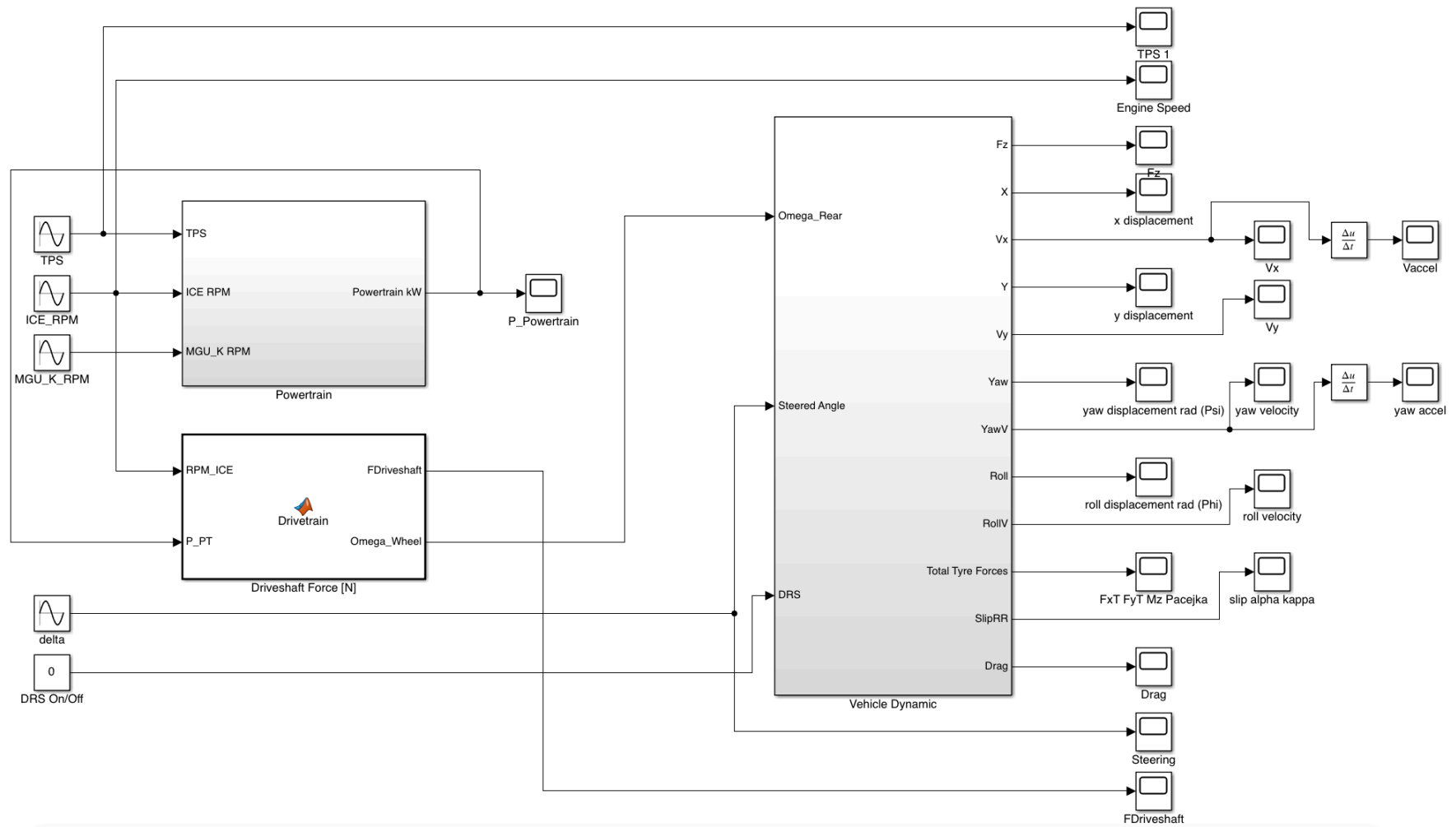


Figure A8.1. Transient dynamic Simulink model - hybrid powertrain and vehicle layout.

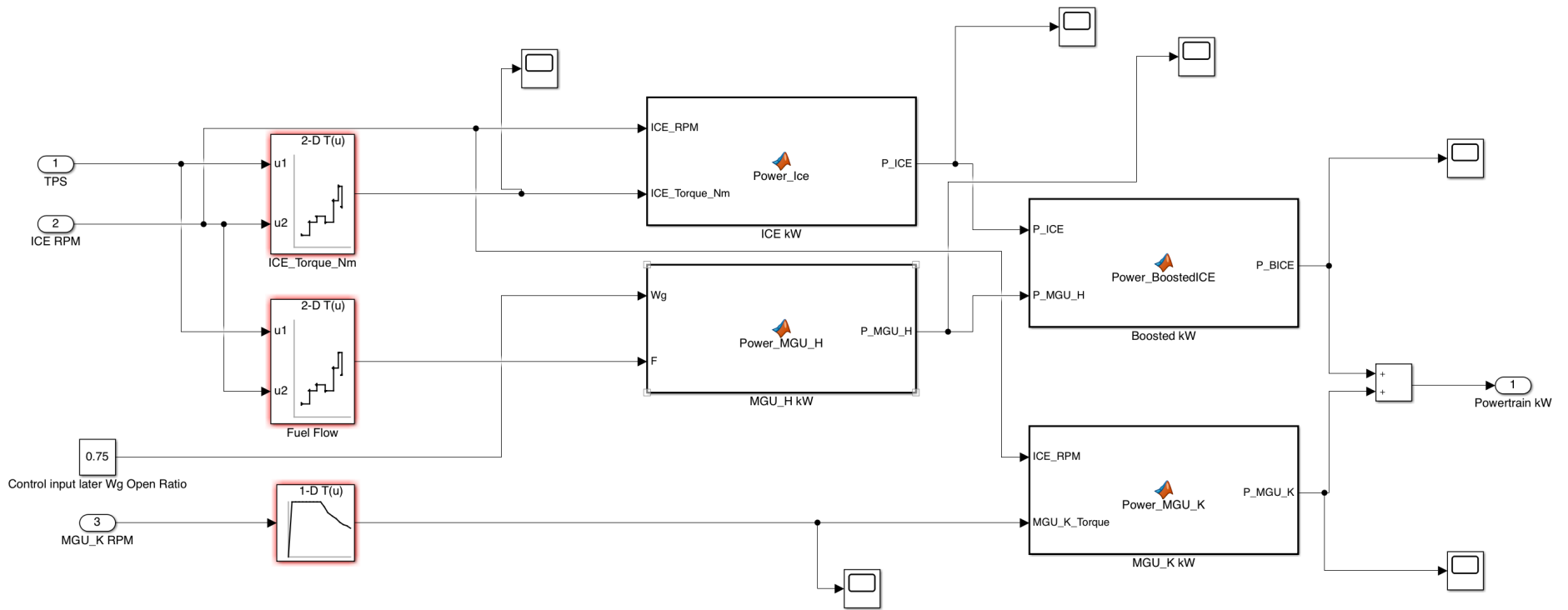


Figure A8.2. Transient dynamic Simulink model - hybrid powertrain sub-system.

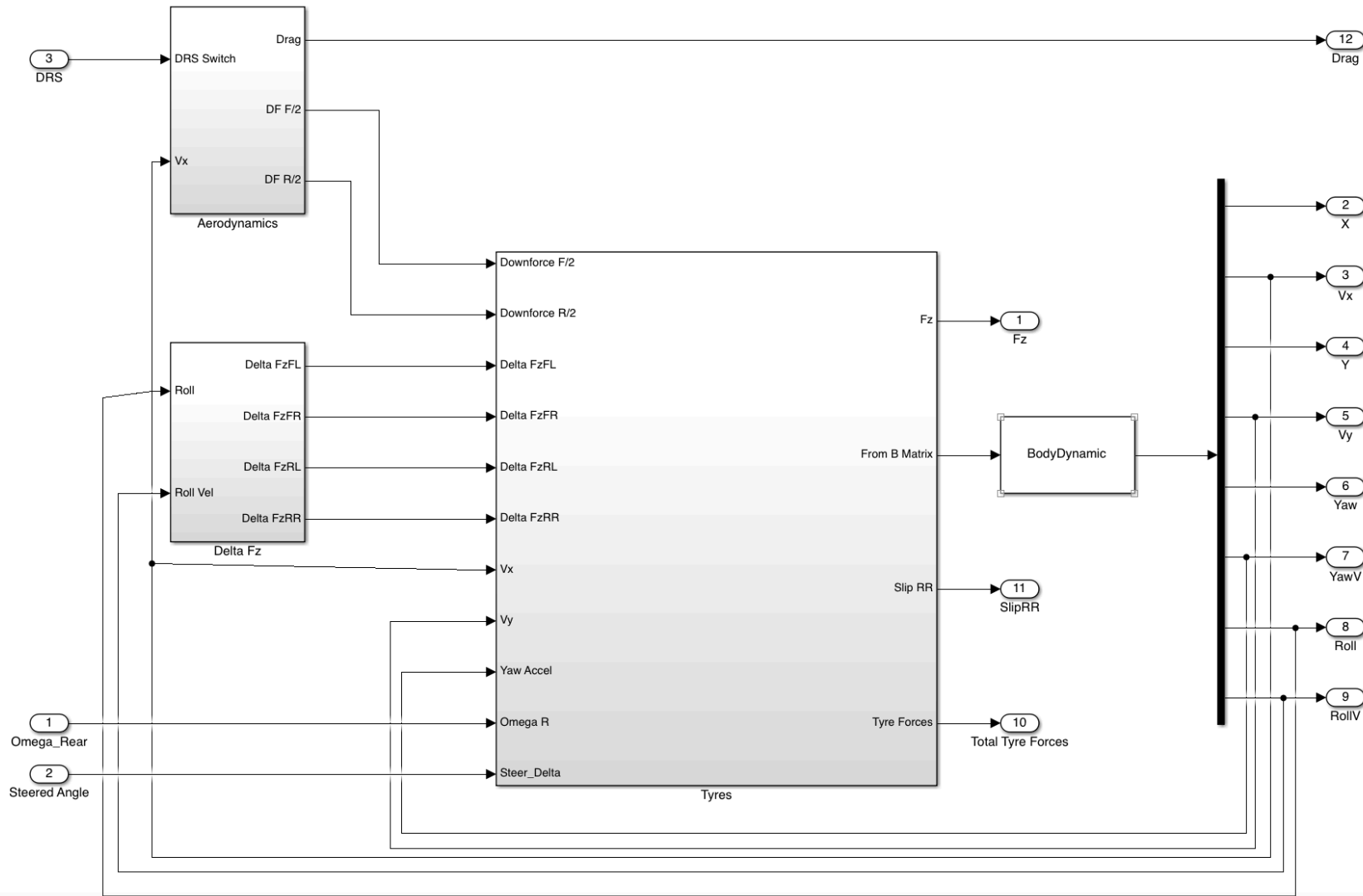
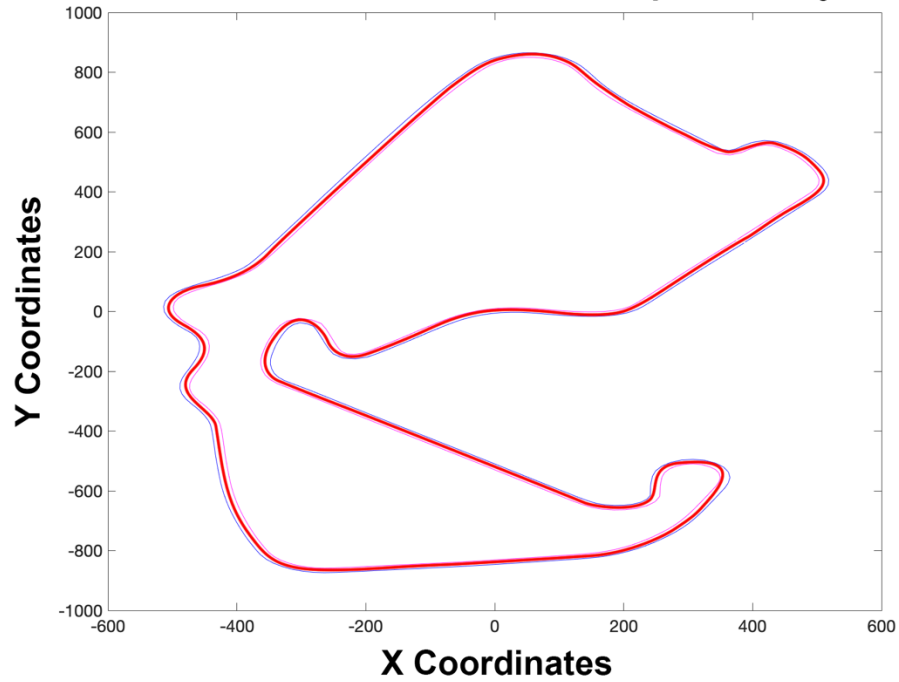


Figure A8.3. Transient dynamic Simulink model – dynamic behaviour sub-system.

Appendix 9. Final Trajectory Plots

Silverstone GP - MOPSO 2.02.106 Lap Time Trajectory



Silverstone GP - 5.3MJ Hybrid Deployment Trajectory

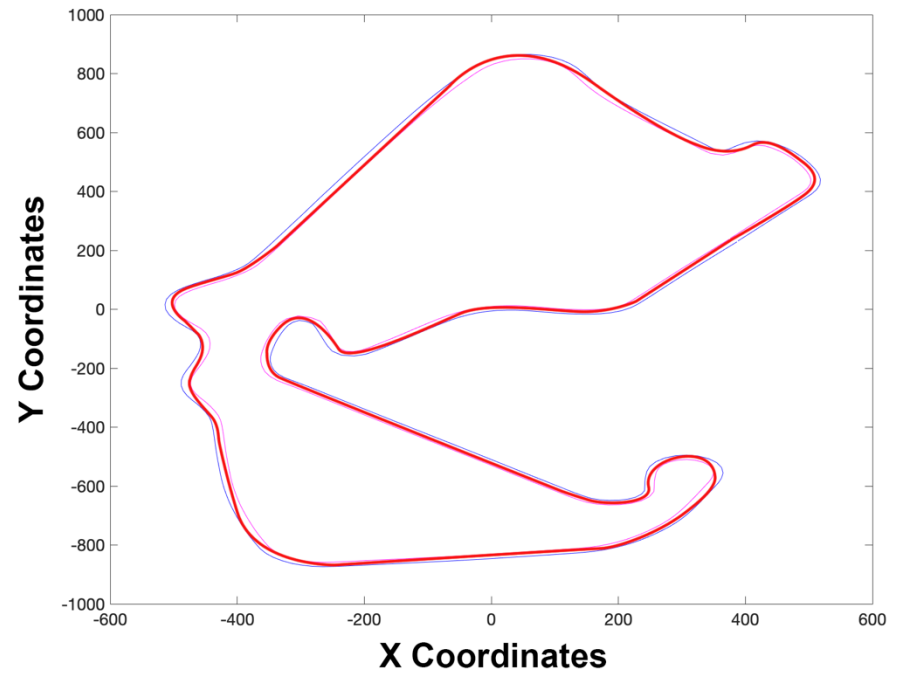


Figure A9.1. Smooth spline interpolation of the 2.02.106 and 1.58.371 MOPSO lap times.

Silverstone GP - MOPSO 2.02.106 Lap Time Trajectory

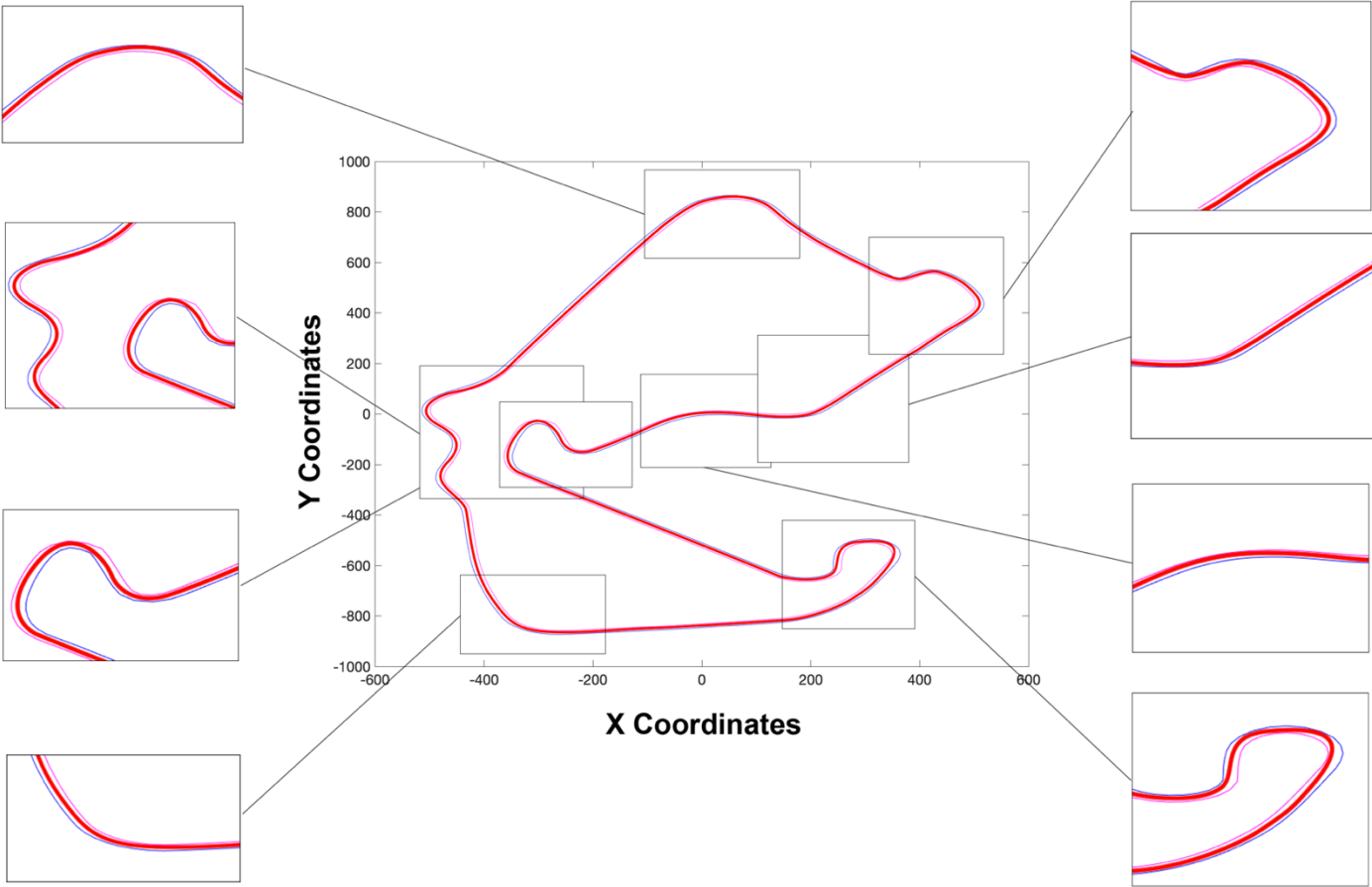


Figure A9.2. Detailed sections of all corners of the Silverstone GP circuit for the best lap-time for a non-hybrid vehicle.

Silverstone GP - 5.3MJ Hybrid Deployment Trajectory

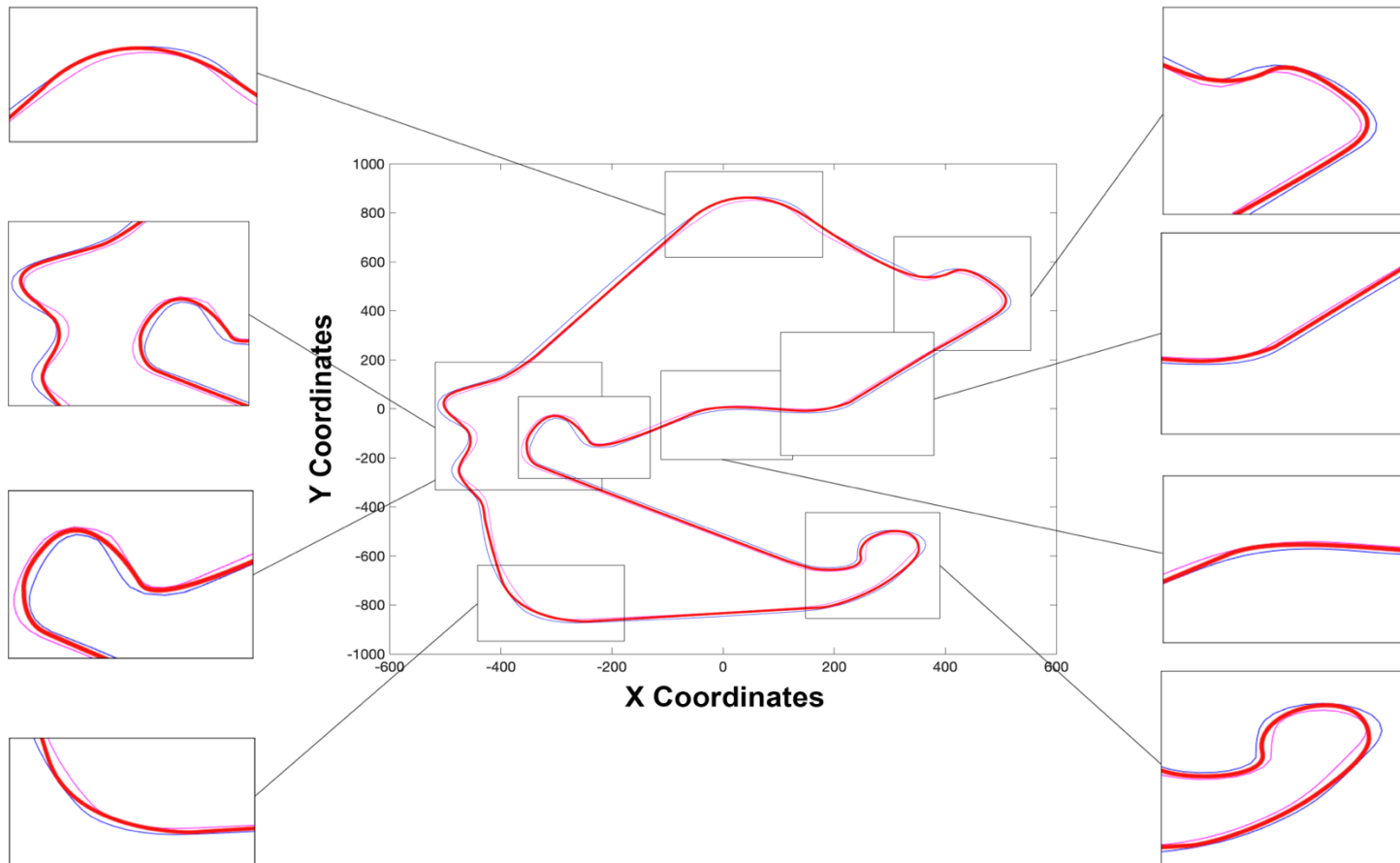


Figure A9.3. Detailed sections of all corners of the Silverstone GP circuit for the best lap-time for a hybrid vehicle.

Appendix 10 – Equations of Motion Derivation

Assuming a three-coordinate system (Figure 1.6), the vehicles fixed frame (V_{FF}), is rotated with a yaw angle (ψ) about the z-axis of the vehicles inertia frame (V_{IF}), where R_V is the vehicle yaw rotation matrix:

$$\mathbf{R}_V = \begin{bmatrix} \cos \psi & -\sin \psi & 0 \\ \sin \psi & \cos \psi & 0 \\ 0 & 0 & 1 \end{bmatrix} \quad (\text{A10.1})$$

Pitch (θ), is the rotation around the y-axis and therefore denoting the chassis rotation frame as V_{CF} , and the chassis rotation matrix:

$$\mathbf{R}_C = \begin{bmatrix} \cos \theta & 0 & \sin \theta \\ 0 & 1 & 0 \\ -\sin \theta & 0 & \cos \theta \end{bmatrix} \quad (\text{A10.2})$$

The final rotation frame around the body (V_{BF}), is the roll angle (ϕ) around the x-axis, creating the body rotation matrix:

$$\mathbf{R}_B = \begin{bmatrix} 1 & 0 & 0 \\ 0 & \cos \phi & -\sin \phi \\ 0 & \sin \phi & \cos \phi \end{bmatrix} \quad (\text{A10.3})$$

The centre of gravity position in the body rotational frame is \hat{h}_B which is equal to $[0 \ 0 \ h]^T$, the centre of gravity height above ground with the body sat on a flat plane with no roll or pitch angle. Therefore, the centre of gravity position in V_{FF} :

$$\hat{h}_V = \mathbf{R}_C \mathbf{R}_B \hat{h}_B \quad (\text{A10.4})$$

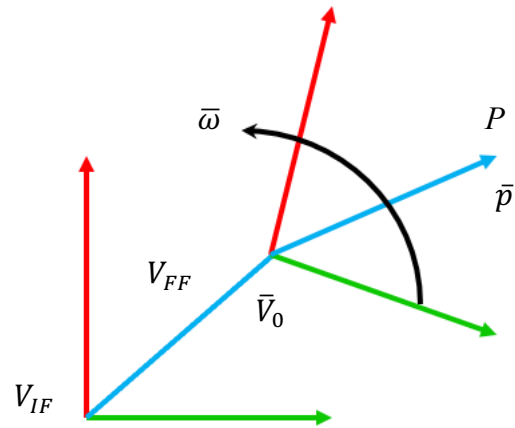


Figure A10.1 – Inertia Frame and vehicle fixed frame, rotating and translating.

Point P , consists of coordinates \bar{p} with respect to the vehicle frame that is travelling at a velocity with respect to the inertia frame. Given a vector \bar{V} , then $\frac{d}{dt}\Big|_{IF} \bar{V} = \frac{d}{dt}\Big|_{FF} \bar{V} + \bar{\omega} \times \bar{V}$, the velocity of P is therefore:

$$\bar{V}_P = \bar{V}_0 + \frac{d}{dt}\Big|_{IF} \bar{p} = \bar{V}_0 + \frac{d}{dt}\Big|_{FF} \bar{p} + \bar{\omega} \times \bar{p} \quad (\text{A10.5})$$

Acceleration is therefore

$$\begin{aligned}
 \bar{a}_p &= \frac{d}{dt}\Big|_{FF} \left(\bar{V}_0 + \frac{d}{dt}\Big|_{FF} \bar{p} + \bar{\omega} \times \bar{p} \right) + \bar{\omega} \times \left(\bar{V}_0 + \frac{d}{dt}\Big|_{FF} \bar{p} + \bar{\omega} \times \bar{p} \right) \\
 &= \frac{d}{dt}\Big|_{FF} \bar{V}_0 + \frac{d^2}{dt^2}\Big|_{FF} \bar{p} + \frac{d}{dt}\Big|_{FF} \bar{p} + \bar{\omega} \times \bar{p} \times \bar{\omega} \times (\bar{\omega} \times \bar{p}) + 2\bar{\omega} \times \frac{d}{dt}\Big|_{FF} \bar{p}
 \end{aligned}
 \tag{A10.6}$$

External forces acting on a rigid body (B), utilising the Newton-Euler rule is defined as:

$$\int_B \bar{a}_p dm_p = m\bar{a}_G = \bar{F}
 \tag{A10.7}$$

where

dm_p are all mass elements

\bar{a}_G is the acceleration at the centre of mass.

Therefore, the total external moments are;

$$\frac{d}{dt}\Big|_{IF} \int_B \bar{p} \times \bar{V}_p dm_p = \frac{d}{dt}\Big|_{IF} \mathbf{I}_{VFF} \bar{\omega}_{IF} = \bar{M}
 \tag{A10.8}$$

where

\mathbf{I}_{VFF} is the inertia moments matrix in respect to the vehicle fixed frame.

$$\bar{\omega}_{IF} = [\dot{\phi} \quad \dot{\theta} \quad \dot{\psi}]^T$$

Utilising (A10.7) and (A10.8) and where the angular velocity of the vehicle fixed frame equals $\bar{\omega}_V = [0 \quad 0 \quad \dot{\psi}]^T$ then

$$\mathbf{I}_{VFF} \bar{\omega}_{IF} + \bar{\omega}_V \times \mathbf{I}_{VFF} \bar{\omega}_{IF} = \bar{M} \quad (\text{A10.9}).$$

In (A10.9) the inertia is constant with respect to the vehicle fixed frame, whereas the inertia is typically measured from the body frame. The inertia, however, can be calculated using:

$$\mathbf{I}_{VFF} = \mathbf{R}_C \mathbf{R}_B \mathbf{I}_B \mathbf{R}_B^T \mathbf{R}_C^T$$

where

\mathbf{I}_B is the moment of inertia around the body frame. It is assumed for simplicity with cross terms neglected that

$$\mathbf{I}_B = \begin{bmatrix} I_{xx} & 0 & 0 \\ 0 & I_{yy} & 0 \\ 0 & 0 & I_{zz} \end{bmatrix} \quad (\text{A10.10})$$

which gives

$$\mathbf{I}_{VFF} = \begin{bmatrix} I_1 & I_2 & I_3 \\ I_2 & I_4 & I_5 \\ I_3 & I_5 & I_6 \end{bmatrix} \quad (\text{A10.11})$$

where

$$I_1 = \cos^2(\theta) I_{xx} + \sin^2(\theta) \sin^2(\phi) I_{yy} + \sin^2(\theta) \cos^2(\phi) I_{zz}$$

$$I_2 = \sin(\theta) \sin(\phi) \cos(\phi) (I_{yy} - I_{zz})$$

$$I_3 = -\sin(\theta) \cos(\theta) (I_{xx} - I_{yy} + \cos^2(\phi) (I_{yy} - I_{zz}))$$

$$\begin{aligned}
I_4 &= \cos^2(\phi)I_{yy} + \sin^2(\phi)I_{zz} \\
I_5 &= \sin(\phi) \cos(\phi) \cos(\theta) (I_{yy} - I_{zz}) \\
I_3 &= \sin^2(\theta)I_{xx} + \cos^2(\theta) (\sin^2(\phi)I_{yy} + \cos^2(\phi)I_{zz})
\end{aligned}$$

Assuming the vehicle frame is at the centre of mass in the x-y plane, $\bar{p} = 0$ in (A10.5). Therefore, the velocity in the x and y directions are $\bar{V} = [V_x \ V_y]^T$.

The force equations are found by a combination of (1.10), (1.11) from Chapter 1 and (A10.6), (A10.7). It is assumed $\bar{p} = 0$ and all derivatives thereof. Similar can be carried out for the equations of motion around the yaw axis by combining (1.10), (1.11), (1.12), (A10.9) and (A10.11). Reshuffling of the equations final equations of motion are provided in (1.6) to (1.9).